Universidad de Málaga

Escuela Técnica Superior de Ingeniería de Telecomunicación

Programa de Doctorado en Ingeniería de Telecomunicación

TESIS DOCTORAL

Metasurface-Based Leaky-Wave Antennas with Aperture Synthesis Capabilities

Autor:

Pablo Mateos Ruiz

Directores:

Elena Abdo Sánchez

Carlos Camacho Peñalosa

Málaga, 2025

AUTOR: Pablo Mateos Ruiz

http://orcid.org/0000-0002-1299-4511

EDITA: Publicaciones y Divulgación Científica. Universidad de Málaga

DECLARACIÓN DE AUTORÍA Y ORIGINALIDAD DE LA TESIS PRESENTADA PARA OBTENER EL TÍTULO DE DOCTOR

D. PABLO MATEOS RUIZ
Estudiante del programa de doctorado EN INGENIERÍA DE TELECOMUNICACIÓN de la Universidad de Málaga, autor/a de la tesis, presentada para la obtención del título de doctor por la Universidad de Málaga, titulada: METASURFACE-BASED LEAKY-WAVE ANTENNAS WITH APERTURE SYNTHESIS CAPABILITIES

Realizada bajo la tutorización de ELENA ABDO SÁNCHEZ y dirección de ELENA ABDO SÁNCHEZ Y CARLOS CAMACHO PEÑALOSA

DECLARO QUE:

La tesis presentada es una obra original que no infringe los derechos de propiedad intelectual ni los derechos de propiedad industrial u otros, conforme al ordenamiento jurídico vigente (Real Decreto Legislativo 1/1996, de 12 de abril, por el que se aprueba el texto refundido de la Ley de Propiedad Intelectual, regularizando, aclarando y armonizando las disposiciones legales vigentes sobre la materia), modificado por la Ley 2/2019, de 1 de marzo.

Igualmente asumo, ante a la Universidad de Málaga y ante cualquier otra instancia, la responsabilidad que pudiera derivarse en caso de plagio de contenidos en la tesis presentada, conforme al ordenamiento jurídico vigente.

En Málaga, a 2 de DICIEMBRE de 2025

Fdo.: PABLO MATEOS RUIZ Doctorando	Fdo.: ELENA ABDO SÁNCHEZ Tutora
Fdo.: ELENA ABDO SÁNCHEZ Directores de tesis	CARLOS CAMACHO PEÑALOSA

Edificio Pabellón de Gobierno. Campus El Ejido. 29071
Tel.: 952 13 10 28 / 952 13 14 61 / 952 13 71 10
E-mail: doctorado@uma.es

UNIVERSIDAD DE MÁLAGA

Departamento de Ingeniería de Comunicaciones

AUTORIZACIÓN PARA LA LECTURA DE LA TESIS

D. Carlos Camacho Peñalosa y D.ª Elena Abdo Sánchez, profesores doctores del Departamento de Ingeniería de Comunicaciones de la Universidad de Málaga,

CERTIFICAN:

Que D. Pablo Mateos Ruiz, ha realizado en el Departamento de Ingeniería de Comunicaciones de la Universidad de Málaga bajo su dirección el trabajo de investigación correspondiente a su TESIS DOCTORAL titulada:

"METASURFACE-BASED LEAKY-WAVE ANTENNAS WITH APERTURE SYNTHESIS CAPABILITIES"

En dicho trabajo, se han desarrollado antenas de onda de fuga (LWA) basadas en metasuperficies, buscando mejorar el ancho de banda, la eficiencia y el control del haz. Se combinan enfoques de óptica geométrica y ondas de fuga para superar limitaciones de las antenas Fabry-Pérot. Además, se han diseñado LWA unidimensionales y bidimensionales con metasuperficies de Huygens bianisótropas, logrando control total del campo y del diagrama de radiación sin necesidad de quiralidad. Finalmente, se han estudiado cristales líquidos como materiales sintonizables, sentando bases para antenas reconfigurables y más eficientes. Esto ha dado lugar a varias publicaciones científicas y aportaciones a congresos internacionales, demostrando que se trata de un trabajo original de investigación.

Por todo ello, consideran que esta tesis es apta para su presentación al tribunal que ha de juzgarla. Igualmente, certifican que las publicaciones que avalan la tesis no han sido empleadas en trabajos anteriores a la misma. Y para que conste a efectos de lo establecido en el Real Decreto 99/2011 de 28 de enero (con modificación en el RD 576/2023), por el que se regulan las enseñanzas oficiales de doctorado, AUTORIZAN la presentación de esta tesis en la Universidad de Málaga.

Málaga, 2 de diciembre de 2025

Los directores:

Fdo.: Carlos Camacho Peñalosa

Fdo.: Elena Abdo Sánchez

Agradecimientos

Que me perdonen los lectores no hispanohablantes, pero creo que unos agradecimientos personales se merecen el uso de mi lengua natal. Exhausto tras escribir toda la tesis con estilo muy técnico, finalmente llego a esta sección, paradójicamente la primera, mucho más literaria, y aunque me he imaginado muchas veces escribiendo cosas muy profundas aquí, una última vez vuelvo a bloquearme ante la página en blanco, eterna adversidad para los que no tenemos el don de la escritura creativa. No quisiera pasar por esta sección haciendo uso de los más manidos clichés, aunque las ganas de terminar lo haga muy tentador. Pero asumo que parte de la experiencia humana, y sobre todo la de las personas que hacemos el doctorado, debe ser bastante compartida («¿y si mejor abandono todo esto y me voy a vivir al campo?»), y temo que cualquier cosa que escriba ya se habrá dicho antes de mil maneras distintas, así que sirva esto de excusa preventiva ante mi posible falta de originalidad.

Al terminar la tesis y echar la vista atrás, quiero pensar que es algo bastante generalizado preguntarse algo como «¿esto es todo lo que me ha dado tiempo a hacer en cuatro años?». Y es que supongo que cuando uno empieza el doctorado, aún inocente y algo ingenuo, ve perfectamente factible llegar a todos los objetivos propuestos, e incluso más. Con el paso del tiempo, la realidad se va haciendo evidente, con resultados que acaban tardando en salir muchas semanas o meses más de lo esperado, si es que salen, que no siempre es el caso. Por si de algún modo no lo supieran ya, la investigación puede llegar a ser muy frustrante. No por nada mis directores me han enseñado, y yo he aprendido a la fuerza, que la investigación nunca se termina sino que se abandona. Sin embargo, la satisfacción que se siente cuando algo que te ha llevado mucho tiempo y esfuerzo, y no sabías si llegaría a funcionar, lo acaba haciendo es una sensación que compensa, aunque sea temporalmente, todas los disgustos que muy probablemente se hayan tenido por el camino. Quitando satisfacciones puntuales, en esa incesante lucha contra el tiempo existe una larga lista de pequeñas tareas, pequeños logros, que no destacan individualmente, e incluso uno mismo llega a olvidarlos, pero que son igualmente determinantes para que todo acabe llegando a término. Una gran parte del desarrollo de la tesis es ese esfuerzo invisible, que es realmente lo que poco a poco nos

va haciendo expertos en la materia y, quizás más importante aún, ser conscientes de todo lo que aún nos queda por aprender. Visto así, quizás sí que he hecho bastante en estos cuatro años.

No todo lo que he hecho estos años ha sido técnico, por supuesto, y menos mal, porque a veces la tesis te deja tan absorto como para olvidar que hay vida más allá de ella. Lo cierto es que compaginar el desarrollo de la tesis con la vida personal no siempre es fácil. Por suerte o por desgracia, muchos de mis amigos más cercanos también han estado haciendo el doctorado a la vez que yo, lo que ha facilitado el mantener una relación estrecha, aunque a costa de que haya sido mayoritariamente en los pasillos entre laboratorios. En esos encuentros, aunque hubiera mucho trabajo por hacer, siempre había un hueco para una charla que derivase en la enésima conversación, tan repetitiva como indignante, sobre los caminos inescrutables del mundillo científico, sus dinámicas laborales, las perspectivas a medio y largo plazo, el lucrativo negocio de las grandes editoriales científicas, y la vida en general. Aparte de casi convencerme de que no estoy loco, estos intercambios me llevaron a encontrar algunas vías más constructivas para mi conocido afán por quejarme de todo. Aunque frecuentemente me haya servido como otro pasatiempo más con el que ocupar la parte de la mente que la tesis aún no hubiera conquistado, espero sinceramente que mi participación en algunos colectivos que intentan hacer este mundillo más amable y digno haya contribuido a ayudar a colegas actuales y futuros, y me alegra saber que en ellos hay gente involucrada en sustituir la competitividad por el compañerismo.

Ya sea relacionado con la vida académica o la privada, que haya llegado hasta aquí es gracias a muchas otras personas, como no podría ser de otra manera. En primer lugar, por supuesto, gracias a mis directores, que accedieron a serlo aun conociéndome de antes, han mantenido a raya con más o menos éxito mis impulsos autodestructivos y, ya en serio, siempre me han hecho sentir apreciado tanto técnica como personalmente. Gracias a mis compañeros del grupo mmiRF, que hacen del laboratorio un lugar agradable donde trabajar, y me siguen incluyendo aunque a veces sea menos sociable de lo que debería. Gracias a los investigadores de otras universidades que han accedido a ayudarme desinteresadamente cuando, atascado con algún problema, he acudido a ellos. Gracias a todos mis profesores, por haberme enseñado todo lo que sé y estar dispuestos a seguir resolviéndome dudas incluso años después de haber terminado la carrera. Gracias a mis amigos, por serlo y soportarme cuando me enrollo como actualmente estoy haciendo aquí. Gracias a quienes ya no están, por haberme acompañado durante parte de este viaje, y a los que sí por seguir haciéndolo. Y, por supuesto, gracias a mi familia, por todo.

Pablo

The work for this PhD thesis has been funded by a "Formación de Profesorado Universitario" grant (FPU20/03240) by the Ministerio de Ciencia, Innovación y Universidades. This grant also funded a three–month research stay at the University of Toronto, Canada, under the supervision of Prof. George V. Eleftheriades.

Some of the works presented here have also been funded by projects PID2022-141193OB-I00 and RTI2018-097098-J-I00 by MICIU/AEI and the European Union, project PY20_00452 (PAIDI 2020) from the Junta de Andalucía, and grant UMA20-FEDERJA-001 from the University of Málaga.

Abstract

This Ph.D. thesis explores the design and implementation of metasurface-based leaky-wave antennas (LWAs) built on planar parallel-plate waveguide platforms. The work aims to enhance key radiation characteristics such as bandwidth, aperture efficiency, and beam steering capabilities through analytical methodologies and practical design strategies. Firstly, the inherent limitations of Fabry-Pérot cavity antennas related to their resonant nature are addressed by combining the ray-optics and leaky-wave perspectives, enabling simultaneous control over bandwidth and aperture efficiency. A more complex configuration is then analyzed, comprising a 1-D LWA based on bianisotropic Huygens' metasurfaces (BHMSs), where a variable leakage factor is allowed in the theoretical analysis to enable full aperture field distribution control, thus enabling precise radiation pattern shaping. A novel 2-D BHMS-based LWA configuration is then proposed, achieving linearly polarized beam steering across a whole semi-space with a fully analytical formulation and without requiring chiral properties. In parallel, and anticipating future implementations of reconfigurable antennas, liquid crystals are experimentally characterized as tunable dielectric materials, using a simplified and effective method suited for standard microwave environments. These results offer a solid foundation for further developments in efficient and reconfigurable metasurface-based antennas.

Resumen

Esta tesis doctoral explora el diseño e implementación de antenas de onda de fuga (LWA) basadas en metasuperficies y construidas en guías de placas paralelas. El trabajo tiene como objetivo mejorar características clave de radiación, como el ancho de banda, la eficiencia de apertura y las capacidades de direccionamiento del haz, mediante metodologías analíticas y estrategias de diseño prácticas. En primer lugar, se abordan las limitaciones inherentes de las antenas basadas en cavidades Fabry-Pérot relacionadas con su naturaleza resonante, combinando las perspectivas de óptica geométrica y ondas de fuga, lo que permite un control simultáneo del ancho de banda y la eficiencia de apertura. A continuación, se analiza una configuración más compleja, que consiste en una LWA unidimensional basada en metasuperficies de Huygens bianisótropas (BHMS). En ella se permite un factor de fuga variable en el análisis teórico para lograr un control completo de la distribución del campo en la apertura, lo que permite dar forma al diagrama de radiación. A continuación, se propone una novedosa configuración LWA bidimensional basada en BHMS que permite la orientación en un semiespacio completo del haz polarizado linealmente mediante una formulación totalmente analítica y sin requerir propiedades quirales. Paralelamente, y anticipando futuras implementaciones de antenas reconfigurables, se caracterizan experimentalmente cristales líquidos como materiales dieléctricos sintonizables, utilizando un método simplificado y efectivo adecuado para entornos estándar de microondas. Estos resultados ofrecen una base sólida para futuros desarrollos en antenas basadas en metasuperficies, eficientes y reconfigurables.

Contents

Acronyms

BHMS	bianisotropic Huygens' metasurface
DBP	directivity-bandwidth product
FBW	fractional bandwidth
FFT	Fast Fourier Transform
FPCA	Fabry-Pérot cavity antenna
GSTC	generalized sheet transition conditions
HED	horizontal electric dipole
HFSS	High-Frequency Structure Simulator
HIPS	high-impact polystyrene
HMD	horizontal magnetic dipole
HMS	Huygens' metasurface
HPBW	half-power bandwidth
IF	intermediate frequency
IFFT	Inverse Fast Fourier Transform
LC	liquid crystal
LUT	lookup table
LWA	leaky-wave antenna
PCB	printed circuit board
PEC	perfect electric conductor
PPW	parallel-plate waveguide
PRS	partially reflective surface
RCS	radar cross-section
RF	radio frequency
SLL	sidelobe level

SVAA	slowly varying amplitude approximation
TE	transverse electric
TEM	transverse electromagnetic
TM	transverse magnetic
TL	transmission line
TRL	through-reflect-line
TRM	transverse resonance method

List of Figures

Chapter 1

Introduction

This introductory chapter provides an overview of the scope and motivation of the dissertation. Section 1.1 outlines the broader context in which this thesis is framed. The origins and initial motivations behind this research are discussed in Section 1.2. Section 1.3 then presents the main objectives pursued throughout the thesis. Finally, Section 1.4 offers an overview of the thesis structure and highlights the main contributions of each chapter.

1.1 Contextual Framework

The world around us is undergoing rapid technological transformation. Whereas only a few decades ago access to wireless connectivity was limited and often restricted to low data rates, today it is commonplace for users in developed regions to stream high-definition video content on demand from virtually any location. This evolution has been driven by advances in wireless communication technologies, increasing demands for high data throughput, low latency and ubiquitous coverage. Now, emerging applications such as autonomous vehicles, smart cities, satellite internet constellations and the Internet of Things (IoT) are pushing the boundaries of existing infrastructure, requiring not only faster communication but also more efficient and compact.

One of the key components in these wireless communication systems is the antenna, which serves as the interface between guided and radiated electromagnetic energy. Being only a part of the whole, the antenna design is crucial to properly transmit and receive electromagnetic waves with the desired characteristics. To meet the demands of these next-generation wireless systems, antennas must not only provide high gain and directional radiation but also remain low-profile, highly-efficient and capable of dynamic beam control. Traditional solutions, such as reflector antennas and phased

arrays, often involve bulky structures or complex feeding networks, which limit their integration into compact platforms or mobile devices.

An alternative solution, extensively studied in the last century [1], are leaky-wave antennas (LWAs), which have attracted renewed interest in the last years due to their advantageous characteristics. They are able to produce directive radiation by exploiting controlled leakage from a guiding structure, thus offering simple feeding, a generally passive structure, and compatibility with planar technologies. Furthermore, the inherent frequency scanning capabilities of LWAs increases their appeal for practical applications, like new cellular networks requiring beam direction control. However, conventional LWAs are typically constrained by a tight coupling between the modal properties of the guiding structure and the resulting radiation characteristics. This dependency imposes fundamental trade-offs between directivity, beam shaping flexibility, and operational bandwidth, especially in configurations based on resonant cavities, such as Fabry-Pérot cavity antennas (FPCAs) [2].

In parallel, the field of electromagnetic *metasurfaces* has become increasingly popular over the past decade. Metasurfaces, introduced as two-dimensional analogous of metamaterials [3], are not based on common materials, but instead they are composed of subwavelength engineered particles that enable tailored electromagnetic interactions not commonly found in nature. This way, these artificially-structured surfaces allow unprecedented control over the amplitude, phase and polarization of electromagnetic wavefronts. As planar, generally passive and potentially low-cost platforms, metasurfaces have enabled numerous applications, including flat lenses, polarization converters, absorbers, and holographic beam shapers, among others [4]. In particular, Huygens' metasurfaces (HMSs) stand out due to their ability to implement boundary conditions at will, enabling passive and lossless transformations between arbitrary incident and transmitted wavefronts. This capability arises from the HMS independent control of its electric and magnetic responses while ensuring impedance matching across the interface.

The intersection between metasurface engineering and LWAs opens new possibilities in antenna design. As both technologies are planar, leaky-wave radiation represents a highly convenient mechanism to design metasurface-based antennas. This way, their performance can be enhanced by, for example, decoupling the guided and radiated field characteristics, and thus allowing for improved control over the aperture field distribution, radiation direction, polarization, and overall efficiency. Therefore, increased design flexibility is achieved, enabling the use of the same physical structure to obtain several radiation behaviors by simply modifying the metasurface parameters [5].

In this context, metasurface-based LWAs represent a promising area of research,

attracting significant interest within the electromagnetics and antenna communities. Advancing their capabilities in terms of passive beamforming, bandwidth enhancement, and aperture efficiency is essential for this technology to fully mature and become a robust and well-integrated component in next-generation communication systems and critical infrastructure. Key challenges—such as the macroscopic analysis and synthesis of metasurfaces, their integration into compact antenna architectures, the design and electromagnetic modeling of their unit cells, the inclusion of reconfigurability mechanisms for dynamic beam control, and practical fabrication—remain the focus of intense ongoing research, within which this thesis is framed.

1.2 Genesis

The development of this Ph.D. thesis began with an effort to gain a deeper understanding of the underlying radiation mechanisms of FPCAs. While these antennas are known for their ability to produce directive broadside beams, they suffer from two key drawbacks: narrow bandwidth and low aperture efficiency. These issues are primarily due to the resonant nature of the structure and the radial field decay when fed from the center.

Most prior research has concentrated on bandwidth enhancement, mainly by engineering the frequency response of the periodic unit cells forming the leaky top surface. However, aperture efficiency has received comparatively little attention. Moreover, very limited research had been carried out to tackle both limitations at once from a comprehensive approach. Initial efforts to fill this gap led to the introduction of spatial modulation of the leaky surface. This approach required the design of multiple frequency-engineered unit cells and, consequently, encouraged the development of accurate circuit models to enable analytical, efficient unit cell synthesis without relying solely on computationally intensive parametric full-wave simulations. These steps naturally aligned with the design methodologies used with metasurfaces, revealing more opportunities for innovation.

In parallel, the research group—building on its expertise in metamaterial-based artificial transmission lines, as well as traveling-wave and array antennas—was involved in a project aimed at exploring metasurface-based technologies to develop antennas with improved characteristics for emerging communication systems. This included prior work on HMSs for LWAs [6], where the guided and radiated fields could be independently controlled. Although the concept exhibited high versatility in the antenna design, the theoretical framework in that work limited the leakage factor to be constant along the aperture, thus limiting aperture field distribution control and, hence,

the radiation pattern synthesis.

Another complementary line of research involved liquid crystals as tunable dielectric materials for microwave applications. These materials offer a passive, low-loss alternative to conventional varactors and mechanical actuators, and pose a potential path toward dynamic beam reconfigurability. However, before their integration into specific antenna configurations, and given the challenges associated with handling these liquids without specialized instrumentation, it became clear that an effective way for characterizing their electromagnetic properties within standard microwave structures was necessary.

Ultimately, the convergence of these research directions highlighted the potential of metasurface-enabled antennas. This thesis builds upon these foundations to explore and develop novel configurations that offer enhanced radiation characteristics and lay the groundwork for future dynamic and versatile antenna systems.

1.3 Objectives

The main focus of this Ph.D. thesis is to leverage metasurface-based LWAs to achieve enhanced radiation performance, particularly in terms of beam shaping, steering capabilities, aperture efficiency and bandwidth. The general objective is to develop comprehensive methods that enable synthesis of the aperture field distribution, while maintaining high overall efficiency and practical implementability.

The configurations investigated in this thesis are based on modified parallel-plate waveguides (PPWs), such as FPCAs and the LWAs in [6], where the top plate is engineered to allow controlled leakage. In such designs, the radiation properties are linked to the antenna aperture field distribution, making aperture synthesis a critical tool for performance enhancement.

While the various contributions of this thesis are not linearly incremental, they are unified by the main goal of advancing metasurface-based antenna design. The specific objectives can be outlined as follows:

- Develop a systematic methodology to enhance the performance of FPCAs, particularly targeting their inherently low aperture efficiency while avoiding significant bandwidth deterioration. This includes the engineering of the unit cells frequency response and the exploration of spatially modulated leaky surfaces to support more uniform aperture distributions.

- Extend the HMS-based LWA framework from [6] to allow non-uniform leakage factors, enabling full control over the aperture field distribution. This requires

designing metasurfaces with non-identical unit cells and accounting for near-field coupling and other mutual interactions, thus demanding deeper investigation into practical unit cell implementation.

- Design, fabricate, and measure antenna prototypes to validate theoretical predictions under realistic conditions. This includes ensuring efficient excitation and impedance matching, as well as leveraging standard printed circuit board (PCB) fabrication techniques to facilitate the metasurfaces' practical manufacturing.

- Combine insights from FPCAs and HMS-based LWAs to design two-dimensional metasurface antennas capable of advanced beam control, potentially leading to versatile and reconfigurable antenna designs capable of scanning across the whole positive semi-space.

1.4 Thesis Outline and Contributions

This section provides a brief explanation of the different chapters of this thesis, highlighting the main contributions from each of them.

Chapter 2 gives relevant theoretical background, which serves to introduce several concepts used in the rest of the thesis. The main characteristics of LWAs are described, explaining their radiation mechanisms and the common types they are categorized in. In addition, it is explored how the aperture power distribution behaves both for one- and two-dimensional structures, and the transverse resonance method is explained, relevant for retrieving the dispersion behavior of the guided modes. In this chapter, also a more theoretical introduction to periodic surfaces is given, highlighting their relevance and practicality, and focusing specifically in the fundamental principles and mathematical derivations of HMSs.

The FPCA limitations are tackled in **Chapter 3**, where these antennas are studied from the original, simplified ray model to the more complete leaky-wave perspective. The combination of both gives relevant insight into the mechanisms controlling the cavity resonance responsible for broadside radiation and limiting bandwidth, as well as the field decay rate with respect to the implemented leakage factor. From this, a unified framework is introduced for engineering the leaky surface to enhance both aperture efficiency and bandwidth, based on a positive-slope phase approach combined with spatial modulation. After discussing practical feeding considerations, three prototypes with different aperture distributions are fabricated to verify the proposed method.

Chapter 4 shifts focus to HMS-based 1-D LWAs in a parallel-plate configuration. A key contribution of this work is overcoming previous limitations on constant leakage

factors by introducing a slowly varying amplitude approximation (SVAA), allowing for radiation pattern shaping. The subwavelength metasurface profile leads to the use of thin substrates for the unit cells. Hence, these are efficiently designed with realistic multilayer structures synthesized with a semi-analytical approach able to account for the interlayer near-field coupling effects. Several prototypes are fabricated and measured, validating the theory and showcasing the versatility of HMS-based LWAs for advanced beam control.

Insights from the previous chapters are built upon in **Chapter 5** to propose a novel two-dimensional HMS-based LWA. This configuration seeks to combine the beam shaping and angular control capabilities of HMSs with the 2D radiating aperture of FPCAs. A rigorous field stipulation and design methodology is presented, detailing made assumptions to reduce the problem complexity due to the increase in dimensionality. Several designs are carried out to showcase several capabilities of this configuration, and they are verified through simulations with idealized unit cells. This chapter lays the foundation for future implementations of fully steerable and more efficient 2-D PPW-based metasurface antennas.

Chapter 6 addresses a complementary but essential challenge for future reconfigurable antennas: the practical characterization of liquid crystal (LC) materials used as tunable dielectrics at radio frequencies. Additive manufacturing is used to fabricate a microstrip structure that can be filled with LC to be used as its substrate, and biased through the two main conductors to modulate its permittivity. A time-gating technique is employed to extract the dielectric properties without requiring complex in-fixture calibration and allowing for a single prototype manufacturing. The proposed method is validated both numerically and experimentally, showing results consistent with existing techniques, and confirming its potential for low-cost, efficient LC characterization in reconfigurable antenna applications.

Finally, **Chapter 7** summarizes the main results and insights from the previous chapters and highlights their most relevant contributions. In addition, it outlines possible future research directions to continue and extend the work from this thesis.

Together, these chapters represent a coherent progression toward increasingly complex configurations and synthesis methodologies, while also tackling more practical aspects as implementation and material characterization. It is worth noting that each content chapter provides specific background and a targeted review of the relevant literature to contextualize the presented work.

In addition, two appendices are included to expand on some contents provided in Chapter 4. In particular, **Appendix A** leverages the rigorous theoretical derivation for the 1-D HMS-based LWAs to revisit the well-known leakage factor formula, justi-

fying its validity and quantifying its limitations in the studied scenario. On the other hand, **Appendix B** presents a brief study on the use of two-layer unit cells for the design of the employed HMSs. Although convenient for simplified implementation, the available degrees of freedom are severely limited, and their possibilities are explored. The publications derived from this thesis are enumerated in **Appendix C**. Lastly, **Appendix D** presents the summary of the thesis in Spanish.

Chapter 2

Theoretical Background

The different chapters in this thesis discuss various research works that are based on some common theoretical concepts. Hence, it is convenient to compile some of the most fundamental ones before getting into the actual research carried out. However, the content in this chapter is not intended to be an exhaustive study of the relevant theory, as there is already sufficient in-depth literature on the topics of interest. Instead, a review of the most relevant theoretical aspects is given, serving as support for the next chapters, defining some terminology and important concepts to better understand the rest of the work.

This chapter is organized as follows: Section 2.1 addresses the main aspects of interest related to leaky-wave antennas. In addition, the differences on power propagation between 1-D and 2-D structures are discussed in Subsection 2.1.1, along with a brief transverse resonance method summary for retrieving the relevant wavenumbers in Subsection 2.1.2. Then, Section 2.2 presents the idea of periodic surfaces, their relevance and usefulness. Some practical guidelines to characterize them in simulation are given in Subsection 2.2.1, whereas Subsection 2.2.2 introduces the concept of Huygens' metasurfaces, along with useful theory to better understand mathematical formulations used in some of the following chapters. Finally, Subsection 2.2.3 summarizes a classical aperture antenna method to retrieve the fields radiated by an aperture and the associated far-field pattern, which is useful for metasurface-based antennas.

2.1 Leaky-Wave Antennas

Leaky-wave antennas (LWAs) are waveguiding structures that allow a progressive leakage of power along its propagation direction, resulting in a radiated field with engineered characteristics [7–9]. They are mainly characterized by their longitudinal

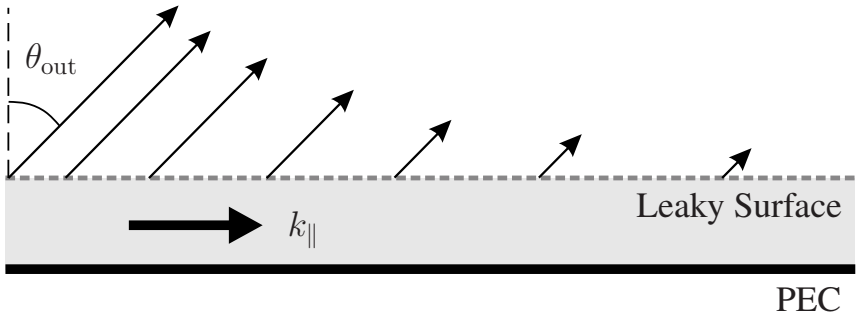

Figure 2.1: Conceptual diagram of a LWA, with rays indicating the direction and magnitude of the radiated wave.

complex wavenumber $k_{\parallel} = \beta_{\parallel} - j\alpha_{\parallel}$, with $\alpha_{\parallel} > 0$. When the structure does not present ohmic losses, then α is the *leakage factor*, which governs the ratio of power being radiated. The *phase constant* β controls the radiation output angle θ_{out} with respect to the broadside direction, as schematically shown in Fig. 2.1 for a generic LWA backed by a perfect electric conductor (PEC). For the usual case in which $\alpha_{\parallel} \ll \beta_{\parallel}$, this relation is given by

$$\beta_{\parallel} \approx k_0 \sin\theta_{\text{out}} \tag{2.1}$$

with $k_0 = 2\pi f/c$ (vacuum is considered here for simplicity), and assuming that there is no wavenumber conversion across the leaky surface. Note that, in practice, α and β can be modulated along the antenna length to accomplish enhanced radiation characteristics, such as higher aperture efficiency, radiation pattern synthesis or near-field focusing, among others.

Although LWAs are a type of traveling-wave antennas, their fundamental particularity is that the radiating mode is a *fast* wave, i.e. that $|\beta_{\parallel}| < k_0$. The physical mechanism by which this fast wave is achieved has traditionally divided the LWA types into two main categories:

- **Uniform**: When the unperturbed mode (with $\alpha_{\parallel} = 0$) already supports a fast wave, then an uniform perturbation or opening (which may present some continuous tapering) along the guiding structure length will already allow for leaked radiation. This would be the case of the classical rectangular waveguide with a side cut along its length, for example. They can radiate in the range $\theta_{\text{out}} \in (0°, 90°)$.
- **Periodic**: Structures presenting surface waves as their operating guided modes, which are slow ($\beta_{\parallel} > k_0$), can still radiate if they are periodically loaded. This allows a Floquet's modes expansion of the fields, which can then be characterized by an infinite number of space harmonics with wavenumbers

$$k_{\parallel,m} = k_{\parallel,0} + \frac{2\pi m}{p}\,, \tag{2.2}$$

where p is the periodicity in the propagation direction. Then, one of these modes (usually the $m = -1$) can be fast, and also positive or negative, thus allowing radiation in the range $\theta_{\text{out}} \in (-90°, 90°)$, as the phase constant from that harmonic would be the one used in (2.1). A typical example of this type of LWAs would be a periodically-loaded microstrip line.

As the frequency changes, the phase constant presents a dispersive behavior, which translates into the well-known LWA frequency scanning capabilities. However, when periodic LWAs scan through broadside ($\theta_{\text{out}} \approx 0°$), the *open-stopband* effect arises, worsening the radiation and the structure input matching. This effect is usually explained through the coupling of a pair of space harmonics or by the in-phase summation of the guided wave reflections with the periodic perturbations. Nevertheless, several methods exist to suppress this effect, such as introducing asymmetry in the periodic loads geometry or, as will be shown in Chapter 4, by employing non-conventional structures, like metasurfaces.

Due to the main focus in this thesis on modified variants of parallel-plate waveguides (PPWs) as the guiding structures of the presented LWAs (as the one in Fig. 2.1 resembles), the discussion is particularized for partially-open waveguide LWAs. These can be categorized as of the uniform type, or *quasi*-uniform when the leaky surface is tapered (spatially modulated). This is the case even when the leaky surface presents some type of periodicity, given that it is subwavelength and can be treated as a homogenized boundary condition (see Section 2.2). However, it will be shown that, when employing the mentioned metasurfaces, limitations of uniform LWAs related to the realizable output angle quadrant can be overcome, gaining capabilities related to periodic LWAs, even when they need not necessarily be physically periodic.

The longitudinal wavenumber is related to the transverse one $k_\perp = \beta_\perp - j\alpha_\perp$ through the usual dispersion relation

$$k_0^2 = k_\parallel^2 + k_\perp^2 \,. \tag{2.3}$$

The transverse attenuation factor $\alpha_\perp$ will then be negative, so the leaky wave amplitude increases transversely (although in a limited sector of space only, to satisfy the radiation condition), revealing its greatly discussed "improper" nature [1, 10]. Condition (2.3) is obtained by assuming separation of variables when solving Maxwell's equations. Hence, its validity strictly holds for the case in which the guiding structure is not tapered along its length, i.e. that the wavenumbers are constant along the guiding structure. However, in practice, tapered structures can benefit from the same modal analysis by treating them as a small perturbation of the closed, non-radiating waveguides. In order to design a waveguide-supported LWA it is crucial to retrieve the wavenumber values

for the used leaky surface geometry. One very popular approach for this purpose is the transverse resonance method (explained in Subsection 2.1.2), which enables the extraction of $k_\perp$, from which $k_\parallel$ can then be calculated through (2.3).

Moreover, LWAs can be one-dimensional (1-D) or two-dimensional (2-D), depending on the number of orthogonal directions in which the leaky wave radiation can be controlled. The former type is able to scan over a single plane, presenting a fan-shaped beam as the one in Fig. 2.2a, while the latter can do it over a semi-sphere, with beam patterns that can be greatly engineered. Furthermore, non-tapered uniform 2-D LWAs that are suitably center-fed can present a pencil beam when radiating at broadside, while for greater angles and excitation configurations it becomes conical [11], similar to the illustration in Fig. 2.2b.

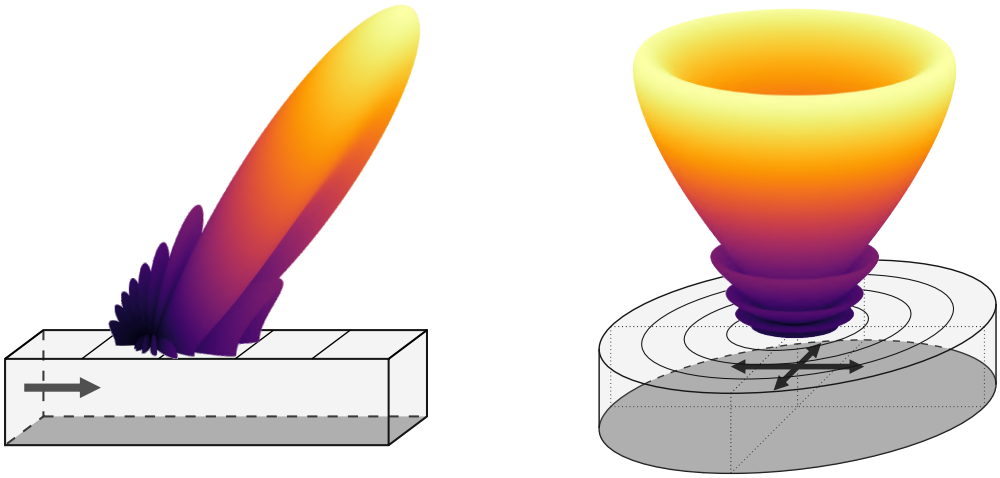

(a) (b)

Figure 2.2: Illustration of common pattern shapes for (a) 1-D and (b) 2-D LWAs.

It is important to note that broadside radiation in these 2-D structures does not require $\beta_\parallel = 0$, as would seem from (2.1), but a sufficiently small phase constant that prevents the pencil beam to split into a cone. In this case, as the leakage factor would be comparable to the phase constant, broadside radiation is produced by satisfying the *splitting* condition [12]:

$$\alpha_\parallel \approx \beta_\parallel \,. \tag{2.4}$$

Physically, this condition can be interpreted as that the guided field with enough remaining power to significantly contribute to radiation must not suffer a considerable phase shift along the aperture. This way, the entire length of the radiating section offers a similar phase, which results in a leaky wave radiating at broadside. Increasing gain levels require lower $\alpha_\parallel$ values, needing larger regions for acceptable radiation efficiencies. However, in this case, $\beta_\parallel$ must also decrease, which may lead to implementation difficulties and limit the achievable gain, as explored in Chapter 3.

he radiation characteristics can be derived from the electromagnetic field illuminating the antenna aperture, which would be the leaky surface. This way, the aperture field distribution, which is related to the far-field pattern through Fourier transforms, can be designed through well-known pattern synthesis methods [13]. This is highly convenient especially when the leakage factor is modulated, making classical formulas for directivity and beamwidth in non-tapered LWAs to lose validity. As a last note, although this section only provides an overview of the main LWA aspects that will be particularly useful for this thesis, much more thorough explanations on LWA theory can be found in the given references.

2.1.1 Aperture Power Distribution in 1-D and 2-D Structures

In order to properly shape the radiation pattern in general, and increase the aperture efficiency in particular, it is crucial to know how the aperture field distribution will behave as a function of the LWA wavenumber. However, although fundamentally similar, some differences related to this aspect between 1-D and 2-D structures must be discussed. First of all, and related to the coordinates convention, the propagation (longitudinal, previously indicated by a "$_{\parallel}$" subscript) direction for 1-D structures will be assumed to be $\hat{y}$, while it will be the radial coordinate $\hat{\rho}$ for 2-D structures. Hence, $\hat{z}$ is the transverse direction (previously indicated by a "$_{\perp}$" subscript) in both cases, consistent with the canonical spherical coordinates definition in relation to (2.1).

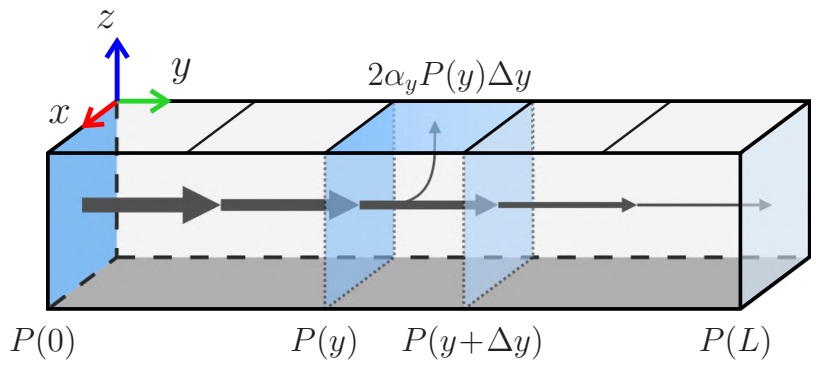

Figure 2.3: Diagram of the power flow along a 1-D LWA.

In the simpler case of a 1-D homogeneous (non-tapered) LWA, the leakage factor is constant along its length, and the power remaining inside the waveguide decays exponentially, as schematically shown in Fig. 2.3. Hence, the aperture power profile would also be exponentially decaying, and the radiation pattern would be fully determined by it: lower leakage factor values would offer more directive patterns, but the antenna has to be made longer in order for a considerable fraction of the field to be radiated before reaching the antenna end. Hence, as previously mentioned, more interesting

aperture power distributions can be designed by modulating the leakage factor along the antenna. For this general case, and from an energy conservation perspective, the approximate scenario graphically stated in Fig. 2.3 for a guided field propagating in the $\hat{y}$ direction (the "1D" subscript is used to avoid confusion between cases)

$$P_{1D}(y) - P_{1D}(y + \Delta y) = 2\alpha_y(y) P_{1D}(y) \Delta y \tag{2.5}$$

can be written in its differential form by taking the limit $\Delta y \to 0$

$$\lim_{\Delta y \to 0} \frac{P_{1D}(y + \Delta y) - P_{1D}(y)}{\Delta y} \triangleq \frac{\partial P_{1D}(y)}{\partial y} = -2\alpha_y(y) P_{1D}(y)\,. \tag{2.6}$$

By solving (2.6) [7], the power distribution along the structure is obtained as

$$P_{1D}(y) = P_{1D}(0)\, e^{-2\int_0^y \alpha_y(\tau)\, d\tau}\,, \tag{2.7}$$

where $P_{1D}(0)$ is the power accepted by the antenna at its beginning. Then, if the desired aperture field distribution is expressed as $A(y)\exp(-j\beta_y y)$, the aperture power distribution relates to the remaining power inside the waveguide as $|A(y)|^2 \propto \alpha_y(y) P_{1D}(y)$. By knowing this and properly integrating (2.6), the well-known expression relating the aperture distribution and the required leakage factor is obtained [7, 14]:

$$\alpha_y(y) = \frac{1}{2} \frac{|A(y)|^2}{\frac{1}{\eta_{rad}} \int_0^L |A(\tau)|^2\, d\tau - \int_0^y |A(\tau)|^2\, d\tau}\,. \tag{2.8}$$

The antenna length is L and the radiation efficiency is calculated as $\eta_{rad} = 1 - P_{1D}(L)/P_{1D}(0)$, representing the ratio of power radiating through the leaky surface before reaching the antenna end[1].

On the other hand, 2-D structures inherently suffer from a radial power decay even in the absence of leakage, as the accepted power must be distributed over increasingly larger cylinders, as schematically shown in Fig. 2.4. In general, the dispersion characteristics of 2-D antennas must not necessarily be radially symmetric, thus allowing the generation of radiation patterns without rotational symmetry, such as tilted pencil beams. Nevertheless, in this thesis only 2-D LWAs with radially-symmetric leakage factors are studied, and hence it is the case analyzed here. In the same fashion as before, Fig. 2.4 depicts a differential problem relating the power propagating through

[1]The radiation efficiency, in a broader sense, refers to the ratio of power effectively radiated with respect to the power accepted by the antenna. Consequently, the LWA losses would also affect that efficiency, as well as how the power dissipates or diffracts at the end of the antenna. As these phenomena are not accounted for in the given radiation efficiency expression nor in (2.8), the selected η_{rad} must be understood as a nominal value assuming a lossless scenario in which the power at $y = L$ is completely dissipated.

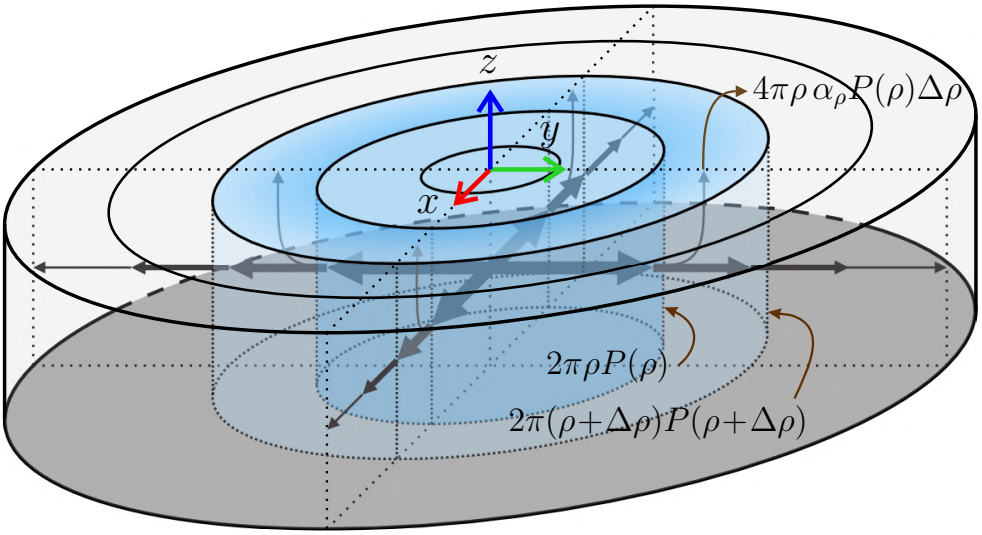

Figure 2.4: Diagram of the power flow along a center-fed 2-D LWA.

the guiding structure and the radiated one, for a 2-D LWA which is radially symmetric and center-fed (again, the "2D" subscript is only used for clarification purposes) [15]:

$$2\pi\rho P_{2\mathrm{D}}(\rho) - 2\pi(\rho+\Delta\rho)P_{2\mathrm{D}}(\rho+\Delta\rho) = 4\pi\rho\,\alpha_\rho(\rho)P_{2\mathrm{D}}(\rho)\Delta\rho\,. \tag{2.9}$$

By taking the limit $\Delta\rho \to 0$ in (2.9), then

$$\lim_{\Delta\rho\to 0}\frac{(\rho+\Delta\rho)P_{2\mathrm{D}}(\rho+\Delta\rho)-\rho P_{2\mathrm{D}}(\rho)}{\Delta\rho} \triangleq \frac{\partial\left(\rho P_{2\mathrm{D}}(\rho)\right)}{\partial\rho} = -2\alpha_\rho(\rho)\rho P_{2\mathrm{D}}(\rho)\,, \tag{2.10}$$

whose solution gives the expression for the power density inside the guiding structure at any distance from its center:

$$P_{2\mathrm{D}}(\rho) = \frac{P_{2\mathrm{D}}(0)}{\rho}\,e^{-2\int_0^\rho \alpha_\rho(\tau)\,d\tau}\,. \tag{2.11}$$

It can be noted that the expression is similar to (2.7), but accounting for the radial decay with ρ in the denominator. Although this would provoke a singularity of power density at the cavity center, in reality the field at the center would be coupling to the structure supported modes from the external source. In order to avoid the singularity, the function can be computed for $\rho > \rho_{\min}$, being $\rho_{\min}$ a radial distance (usually less than $\lambda/4$) that ensures the mode is already coupled and adequately propagating, and thus taking $P_{2\mathrm{D}}(0) = P_{\mathrm{in}} = \rho_{\min}P_{2\mathrm{D}}(\rho_{\min})$. Furthermore, parallel-plate radially-propagating modes follow Hankel functions, which can be approximated as having a field decay proportional to $\rho^{-1/2}$ only over a certain radial distance. Hence, and similarly to (2.7), this is an approximate formula derived from conservation of energy

that does not consider the actual mode configuration nor non-idealities.

Nevertheless, expression (2.11) is sufficiently valid to retrieve the desired relation between the leakage factor and the (in this case, radially-symmetric) aperture power distribution in a similar fashion as done for 1-D structures. In particular for this 2-D case, by knowing that

$$c\,|A(\rho)|^2 = \alpha_\rho(\rho) P_{2\mathrm{D}}(\rho)\,, \tag{2.12}$$

where c is a constant of proportionality, then (2.10) can be rewritten as

$$\frac{\partial\left(\rho P_{2\mathrm{D}}(\rho)\right)}{\partial\rho} = -2c\,\rho|A(\rho)|^2\,, \tag{2.13}$$

which is integrated over the following two sets of integration limits, being $\rho_{\max}$ the maximum antenna radius:

$$2c\int_{\rho_{\min}}^{\rho} \tau|A(\tau)|^2\,d\tau = P_{\mathrm{in}} - \rho P_{2\mathrm{D}}(\rho) \tag{2.14a}$$

$$2c\int_{\rho_{\min}}^{\rho_{\max}} \tau|A(\tau)|^2\,d\tau = P_{\mathrm{in}} - \rho_{\max} P_{2\mathrm{D}}(\rho_{\max})\,. \tag{2.14b}$$

By solving for $\alpha_\rho(\rho)$ in (2.12), using (2.14a) to substitute for $P_{2\mathrm{D}}(\rho)$, and finally employing (2.14b) to eliminate the proportionality constant c, the desired expression is obtained

$$\alpha_\rho(\rho) = \frac{1}{2}\frac{\rho|A(\rho)|^2}{\frac{1}{\eta_{\mathrm{rad}}}\int_{\rho_{\min}}^{\rho_{\max}} \tau|A(\tau)|^2\,d\tau - \int_{\rho_{\min}}^{\rho} \tau|A(\tau)|^2\,d\tau} \tag{2.15}$$

where $\eta_{\mathrm{rad}} = 1 - \rho_{\max} P_{2\mathrm{D}}(\rho_{\max})/P_{\mathrm{in}}$ in this case. As noted, an explicit minimum limit $\rho_{\min} \neq 0$ may be considered if no leakage is desired in the center feed section responsible for adequately coupling the mode, as mentioned before.

Note that expressions (2.8) and (2.15), although very similar, are not identical, hence each one must be properly selected depending on the dimensionality of the LWA. Anyway, for narrow-beam applications as the ones discussed in this thesis, the required leakage factor distribution for the desired pattern shaping needs the phase constant to be a fixed value. This latter requirement can be challenging, as the values of α and β are usually dependent on each other, related to the chosen physical leaky surface configuration. Hence, it is very convenient to have the capability of varying both factors as independently as possible, as will be shown in the following chapters.

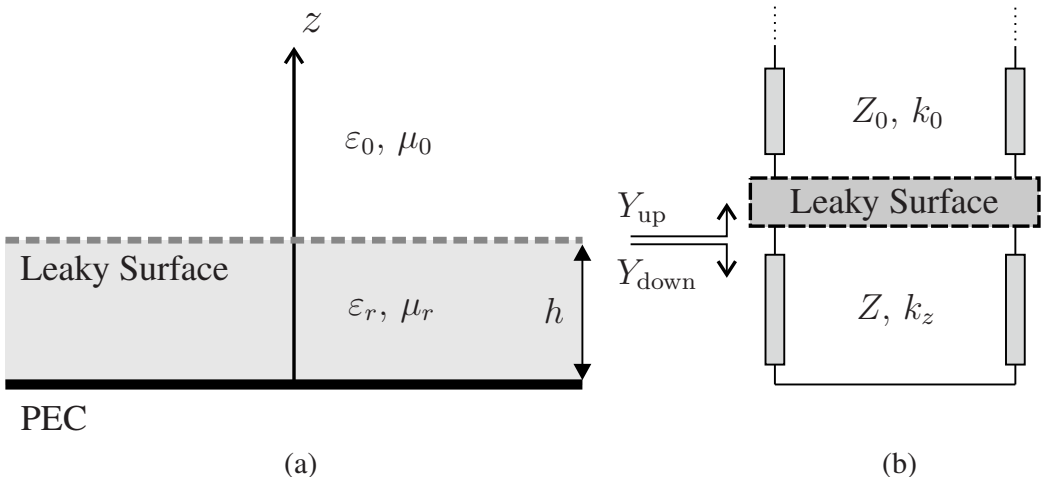

Figure 2.5: Diagram of (a) a leaky waveguide and (b) its transverse equivalent circuit model.

2.1.2 Transverse Resonance Method

Once clear the key role of the wavenumbers in the radiation characteristics of LWAs, it is necessary to know how their values can be obtained from the physical structure. One powerful approach that can be used for the considered PPWs is the *transverse resonance method* (TRM). It allows obtaining a characteristic equation for retrieving the wavenumbers of the supported modes from a transverse equivalent circuit model of the waveguide, as shown in Fig. 2.5. The resonance condition is met when the total input impedance (or admittance) at any given transverse plane equals zero:

$$Z_{\text{up}}(k_z) + Z_{\text{down}}(k_z) = 0 \qquad \text{or} \qquad Y_{\text{up}}(k_z) + Y_{\text{down}}(k_z) = 0\,. \tag{2.16}$$

As noted, the impedances/admittances will be functions of the transverse wavenumber k_z, and the resulting equation will be solved for it, either analytically or numerically. In the waveguide-based LWAs of interest, the simpler option is to compute the resonance condition (2.16) at the plane just below the leaky surface. Regarding the impedance looking up Z_{up}, the leaky surface is assumed to be isotropic. Thus, from a circuit modeling perspective, it can be characterized as presenting an input admittance $Y_{\text{up}} = Y_L$ from inside the waveguide. Regarding the impedance looking down Z_{down}, it can be calculated at the selected reference plane through the usual transmission line input impedance/admittance formula:

$$Z_{in} = Z_0 \frac{1 + \Gamma e^{j2k_z z}}{1 - \Gamma e^{j2k_z z}} \qquad \text{or} \qquad Y_{in} = Y_0 \frac{1 - \Gamma e^{j2k_z z}}{1 + \Gamma e^{j2k_z z}}\,. \tag{2.17}$$

As the bottom waveguide surface is assumed to be a perfect electric conductor,

which implies a short circuit, then $\Gamma = -1$ in this case. In addition, the characteristic transmission line impedance Z_0, or admittance Y_0, will depend on the mode configuration being transverse electric (TE) or transverse magnetic (TM), so it will also be a function of the transverse wavenumber as (in the admittance case)

$$Y^{\mathrm{TE}} = \frac{k_z}{\eta_0 k_0}\,, \tag{2.18a}$$

$$Y^{\mathrm{TM}} = \frac{k_0}{\eta_0 k_z}\,, \tag{2.18b}$$

assuming an air-filled waveguide. Finally, taking $Y_{\mathrm{down}} = Y_{\mathrm{in}}$ under the previous considerations, the admittance version of the characteristic equation can be written as

$$Y_L + Y^{\mathrm{TE/TM}} \frac{1 + e^{-j2k_z h}}{1 - e^{-j2k_z h}} = 0\,, \tag{2.19}$$

where h is the waveguide height, as shown in Fig. 2.5. Although some assumptions may be made in specific cases for this equation to solve it analytically, it is generally solved numerically. Multiple solutions will exist for both mode configurations due to the periodic domain of the complex exponential, which will give the different mode wavenumbers. Then, from the obtained k_z solutions, the longitudinal LWA wavenumber can be obtained from the dispersion relation (2.3), as

$$\beta = \Re\left[\sqrt{k_0^2 - k_z^2}\right], \tag{2.20a}$$

$$\alpha = -\Im\left[\sqrt{k_0^2 - k_z^2}\right]. \tag{2.20b}$$

This way, the LWA wavenumber that relates to the radiation characteristics would be computed from the leaky surface characteristics, which have been assumed known. Hence, the following section will address how to obtain and engineer them.

2.2 Periodic Surfaces

Structures with periodic spatial variation are fundamental tools for controlling the propagation and radiation of electromagnetic waves, as periodicity introduces unique physical effects not always present in homogeneous media. Periodic structures are defined by the repetition of a given physical arrangement in space with some periodicity in one or more dimensions, as depicted in Fig. 2.6. When electromagnetic waves interact with such a structure, their complex field distribution assumes the same periodicity, as stated by Floquet's theorem [1]. This enables the decomposition via Fourier series

expansion of the field solution into a discrete set of *spatial harmonics*, or Floquet modes, with different propagation constants related by the periodicity. This discrete mode structure is key for understanding many wave phenomena in engineered materials. For example, as briefly stated in Section 2.1, in periodic LWAs, while most spatial harmonics remain bound, some can satisfy the condition for radiation into free space.

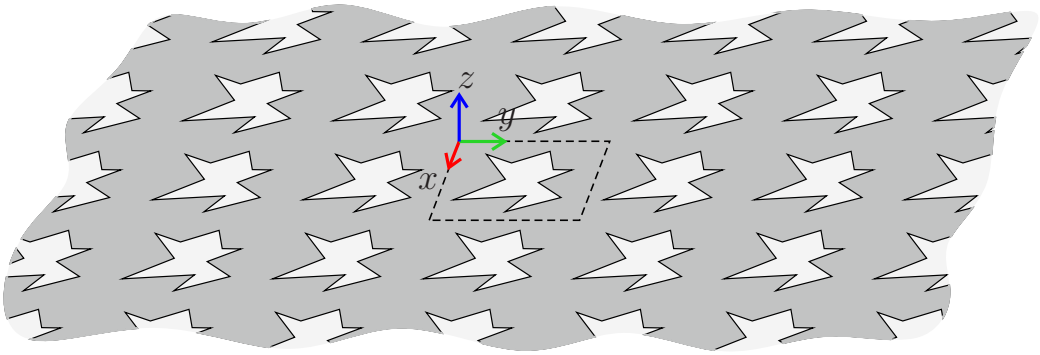

Figure 2.6: Schematic example of a 2-D periodic surface, with the unit cell framed.

This periodic electromagnetic behavior is very relevant as it allows the complete characterization of the electromagnetic field interaction with the periodic structure from its study within a single period, which is commonly called a *unit cell*. In this sense, one of the most well-established frameworks for analyzing wave propagation in periodic media is through *photonic crystals* [16]. As electromagnetic analogs of electronic crystals (periodic arrangements of atoms or molecules) in solid-state physics, they similarly exhibit band structures, which are allowed and forbidden frequency ranges for wave propagation. These band structures are often visualized using *dispersion diagrams*, where frequency is plotted as a function of the wavenumber within the first Brillouin zone. This is the uniquely defined region in the lattice that contains all non-redundant information about wave propagation. Furthermore, depending on the possible symmetries (rotations, reflections and inversions) of the unit cell, there can be additional redundancies within the Brillouin zone. Hence, the smallest region within it that contains no symmetries is called the *irreducible Brillouin zone*, and all the mode solutions can be computed from it.

In this thesis, interest resides in the analysis of 2-D periodic surfaces in particular, as they can offer some of the mentioned wave phenomena in a planar, low-profile, form factor. Such periodic surfaces can be categorized by the electrical size of their unit cells [3]. When the periodicity is comparable to or larger than the wavelength, the aforementioned irreducible Brillouin zone analysis is crucial to predict the dispersion phenomena, such as stopbands. However, when the unit-cell size is significantly smaller than the wavelength, the electromagnetic interaction with the structure becomes smoother and less dispersive. In this case, only the fundamental Floquet mode

is typically significant, and higher-order spatial harmonics are strongly evanescent. As a result, the dispersion relation around the center of the Brillouin zone is approximately linear and can often be described through effective macroscopic parameters by using *homogenization* techniques. These parameters encapsulate the average electromagnetic behavior and allows the replacement of the actual periodic structure with an effective boundary condition, greatly simplifying both analysis and design. This is highly convenient for applications where effective surface parameters are required, such as the leaky surface admittance in Subsection 2.1.2 relating to the LWA radiation properties.

Fortunately, the applicability of homogenized models can be further extended for cases where spatial modulation is introduced in the periodic surface (which, in fact, would cease to be strictly periodic) by employing the concept of *local periodicity*. A structure is said to be locally periodic if its unit-cell parameters vary slowly in space from one to another. Under this assumption, each small region of the surface can still be treated as if it were periodic, and the local effective parameters of each unit cell can be assumed those obtained from the periodic lattice. In practice, this assumption works better when the effective parameters of adjacent unit cells are also similar, i.e. when the expected field interaction between close unit cells does not entail abrupt changes.

The use of these subwavelength periodic surfaces, often referred to as *metasurfaces*, enables the effective synthesis of engineered boundary conditions, even when they are spatially varying. Moreover, they benefit from the theoretical framework developed for periodic structures, which enables their efficient electromagnetic characterization by suitable simulations of their unit cells.

2.2.1 Scattering Parameter Characterization

The use of commercial electromagnetic simulators, such as Ansys High-Frequency Structure Simulator (HFSS) or Dassault Systèmes' CST Studio, is customary in the characterization of periodic surfaces. As the surfaces of interest are subwavelength and can be homogenized, the fact that only the fundamental Floquet mode is usually relevant can be exploited. This way, the electromagnetic behavior of the surface can be characterized by the scattering parameters of a fundamental Floquet mode wave impinging on it. Physically, this means the extraction of the reflection and transmission coefficients of a plane wave impinging on the surface from an angle. As the surface is periodic, only one unit cell needs to be simulated. In particular, in this thesis HFSS has been used, in which the simulation is carried out as depicted in Fig. 2.7: with periodic boundary conditions as the lateral walls (touching the edges of the unit cell, and defining the lattice shape), and Floquet ports on both sides parallel to the surface and sufficiently far from it to ensure the evanescent modes have completely attenuated.

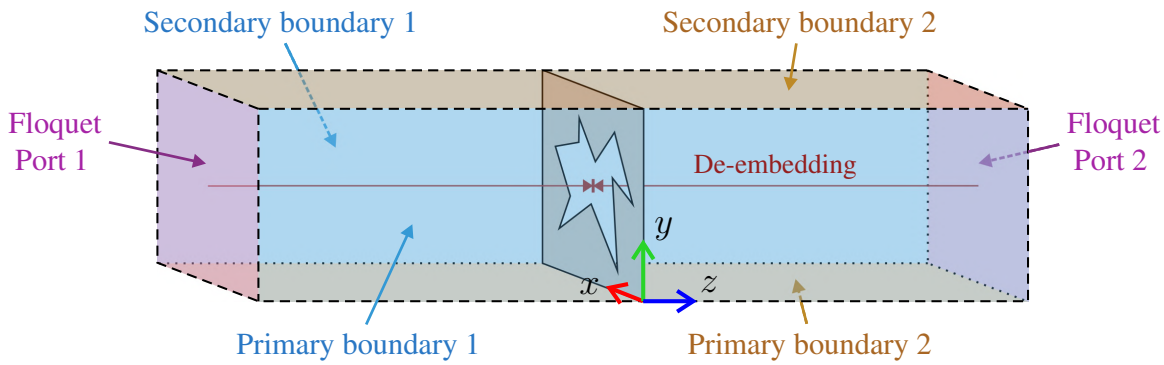

Figure 2.7: Simulation setup for a 2-D periodic unit cell.

In order to obtain the scattering properties of the periodic surface only, the simulated results must be de-embedded to the outer unit-cell interfaces, as shown in Fig. 2.7. This results in the 2×2 $\overline{S}$ matrix of interest which, in fact, would only describe the electromagnetic behavior for a single wave polarization. Depending on the application, the periodic surface may be designed to present a different behavior for each of the both orthogonal plane wave polarizations. In this case, both TE and TM waves should be characterized in simulations. This way, a 4×4 $\overline{S}$ matrix would be obtained, describing the reflection and transmission for both modes and the coupling between each other. Note that, although plane waves are strictly transverse electromagnetic (TEM) modes, here TE refers to the case in which, for any incidence angle, the electric field is normal to the plane of incidence, and correspondingly the magnetic field for the TM case.

These scattering parameters can then converted to other more convenient network matrix parameters, or be related to several surface parameters as needed. The inverse path can also be useful in some cases, i.e. converting from other network parameters to scattering ones. For example, when a metasurface changes the direction of the electromagnetic wavefront, the wave impedance is different when seen from each of both surface sides. Consequently, if a physical interpretation of the S-parameters is desired, each port must be referenced to the proper wave impedance on its side. This can be done with the generalized S-parameters, that allow defining different reference impedances on each port. Furthermore, some cases may present a complex wave impedance, for which the *pseudo-wave* scattering parameters convention can be used. It allows for complex reference impedances while conserving the usual reflection coefficient behavior [17]. A straightforward way of retrieving these parameters is from the Z ones as follows:

$$\overline{\overline{S}} = \overline{\overline{F}} \left(\overline{\overline{Z}} - \overline{\overline{Z}}_0 \right) \left(\overline{\overline{Z}} - \overline{\overline{Z}}_0 \right)^{-1} \overline{\overline{F}}^{-1} \tag{2.21}$$

$\overline{\overline{Z}}_0$ is the diagonal matrix of the port characteristic impedances Z_{0i}, and $\overline{\overline{F}}$ is a diagonal matrix whose elements are $\sqrt{\Re[Z_{0i}]}/|Z_{0i}|$, where $i \in \{1, 2, ..., N\}$ is the port index.

In the particular case of a 2-port network, the expanded conversion formulas are

$$\Delta Z = (Z_{11} + Z_{01})(Z_{22} + Z_{02}) - Z_{12}Z_{21}\,, \tag{2.22a}$$

$$S_{11} = \frac{(Z_{11} - Z_{01})(Z_{22} + Z_{02}) - Z_{12}Z_{21}}{\Delta Z}\,, \tag{2.22b}$$

$$S_{12} = \frac{2Z_{12}}{\Delta Z}\frac{Z_{01}\sqrt{\Re[Z_{01}]}}{|Z_{01}|}\frac{|Z_{02}|}{\sqrt{\Re[Z_{02}]}}\,, \tag{2.22c}$$

$$S_{21} = \frac{2Z_{21}}{\Delta Z}\frac{|Z_{01}|}{\sqrt{\Re[Z_{01}]}}\frac{Z_{02}\sqrt{\Re[Z_{02}]}}{|Z_{02}|}\,, \tag{2.22d}$$

$$S_{22} = \frac{(Z_{11} + Z_{01})(Z_{22} - Z_{02}) - Z_{12}Z_{21}}{\Delta Z}\,, \tag{2.22e}$$

which, if particularized for $Z_{01} = Z_{02} = Z_0 \in \mathbb{R}$, are simplified to the common formulas shown in [18], where $S_{12} = 2Z_{12}Z_0/\Delta Z$ and $S_{21} = 2Z_{21}Z_0/\Delta Z$.

2.2.2 Huygens' Metasurfaces

The famous Huygens' principle described in [19] by Dutch physicist Christiaan Huygens states that each point on a wavefront can be treated as a virtual source, and the interference from all of them forms the next wavefront. Huygens' metasurfaces (HMSs) are named after this principle, as they are able to control the shape of electromagnetic wavefronts by physically implementing Huygens' sources.

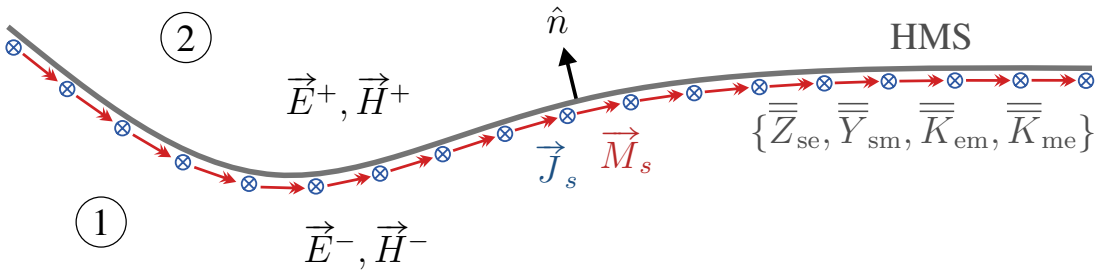

Figure 2.8: Diagram of a HMS supporting a discontinuity between the fields at both sides through the induced current densities.

The HMS characteristics can be retrieved through the general equivalence principle, derived from the interface boundary conditions. It states that an arbitrary transformation of the electromagnetic field across a surface can be modeled by introducing equivalent electric and magnetic surface current densities on that surface. Let region 1 and 2 be separated by a surface with normal unit vector $\hat{n}$ pointing toward region 2, as depicted in Fig. 2.8, and let $\{\vec{E}^-, \vec{H}^-\}$ and $\{\vec{E}^+, \vec{H}^+\}$ denote the total fields on each respective side. The required equivalent electric and magnetic surface current

densities, respectively $\vec{J}_s$ and $\vec{M}_s$, are given by

$$\vec{J}_s = \hat{n} \times (\vec{H}^+ - \vec{H}^-)\,, \tag{2.23a}$$
$$\vec{M}_s = -\hat{n} \times (\vec{E}^+ - \vec{E}^-)\,, \tag{2.23b}$$

Note that this field discontinuity condition only depends on the field components tangential to the surface. This way, a mathematical representation of the required boundary condition for a given field transformation can be calculated, which is how HMSs are macroscopically modeled. Nevertheless, it must be taken into account that, evidently, both region's electromagnetic fields must satisfy Maxwell's equations, so non-physical field configurations cannot be stipulated.

However, in order to model and synthesize the HMS electromagnetic characteristics producing the equivalent surface currents, it is convenient to relate these to the total fields at both sides of the HMS through additional surface parameters. Although different conventions exist [20], here the surface electric impedance $\overline{\overline{Z}}_{\text{se}}$, surface magnetic admittance $\overline{\overline{Y}}_{\text{sm}}$, magnetoelectric coupling coefficient $\overline{\overline{K}}_{\text{em}}$, and electromagnetic coupling coefficient $\overline{\overline{K}}_{\text{me}}$ second-order tensors are used. The boundary conditions representing the HMS response can then be expressed, in the most general form, as the following version of the generalized sheet transition conditions (GSTC)

$$\frac{1}{2}(\vec{E}_t^- + \vec{E}_t^+) = \overline{\overline{Z}}_{\text{se}} \cdot \vec{J}_s - \overline{\overline{K}}_{\text{em}} \cdot (\hat{n} \times \vec{M}_s)\,, \tag{2.24a}$$
$$\frac{1}{2}(\vec{H}_t^- + \vec{H}_t^+) = \overline{\overline{Y}}_{\text{sm}} \cdot \vec{M}_s + \overline{\overline{K}}_{\text{me}} \cdot (\hat{n} \times \vec{J}_s)\,, \tag{2.24b}$$

where the subscript t denotes the field component tangential to the HMS. Then, by using (2.23) to expand the current densities in (2.24), it follows

$$\frac{1}{2}(\vec{E}_t^- + \vec{E}_t^+) = \overline{\overline{Z}}_{\text{se}} \left(\hat{n} \times (\vec{H}^+ - \vec{H}^-)\right) - \overline{\overline{K}}_{\text{em}} \left[\hat{n} \times \left(-\hat{n} \times (\vec{E}^+ - \vec{E}^-)\right)\right], \tag{2.25a}$$
$$\frac{1}{2}(\vec{H}_t^- + \vec{H}_t^+) = \overline{\overline{Y}}_{\text{sm}} \left(-\hat{n} \times (\vec{E}^+ - \vec{E}^-)\right) + \overline{\overline{K}}_{\text{me}} \left[\hat{n} \times \left(\hat{n} \times (\vec{H}^+ - \vec{H}^-)\right)\right]. \tag{2.25b}$$

As can be seen, $\overline{\overline{K}}_{\text{em}}$ and $\overline{\overline{K}}_{\text{me}}$ enable the coupling of the electric and magnetic responses. When they are not zero, bianisotropic Huygens' metasurfaces (BHMSs) are obtained, which in practice translates into non-symmetrical behaviors, and in general different for each field polarization. As lexical clarification, in "bianisotropic", the "bi" prefix refers to the coupling coefficients not being zero, while the "anisotropic" part refers to the potential different behavior for each polarization.

In this thesis, only reciprocal metasurfaces are addressed, for which the following

conditions are derived [21]

$$\left(\overline{\overline{Z}}_{\mathrm{se}}\right)^{T} = \overline{\overline{Z}}_{\mathrm{se}}\,, \tag{2.26a}$$

$$\left(\overline{\overline{Y}}_{\mathrm{sm}}\right)^{T} = \overline{\overline{Y}}_{\mathrm{sm}}\,, \tag{2.26b}$$

$$\begin{bmatrix} K_{\mathrm{me}}^{xx} & K_{\mathrm{me}}^{xy} \\ K_{\mathrm{me}}^{yx} & K_{\mathrm{me}}^{yy} \end{bmatrix} = \begin{bmatrix} -K_{\mathrm{em}}^{yy} & K_{\mathrm{em}}^{xy} \\ K_{\mathrm{em}}^{yx} & -K_{\mathrm{em}}^{xx} \end{bmatrix}, \tag{2.26c}$$

where $K_{\mathrm{me/em}}^{ij}$ with $i,j \in \{x,y\}$ are the elements of the corresponding coupling coefficient tensors, assuming that the metasurface is contained in a constant z plane. In addition, the type of bianisotropy is categorized according to the configuration of the coupling coefficient tensors. For example, two types of reciprocal bianisotropy are usually discussed in the literature, namely *omega*-type when $\overline{\overline{K}}_{\mathrm{em}}$ and $\overline{\overline{K}}_{\mathrm{me}}$ have diagonal nonzero elements (controlling co-polarized responses), and *chiral* when they have off-diagonal nonzero elements (controlling cross-polarized responses).

By using conditions (2.26), then (2.25) can be expressed in expanded form as

$$\frac{1}{2}\begin{bmatrix} (E_x^+ + E_x^-) \\ (E_y^+ + E_y^-) \end{bmatrix} = \begin{bmatrix} Z_{\mathrm{se}}^{xx} & Z_{\mathrm{se}}^{xy} \\ Z_{\mathrm{se}}^{xy} & Z_{\mathrm{se}}^{yy} \end{bmatrix} \begin{bmatrix} -(H_y^+ - H_y^-) \\ (H_x^+ - H_x^-) \end{bmatrix} - \begin{bmatrix} K_{\mathrm{em}}^{xx} & K_{\mathrm{em}}^{xy} \\ K_{\mathrm{em}}^{yx} & K_{\mathrm{em}}^{yy} \end{bmatrix} \begin{bmatrix} (E_x^+ - E_x^-) \\ (E_y^+ - E_y^-) \end{bmatrix}, \tag{2.27a}$$

$$\frac{1}{2}\begin{bmatrix} (H_x^+ + H_x^-) \\ (H_y^+ + H_y^-) \end{bmatrix} = \begin{bmatrix} Y_{\mathrm{sm}}^{xx} & Y_{\mathrm{sm}}^{xy} \\ Y_{\mathrm{sm}}^{xy} & Y_{\mathrm{sm}}^{yy} \end{bmatrix} \begin{bmatrix} (E_y^+ - E_y^-) \\ -(E_x^+ - E_x^-) \end{bmatrix} - \begin{bmatrix} -K_{\mathrm{em}}^{yy} & K_{\mathrm{em}}^{xy} \\ K_{\mathrm{em}}^{yx} & -K_{\mathrm{em}}^{xx} \end{bmatrix} \begin{bmatrix} (H_x^+ - H_x^-) \\ (H_y^+ - H_y^-) \end{bmatrix}. \tag{2.27b}$$

The system of equations (2.27) allows for describing the boundary condition implemented by a HMS as a function of its surface parameters, for the case in which the metasurface is reciprocal and planar. However, these equations are often too general to design the HMS, and more conditions may be considered. For example, it is usually required that the HMS is lossless, to optimize its efficiency, and passive, to avoid the increase in complexity associated with including active elements. These conditions are satisfied if $\Re\{\overline{\overline{Z}}_{\mathrm{se}}\} = \Re\{\overline{\overline{Y}}_{\mathrm{sm}}\} = \Im\{\overline{\overline{K}}_{\mathrm{em}}\} = \Im\{\overline{\overline{K}}_{\mathrm{me}}\} = 0$, which also greatly decreases the number of degrees of freedom. Moreover, these imply that the real power crossing the metasurface should be locally conserved, which can be mathematically expressed through the *local power conservation* condition [22], in general, as

$$\langle P \rangle_n^- = \frac{1}{2}\Re\left\{\vec{E}^- \times \vec{H}^{-*}\right\} \cdot \hat{n} = \frac{1}{2}\Re\left\{\vec{E}^+ \times \vec{H}^{+*}\right\} \cdot \hat{n} = \langle P \rangle_n^+ . \tag{2.28}$$

Furthermore, for omega-type bianisotropic Huygens' metasurface (O-BHMS) applications, where no cross-polarization coupling is required, (2.27) can be reduced to

$$\frac{1}{2}\begin{bmatrix}(E_x^+ + E_x^-)\\(E_y^+ + E_y^-)\end{bmatrix} = \begin{bmatrix}Z_{\text{se}}^{xx} & 0\\0 & Z_{\text{se}}^{yy}\end{bmatrix}\begin{bmatrix}-(H_y^+ - H_y^-)\\(H_x^+ - H_x^-)\end{bmatrix} - \begin{bmatrix}K_{\text{em}}^{xx} & 0\\0 & K_{\text{em}}^{yy}\end{bmatrix}\begin{bmatrix}(E_x^+ - E_x^-)\\(E_y^+ - E_y^-)\end{bmatrix}, \tag{2.29a}$$

$$\frac{1}{2}\begin{bmatrix}(H_x^+ + H_x^-)\\(H_y^+ + H_y^-)\end{bmatrix} = \begin{bmatrix}Y_{\text{sm}}^{xx} & 0\\0 & Y_{\text{sm}}^{yy}\end{bmatrix}\begin{bmatrix}(E_y^+ - E_y^-)\\-(E_x^+ - E_x^-)\end{bmatrix} + \begin{bmatrix}K_{\text{em}}^{yy} & 0\\0 & K_{\text{em}}^{xx}\end{bmatrix}\begin{bmatrix}(H_x^+ - H_x^-)\\(H_y^+ - H_y^-)\end{bmatrix}, \tag{2.29b}$$

thus transforming the O-BHMS conditions into two equations for each polarization, which are decoupled from each other. For the particular case in which only E_x and H_y tangential components are considered in the stipulated electromagnetic scenario, then these simplified boundary conditions become

$$\frac{1}{2}(E_x^+ + E_x^-) = -Z_{\text{se}}^{xx}(H_y^+ - H_y^-) - K_{\text{em}}^{xx}(E_x^+ - E_x^-)\,, \tag{2.30a}$$

$$\frac{1}{2}(H_y^+ + H_y^-) = -Y_{\text{sm}}^{yy}(E_x^+ - E_x^-) + K_{\text{em}}^{xx}(H_y^+ - H_y^-)\,. \tag{2.30b}$$

This special case, although heavily simplified from the original tensor boundary conditions (assuming a metasurface contained in a z plane, reciprocal, lossless, passive and locally power conserved for a single linear polarization) is still powerful to realize relevant field transformations while greatly reducing the analytical complexity, and is of particular interest in this thesis. For this case, the local power conservation condition (2.28) is particularized as

$$\langle P\rangle_z^- = \frac{1}{2}\Re\left[E_x^- H_y^{-*}\right] = \frac{1}{2}\Re\left[E_x^+ H_y^{+*}\right] = \langle P\rangle_z^+\,. \tag{2.31}$$

In addition, this case allows for a straightforward, analytical extraction of the O-BHMS parameters from the stipulated fields on both regions [23] (refer to [24] for further mathematical development and more extensive explanations on this topic):

$$K_{\text{em}}^{xx} = \frac{1}{2}\frac{\Re\left[E_x^+ H_y^{-*} - E_x^- H_y^{+*}\right]}{\Re\left[(E_x^+ - E_x^-)\left(H_y^+ - H_y^-\right)^*\right]} \tag{2.32a}$$

$$Z_{\text{se}}^{xx} = -j\left(\frac{1}{2}\Im\left[\frac{E_x^+ + E_x^-}{H_y^+ - H_y^-}\right] + K_{\text{em}}^{xx}\Im\left[\frac{E_x^+ - E_x^-}{H_y^+ - H_y^-}\right]\right) \tag{2.32b}$$

$$Y_{\text{sm}}^{yy} = -j\left(\frac{1}{2}\Im\left[\frac{H_y^+ + H_y^-}{E_x^+ - E_x^-}\right] - K_{\text{em}}^{xx}\Im\left[\frac{H_y^+ - H_y^-}{E_x^+ - E_x^-}\right]\right). \tag{2.32c}$$

The HMS parameters will, in general, vary along the boundary condition. However, although useful information and physical properties can be derived from these parameters, it is not evident how they can be physically implemented. Hence, it is useful to translate them into an equivalent microwave network that locally relates the fields at both sides of the metasurface. In this sense, as these fields can be associated with input and output voltages and currents, then they can be related through a Z-parameters matrix of a 2×2 network [25]:

$$\begin{bmatrix} E_x^- \\ E_x^+ \end{bmatrix} = \begin{bmatrix} Z_{11} & Z_{12} \\ Z_{21} & Z_{22} \end{bmatrix} \begin{bmatrix} H_y^- \\ -H_y^+ \end{bmatrix}. \tag{2.33}$$

For the simplified case of equations (2.32), the boundary conditions in (2.30) can be rearranged and casted to a matrix form equivalent to (2.33). From it, the relation between the Z and O-BHMS parameters is obtained:

$$\begin{aligned} Z_{11} &= Z_{\text{se}}^{xx} + \frac{(1+2K_{\text{em}}^{xx})^2}{4Y_{\text{sm}}^{yy}}, \\ Z_{12} &= Z_{21} = Z_{\text{se}}^{xx} - \frac{(1-2K_{\text{em}}^{xx})(1+2K_{\text{em}}^{xx})}{4Y_{\text{sm}}^{yy}}, \\ Z_{22} &= Z_{\text{se}}^{xx} + \frac{(1-2K_{\text{em}}^{xx})^2}{4Y_{\text{sm}}^{yy}}. \end{aligned} \tag{2.34}$$

From inspection, it is clear that all S-parameters are purely imaginary, confirming that the boundary conditions are passive and lossless, in addition to reciprocal due to $Z_{12} = Z_{21}$. These parameters can be transformed to other microwave network representations that may be more convenient. S-parameters, for example, often provide more insight on the physical behavior, in terms of reflection and transmission, which can be computed from (2.22). Finally, the HMS can be physically implemented by realizing unit cells that locally synthesize the obtained parameters.

A common ideal way of implementing the local network parameters of the unit cells is with stacks of three impedance sheets cascaded by dielectric substrates, as shown in Fig. 2.9a. Under plane-wave illumination, and provided that near-field coupling effects can be neglected, this structure can be modeled with parallel admittances representing the impedance sheets and transmission lines for the dielectrics between them, as depicted in Fig. 2.9b. When the magnetoelectric coupling coefficient is non-zero, the three different components of the reciprocal lossless Z-matrix in (2.34) can be directly related to the three degrees of freedom given by the purely-imaginary parallel impedances

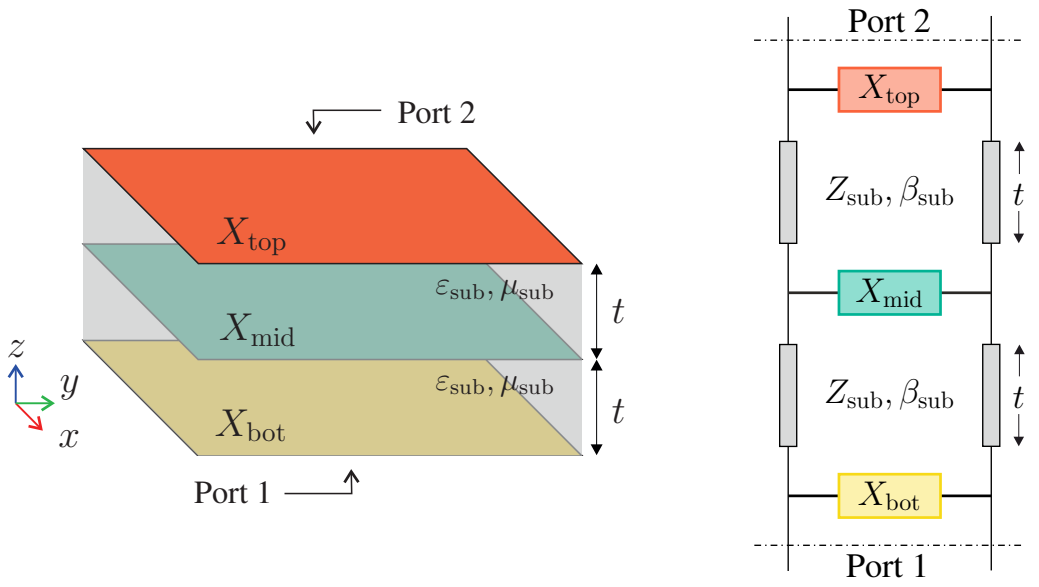

(a) (b)

Figure 2.9: Ideal three stacked impedance sheets unit-cell configuration. (a) Illustration and (b) corresponding equivalent circuit based on a transmission line model.

through closed-form expressions [23], once the dielectric properties are fixed, as

$$Z_{\text{bot}} = \frac{Z_{\text{sub}} \tan(\beta_{\text{sub}} t)}{j + Z_{\text{sub}} \tan(\beta_{\text{sub}} t) \frac{Z_{22}+Z_{12}}{\Delta Z}}\,, \tag{2.35a}$$

$$Z_{\text{mid}} = -\frac{[Z_{\text{sub}} \tan(\beta_{\text{sub}} t)]^2 \frac{Z_{12}}{\Delta Z}}{\sec^2(\beta_{\text{sub}} t) - 2j Z_{\text{sub}} \tan(\beta_{\text{sub}} t) \frac{Z_{12}}{\Delta Z}}\,, \tag{2.35b}$$

$$Z_{\text{top}} = \frac{Z_{\text{sub}} \tan(\beta_{\text{sub}} t)}{j + Z_{\text{sub}} \tan(\beta_{\text{sub}} t) \frac{Z_{11}+Z_{12}}{\Delta Z}}\,, \tag{2.35c}$$

with

$$\Delta Z = Z_{11} Z_{22} - Z_{12}^2\,. \tag{2.36}$$

Thus, this ideal circuit model allows simple synthesis of the required parameters for each unit-cell, as the three layers can be independently designed to present the needed impedance. Note that using only two impedance layers may be possible, but it can offer limited operation (see Appendix B).

Although this ideal unit-cell configuration is useful for testing purposes in simulated environments, their realistic implementation often entails a considerable difficulty. Nevertheless, this process benefits greatly from the subwavelength periodic surfaces properties discussed at the beginning of this section, as they enable the realization of the required homogenized surface parameters in an effective way.

2.2.3 Calculation of Fields Radiated from a Metasurface

From classical aperture antenna theory, it is possible to calculate the radiation characteristics of an aperture mounted on an infinite ground plane through spectral domain Fourier transforms [13, Chapter 12]. This is very convenient when the fields in an aperture are known, as both the complete field configuration propagating into free space and the corresponding far-field pattern can be calculated from them. Specifically, in scenarios where HMSs are used as the aperture of an antenna, as will be shown in Chapter 4, the fields at both sides of the metasurface are known, as they have to be stipulated beforehand. Hence, it is straightforward to use this approach to numerically calculate the radiated fields and radiation pattern from the aperture formed by the metasurface. Even though practical scenarios do not present infinite ground planes on which the apertures are mounted, the method presented in this section can serve as a good approximation before moving on to simulation. In addition, as long as the fields at the aperture are stipulated to radiate, the relation between the electric and magnetic fields is known, and hence only the tangential electric field is needed for the calculations in this method.

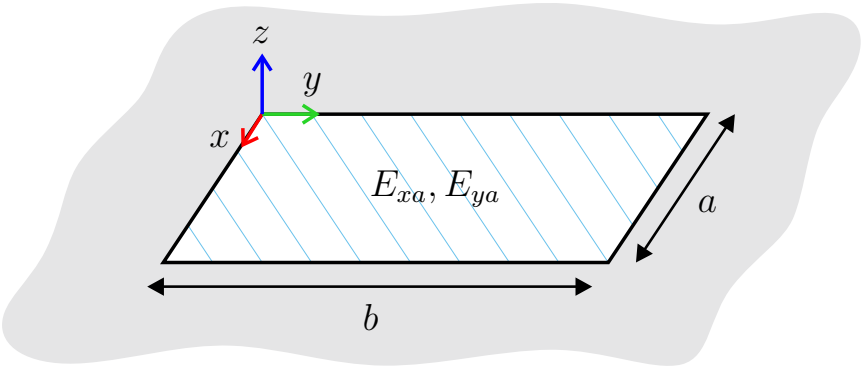

Figure 2.10: Rectangular radiating aperture mounted on an infinite ground plane.

Consider an aperture, situated in the $z = 0$ plane, with side lengths a and b in the x and y directions, respectively, as shown in Fig. 2.10. Assuming the source-free region is $z > 0$, the radiated field $\vec{E}(x, y, z)$ can be expressed as a superposition of plane waves, with different amplitudes and traveling in different directions, of the form $\vec{f}\,(k_x, k_y)e^{-j\vec{k}\cdot\vec{r}}$, where k_x and k_y are the spectral frequencies, $\vec{k} = (\hat{x}k_x + \hat{y}k_y + \hat{z}k_z)$ is the wavevector, and $\vec{r} = (\hat{x}x + \hat{y}y + \hat{z}z)$ is the direction of propagation:

$$\begin{aligned}\vec{E}(x, y, z) &= \frac{1}{4\pi^2}\int_{-\infty}^{+\infty}\int_{-\infty}^{+\infty}\vec{f}\,(k_x, k_y)e^{-j\vec{k}\cdot\vec{r}}\,dk_x\,dk_y \\ &= \frac{1}{4\pi^2}\int_{-\infty}^{+\infty}\int_{-\infty}^{+\infty}\vec{f}\,(k_x, k_y)e^{-jk_z z}e^{-j(k_x x+k_y y)}\,dk_x\,dk_y\,.\end{aligned} \tag{2.37}$$

The goal is to obtain the vector amplitudes of the $\vec{f}(k_x, k_y)$ functions to obtain the radiated fields. In this sense, fortunately it can be proven that it is sufficient to know the tangential components of the electric fields at the aperture ($z = 0$), which in this case would be $E_{xa}(x, y) = E_x(x, y, 0)$ and $E_{ya}(x, y) = E_y(x, y, 0)$, as depicted in Fig. 2.10. Hence, the x and y components of the spectral functions can be found as

$$f_x(k_x, k_y) = \int_{-b/2}^{+b/2} \int_{-a/2}^{+a/2} E_{xa}(x', y') e^{+j(k_x x' + k_y y')} \, dx' \, dy' \,, \tag{2.38a}$$

$$f_y(k_x, k_y) = \int_{-b/2}^{+b/2} \int_{-a/2}^{+a/2} E_{ya}(x', y') e^{+j(k_x x' + k_y y')} \, dx' \, dy' \,, \tag{2.38b}$$

where primes indicate source points at the aperture. Then, the z component is calculated as

$$f_z = -\frac{f_x k_x + f_y k_y}{k_z} \tag{2.39}$$

where k_z is related to k_x and k_y through the usual separation equation, giving

$$k_z = \begin{cases} \sqrt{k_0^2 - (k_x^2 + k_y^2)} & \text{when } k_0^2 \geq k_x^2 + k_y^2 \\ -j\sqrt{(k_x^2 + k_y^2) - k_0^2} & \text{when } k_0^2 < k_x^2 + k_y^2 \end{cases} \tag{2.40}$$

Hence, calculating (2.38)–(2.40) and using those results inside (2.37), the complete electric field radiated from the aperture can be numerically computed from the aperture tangential fields knowledge only. Furthermore, if needed, the magnetic fields can also be computed as

$$\vec{H}(x, y, z) = -\frac{1}{4\pi^2 k \eta} \int_{-\infty}^{+\infty} \int_{-\infty}^{+\infty} (\vec{f} \times \vec{k}) e^{-j\,\vec{k}\cdot\vec{r}} \, dk_x \, dk_y \,. \tag{2.41}$$

As a note related to Subsection 2.2.2, the fact that only the aperture tangential field components are needed is particularly convenient when applied to HMSs, as their boundary condition synthesis also relies on these components only. Thus, if the fields on one region are known for a given HMS transformation, then the tangential fields on the other side of the metasurface can be calculated from the HMS expressions, and from them the complete radiated fields on the other side (given that it is free space) can be computed through the method presented above. This is, in fact, the approach used in the following chapters regarding BHMS-based antennas to compute the radiated fields.

Furthermore, this method can also be particularized to calculate the far-field pattern. As only the θ and ϕ components of the electromagnetic field are dominant in the far-field region, then for each far-field observation point, only the coefficient of the plane wave traveling towards it must be calculated. Hence, it is sufficient to consider

$k_x = k_1 = k_0 \sin\theta\cos\phi$ and $k_y = k_2 = k_0 \sin\theta\sin\phi$ in (2.37). This way, the electric field can be approximated as

$$\vec{E}^{\mathrm{FF}}(r,\theta,\phi) \simeq j\frac{k\, e^{-jkr}}{2\pi r}\left[\hat{\theta}(f_x^{\mathrm{FF}}\cos\phi + f_y^{\mathrm{FF}}\sin\phi) + \hat{\phi}\cos\theta(-f_x^{\mathrm{FF}}\sin\phi + f_y^{\mathrm{FF}}\cos\phi)\right] \tag{2.42}$$

where the "FF" superscript stands for "far-field". In that case, the x and y spectral function components are calculated from (2.38) as

$$f_x^{\mathrm{FF}} = f_x(k_1,k_2) = \int_{-b/2}^{+b/2}\int_{-a/2}^{+a/2} E_{xa}(x',y')e^{jk(x'\sin\theta\cos\phi + y'\sin\theta\sin\phi)}\,dx'\,dy'\,, \tag{2.43a}$$

$$f_y^{\mathrm{FF}} = f_y(k_1,k_2) = \int_{-b/2}^{+b/2}\int_{-a/2}^{+a/2} E_{ya}(x',y')e^{jk(x'\sin\theta\cos\phi + y'\sin\theta\sin\phi)}\,dx'\,dy'\,. \tag{2.43b}$$

Finally, the magnetic field can also be obtained as

$$\vec{H}^{\mathrm{FF}}(r,\theta,\phi) = \sqrt{\frac{\varepsilon}{\mu}}\left[\hat{r}\times\vec{E}^{\mathrm{FF}}(r,\theta,\phi)\right]\,. \tag{2.44}$$

However, only the electric field is needed to calculate the normalized radiation intensity

$$U_n(\theta,\phi) = |E_\theta^{\mathrm{FF}}(\theta,\phi)|^2 + |E_\phi^{\mathrm{FF}}(\theta,\phi)|^2\,, \tag{2.45}$$

from which the directivity pattern can be obtained as usual, but with the particularity of using the integration limits $0 \le \theta \le \pi/2$ due to the aperture radiating into the $z > 0$ region only:

$$D(\theta,\phi) = 4\pi\frac{U_n(\theta,\phi)}{\int_0^{2\pi}\int_0^{\pi/2} U_n(\theta,\phi)\sin\theta\,d\theta\,d\phi} \tag{2.46}$$

Chapter 3

Spatially-Modulated Fabry-Pérot Cavity Antennas with Enhanced Bandwidth

Fabry-Pérot cavity antennas (FPCAs) are low-profile, highly directive antennas formed by a resonant cavity between a fully reflective ground plane (GND) and a partially reflective surface (PRS). Usually a single feed source excites the cavity, as shown in Fig. 3.1. Since their introduction by Trentini [26], these structures have seen widespread research interest due to their compactness and high gain, with enhancements enabling multi-band operation [27], circular polarization [28], reconfigurability [29], and low radar cross-section (RCS) [30].

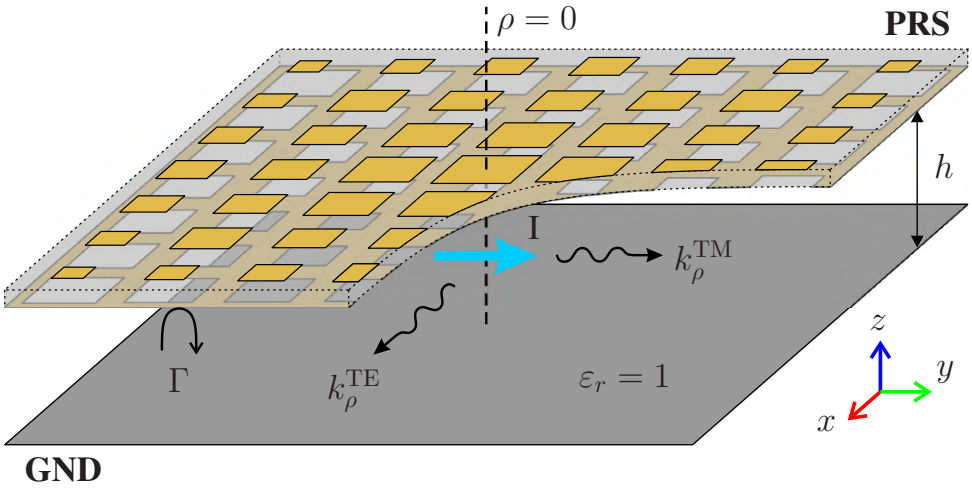

Figure 3.1: Diagram of the FPCA under study, with an horizontal electric current source at its center.

A fundamental limitation of FPCAs is their inherently narrow bandwidth, a result of the cavity's resonant nature. A common approach to address this has been the use of multilayer PRSs engineered to maintain resonance over frequency by exhibiting a positive reflection phase gradient [31–34], a method derived from the ray-tracing analysis of these antennas. Alternative strategies involve spatially tapered or modulated PRSs, approaching the concept of metasurfaces, which have been used to improve both bandwidth and aperture efficiency [35] and suppress sidelobes [36]. However, such designs often rely on heuristic methods, limiting their effectiveness.

A more rigorous modeling approach treats FPCAs as 2-D LWAs, grounded in leaky-wave theory [2, 37–39]. This framework enables more precise PRS modulation for tailored aperture illumination, as explored in previous works where efficient PRS illumination was achieved [40], though frequency behavior is often not accounted for in those cases.

Another critical, yet often underexplored aspect in FPCA design, is finding an appropriate feeding source. Because of the resonant nature of these antennas and reflective characteristics of the PRS, improper excitation can lead to significant impedance mismatches, and even degraded performance if undesired modes are excited. While various feeding structures have been used, such as coaxial probes [34, 41], patches [32, 42], microstrip-fed [43] and waveguide-fed slots [31, 33, 38, 44], challenges remain in the efficient excitation and matching, especially when aiming for high aperture efficiency and enhanced bandwidth.

This chapter introduces a systematic and non-heuristic approach to broadband FPCA aperture synthesis, integrating ray-tracing and leaky-wave perspectives. The method enables engineered PRS properties for optimized bandwidth and radiation performance using a single double-layer laminate, avoiding complex multilayer structures. Practical feeding considerations are also addressed, identifying excitation limitations and offering design guidelines for efficient implementation.

The chapter is based on the author's work in [J2], and is structured as follows: Section 3.1 presents the relevant theory, linking FPCA behavior with LWA concepts introduced in Chapter 2. Then, Section 3.2 illustrates how the PRS is analyzed and modeled, while Section 3.3 describes the methodology for its design. Considerations about the proper selection of the realistic feeding are given in Section 3.4. Section 3.5 presents the studied design examples, and their simulated and experimental results are shown in Section 3.6. Finally, some conclusions are drawn in Section 3.7.

3.1 Ray Optics and Leaky-Wave Perspectives

One of the simplest approaches to study FPCAs is through the simplified ray model from [26]. Essentially, rays originating at the point source are traced along their multiple reflections inside the cavity. Assuming that the structure is homogeneous, air-filled, and of infinite extent, all the transmitted rays are summed at the wavefront to obtain the following expression from a purely geometrical approach:

$$\frac{|\vec{E}_T(\omega,\theta)|^2}{|\vec{E}_0 f(\theta)|^2} = \frac{(1-|\Gamma|^2)}{1+2|\Gamma|\cos\left(\phi+\pi-\frac{4\pi}{\lambda}h\cos\theta\right)+|\Gamma|^2}\,. \tag{3.1}$$

This expression gives the ratio of source-originated $\vec{E}_0$ (with $f(\theta)$ as primary radiation pattern) to radiated field $\vec{E}_T$ as a function of frequency, cavity height h, spherical polar angle θ and the reflection coefficient $\Gamma(\omega) = |\Gamma|\,e^{j\phi}$ presented by the PRS from inside the cavity. For the usual case in which maximum radiation at broadside is desired ($\theta = 0°$), the resonance condition comes from the denominator in (3.1), and reduces to

$$\phi+\pi-\frac{4\pi}{\lambda_r}h = 2\pi n, \quad \text{with } n\in\mathbb{N}\,, \tag{3.2}$$

which relates the PRS reflection phase ϕ at the desired wavelength λ_r with the needed distance h between the PRS and the ground plane, as depicted in Fig. 3.1. Usually, $n = 0$ is chosen to account for the fundamental mode, which offers the lowest h value. Although expression (3.1) gives little insight about the electromagnetic field behavior inside the antenna, the resonance condition (3.2) is still used nowadays in state-of-the-art literature due to its simplicity and usefulness. Nevertheless, it was demonstrated that, getting rid of the ray optics approximation, this expression can also be obtained via reciprocity under normal plane wave arrival [38], thus rigorously proving its validity.

In fact, the most commonly used approach to increase the bandwidth of these antennas comes from a rearrangement of (3.2) [31]:

$$\phi = \frac{4\pi h}{c}f_r + (2n-1)\pi, \quad \text{with } n\in\mathbb{N}\,, \tag{3.3}$$

where c is the speed of light in vacuum and f_r is the design frequency. From this expression, it is deduced that the resonance condition can be satisfied over a larger bandwidth if the PRS reflection phase ϕ linearly increases with frequency. This is often referred to as the *positive-slope phase technique*, which requires a precise control of the PRS frequency response to achieve the desired non-Foster behavior [45]. Moreover, the ray approach already shows that the PRS design is relevant for the achievable

directivity. For higher values of $|\Gamma|$, the resonance quality factor will increase. This generally makes the antenna more directive (if the cavity is large enough) at the expense of a narrower bandwidth, as usual in any resonant structure.

Nevertheless, the actual near-field regime inside the cavity cannot be analyzed through this simplified ray model. Hence, no information can be obtained about the cavity supported modes, dispersion characteristics, or the rate at which the power decays, among others. This hinders the development of more complex FPCA designs, or even a comprehensive addressing of the actual finite lateral size. Therefore, the need for a more electromagnetically insightful design approach becomes evident.

FPCAs essentially are lossy PPW, in which the field propagating inside leaks outwards in a controlled manner. Thus, these structures can also be treated as two-dimensional (2-D) LWAs. This is, in fact, what has been done in several recently published works [38, 46]. From this perspective, the field inside the cavity is a leaky wave radially propagating from the center of the structure, and characterized by a radial wavenumber $k_\rho = \beta - j\alpha$ (see Fig. 3.1), which relates to the far-field behavior of the antenna. As the fundamental characteristics of LWAs have been described in Section 2.1, it is already known that for maximum radiation intensity at broadside, the *splitting condition* (2.4) must be satisfied. Furthermore, this condition directly relates to the resonance condition (3.2) for highly directive antennas [38].

Moreover, the value of k_ρ can be retrieved from the PRS characteristics through a transverse equivalent network, as explained in Subsection 2.1.2. By using the TRM, the dispersion relation for the vertical wavenumber k_z can be obtained in terms of Γ through (2.19). In this case, the input PRS admittance Y_L in that formula can also be expressed in terms of Γ through (2.17) as

$$Y_L = \frac{1}{\eta_0}\frac{1-\Gamma}{1+\Gamma}\,. \tag{3.4}$$

The resolution of the TRM depends on the excited mode being a TE or TM configuration. However, for very directive FPCAs, k_ρ will tend to zero, consequently making k_z approach the value of k_0. Then, from (2.18), $Y^{\mathrm{TE}} \simeq Y^{\mathrm{TM}} \simeq 1/\eta_0$, as both modes converge to a quasi-TEM configuration (see Subsection 5.1.1 for a more in-depth explanation). In that case, (2.19) can be analytically solved:

$$\beta_z = \frac{1}{2h}\left(\phi + \pi(2n+1)\right), \quad n \in \mathbb{Z} \tag{3.5a}$$

$$\alpha_z = \frac{1}{2h}\log|\Gamma|\,. \tag{3.5b}$$

Assuming this scenario, the value of Γ can be easily extracted from electromag-

netic simulations of the desired unit cell surrounded by periodic boundary conditions and excited by a normally-incident plane wave, as explained in Subsection 2.2.1. As aperture illumination control is desired to achieve different broadside radiation pattern characteristics, the PRS reflection will not be homogeneous and, in general, will follow some function of the antenna radial direction. By assuming local periodicity of the PRS, the explained leaky-wave perspective enables the acquisition of the local dispersion characteristics of the field propagating inside the cavity. This is highly helpful for calculating the remaining power at each radial section, as explained in Subsection 2.1.1, which enables a precise control of the transmitted power throughout the PRS.

In particular, and similarly to [40, 47], in the absence of resistive losses, the power density remaining inside the cavity at any distance from its center is given by (2.11). Hence, the required leakage factor for a desired radially-symmetric aperture field distribution $A(\rho)$ can be computed through (2.15). This expression, together with the quasi-TEM TRM resolution (3.5) and the dispersion relation (2.20), enables the calculation of the magnitude of the PRS reflection coefficient along the radial distance $\Gamma(\rho)$ for a given aperture field distribution that is desired. Of course, the reflection phase $\phi(\rho)$ must remain constant throughout the PRS to satisfy the resonance (or splitting) condition (3.2) everywhere, thus guaranteeing a broadside beam.

3.2 PRS Analysis and Modeling

The required reflection coefficient function must be synthesized by some realistic PRS geometry. In principle, as its phase and magnitude must be controlled independently, the PRS will need to present at least two degrees of freedom. Furthermore, its frequency behavior also needs to be engineered to achieve a positive slope phase following (3.3), thus widening the bandwidth. At least one partial PRS resonance is needed to obtain a positive slope phase over a localized band centered on the resonance frequency. From a circuit-modeling perspective, again, this translates into a minimum of two degrees of freedom required. Having more degrees of freedom would allow for a better frequency control, but at the expense of higher design complexity.

Therefore, for simplicity, a PRS comprising two layers is chosen. Multi-layer PRSs are customary as they are easy to fabricate with printed circuit board (PCB) technologies, and easy transmission line (TL) circuit models can usually be employed, enabling the design of each layer independently. This makes the PRS parametrization process much more efficient, as it allows the computation of every possible unit-cell configuration characteristics without the need for all the corresponding full-wave simulations. In the same fashion as metasurfaces, these PRSs comprise a periodic array of unit cells,

which are subwavelength in size for them to serve as a homogenized boundary condition (see Section 2.2). As the quasi-TEM mode scenario is assumed, the field impinging on the PRS is considered normal to it. The PRS modeling can then be approached as a normally incident plane wave problem, in which it travels through different media with discontinuities. In particular, for every unit cell, each layer consists of printed copper traces, which can be modeled as a shunt impedance, while a transmission line models the substrate between the layers. Thus, each two-layer unit cell is modeled as shown in Fig. 3.2.

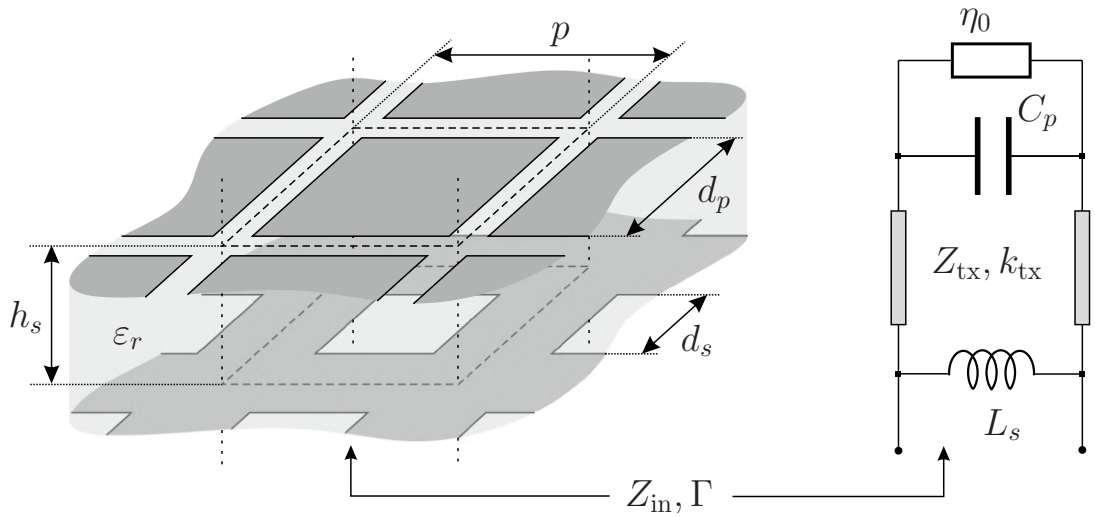

Figure 3.2: Diagram of the unit-cell geometry, and its equivalent TL model assuming a locally periodic scenario.

In this work, the bottom and upper layers consist of squared slots (with side d_s) and squared patches (with side d_p), respectively, and the design frequency is $f_r = 14\,\text{GHz}$ ($\lambda_r \approx 21.4\,\text{mm}$). Both layers are separated by a Rogers RO4350B substrate ($\varepsilon_r = 3.66$, $\tan\delta = 0.0037$) with thickness $h_s = 1.524\,\text{mm}\,(60\,\text{mils})$. The substrate is considerably thick (around $\lambda/7$ in the medium) to minimize the effects of near-field coupling between layers, which would invalidate the simple TL model. While further increasing the thickness could enhance the frequency response, this was avoided to limit inter-cell coupling under spatial modulation (unaccounted for by the local periodicity assumption) and due to commercial substrate availability. Unit cells form a squared lattice with a periodicity of $p = 5\,\text{mm}$ in both orthogonal directions. Being less than $\lambda_r/4$, it allows a proper boundary condition homogenization and fine discretization sampling while easing fabrication by avoiding a too small unit-cell size.

For both layers, their individual scattering characteristics are extracted from electromagnetic simulations carried out with Ansys HFSS. The process described in Subsection 2.2.1 is followed, and both ports are de-embedded to the copper layer itself. In these individual layer simulations, one semi-space is filled with air and the other with a

substrate with the Rogers RO4350B permittivity, but lossless (justified by its low $\tan\delta$) not to introduce additional attenuation up to the port. The patches and slots can be modeled, with minimal parasitics, as shunt capacitances (C_p) and inductances (L_s), respectively. This explains why this specific layer configuration has been chosen (and not a different layer order, or both with the same geometry), as it achieves a positive slope phase response, as detailed in [32]. The capacitance and inductance values are obtained from parametric simulations, correspondingly varying d_p or d_s in the interval $\{1, 1.1, ..., 4.8\}$ mm, and are represented in Fig. 3.3. These characteristics remain equal for both orthogonal polarizations due to the square symmetry of the chosen geometries. As a side note related to fabrication, the previous interval limits are chosen to avoid issues in that stage. In particular, the maximum value is chosen to avoid excessively thin lines (gaps) in the slots (patches) layer, and the minimum limit relates to the slots having rounded corners with radius 0.5 mm to ease prototype manufacturing.

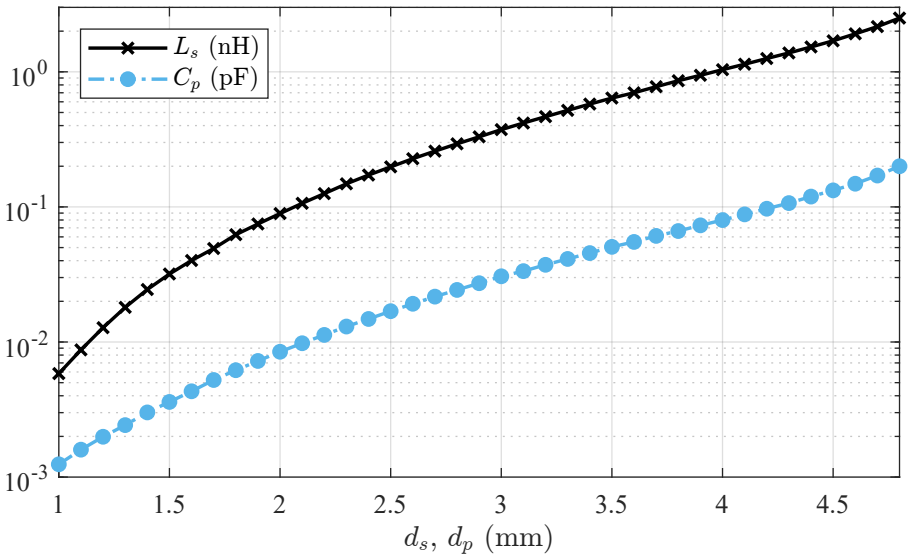

Figure 3.3: Slot inductance and patch capacitance values obtained from parametric simulations.

The obtained C_p and L_s values are used to semi-analytically calculate the input impedance of the circuit model in Fig. 3.2 through simple circuit theory as

$$Z_{\text{in}} = \frac{1}{\frac{1}{Z_2} + \frac{1}{jwL_s}}, \tag{3.6a}$$

$$Z_2 = Z_{\text{tx}} \frac{Z_1 + jZ_{\text{tx}} \tan(k_{\text{tx}} h_s)}{Z_{\text{tx}} + jZ_1 \tan(k_{\text{tx}} h_s)}, \tag{3.6b}$$

$$Z_1 = \frac{1}{\frac{1}{\eta_0} + jwC_p}. \tag{3.6c}$$

As normal plane wave incidence is assumed, the equivalent TL characteristics are calculated as $Z_{\text{tx}} = \eta_0/\sqrt{\varepsilon_{rc}}$ and $k_{\text{tx}} = \omega\sqrt{\varepsilon_{rc}}/c$, with $\varepsilon_{rc} = \varepsilon_r(1 - j\tan\delta)$. Then, as the considered cavity is filled with air, the vacuum intrinsic impedance η_0 is used as reference to compute the $\Gamma(f)$ functions from Z_{in}, in accordance with (3.4).

As verification of the simple circuit model validity, a parametric study was carried out sweeping the PRS substrate thickness, to check if the chosen value correctly avoids near-field coupling effects. Hence, several complete unit cells with different slot and patch dimensions were simulated under periodic conditions, and their reflection results were compared to those calculated from (3.6). An example for dimensions $d_s = d_p = 3.15\,\text{mm}$ is shown in Fig. 3.4, where it can be seen that, for the chosen $h_s = 1.524\,\text{mm}\,(60\,\text{mils})$, the simulated Γ is highly similar to the semi-analytically obtained one. This agreement is also found for the other tested unit cells, thus validating the circuit model, and avoiding the use of more complex methods.

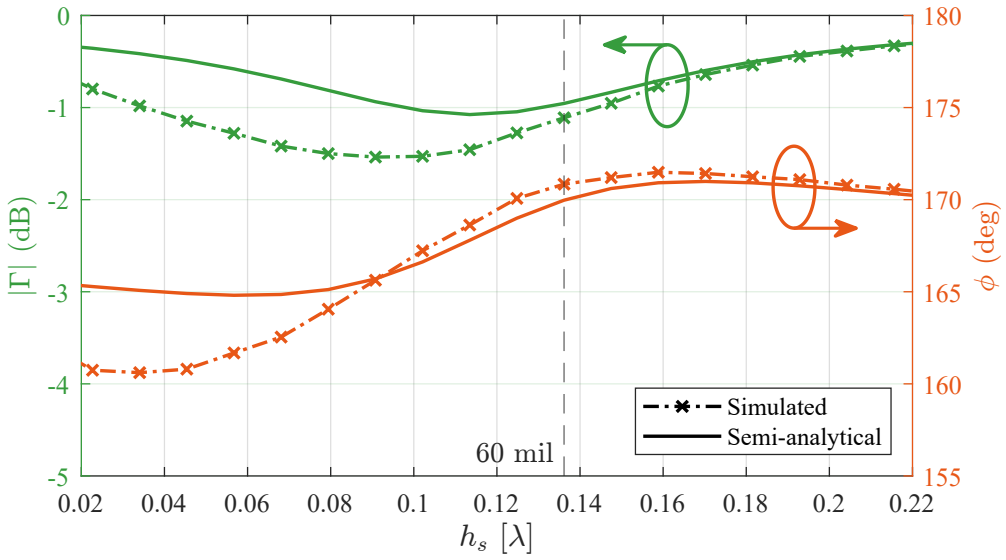

Figure 3.4: Comparison between semi-analytically calculated and simulated PRS reflection coefficient for different substrate thicknesses, for the case $d_s = d_p = 3.15\,\text{mm}$.

Finally, the whole synthesizable solution space of local PRS reflection coefficients with the considered unit-cell geometry is efficiently obtained from (3.6). Furthermore, their frequency behaviors are also extracted for a band centered around the design frequency. The Γ solution space at the design frequency f_r is displayed in Fig. 3.5 with an isoline graph. This way, the achievable magnitude and phase values for different slot and patch dimensions can be easily visualized.

More importantly, it is clear that this unit-cell configuration is able to synthesize a fixed reflection phase for a wide range of magnitude values, which is a prerequisite for designing tapered PRSs. As the frequency behavior can also be extracted from the circuit model, additional useful information is also displayed in the graph. In

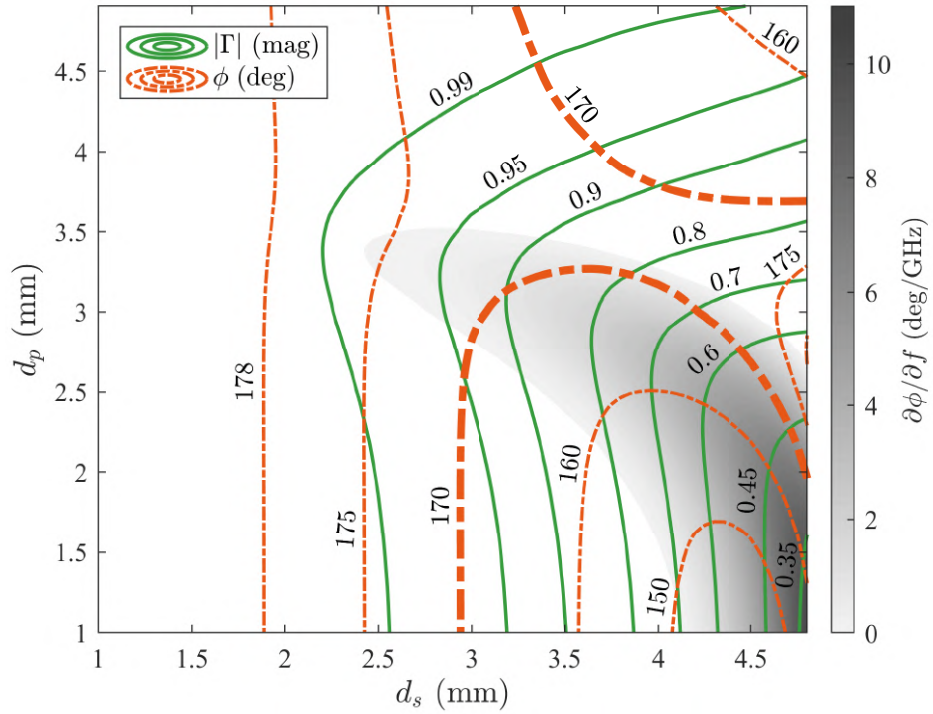

Figure 3.5: PRS reflection magnitude and phase for every possible unit cell at $f_r = 14\,\text{GHz}$. Darker background shading indicates greater positive ϕ slope.

particular, for unit cells presenting a positive slope phase, the background is shaded, being darker for increasing slope values. Naturally, greater phase slopes are found for unit cells with lower reflection magnitudes at their self resonances. Hence, for any given PRS design, and for a fixed reflection magnitude, unit cells within a darker shade area in Fig. 3.5 will generally offer larger bandwidth. As previously mentioned, greater phase slope values could be achieved if the substrate was chosen thicker, but this would increase the inter-cell coupling effects, greatly increasing the unit-cell characterization complexity under spatial modulation. Moreover, note that the bandwidth for which any given phase slope is maintained is fixed by the chosen geometry, but could be improved by adding more layers, which would also increase the design complexity.

3.3 Design Methodology

In general, for a directive homogeneous FPCA, a sufficiently reflective unit cell must be chosen. In order to know a first estimate of the required reflection magnitude as a function of the desired leakage factor, a helpful, simple approximate expression can be obtained by making some sensible assumptions. These are that the first transverse mode ($n = 0$) is used, the splitting condition is fulfilled ($\beta \approx \alpha$) and the antenna is highly directive ($\alpha \ll k$). Then, the value of $|\Gamma|$ can be calculated, once the reflection

phase is chosen, by rearranging (3.5b), expanding it using (3.2), and taking the Taylor series expansion $\sqrt{1-x^2}-1 \approx -x^2/2$ around $x=0$, as

$$|\Gamma| \approx \left| \exp\left[j(\phi+\pi)\left(\sqrt{1-\left(\frac{\alpha(1-j)}{k_0}\right)^2} - 1 \right) \right] \right| \approx \exp\left[-(\phi+\pi)\left(\frac{\alpha}{k_0}\right)^2 \right]. \quad (3.7)$$

In addition, the unit cell should present a reflection phase $\phi(f)$ that closely follows expression (3.3) around the design frequency to obtain a wideband behavior. For a tapered PRS design, all unit cells must present the same reflection phase value at the design frequency, meaning that they must lie along equal-valued isolines in Fig. 3.5. The chosen phase value will then depend on several criteria. First, its isoline should be contained in the shaded area for the majority of the unit cells to present a positive reflection phase slope, thus guaranteeing a wideband behavior to an extent. Secondly, a wide range of reflection magnitude values should be achievable to enable the synthesis of the required $\alpha(\rho)$ variation from (2.15). This translates into the phase isoline crossing several magnitude isolines.

For the studied unit-cell configuration, the value of $\phi = 170°$ achieves a good balance between the mentioned criteria, whose isolines are thicker in Fig 3.5. As two isolines exist for this phase value, for each $|\Gamma|$ value available on both, the unit cell exhibiting greater phase slope is selected to further improve the bandwidth. Hence, the dimensions of the best achievable unit cells are represented in Fig. 3.6 as a function of $|\Gamma|$. The maximum range of synthesizable reflection magnitude values is then $|\Gamma| \in [0.385, 0.995]$. Consequently, the range of leakage factor values can be obtained approximately from (3.7), or more precisely by numerically calculating (3.5) and (2.20), thus obtaining

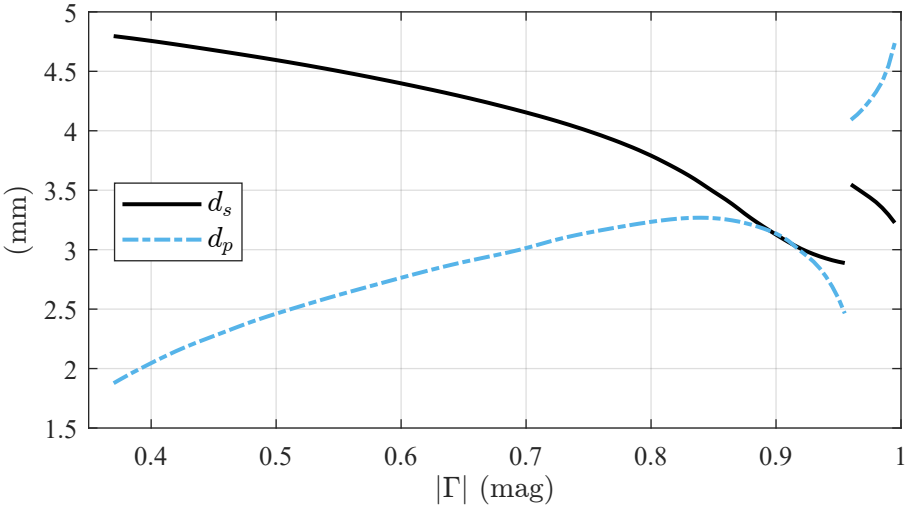

Figure 3.6: Slot and patch dimensions for unit cells presenting $\phi = 170°$ and different reflection magnitudes.

$\alpha \in [0.03, 0.38]k_0$ at 14 GHz.

The chosen ϕ value already determines the cavity height through the resonance condition (3.2), obtaining $h = 10.41$ mm for any design. Furthermore, the optimal phase slope for broadband operation is derived from (3.3), yielding $\partial\phi/\partial f = 25°/\text{GHz}$. However, such a high phase slope cannot be achieved with the considered unit-cell configuration, as deduced from Fig. 3.5. Nevertheless, selecting unit cells offering a positive phase slope (along $\phi = 170°$ isolines in this case) will already make the response less narrowband. More complex printed geometries or added number of layers could help enhancing the frequency behavior. Nevertheless, exhaustive unit-cell optimization is not the focus in this dissertation, but rather validating the proposed methodology.

The frequency dependence of the dispersion characteristics for the potential unit cells in Fig. 3.6 can also be calculated from expressions (3.5) and (2.20), as the cavity height is already fixed. Thus, they are represented in Fig. 3.7 for several unit-cell cases

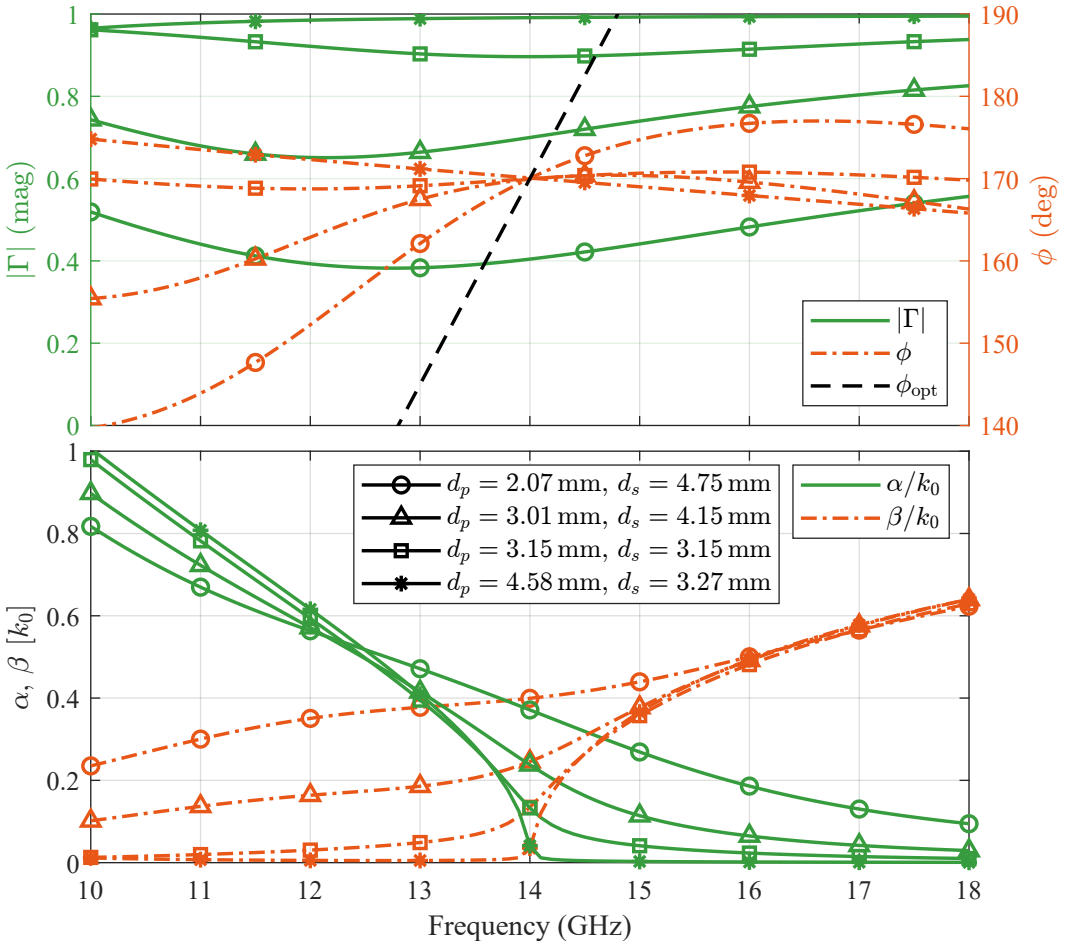

Figure 3.7: Frequency-dependent PRS reflection characteristics (top) and corresponding cavity dispersion behavior for $h = 10.41$ mm (bottom) for several unit cells. ϕ_{opt} is the optimum phase from (3.3) for maximum bandwidth.

presenting different $|\Gamma|$ values. It is indeed seen that $\alpha \approx \beta$ at the design frequency for all cases. Furthermore, the positive phase slope technique translates into a flattening of the $\alpha(f)$ and $\beta(f)$ curves around the design frequency, thus maintaining the splitting condition relatively satisfied over a larger bandwidth. This effect is more noticeable for unit cells with lower reflection (higher leakage factor), as they present a higher phase slope (see Fig. 3.5). As aforementioned, no variation of this unit-cell configuration gets to completely flatten the dispersion curves, as the ideal phase slope cannot be achieved.

For a tapered PRS design, the last step is to stipulate the desired radial aperture power distribution $|A(\rho)|^2$ and radiation efficiency. Then, from (2.15) the leakage factor function is obtained, which is related to the PRS reflection magnitude through the expressions in Section 3.1. Lastly, the required unit-cell dimensions as a function of the radial distance can be retrieved from the relation shown in Fig. 3.6.

Finally, the directivity of the antenna will be determined by the antenna size and the aperture efficiency. For homogeneous PRS designs, an exponentially decaying power profile is expected, and approximate formulas are available that relate the estimated maximum directivity to the PRS characteristics for a cavity of infinite extent [48]. More generally, for tapered, finite-size PRS designs, directivity can be qualitatively estimated from the designed aperture power profile from (2.11)–(2.15) and its relation to the far-field pattern via Fourier transforms, as explained in Subsection 2.2.3. However, exact directivity calculations are not possible here, since the required aperture field expressions to compute (2.38) are not available in the adopted framework.

3.4 Excitation and Realistic Feeding

The excitation of FPCAs is not always straightforward, and it needs special attention when very high directivity is desired, as radiation characteristics can highly degrade depending on the cavity supported modes. As previously explained, a pair of $\mathrm{TE}^z/\mathrm{TM}^z$ modes are responsible for the designed dispersion characteristics. In this case, as it is usual in these structures, the first transverse modes are used [$n = 0$ in (3.3)]. Thus, three modes are excitable in total, as the TEM^ρ of the PPW is also supported. However, this latter mode is undesired, as it will contribute to unwanted endfire radiation. The desired modes have an horizontal (contained in the xy plane) electric field component, whereas for the TEM^ρ mode it is vertical only. Hence, one ideal way of properly exciting the structure is with an horizontal electric dipole (HED) [2], as its polarization would be orthogonal to the undesired mode. It would be located approximately at the middle of the cavity, where the horizontal electric field intensity is maximum. Assuming that the HED is oriented in the y-direction and located at the origin of the ρ-coordinate,

as in Fig. 3.1, both modes of interest will be excited, with the field being a pure TE^z (TM^z) along the x (y) axis, and an hybrid mode in any other direction [37].

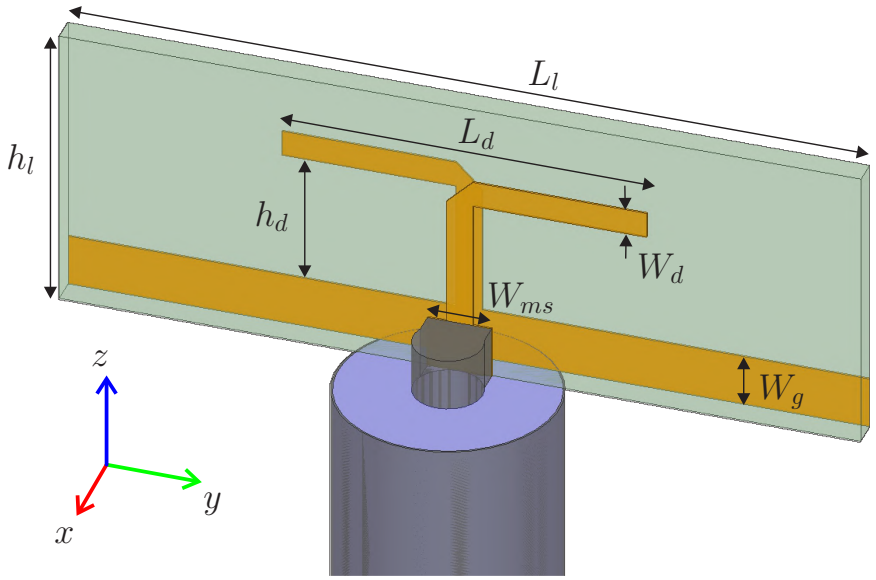

Figure 3.8: Diagram with the main dimensions of the considered printed dipole, fed by a coaxial probe.

The described HED is used as an ideal source in simulations to validate the designed PRS performance. However, a floating HED is not a realistic source for practical implementations. A parallel-strip-transmission-line-fed printed dipole, depicted in Fig. 3.8 and detailed in [49], offers a suitable alternative, balancing fabrication simplicity with a field polarization highly similar to the HED. Note that the polarization purity of the feeder is increasingly important as the FPCA becomes more directive. Higher directivity levels require smaller values of the leakage factor, which implies that the phase constant of the modes of interest also decreases due to the splitting condition ($\beta \approx \alpha$), approaching cut-off. This effect is clearly seen in Fig. 3.7, where unit cells presenting very small values of α and β at the design frequency have their dispersion diagram approaching that of the degenerate case of a closed, loaded PPW. Consequently, two main feed-related problems arise for FPCAs with highly reflective PRSs:

- Matching difficulty due to an increasingly reactive input impedance. Hence, very directive FPCAs become practically unexcitable at their design frequency and below.

- Rapid degradation of the desired broadside radiation pattern for realistic sources that deviate from the ideal HED polarization. As the value of β decreases, a higher ratio of accepted power is coupled to the undesired TEM^ρ mode, as it becomes the only one in propagation regime.

Other feeders such as waveguide-fed slots [31, 33, 38, 44] are also appropriate for this type of FPCAs, as they act as a magnetic dipole located at the ground plane, which would correctly excite the desired modes (although requiring an usually less convenient rectangular waveguide connector). However, other common sources such as patch antennas [32, 42], or bent coaxial probes [34, 41] (which mainly act as loaded vertical monopoles), present field polarizations less aligned with the desired modes. Thus, although sufficient power coupling to these modes may be provided for moderate directivity levels, they would struggle for highly directive configurations, more rapidly deteriorating the radiaton characteristics at the design frequency. Hence, it is important to carefully select a realistic source to achieve the targeted directivity at the design frequency, especially when employing highly reflective PRSs. This consideration is vital to mitigate the inherent trade-offs between high directivity and practical excitation in FPCAs.

The optimization of the selected source dimensions for a good matching is a task usually carried out through full-wave simulations. A first step usually involves ensuring proper radiation and matching in the absence of the PRS. Afterwards, if the PRS is not highly reflective, its loading effect on the source may not be considerably strong, and the previously obtained dimensions could provide good matching in this case too [32, 41]. When the PRS is highly reflective, this is not usually the case, and dimensions must be readjusted inside the complete FPCA configuration. As these structures are often electrically large, using analytical conditions is useful to reduce the computational load in simulations. In particular, Ansys HFSS electromagnetic simulator allows modeling the PRS layers with impedance boundary conditions, thus enabling the optimization of the feeder dimensions through parametric simulations in a reasonable time.

3.5 Design Descriptions

Three different PRSs are designed to showcase several aspects related to the presented methodology and feeding considerations. All designs present a squared PRS of side $L = 75\,\text{mm} \approx 3.5\lambda_r$ (15 unit cells). The square footprint of the PRS poses an uncertainty in the determination of ρ_{max} for the leakage factor calculations in (2.15), which will be individually decided for each tapered design. In addition, η_{rad} in that expression refers to the radiation inside the circle up to $\rho = \rho_{\text{max}}$. Thus, to obtain the actual radiation efficiency in the squared PRS, which shall be named η'_{rad}, the power density (2.11) along its perimeter is numerically integrated. This figure of merit is approximately equal for the three designs in order to guarantee a fair comparison, where the same ratio of the power is radiated through the PRS. Lastly, the unit cells will be chosen to present $\phi = 170°$, as done in Section 3.3, so the cavity height is always $h = 10.41\,\text{mm}$.

Furthermore, by using the unit-cell mapping from Fig. 3.6, the designs are ensured to present an optimized bandwidth.

For the ideal source simulations, the HED described in Section 3.4 is employed, with length 9.5 mm and located 5 mm above the ground plane. The printed dipole is used as the realistic feeder which, in turn, is fed by a 50 Ω coaxial probe through the ground plane, as seen in Fig. 3.8. Good matching is guaranteed for each design by optimizing the feeder dimensions using ideal impedance conditions for both layers of every unit cell in the PRS, as explained in Section 3.4. A 0.508 mm (20 mils) thick Rogers RO4350B laminate is used for the printed dipole, and some dimensions are fixed for all designs, such as $L_l = 15$ mm, $W_g = 1$ mm and $W_{ms} = 1.2$ mm.

3.5.1 Design 1: Quasi-Uniform Aperture

In order to maximize the aperture efficiency, an aperture field distribution $|A(\rho)| =$ const. is chosen. Modulating the leakage factor from $\rho_{\min} = 0$, the following analytical function is obtained from (2.15):

$$\alpha(\rho) = \frac{\rho}{\frac{\rho_{\max}^2}{\eta_{\text{rad}}} - \rho^2}\,. \tag{3.8}$$

A reasonable $\eta_{\text{rad}} = 90\%$ is chosen, and $\rho_{\max} = L/2$ is selected. This way, the $\alpha(\rho)$ function will vary up to PRS sides midpoint, and for $\rho > \rho_{\max}$ its value will be fixed to $\alpha(\rho_{\max})$, resulting in the function shown in Fig. 3.9 in black with squared markers.

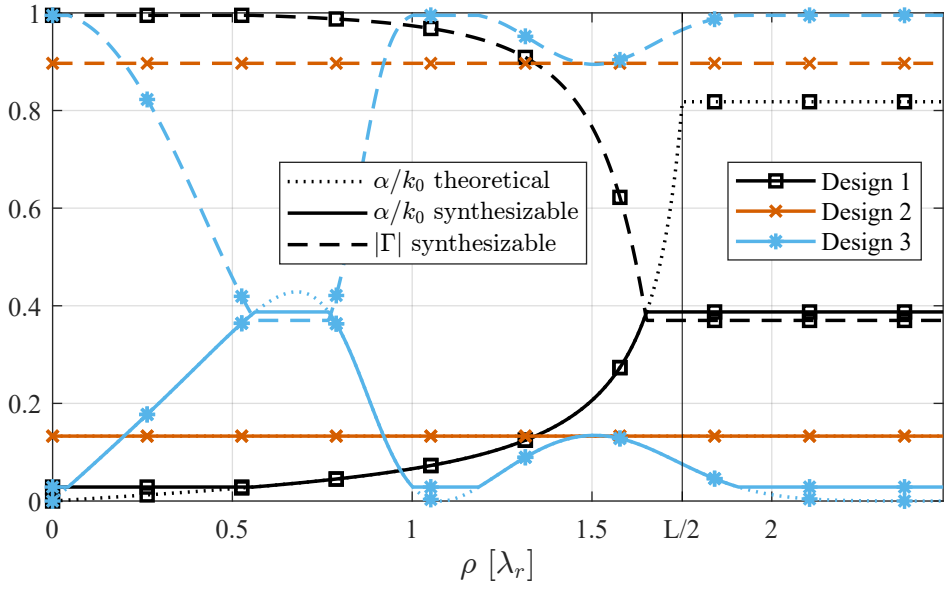

Figure 3.9: Theoretical and synthesizable radial leakage factor and required PRS reflection magnitude for the different designs.

The practically synthesizable function, also depicted, is obtained after truncating it to the minimum and maximum achievable α values achieved in Section 3.3. For $\rho \to 0$, the value of α is limited to a minimum also not to completely reach a cut-off condition, which would make the excitation impossible. Its maximum value is truncated very close to the PRS edge, where the remaining power density will be low, so it should not pose a significant behavior degradation. The associated $|\Gamma(\rho)|$ is also shown, which directly relates the distance of each unit cell from the PRS center to its dimensions through the mapping in Fig. 3.6, resulting in the final layers shown in Fig. 3.10. From the leakage factor function, the actual $\eta'_{\text{rad}} = 97.3\%$ is numerically calculated.

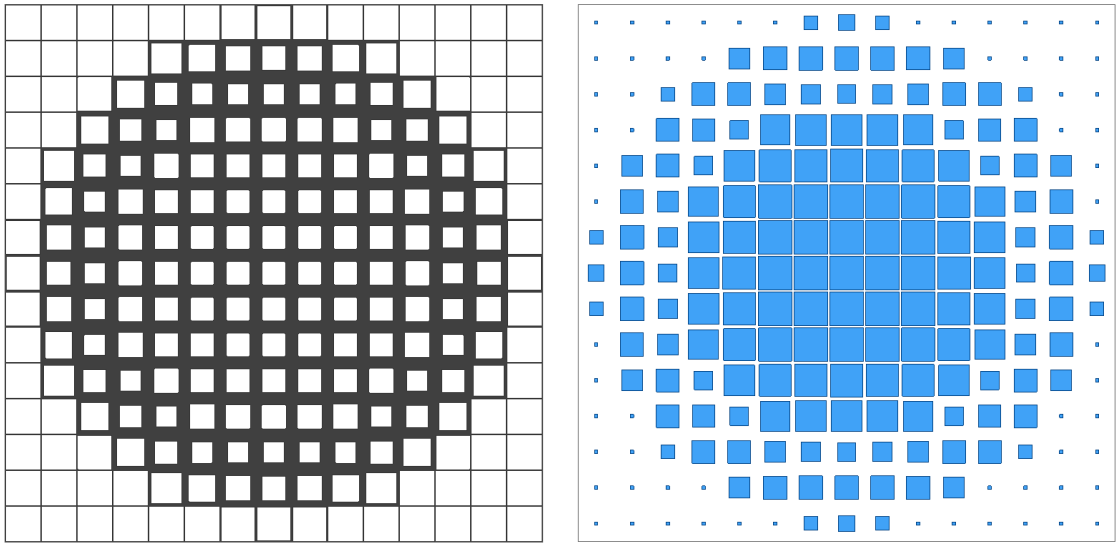

(a) (b)

Figure 3.10: Top view of the (a) slots and (b) patches layers of Design 1.

The printed dipole unfixed dimensions are optimized, obtaining $L_d = 7\,\text{mm}$, $W_d = 0.5\,\text{mm}$, $h_d = 2.5\,\text{mm}$ and $h_l = 5.5\,\text{mm}$. The simulated antenna matching with the PRS of analytical impedance conditions is shown in Fig. 3.11 with a black, dash-dotted line. The antenna accepts almost no power for frequencies below the design one (14 GHz), as expected due to the very high PRS reflectivity just above the feeder. However, a good matching is observed for higher frequencies, as the modes of interest begin propagating adequately. The response of the dipole only (without the PRS above) is also plotted with a black, dashed line for comparison. It is clear that the cavity loading effect is significant and needs to be taken into account for a correct matching.

3.5.2 Design 2: Homogeneous PRS

A design with a non-tapered PRS is also carried out mainly for comparison. The unit cells present $d_s = d_p = 3.15\,\text{mm}$, which involves a $|\Gamma| = 0.9$ and $\alpha \approx \beta = 0.133k_0$. This

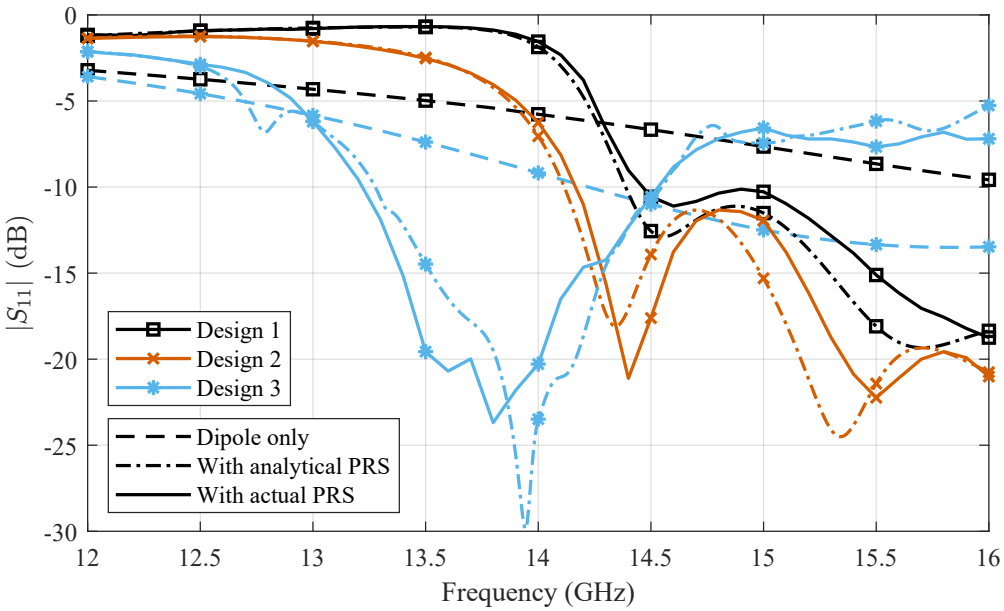

Figure 3.11: Simulated reflection coefficient of the printed dipole, alone and inside the FPCA. Matching with ideal impedance conditions is also compared to using the actual PRS geometry.

configuration, shown in Fig. 3.7 with square markers, is the one that both achieves the maximum possible reflection phase slope for the required magnitude and the same $\eta'_{\text{rad}} = 97.3\%$ as the previous design. This way, the improvement in the radiation characteristics of the tapering in Design 1 can be directly visualized and quantified, as well as its impact on bandwidth. Using the same printed dipole dimensions as in Design 1, the orange, dash-dotted and cross-marked curve in Fig. 3.11 is obtained. As the PRS is less reflective, the input resistance increases and more power is accepted at the design frequency, resulting in a better matching. As the PRS is homogeneous, its layers' physical appearance is straightforward, and it is not shown here for brevity. Note that the dipole-only curve for this design is the same as for Design 1 in Fig. 3.11.

3.5.3 Design 3: Flat-Top Aperture

The third presented design is a tapered PRS with a different aperture field distribution, which also serves to better showcase some of the aforementioned feeding considerations. In particular, a flat-top window is employed using the coefficients from the Matlab signal processing toolbox [50], obtaining the following radial aperture field distribution

$$A(\rho) = a_0 + \sum_{k=1}^{4} a_k \cos\left(\frac{k\pi\rho}{\rho_{\max}}\right), \tag{3.9}$$

with $a_k = \{0.215,\ 0.417,\ 0.277,\ 0.0836,\ 0.0069\}$.

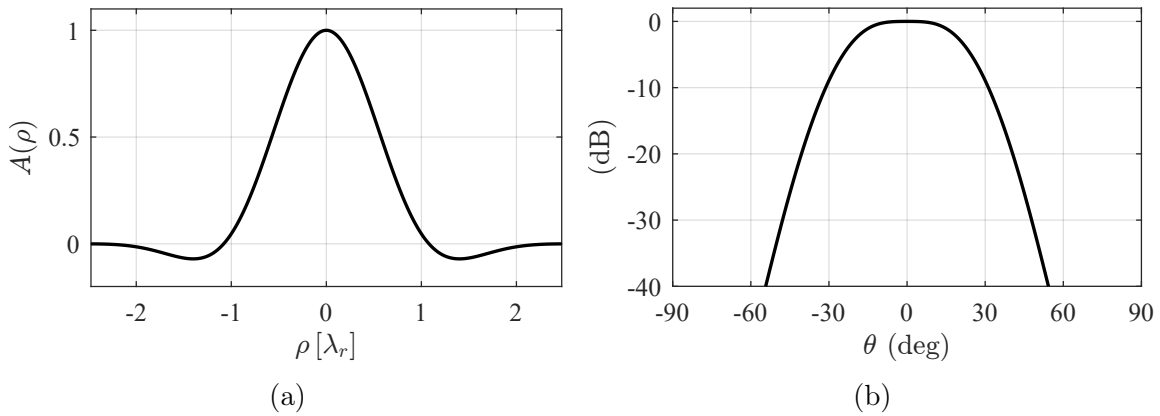

Figure 3.12: Flat-top window characteristics: (a) Normalized aperture field distribution and (b) associated normalized Fourier transform.

This aperture presents the variation shown in Fig. 3.12a, where negative ρ values are also represented to improve visualization. It is interesting as the distinctive characteristic of the radiation pattern is located in the main beam, which presents a flat top with very low ripple, as observed in the theoretical aperture Fourier transform of Fig. 3.12b. This facilitates its proper realization and verification, as the undesired endfire radiation from the refracted field at the cavity edges would mask any subtle characteristics in the sidelobes. In this case, as the window tends to zero at the end, $\rho_{\max} = L/\sqrt{2}$ is chosen to modulate the PRS up to its diagonal, thus using more available area for radiation. The resulting leakage factor function is calculated from (2.15) using $\rho_{\min} = 0$ and $\eta_{\text{rad}} = 98\%$, and shown in Fig. 3.9 in blue with star markers. It is also truncated to the maximum and minimum achievable α values, as illustrated. The physical aspect of the realized PRS layers is shown in Fig. 3.13. In this case, a $\eta'_{\text{rad}} = 98.3\%$ is numerically calculated, similar to the previous designs, and very close to the nominal η_{rad} as the power is mainly radiated through the central are of the PRS. Consequently, also low aperture efficiency is expected.

As seen in Fig. 3.9, the leakage factor is considerably big for small radial distances. Therefore, the unit cells close to the cavity center will be weakly reflective, making the desired modes more easily excitable for $f \leq f_r$. This effect is visualized in the blue, dash-dotted, star-marked matching curve from Fig. 3.11. In this case, the printed dipole dimensions need to be readjusted to present $L_d = 6.5\,\text{mm}$, $W_d = 1\,\text{mm}$, $h_d = 4.5\,\text{mm}$ and $h_l = 7.5\,\text{mm}$, as the values from Design 1 and 2 did not offer a good return loss. The matching at and around the design frequency is now very good. Hence, this design also serves as validation of the aforementioned trade-off between directivity and ease of feeding. Lastly, note that the matching of the dipole significantly differs from that of the complete FPCA, showing that even for a low $|\Gamma|$, the influence of the PRS cannot be neglected in this case.

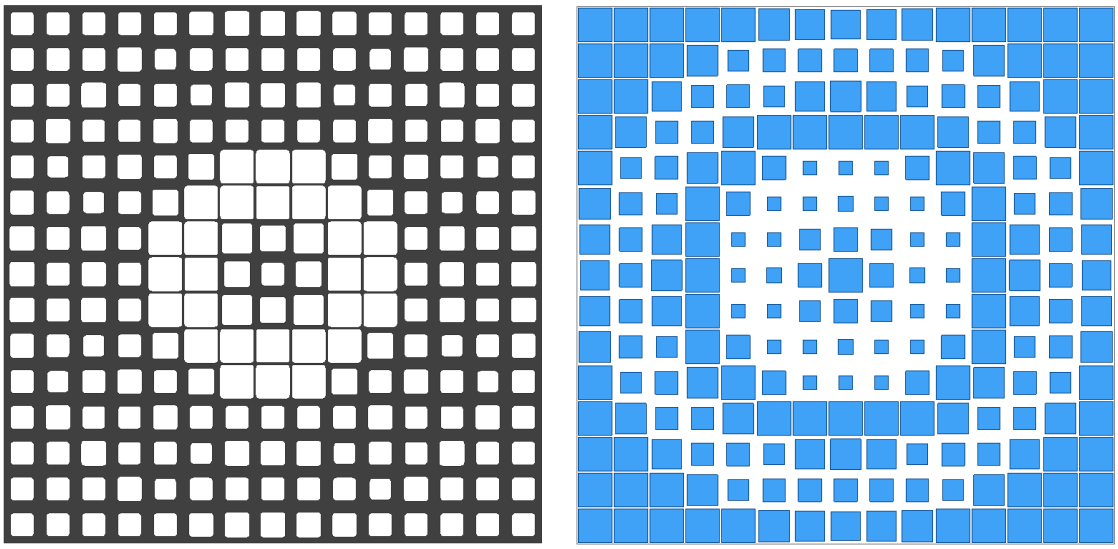

(a) (b)

Figure 3.13: Top view of the (a) slots and (b) patches layers of Design 3.

3.6 Results

3.6.1 Simulations with Ideal and Realistic Feeder

The described FPCA designs are simulated in Ansys HFSS both with the HED and the corresponding printed dipoles described in Section 3.5. The obtained directivity diagrams at the design frequency are shown in Fig. 3.14 for the three designs. Firstly, regarding the ideal source simulations, all designs present a broadside beam at the design frequency, as desired. Design 1 successfully achieves a higher directivity than Design 2 for the same PRS radiation efficiency, thus verifying the advantage of the PRS tapering. This translates into a great increase in the aperture efficiency η_{ap}, as seen in Table 3.1, approaching the maximum achievable directivity of 21.9 dBi for this physical area. On the other hand, Design 3 effectively presents a flat top in the main beam, at the expense of a considerably lower directivity level and higher beamwidth. Note that only the xz-plane diagrams are shown for brevity, as due to the PRS symmetry the yz patterns are very similar, except for slightly lower sidelobes.

In addition, Fig. 3.15 displays the broadside directivity level with respect to frequency. The half-power bandwidth (HPBW) (referred to the maximum broadside directivity level in the frequency band) of Design 1 not only does not worsen with respect that of Design 2, but even improves. This is a remarkable behavior, taking into account the increase in directivity of Design 1, and it shows the usefulness of the positive-slope phase technique, which helps roughly satisfying the required $\alpha(\rho)$ function for an enhanced band around the design frequency. In this case, although

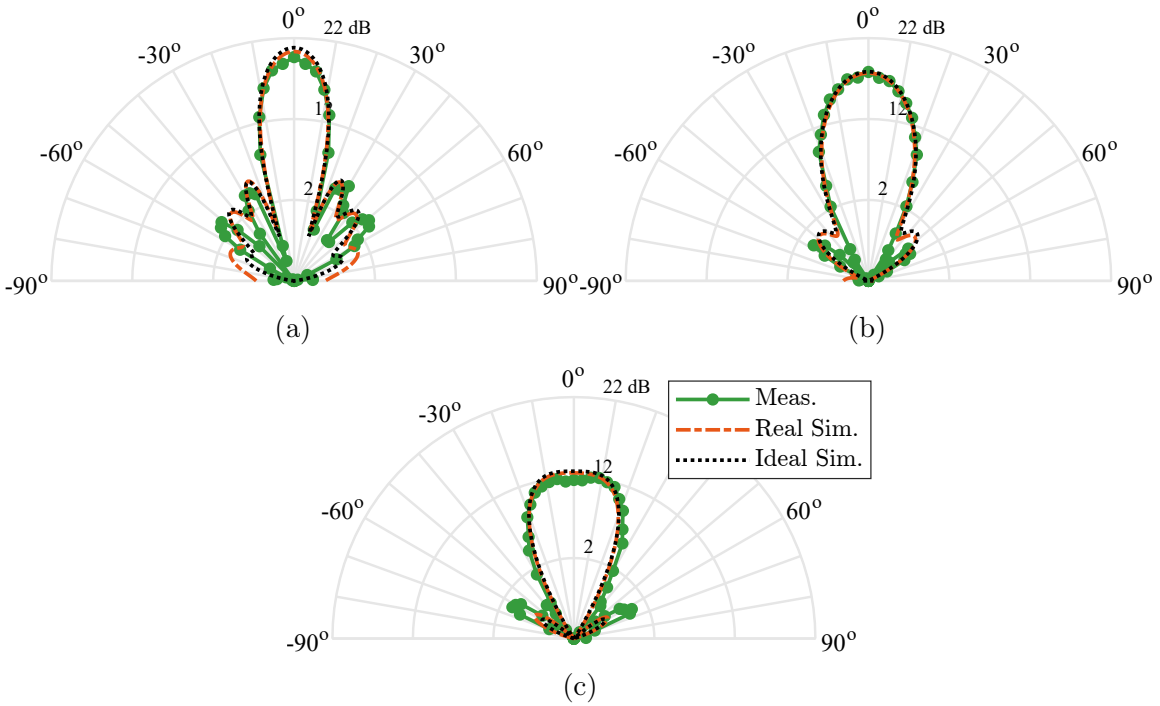

Figure 3.14: Directivity radiation patterns in the xz plane at 14 GHz from simulations (using ideal and real sources) and measurements: (a) Design 1, (b) Design 2, and (c) Design 3.

Table 3.1: Radiation figures of merit of the presented designs at 14 GHz

		D_0 (dBi)	η_{ap} (%)	HPBW (GHz)	FBW (%)	DBP (-)
Design 1	Ideal Sim.	20.8	78.4	2.22	15.6	14.89
	Real. Sim.	20.3	70.3	1.80	12.4	11.01
	Measurements	19.7	60.2	1.94	13.5	9.71
Design 2	Ideal Sim.	17.9	39.6	1.39	9.7	5.81
	Real. Sim.	17.7	38.1	1.26	8.9	5.26
	Measurements	17.8	39.2	1.62	11.6	5.66
Design 3	Ideal Sim.	12.8	12.3	> 2.65	> 19.9	> 3.85
	Real. Sim.	12.6	11.8	> 2.67	> 20.0	> 3.55
	Measurements	11.8	9.9	2.57	16.2	3.15

the unit cells at the PRS center cannot present a positive slope phase due to their very high reflection magnitude, this is compensated by those farther away, presenting greater phase slopes than that of the Design 2 identical unit cells (see Fig. 3.7). Additional figures of merit are shown in Table 3.1, where D_0 is the broadside directivity level at the design frequency, FBW = HPBW/f_c is the directivity-related fractional

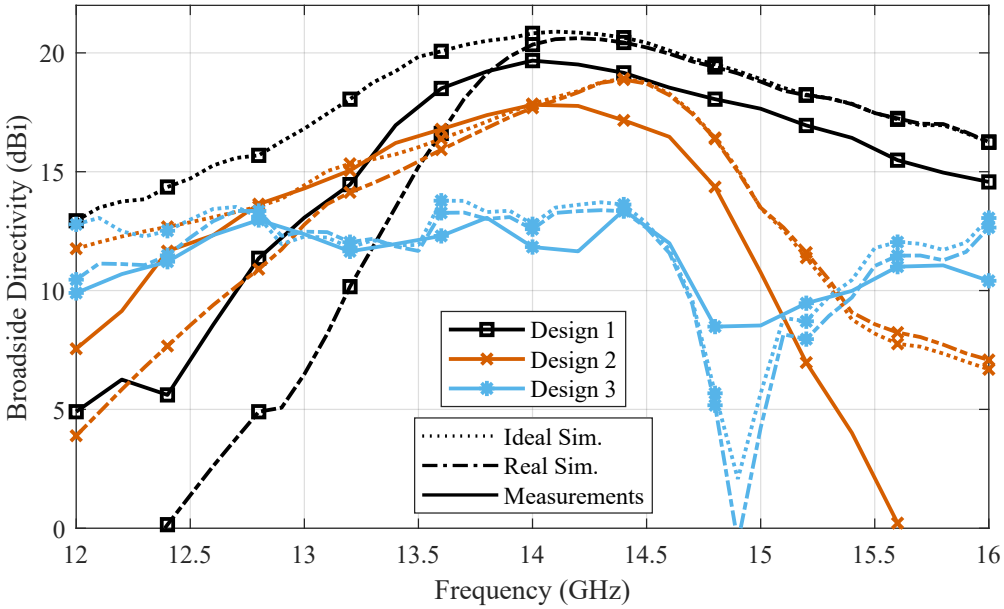

Figure 3.15: Comparison of the broadside directivity for the three designs, from simulations and measurements. Both ideal (HED source) and real (printed dipole source) simulations are shown.

bandwidth, with $f_c = (f_{\max} + f_{\min})/2$ being the band center frequency, and DBP is the directivity-bandwidth product, calculated as

$$\mathrm{DBP} = \frac{\int_{f_{\min}}^{f_{\max}} D_0(\tau)\, d\tau}{f_{\max} - f_{\min}} \cdot \frac{f_{\max} - f_{\min}}{f_c} = \overline{D_0(f)} \cdot \mathrm{FBW}\,. \tag{3.10}$$

When the realistic source is used, the radiation patterns are very similar to those from the ideal source simulations, as seen in Fig. 3.14, but the directivity level slightly drops, especially for Design 1. The bigger picture can be seen in Fig. 3.15, where a rapid deterioration occurs—the more the higher directivity is expected—for frequencies below the design one. As explained in Section 3.4, the root of this divergence between both simulations is the excitability of the cavity modes. Essentially, directivity increases as the leakage factor diminishes, approaching the cut-off condition of the hybrid mode, where it hardly accepts any power, as seen in Fig. 3.11 for Design 1. Hence, the low level of accepted power is, in fact, coupling to the unwanted TEM$^\rho$ mode, leading to different dispersion characteristics and spoiling the desired radiation behavior. This does not happen with the ideal HED excitation as its pure polarization is incapable of exciting the TEM$^\rho$ mode. Even so, the HPBW of Design 1 remains greater than that of Design 2, as seen in Table 3.1, which translates into a significant increase in the DBP. Thus, this effect can be taken into account, for example assuming that the highly directive FPCA is designed for the lower limit of the band of interest. Finally, although the directivity frequency behavior of Design 3 is not of much interest (the directivity

minimum around 15 GHz is related to the beam splitting), it serves to corroborate that as the cavity modes get more easily excitable, the ideal and realistically fed antennas present almost identical characteristics.

3.6.2 Experimental Validation

The PRSs, ground planes, and printed dipoles were fabricated using a LPKF ProtoMat S103 PCB milling machine. Screw holes were drilled in the corners of both the PRSs and ground planes, and nylon screws were used not to shorten both surfaces. In order to ensure the nominally designed cavity height, hollow plastic spacers were 3D-printed with the proper height of 10.41 mm, through which the nylon screws were inserted. For both printed dipole designs, a Multicomp 50 Ω SMA jack connector was soldered to the ground plane. Then, the coaxial probe was cut to be 1 mm long and soldered to the front printed strip. On the opposite layer, the back strip was soldered to the

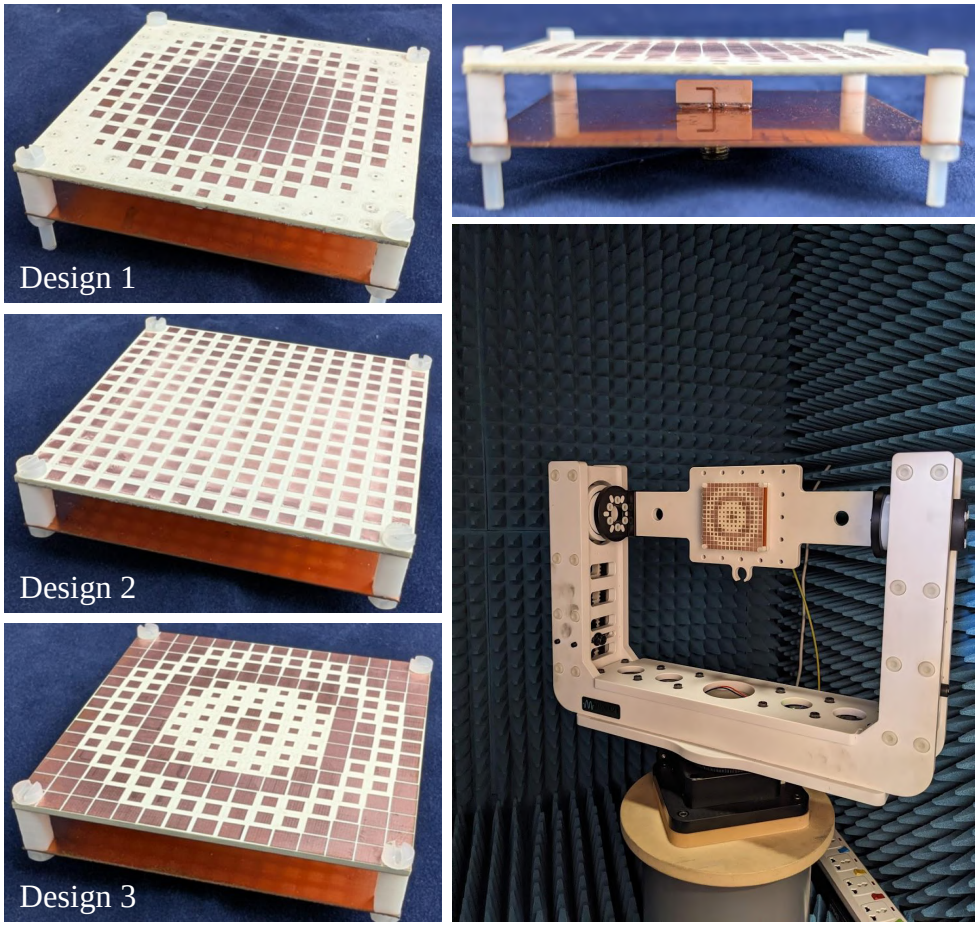

Figure 3.16: Photographs of the three FPCA prototypes (left), side view of Design 1 with its printed dipole source soldered inside (top right) and FPCA mounted on the positioner inside the anechoic chamber (bottom right).

ground plane, effectively realizing the required balun. The final prototypes are shown in Fig. 3.16. The radiation patterns were measured in the radio frequency (RF) anechoic chamber of the TELMA Research Institute premises at the University of Málaga.

The measured directivity is computed from integrating a fine spatial sampling of the total radiated power along the positive antenna semi-space. The measured broadside directivity for each design is shown in Fig. 3.15 along with the simulated results, as well as the impedance matching in Fig. 3.17. A good agreement is seen between the realistically-fed simulations and the measurements, which qualitatively present the expected behavior, and whose actual feeding configuration is shown in the top right image of Fig. 3.16. Design 1 achieves a slightly lower directivity level at the design frequency than its simulated counterpart, but it is higher for lower frequencies. This could be attributed to tolerances related to the PRS fabrication or the actual cavity height, which could be slight higher, hence achieving a less uniform aperture distribution but facilitating the TE^z/TM^z modes excitation, as suggested by the lightly better measured matching in Fig. 3.17. Even so, Design 1 remains better than Design 2 both at the directivity level and bandwidth, as expected, and both present impedance matching behaviors that highly match the simulated ones.

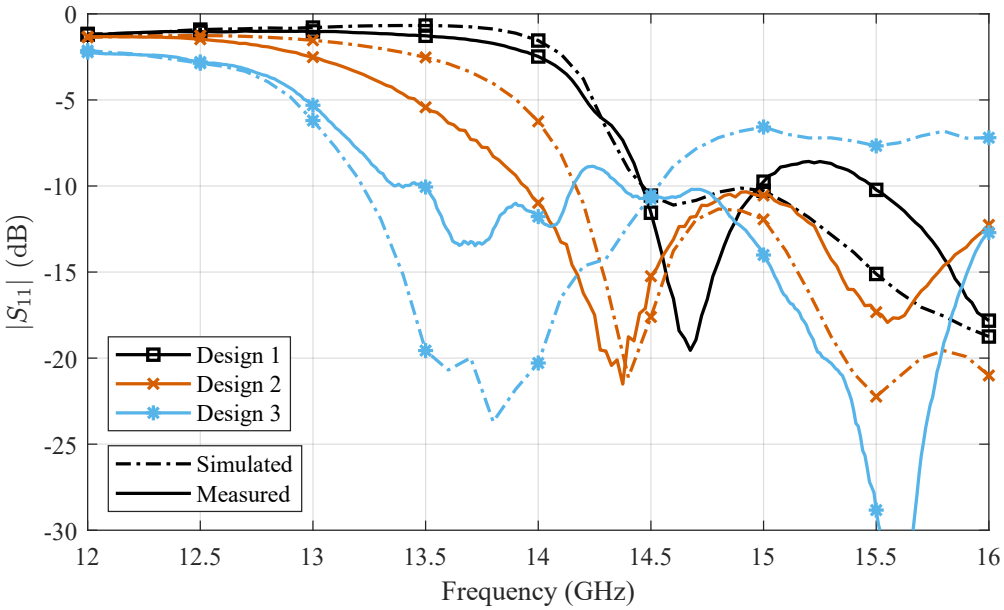

Figure 3.17: Measured reflection coefficient of the three FPCA designs. Simulation results are shown again for comparison.

Again, from Design 1 primarily, the physical limitations that arise from requiring a very high aperture efficiency for this thin-PRS FPCA configuration are observed. Even though the accepted power would be low in this case for the design frequency and below, it is coupled to the modes of interest and not the unwanted TEM^ρ. Thus, the radiation characteristics are not considerably degraded, in case an external matching

network is used. Design 3 shows a frequency dependency that highly matches that from simulation, and the minor directivity level deviation is attributed to measurement and fabrication tolerances. Its reflection coefficient, although not as similar to simulations due to prototyping tolerances mainly attributed to the dipole fabrication and soldering, successfully remains mostly below $-10\,\mathrm{dB}$ around the design frequency, as expected for this less critically reflective design. The measured figures of merit at the design frequency are also shown in Table 3.1 for comparison.

The measured directivity diagrams are displayed in Fig. 3.14 for the design frequency. The high similarity of the radiation patterns with the simulated ones is notable, even with the slight differences in the maximum directivity level. Note that even the observed side-lobe levels for the three designs significantly match those from simulations. The flat top in the main beam is also appreciated in Design 3, as expected. The improvement from Design 2 to Design 1 is clearly observed, with the latter achieving a pattern that considerably resembles the desired sinc function, and resulting in a significant improvement in the measured DBP too. Moreover, this figure of merit, normalized by the antenna footprint, is comparable or even better than those from some of the relevant works reported in [36]. This way, the measured radiation and frequency characteristics of the three designs, and the observed differences between each other, agree with the predictions, thus validating the presented approach.

3.7 Conclusions

In this chapter, a comprehensive approach has been presented to design tapered FPCAs with widened operational bandwidths. Thus, desired radial aperture field distributions can be engineered, resulting in improved radiation characteristics such as higher aperture efficiency. Bandwidth enhancement is achieved by employing a customary positive-slope phase technique for the PRS reflection. The presented methodology, which combines ray-optics and leaky-wave perspectives, offers a significant improvement over heuristic PRS tapering approaches. Moreover, it allows understanding and addressing the practical excitation challenges of FPCAs. Hence, valuable insight is provided on the fundamental excitation limitations whereby the input impedance becomes more purely reactive as directivity increases, guiding the selection of suitable feeding sources.

The proposed methodology has been validated through the design, fabrication, and measurement of three distinct FPCAs with single both-side-etched laminate PRSs. Experimental results show strong agreement with simulations, confirming the benefits of tapered PRSs in achieving an efficient illumination, the desired radiation pattern and,

ultimately, a directivity-bandwidth product that surpasses that of an homogeneous design. Furthermore, selecting a realistic printed dipole as the feeding source based on a mode compatibility perspective has proven successful in adequately exciting the fabricated prototypes. This underscores the importance of accounting for the fundamental excitation limitations, particularly in highly directive FPCA designs.

Chapter 4

Rigorous Aperture Control in 1-D Bianisotropic Huygens' Metasurface-Based LWAs

Planar leaky-wave antennas (LWAs) are a promising alternative for emerging wireless communication systems with demanding specifications, such as low profile, high directivity, beamforming and scanning capabilities. These structures have been studied since the last century [1, 7] and they still maintain the interest up to the day [51, 52]. As already seen, pattern shaping capabilities require great control of the LWA wavenumber along its extent. However, as briefly mentioned in Section 2.1, these antennas have traditionally suffered from a dependency between their phase constant and leakage factor (e.g. [53]), which limits the flexibility in the achievable radiation characteristics. In fact, a similar wavenumber components' dependency has already been observed in Chapter 3 for the FPCA design methodology, while allowing the generation of broadside—or conical, in general—beams only. In this sense, a more versatile selection of the radiation direction would be desirable.

On the other hand, metasurfaces are a very powerful tool to manipulate electromagnetic waves at will. Their ability to achieve field transformations has made them increasingly popular [4]. Although the general idea behind metasurfaces was already covered in Section 2.2, they are particularly interesting in this context as they have shown potential in providing antennas with enhanced versatility and efficiency [5, 54–58]. Moreover, the metasurfaces' low-profile and precise control over the radiation characteristics makes them greatly suitable for their use in planar LWAs. For example, by properly modulating the surface impedance, they can transform propagating modes into leaky modes with specific amplitude, phase and polarization [59–61].

In particular, Huygens' metasurfaces (HMSs) have been proposed in recent years as a powerful tool to achieve arbitrary wavefront manipulation [62–64]. They are able to implement a specific boundary condition for a given field transformation through the equivalence principle, as described in Subsection 2.2.2 along with their fundamental theoretical analysis. In their more general form, bianisotropic HMSs (BHMSs) offer great versatility for the macroscopic design in applications where the electromagnetic problem can be rigorously defined, avoiding the need for developing a different methodology specific to that structure. For example, they have been used to convert a propagating wave into a surface wave with near-perfect efficiency [65], to successfully achieve electromagnetic invisibility in practical realizations [66], or to reduce the beam-squinting effect in LWAs [67].

Specifically, a 1-D BHMS-based periodic LWA was already developed in [6] which allowed transforming a waveguide mode into a leaky mode with several degrees of freedom. The open stop-band effect was completely suppressed by allowing a single spatial harmonic to carry power without limitations in the selection of the period. In addition, independent control of the phase constant and the leakage factor was achieved, thus overcoming a main limitation of traditional LWAs. However, unlike other tapered LWA design methodologies where the leakage factor can be varied [52, 60, 68], the rigorous mathematical derivation of the BHMS-based LWA in [6] limited the wavenumber to being constant. This fact meant that the radiation pattern could not be engineered once the α and β values were chosen.

This chapter addresses this gap, extending the work in [6] to allow versatile radiation patterns using a simple, semi-analytically designed, LWA configuration. Therefore, the chapter is based on one of the author's works [J3], and structured as follows: Section 4.1 presents the rigorous macroscopic field stipulation incorporating arbitrary aperture illumination synthesis, whereas Section 4.2 offers the detailed resolution of the wave equation. Section 4.3 gives details on the macroscopic design methodology, whereas Section 4.4 explains how the BHMS unit cells are physically implemented through a novel field-based semi-analytical synthesis algorithm. Several designs are presented in Section 4.5, and their theoretical characteristics are compared to their simulated results in Section 4.6. Finally, some designs are fabricated, and their experimental validation shown in Section 4.7, whereas some conclusions are drawn in Section 4.8.

4.1 Structure Description and Field Stipulation

A 2-D configuration (1-D LWA) is assumed, in which the BHMS is infinite and invariant in the x-coordinate. Placing a parallel PEC plate at a distance d below the BHMS

would result in a variation of a PPW, thus creating a guiding structure as shown in Fig. 4.1. The main objective of the BHMS will then be transforming the field propagating along its bottom side to a leaky-wave field with the desired characteristics at its top side. Furthermore, the BHMS can also enforce the necessary conditions for the guided field to propagate between both plates. Particularly, in this case the structure has a length L in the y-coordinate and is excited with a TE polarized field ($E_y = E_z = H_x = 0$) at $y = 0$. The media above and below the metasurface are assumed non-magnetic and characterized by their relative electric permittivities ε_r^+ and ε_r^-, respectively. Both media present an intrinsic impedance $\eta^\pm = \sqrt{\mu_0/(\varepsilon_0\varepsilon_r^\pm)}$ and wavenumber $k^\pm = \omega\sqrt{\mu_0\varepsilon_0\varepsilon_r^\pm}$.

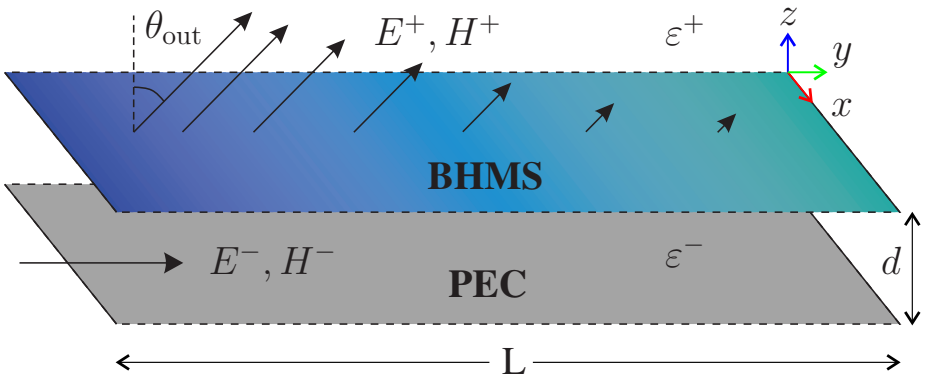

Figure 4.1: Diagram of the proposed BHMS-based LWA configuration.

The first step in the BHMS theoretical synthesis is the macroscopic design, which entails the stipulation of the desired electromagnetic fields on both of its sides. In accordance with the proposed structure, a guided-wave mode is stipulated below the BHMS, inside the PPW, while the desired field above the BHMS is stipulated as a leaky-wave mode radiating to the free space region at a certain angle with respect to the surface normal. The metasurface will impose the necessary boundary conditions at $z = 0$, so the only constraint for the guided field is to vanish at the PEC plane ($z = -d$), as described in [6]. However, in that previous work, the theoretical derivation constrained the wavenumbers to being constant. In this case, the goal is to engineer arbitrary aperture field distributions, for which spatially-varying wavenumbers are necessary. In order to take this variation into account, the field expressions from the previous work are modified, integrating the longitudinal wavenumber along the propagation direction (y-coordinate). Thus, the electromagnetic field tangential components below (-) the metasurface are stipulated as

$$E_x^- = 2j|E_{\text{in}}|\sin(k_z^-(z+d))\, e^{-j\int_0^y k_y^-(\tau)\,d\tau}\,, \tag{4.1a}$$

$$H_y^- = \frac{j}{k^-\eta^-}\frac{\partial E_x^-}{\partial z} = -2|E_{\text{in}}|\frac{k_z^-}{k^-\eta^-}\cos(k_z^-(z+d))\, e^{-j\int_0^y k_y^-(\tau)\,d\tau}\,, \tag{4.1b}$$

whereas, above (+) the metasurface, they are

$$E_x^+ = |E_{\text{out}}|\, e^{-jk_z^+ z} e^{-j\int_0^y k_y^+(\tau)\,d\tau} e^{j\xi}\,, \tag{4.2a}$$

$$H_y^+ = \frac{j}{k^+\eta^+}\frac{\partial E_x^+}{\partial z} = |E_{\text{out}}|\frac{k_z^+}{k^+\eta^+}\, e^{-jk_z^+ z} e^{-j\int_0^y k_y^+(\tau)\,d\tau} e^{j\xi}\,, \tag{4.2b}$$

where ξ is an added degree of freedom indicating an optional constant phase shift of the radiated wave. Note that the magnetic field will also present $\hat{z}$-directed components, but they are not explicitly derived here because their orthogonality to the BHMS makes them unnecessary for the metasurface parameters acquisition, as recalled from (2.24).

The longitudinal and transverse (to the guided wave propagation) wavenumbers are complex with attenuation factors α which are non-zero (to let the structure radiate):

$$k_y^-(y) = \beta^- - j\alpha^-(y); \quad k_z^-(y) = \beta_z^-(y) - j\alpha_z^-(y)\,, \tag{4.3a}$$

$$k_y^+(y) = \beta^+ - j\alpha^+(y); \quad k_z^+(y) = \beta_z^+(y) - j\alpha_z^+(y)\,. \tag{4.3b}$$

As aperture field distribution control is desired, the longitudinal attenuation factors are dependent on the y-coordinate, while $\beta^\pm$ is kept constant. Hence, as both wavenumbers will be related, the transverse wavenumber components will also be y-dependent, in general, as explicitly noted in (4.3).

The stipulated electromagnetic field is a TE mode on both semi-spaces, so the metasurface does not have to provide polarization conversion capabilities. Thus, the BHMS is of the omega-type, for which expressions (2.30) apply in this scenario. Furthermore, the desired arbitrary field transformation can be implemented with passive and lossless particles by satisfying the *local power conservation* condition (2.31). In this case, the stipulated fields (4.1) and (4.2) yield the following power profiles at the metasurface plane ($z \to \pm 0$), respectively:

$$P_z^-(y) = -\frac{|E_{\text{in}}|^2}{\eta^- k^-}\left(\beta_z^-(y)\sinh(2\alpha_z^-(y)d) - \alpha_z^-(y)\sin(2\beta_z^-(y)d)\right) e^{-2\int_0^y \alpha^-(\tau)\,d\tau}\,, \tag{4.4a}$$

$$P_z^+(y) = \frac{1}{2}|E_{\text{out}}|^2\frac{\beta_z^+(y)}{\eta^+ k^+}\, e^{-2\int_0^y \alpha^+(\tau)\,d\tau}\,. \tag{4.4b}$$

In order to satisfy the local power conservation constraint, one option is to impose that the fields have the same decay rate, even if they are spatially varying. This is, in fact, a generalization of the result presented in [6] in this context. Thus, $\alpha^-(y) = \alpha^+(y) = \alpha(y)$, where the latter is the leakage factor of the antenna. This way, the amplitude of the leaky field above the metasurface is fully determined from the rest of

known values (y-dependencies omitted for compactness):

$$\frac{|E_{\text{out}}|}{|E_{\text{in}}|} = \sqrt{2\frac{\eta^+ k^+}{\eta^- k^- \beta_z^+}\left(\alpha_z^- \sin(2\beta_z^- d) - \beta_z^- \sinh(2\alpha_z^- d)\right)}\,. \tag{4.5}$$

The value of $|E_{\text{out}}|$ will then be, in general, variable along y, in order to compensate for the power decay from $\alpha(y)$ and, thus, giving $P_z^+(y)$ the shape of the desired aperture distribution at the metasurface plane, and equal to $P_z^-(y)$.

4.2 Wave Equation Resolution

The validity of the stipulated field expressions (4.1) and (4.2) could reasonably be questioned: although the integration of the longitudinal wavenumber along the propagation direction might make intuitive sense, its physical feasibility is not directly proven. Taking a step back, it is important to recall that the field expressions stipulated in [6] (equal to (4.1)–(4.2) but with constant wavenumbers) were composed of harmonic functions as these are the set of valid solutions to the wave equation (named *elementary wave functions*) when the separation of variables technique is applied in cartesian coordinates [69]. Hence, when the wavenumbers are constant, a sinusoidal z-coordinate variation and a complex exponential along the y direction form a valid solution. Of course, proper boundary conditions must be then found for that solution to physically exist, which is the role of the PEC and BHMS plates. However, once the wavenumbers are not assumed constant, the technique of separation of variables cannot continue to be applied for the wave equation resolution. Consequently, the elementary wave functions will cease to necessarily be harmonic.

Nevertheless, it is common to approach these problems as small perturbations of the known, analytically-solved, case. This is why the harmonic functions from the constant wavenumbers scenario have been used, assuming they may not be completely invalidated. In any case, as the stipulated field with the integral in the exponential does not follow an elementary wave function, it must be verified whether it satisfies Maxwell's wave equation. Moreover, its solution will give the relation between the vertical and horizontal wavenumbers.

For this particular case, as $\partial/\partial x = 0$ is assumed, the corresponding Helmholtz equation reduces to

$$\nabla^2 \vec{E} + k^2 \vec{E} = \frac{\partial^2 E_x}{\partial y^2} + \frac{\partial^2 E_x}{\partial z^2} + k^2 E_x = 0\,. \tag{4.6}$$

The partial derivatives of the electric field with respect to the z-coordinate are

straightforward. They have the same form for (4.1) and (4.2) and their solutions are identical to those for the constant wavenumbers case:

$$\frac{\partial^2 E_x^{\pm}}{\partial z^2} = -k_z^{\pm 2}(y) E_x^{\pm} \,. \tag{4.7}$$

However, this is not the case for the partial derivatives with respect to y, as k_z and $|E_{\text{out}}|$ are now dependent on this coordinate. By using the fundamental theorem of calculus, the following expressions are obtained:

$$\frac{\partial E_x^{-}}{\partial y} = \left[(z+d) \frac{\partial k_z^{-}(y)}{\partial y} \cot\left((z+d) k_z^{-}(y) \right) - j k_y^{-}(y) \right] E_x^{-} \,, \tag{4.8a}$$

$$\frac{\partial E_x^{+}}{\partial y} = \left[\frac{1}{|E_{\text{out}}|} \frac{\partial |E_{\text{out}}|}{\partial y} - jz \frac{\partial k_z^{+}(y)}{\partial y} - j k_y^{+}(y) \right] E_x^{+} \,. \tag{4.8b}$$

Substituting (4.7) and the second order derivatives from (4.8) into (4.6), the complete relationship between wavenumbers for both regions of space, taking into account the variation along y, can be found to be a pair of quite intricate differential equations:

$$\begin{aligned} k^{-2} = {} & k_y^{-2}(y) + k_z^{-2}(y) \\ & - (z+d) \cot\left((z+d) k_z^{-}(y) \right) \frac{\partial^2 k_z^{-}(y)}{\partial y^2} + (z+d)^2 \left(\frac{\partial k_z^{-}(y)}{\partial y} \right)^2 \\ & + 2j(z+d) \cot\left((z+d) k_z^{-}(y) \right) \frac{\partial k_z^{-}(y)}{\partial y} k_y^{-}(y) + j \frac{\partial k_y^{-}(y)}{\partial y} \,, \end{aligned} \tag{4.9a}$$

$$\begin{aligned} k^{+2} = {} & k_y^{+2}(y) + k_z^{+2}(y) \\ & + jz \frac{\partial^2 k_z^{+}(y)}{\partial y^2} + z^2 \left(\frac{\partial k_z^{+}(y)}{\partial y} \right)^2 + 2z \frac{\partial k_z^{+}(y)}{\partial y} k_y^{+}(y) + j \frac{\partial k_y^{+}(y)}{\partial y} \\ & - \frac{1}{|E_{\text{out}}|} \frac{\partial^2 |E_{\text{out}}|}{\partial y^2} + j2 \left(z \frac{\partial k_z^{+}(y)}{\partial y} + k_y^{+}(y) \right) \frac{1}{|E_{\text{out}}|} \frac{\partial |E_{\text{out}}|}{\partial y} \,. \end{aligned} \tag{4.9b}$$

These dispersion relations make it difficult to effectively design a metasurface with the described stipulated fields. However, it can be noted that the expressions in (4.9) are, in fact, the usual Pythagorean sum of the longitudinal and transverse wavenumbers, with added terms related to their first- and second-order derivatives. Furthermore, the longitudinal wavenumber (k_y) is responsible for the variation of the transverse wavenumber (k_z) along y, hence the partial derivative of the latter can be expressed in terms of the former's, for both regions:

$$\frac{\partial k_z^{\pm}(y)}{\partial y} = \frac{\partial k_z^{\pm}(y)}{\partial k_y^{\pm}(y)} \frac{\partial k_y^{\pm}(y)}{\partial y} \,. \tag{4.10}$$

Now every differential term in (4.9) is ensured to be proportional to the derivatives of k_y^- or k_y^+. Moreover, as β^- and β^+ are fixed, and α is imposed to be the same in both regions through the local power conservation condition, then, from (4.3):

$$\frac{\partial k_y^-(y)}{\partial y} = \frac{\partial k_y^+(y)}{\partial y} = -j\frac{\partial \alpha(y)}{\partial y}\,. \tag{4.11}$$

This way, every differential term in (4.9) explicitly depends on the value of $\partial\alpha(y)/\partial y$, as ($y$-dependencies omitted for compactness):

$$\begin{aligned} k^{-^2} &= k_y^{-^2}(y) + k_z^{-^2}(y) \\ &\quad + (z+d)\cot\left[(z+d)k_z^-\right]\left[2\frac{\partial k_z^-}{\partial k_y^-}k_y^- + 1 + j\frac{\partial}{\partial y}\left(\frac{\partial k_z^-}{\partial k_y^-}\right)\right]\frac{\partial\alpha}{\partial y} \\ &\quad + j(z+d)\cot\left[(z+d)k_z^-\right]\frac{\partial k_z^-}{\partial k_y^-}\frac{\partial^2\alpha}{\partial y^2} - (z+d)^2\left(\frac{\partial k_z^-}{\partial k_y^-}\right)^2\left(\frac{\partial\alpha}{\partial y}\right)^2, \end{aligned} \tag{4.12a}$$

$$\begin{aligned} k^{+^2} &= k_y^{+^2}(y) + k_z^{+^2}(y) \\ &\quad + \left[z\frac{\partial}{\partial y}\left(\frac{\partial k_z^+}{\partial k_y^+}\right) + 1 - j2z\frac{\partial k_z^+}{\partial k_y^+}k_y^+ + 2\frac{\partial k_z^+}{\partial k_y^+}\frac{1}{|E_{\text{out}}|}\frac{\partial|E_{\text{out}}|}{\partial y}\right]\frac{\partial\alpha}{\partial y} \\ &\quad + z\frac{\partial k_z^+}{\partial k_y^+}\frac{\partial^2\alpha}{\partial y^2} - z^2\left(\frac{\partial\alpha}{\partial y}\right)^2 + j2k_y^+\frac{1}{|E_{\text{out}}|}\frac{\partial|E_{\text{out}}|}{\partial y} - \frac{1}{|E_{\text{out}}|}\frac{\partial^2|E_{\text{out}}|}{\partial y^2}\,. \end{aligned} \tag{4.12b}$$

Terms related to $|E_{\text{out}}|$ are differential and, per (4.5), it is evident that each constituent term will be multiplied by a derivative. However, for brevity, its explicit $\alpha(y)$ expansion is omitted. Thus, if a slowly varying amplitude approximation (SVAA) approach is assumed in (4.12) for the value of $\alpha(y)$, its derivative can be neglected. Consequently, all differential terms in (4.9) can be discarded, resulting in the common, simpler form of the dispersion relation:

$$k^{-^2} \simeq k_y^{-^2}(y) + k_z^{-^2}(y)\,, \tag{4.13a}$$

$$k^{+^2} \simeq k_y^{+^2}(y) + k_z^{+^2}(y)\,. \tag{4.13b}$$

These expressions allow a more straightforward design of the LWAs under study. However, as $\partial k_z^\pm(y)/\partial k_y^\pm(y)$ is a recurrent multiplicative factor in (4.12), it is important to ensure that it is big enough to invalidate the SVAA. Hence, assuming that (4.13) is valid and using (2.1) to relate $\beta^\pm$ to $\theta_{\text{in/out}}$, then:

$$\frac{\partial k_z^\pm(y)}{\partial k_y^\pm(y)} = \frac{1}{\sqrt{\left(\frac{k^\pm}{k_y^\pm}\right)^2 - 1}} \approx \tan\theta_{\text{in/out}}\,. \tag{4.14}$$

This factor would surpass a value of 10 in the media below (above) the metasurface for θ_{in} (θ_{out}) higher than 85°, which is not usually practical as it is too extreme. Therefore, this factor would not considerably alter the order of magnitude in (4.10). Consequently, by deduction, the approximate dispersion relation (4.13) remains valid.

4.3 Design Methodology and Considerations

The selection of the key LWA properties, namely the pointing angle and the desired radiation pattern, is the first step to carry out a design. As shown in (2.1), the pointing angle θ_{out} can be related to the phase constant above the metasurface β^+. Similarly, the angle of incidence θ_{in} inside the PPW—regarding the two interfering plane waves interpretation of the guided mode—can also be related to the phase constant under the metasurface β^-. For convenience, both expressions are shown below:

$$\beta^+ \simeq k^+ \sin(\theta_{\text{out}})\,, \tag{4.15a}$$

$$\beta^- \simeq k^- \sin(\theta_{\text{in}})\,. \tag{4.15b}$$

On the other hand, a proper control of the radiation pattern requires a leakage factor $\alpha(y)$ decoupled from the phase constant values. Indeed, the stipulated field expressions (4.1) and (4.2) explicitly allow for an arbitrary variable leakage factor, unlike in [6]. Hence, the omega-type BHMS will present the electromagnetic properties that provide the required field transformation, without any restrictions related to other antenna properties.

After deciding the antenna length L, and knowing the desired aperture field distribution $|A(y)|$, expression (2.8) can be used to extract the required leakage factor along the y-coordinate. In this sense, to better exploit the aperture area, the power remaining at the end of the antenna should be as low as possible. However, this entails a radiation efficiency η_{rad} very close to 1, which translates into $\alpha(y)$ taking very large values. Although this behavior is general for tapered LWAs, it is mostly relevant for the BHMS-based LWA discussed herein, as the validity of (4.13) depends on the taken SVAA approach, which assumes that the leakage factor value changes slowly. Thus, the use of very high values of η_{rad} could invalidate the theoretical derivation in Section 4.1. Moreover, (2.8) assumes a lossless scenario and can deviate significantly if considerable losses are present [70, 71], while the radiation efficiency increasingly depends on the phase constant value if the condition $\beta^- \gg \alpha^-$ is not satisfied [72]. These constraints must be taken into account to obtain the expected radiation characteristics with minimal degradation in practical cases.

It also must be taken into account that (2.8) is an approximation that assumes that the power decay in the aperture only depends on the $\alpha(y)$ value, i.e. that the vertical field profile remains unchanged for every transversal cut of the waveguide, which implies that k_z^- is constant in (4.1). Although this condition is roughly satisfied by the SVAA, if $\alpha(y)$ varies sufficiently along the antenna length, it will affect the value of $k_z^-(y)$, which will consequently influence the real power at the metasurface plane, as deduced from (4.4a). Numerical optimization of the leakage factor could refine the power profile but, for the sake of simplicity, the value from (2.8) is kept, as it should be accurate enough. A more extensive discussion on this topic along with its implications can be found in Appendix A.

Once the phase constants and leakage factor are specified, every wavenumber, both horizontal and vertical and for both regions of space, is uniquely defined by (4.13). Thus, the waveguide height d is another degree of freedom, such as the incidence angle θ_{in}, having the radiation and waveguiding problems effectively decoupled. In fact, the BHMS will force the boundary conditions necessary for the electromagnetic field to propagate below it, without forcing any relation between d and θ_{in}, and even when the waveguide height would be small enough, in normal circumstances, to put the waveguide under cut-off. These values can then be chosen following the most appropriate criteria, e.g., for maximum gain-bandwidth product, similar to [73], or for specific scanning capabilities as in [74].

With all the parameters set, the macroscopic design is completed. For the microscopic counterpart, the metasurface must first be discretized along the y-coordinate in order to allow the physical implementation of the theoretically continuously-varying boundary condition. Thus, the BHMS is subdivided into its meta-atoms, which will be sub-wavelength in size to allow a fine sampling of the required metasurface constituents $\{Z_{\text{se}}, Y_{\text{sm}}, K_{\text{em}}\}$. In this case, the sampling rate and, consequently, the meta-atoms' length, is chosen to be $\Delta_y = \lambda_0/4$, which could be considered as *coarse* discretization since it is not considerably smaller than a wavelength. Nevertheless, larger unit cells pose an advantage, easing the manufacturing process, as long as the homogenization approximation keeps working, which has been verified by numerical simulations.

Each meta-atom implements the local properties of the metasurface at a given $y = n\Delta_y$, with $n = 1, 2, \ldots, \lfloor L/\Delta_y \rfloor$, by assuming local periodicity, as explained in Section 2.2. In this case, the omega-type BHMS is governed by the GSTC given by (2.30), and its local properties can be retrieved through (2.32) with the tangential field components $[E_x^-, H_y^-, E_x^+, H_y^+]$ evaluated at $z \to \pm 0$. Hence, from a microwave network perspective, an equivalent circuit characterizing each unit cell as a 2×2 impedance matrix $[\mathbf{Z}]$ can be obtained as in (2.33), and whose components can be calculated from the BHMS ones through (2.34). Finally, by using equations (2.22), these local Z-

matrices can be converted to S-matrices, which may be more insightful on the unit-cell behavior.

In this sense, the LWA will partially transmit and reflect the leaky guided mode at each point. Thus, the reflection and transmission scattering parameters may adopt any given passive magnitude, in order to fulfill the required leakage factor function from (2.8). Furthermore, these parameters will need to present any given phase value, determined by the specific design requirements. Therefore, the unit cell should be able to synthesize any arbitrary lossless, reciprocal 2×2 S-matrix. Moreover, although the lossless characteristic is a requirement for the BHMS analysis to be valid, in practice, metasurfaces will not be completely lossless. Thus, for the metasurface behavior not to degrade much from the desired one, low-losses particles must be carefully selected.

As a last note, in [6] it was demonstrated that, when α is constant, the values of $[K_{\mathrm{se}}, Y_{\mathrm{sm}}, K_{\mathrm{em}}]$ are periodic with a period given as

$$p = \frac{2\pi}{|\beta^{+} - \beta^{-}|}\,. \tag{4.16}$$

This periodicity expression is in accordance with Floquet's theorem, as explained in Section 2.1 for periodic LWAs. In fact, (4.16) indicates that the LWA radiates from one of the first higher order spatial harmonics [$m = \pm 1$ in (2.2)], and the metasurface guarantees that no power is transferred to any other mode. However, once the wavenumber is variable, the metasurface constituents will cease to be periodic, in general. Nevertheless, the metasurface theoretical derivation guarantees the correct operation of the field transformation due to the uniqueness theorem. In fact, the exact conversion from the guided mode to a single leaky mode also guarantees the suppression of the open stop-band effect. This advantageous side effect is produced by the perfect interface matching provided by the BHMS, which avoids the chained reflections that cause the performance degradation at broadside.

4.4 Physical Implementation

The implementation of the meta-atoms with real geometries entails several challenges, due to the difficulty of synthesizing the lossless scattering properties required by any BHMS design. Starting from the ideal three stacked impedance sheets configuration described in Subsection 2.2.2, the first question arises on how to achieve the required reactance values for each layer. Usually, different geometries are printed on the copper metallization layers of the dielectric substrates. Depending on the shape of these copper traces, a wide range of impedance values can be synthesized under plane-wave illumination. However, the metal used for these geometries, as well as the dielectric

substrates over which they are printed, will present non-zero resistances, which will materialize as losses. Therefore, the actual impedance sheets will not be purely reactive and the practical implementation will diverge from the theoretical design. Furthermore, as already stated in [6], for this LWA application in particular, smaller values of θ_{in} mean that the wave impinges more times on the metasurface (from the perspective of the two interfering plane waves interpretation), which translates into an increase in total losses. From classical leaky-wave dispersion behavior, this effect can be interpreted as a rapidly increasing leakage factor as the leaky guided mode approaches its cut-off condition when θ_{in} tends to 0.

On the other hand, although the ideal stack of three pure-reactance sheets is a suitable configuration for proofs of concept in simulations, it offers an unique solution for the required reactance values[1]. Thus, depending on the specific properties needed for a meta-atom, those required values could be considerably hard to correctly synthesize. For example, a required reactance could be very small, which is hard to achieve in practical implementations with a sufficiently low resistance in comparison. Or, assuming that the chosen printed geometry is capable of synthesizing any reactance value (which is not usually the case either), its associated resistance is fixed, with very little to no loss minimization capability. Therefore, configurations with more than three impedance layers are often used, thus increasing the available degrees of freedom and broadening the solution space [6, 75]. This way, there is a higher probability of finding a set of printed geometries that better adjust the scattering parameters of a given unit cell, and resulting in lower total losses.

Increasing the number of layers, however, entails more complexity in the design. There is no initial solution for the reactance values [the closed-form expressions (2.35) do not hold anymore], thus their optimization becomes more complicated. In addition, as more layers are used, the total BHMS thickness grows, which usually deteriorates its performance due to lateral field interactions between adjacent unit cells [76]. In this sense, thinner substrates are preferred. Furthermore, when real implementation is considered, the near-filed coupling between the copper traces of the different layers can invalidate the simple transmission line model, as previously seen in Fig. 3.4.

In this work, the dimensions of the unit cells are $\lambda_0/6 \times \lambda_0/4$ using a design frequency of $f_0 = 15\,\text{GHz}$. Four Rogers RO3003 ($\varepsilon_r = 3$, $\tan\delta = 0.001$) laminates [77] of thickness $t = 0.762\,\text{mm}$ (30 mil) each are stacked and bonded with $t_{\text{bp}} = 50.8\,\mu\text{m}$ (2 mil) thick Rogers 2929 Bondply ($\varepsilon_{r,bp} = 2.94$, $\tan\delta = 0.003$) laminates [78], resulting in a total unit-cell height of $\lambda_0/6.25$. The copper traces are $18\,\mu\text{m}$ thick, have a width

[1] If only two layers are used, a solution may not even exist for certain scattering parameter combinations. However, if the aim is to minimize the unit-cell complexity, limited operation can be achieved in that case, as explored in greater detail in Appendix B.

of 0.1 mm and consist of dogbone, or dumbbell, shapes in every layer, as shown in Fig. 4.2. In addition, the media above and below the BHMS are assumed to be vacuum ($\varepsilon^- = \varepsilon^+ = \varepsilon_0$ in Fig. 4.1).

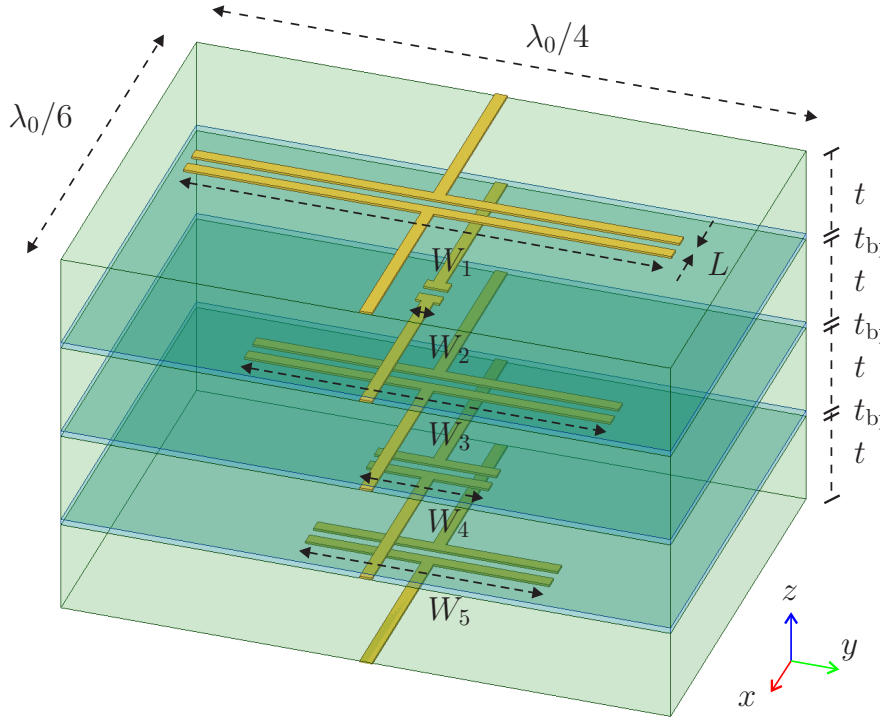

Figure 4.2: Real unit-cell configuration with 5 copper layers.

The low permittivity of the laminates, in addition with their thin thickness, are the right combination to favor a strong near-field coupling between layers. In fact, it has been verified through electromagnetic simulations that the simple equivalent circuit does not properly model the chosen meta-atom configuration. Thus, electromagnetic coupling between the different copper traces must be taken into account. In this sense, directly simulating the unit cells with every possible permutation of the 5-layers geometries would be unfeasible. Thus, some near-field aware analytical model is required.

Following the approach presented in [79–81], and recently implemented in [82], the scattering parameters of the meta-atoms can be obtained through a systematic formulation that addresses the near-field phenomena. This scheme analytically calculates the fields scattered by the stratified media configuration and the ones produced by the induced currents in the copper traces. For this specific implementation of the synthesis methodology, the conductor geometries are capacitively-loaded strips with a variable capacitor width W_n, n being the layer number. This specific copper geometry is needed to be modeled as a wire with an associated effective load impedance, which will directly relate to the induced currents from which the near-field interactions can be computed.

This was the reason for the use of this specific geometry in the first place and, thus, a very small $L = 0.1\,\text{mm}$ is chosen as the capacitor strips separation for all layers.

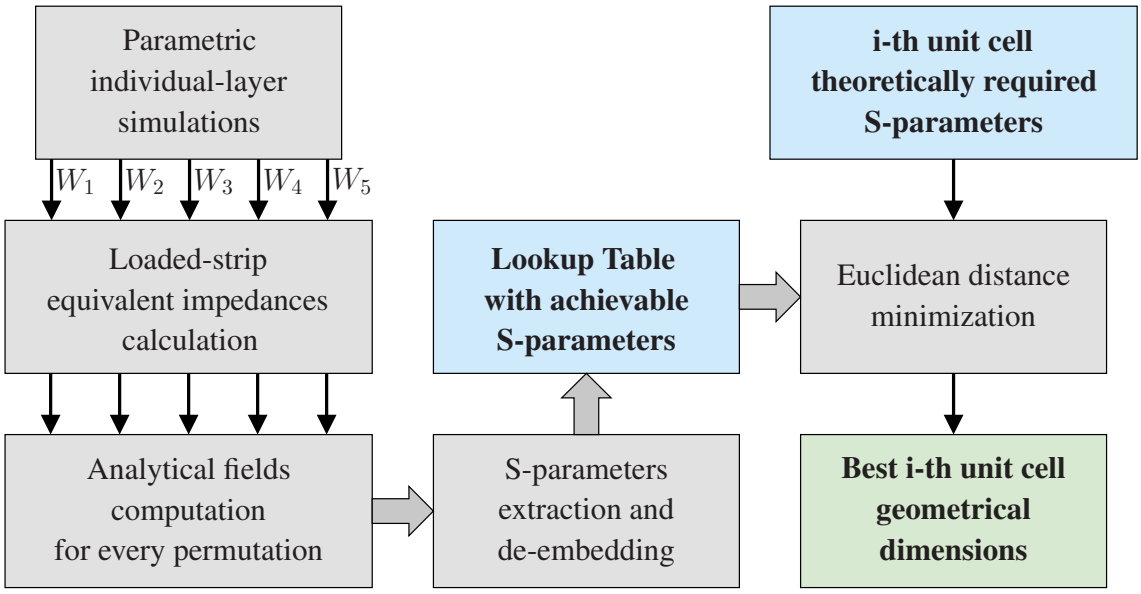

Figure 4.3: Block diagram of the semi-analytical unit-cell synthesis algorithm.

The semi-analytical unit-cell synthesis algorithm is summarized in the diagram depicted in Fig. 4.3, and explained as follows. In order to obtain the equivalent impedance of the loaded strips, parametric electromagnetic simulations are carried out for every copper strip placed alone in its interface within the complete layered substrates configuration. These simulations are performed in Ansys HFSS, under normally-incident, TE-polarized plane wave excitation from Floquet ports, and with periodic master-slave boundary conditions, as explained in Subsection 2.2.1. The capacitor width is swept in the range $W_n \in \{0.1, 0.2, ..., 4.9\}$ for every individual-layer simulation. The ports are referenced to the same plane, which is the first air-substrate interface from the bottom of the cell. This way, from the reflection and transmission coefficients of these simulations, using the expressions from [80], the equivalent impedances of the loaded strips for every W_n are calculated in the absence of the other ones. Note that these impedances do not refer to the homogenized layer impedances from Fig. 2.9, which cannot provide information about the higher-order modes excited by this particular copper geometry. Then, using those values, the external, scattered and strips-induced fields are analytically computed for all the possible permutations of W_n for the five layers. Note that only single-layer HFSS simulations are needed, and not for multilayer, which results in combinatorial savings. This way, a lookup table (LUT) is created containing the achievable local S-parameters [related to the Z-matrix in (2.33)], corresponding to all the realizable meta-atoms with capacitor widths $\{W_1, W_2, W_3, W_4, W_5\}$.

The scattering coefficients obtained from the previous scheme are referenced to the

vacuum intrinsic impedance η_0 and both ports are placed in the same plane. Thus, to get the S-parameters conveniently calculated at the planes interacting with the outer regions, all S-matrices in the LUT are de-embedded to have the second port referenced to the substrate-air interface at the top of the meta-atom. Finally, the best geometrical parameters for every unit cell in a design are chosen by searching for the S-matrix from the LUT that minimizes the difference with respect to the required ones, obtained from (2.34) as explained in Section 4.3. This difference is computed as the Euclidean distance

$$\Delta S = |\hat{S}_{11} - S_{11}|^2 + |\hat{S}_{21} - S_{21}|^2 + |\hat{S}_{22} - S_{22}|^2, \tag{4.17}$$

with the hat symbol indicating the goal unit-cell parameters. This method has given better results in general than computing the difference as a sum of weighted errors for the coefficients magnitude and phase separately. In summary, this semi-analytical approach outputs the final dimensions of a unit cell for any desired scattering parameters it is desired to offer. Furthermore, it poses a great advantage regarding previous works as is able to do so while taking into account the near-field coupling phenomena, so the unit-cell substrate thickness can be chosen as thin as desired. Finally, only individual-layer simulations are carried out, with the associated time savings by avoiding any complete unit-cell simulation.

As the copper traces are restricted to present capacitive responses, potentially better solutions requiring inductive loads are not considered. For this particular meta-atom configuration, at least five impedance layers have been necessary to synthesize a suitable range of amplitude and phase values for both reflection and transmission of the S-parameters. This is clearly shown in Fig. 4.4, where a fraction of the whole set of achievable S-parameters is represented, as to give a qualitative view of how much of the potentially required solution space is fulfilled with the obtained LUT. Although the transmission coefficient magnitude $|S_{21}|$, its phase $\angle S_{21}$ and the reflection coefficient phase $\angle S_{11}$ do not completely describe the S-matrix when it is not lossless, it does give an approximate idea of the synthesizable values as losses are limited up to 10%. Ensuring that the meta-atoms present low losses is essential not to compromise the ideally-lossless BHMS theoretical analysis. Note that the same meta-atom configuration with only four copper layers lacks a considerable portion of the solution space (Fig. 4.4a), especially in comparison with its five-layers counterpart (Fig. 4.4b).

It is worth noting that the angle of incidence inside the LWA waveguide will not be normal to the BHMS. Therefore, formally, the characterization of the BHMS meta-atoms should be obtained under plane wave excitation with an incidence angle determined by the θ_{in} of the desired design. In this sense, a single dogbone-shaped copper geometry has been characterized in simulations under periodic boundary conditions and

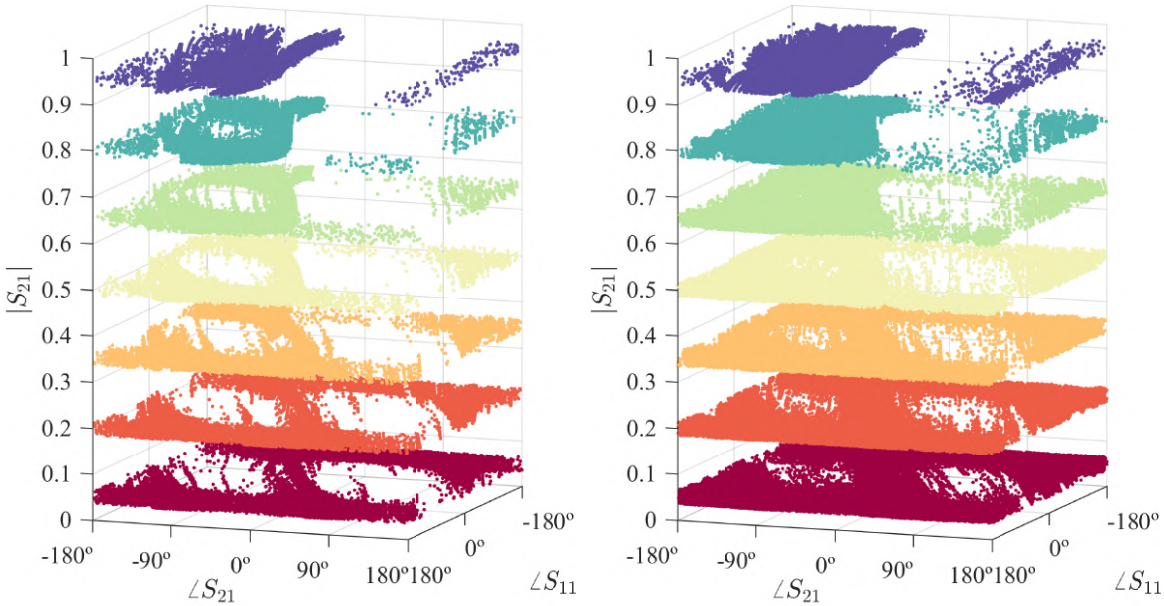

Figure 4.4: Achievable S-parameters with losses limited to a maximum of 10% for the (a) 4 layers and (b) 5 layers unit-cell configurations. Several cuts of the complete LUT of synthesizable parameters are plotted to facilitate a qualitative visualization.

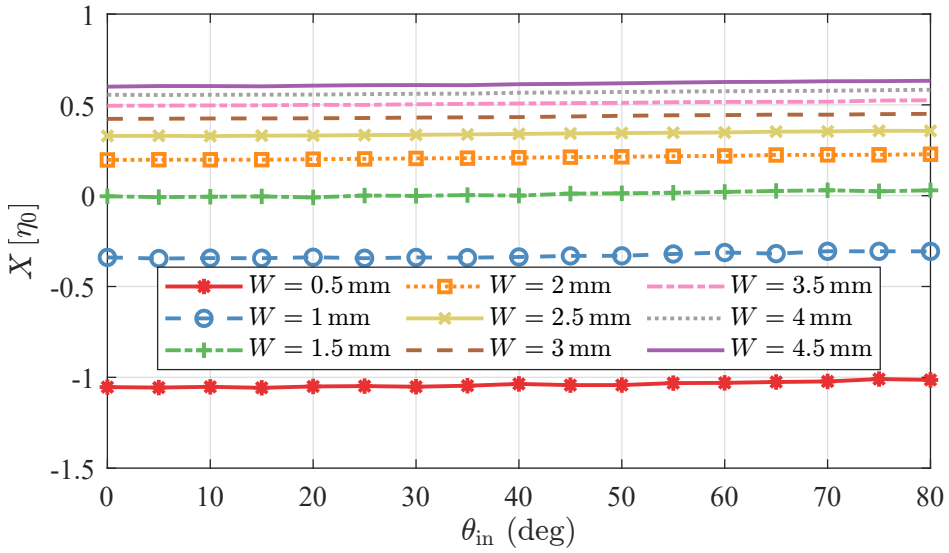

Figure 4.5: Normalized equivalent parallel reactance of a single copper geometry with respect of the obliquely-incident plan wave angle, for different capacitor widths.

oblique incidence, with a semispace filled with air and the other with Rogers RO3003. Fig. 4.5 shows the obtained equivalent parallel impedance for a range of angles. The observed reactance variation is low, so the scattering properties will change with the incidence angle mainly due to the different impedance mismatches produced by the change in the wave impedance as $Z_{\text{wave}} = \eta / \cos\theta_{\text{in}}$. Consequently, as the complete

unit cells are electrically thin, the scattering behavior of the metasurface can be approximated as that characterized for normal incidence, for angles that do not deviate much from it.

4.5 Design Descriptions

Several designs are carried out in order to test the validity of the theoretical derivations and the synthesis methodology. Three different pointing angles have been chosen along with several goal radiation patterns, to verify that the LWA properties can be selected at will while successfully enforcing the required aperture field distribution. For each pointing angle, a design is carried out without engineering the aperture distribution, i.e. with a constant α, for which the periodic nature of the LWA can be observed. This period relates θ_{in} with the value of θ_{out} through (4.16) and (4.15). This way, subsequent designs that implement variable leakage factors use the previously obtained θ_{in}, although there is no longer a physical period relating it to the pointing angle.

These designs are all carried out at 15 GHz, which is the same frequency for which the meta-atoms have been characterized. In addition, they all have a total length of $L = 10\lambda_0$ in order to obtain a fair comparison between them and facilitate the experimental validation with the same fabricated waveguide. For the latter reason, all the metasurfaces are also conceived for a waveguide of height $d = 0.5\lambda_0$ and filled with air. The rest of the parameters for each design is described in Table 4.1.

Table 4.1: LWA parameters for the different designs.

	θ_{out} (°)	θ_{in} (°)	$p\,[\lambda_0]$
Design 1	0	26.4	9/4
Design 2	-30	30	4/4
Design 3	60	21.5	8/4

The three designs cover representative cases, namely broadside radiation for Design 1 (special and complicated case for LWAs due to the open stop-band issue [10]), backwards radiation for Design 2 and extreme-angle beam for Design 3 (which radiates from the opposite spatial harmonic than the other designs). The chosen values of θ_{in} are not considerably high in order to enable the use of the normal-incidence characterization of the unit cells, as discussed in Section 4.4. In addition, those values, which are similar for all the designs, guarantee an electric field profile inside the waveguide that would be under cut-off if no BHMS was used, thus showcasing yet another of its capabilities. Nevertheless, the field profile is similar to that of a typical TE_{10} mode for HFSS to be able to successfully converge.

The aperture distribution is also modified for each pointing angle. In particular, applying Uniform and Hamming windows, respectively

$$|A(y)|\big|_{\text{Uniform}} = 1\,, \tag{4.18}$$

$$|A(y)|\big|_{\text{Hamming}} = 0.54 - 0.46\cos(2\pi y/L)\,, \tag{4.19}$$

with different required radiation efficiencies η_{rad}, in addition to the base constant-α variants. By using (2.8), the required dependency for the leakage factor of each design is calculated, and shown in Fig. 4.6. A variety of combinations for the aperture distribution and radiation efficiency are selected in order to obtain a wide range of examples. The chosen η_{rad} are also considerably high to test the applicability of the SVAA approach also in these extreme cases. Note also that the pointing angle does not affect the variation in $\alpha(y)$. Hence, for example, the curves for the Uniform aperture with $\eta_{\text{rad}} = 99\%$ are equal for Designs 1 and 3.

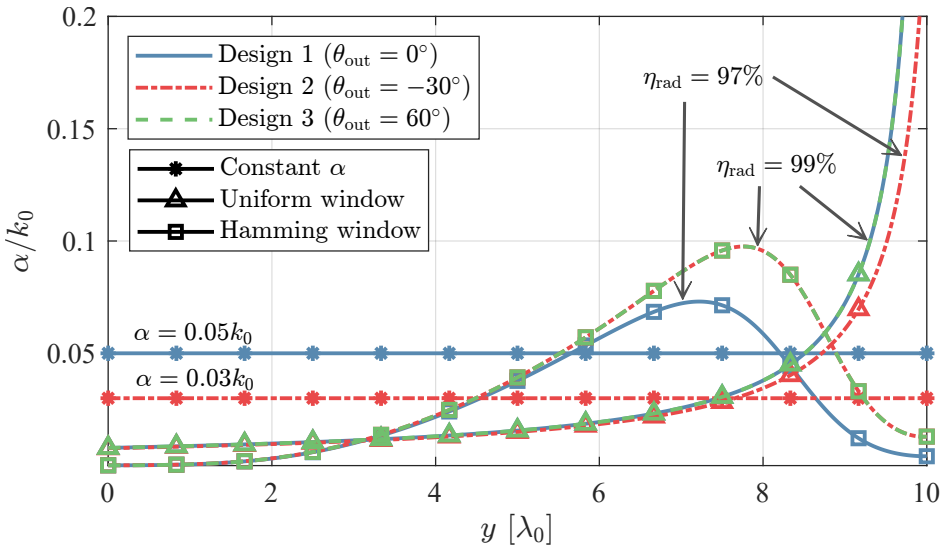

Figure 4.6: Comparison of the leakage factor functions for each design variant.

As specified in Table 4.1, the periods are chosen to be natural number of times the length of the unit cells ($\lambda_0/4$). Hence, for the constant α cases, only the unit cells inside one period must be synthesized, and then they are periodically reused. However, as the metasurfaces are no longer periodic when the aperture field distribution is engineered to manifest spatially-varying decay coefficients $\alpha(y)$, every unit cell along the antenna length will be, in general, different from the others. Consequently, the fact that the meta-atoms are synthesized following the powerful semi-analytical approach described in Section 4.4, leading to fabrication-ready layouts without any further full-wave optimization, possess a great advantage for the efficient realization of these designs.

With the previous parameters, the wavenumbers are completely defined using (4.13)

and the fields are calculated with (4.1) and (4.2). Hence, for each design, those field values are input into (2.32) to obtain the BHMS parameters (computed only at discrete steps related to the meta-atoms coordinates, as discussed in Section 4.3), which can be converted to the impedance matrices required for each meta-atom through (2.34). Finally, these are transformed to the η_0-referenced S-matrices through (2.22), for which the synthesis algorithm will find the closest ones in the LUT, as defined in (4.17).

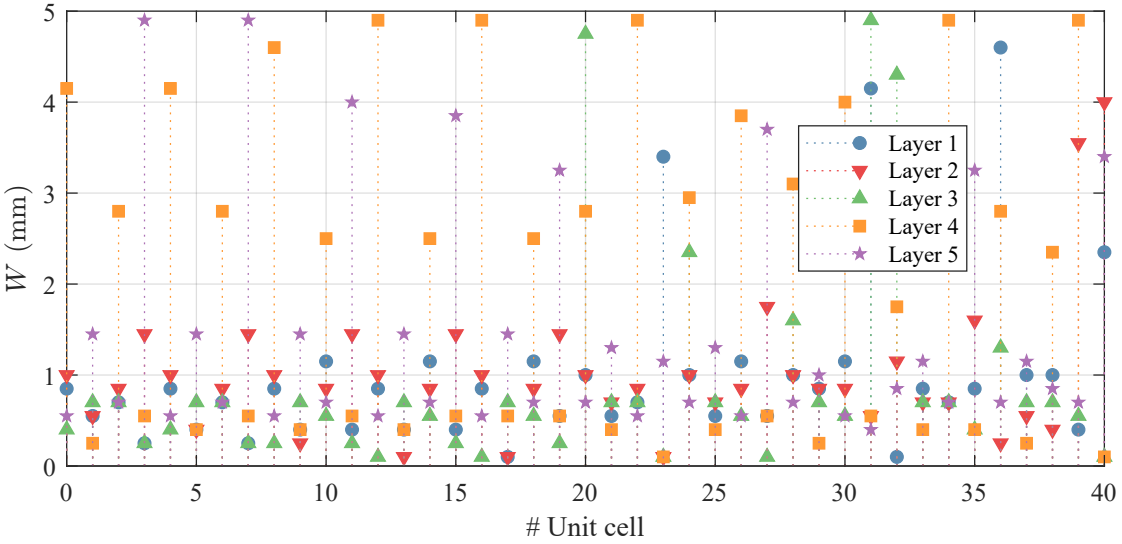

Figure 4.7: Unit-cell capacitor widths for Design 2 with Uniform window aperture distribution.

As an illustrative example, the W_n dimensions obtained from the synthesis algorithm for each unit cell of the Design 2 with Uniform window aperture distribution are shown in Fig. 4.7. In Fig. 4.8a, their semi-analytically synthesized S-parameters are shown and compared to the goal ones. In addition, the scattering properties of those unit cells, individually obtained via full-wave simulation under periodic conditions, are also displayed. Note that the represented S-parameters are renormalized by using $Z_{01} = \eta_0/\cos\theta_{\text{in}}$ and $Z_{02} = \eta_0/\cos\theta_{\text{out}}$ as reference impedances in (2.22). This provides a better physical interpretation, avoiding ripples from the mismatch between the physical wave impedance and the reference one. A very high similarity between the desired and achieved parameters is seen for all unit cells, thus demonstrating the great accuracy of the algorithm predictions. As physical intuition, note that $\angle S_{11}$ is kept practically constant to guarantee the proper guided mode propagation, $\angle S_{21}$ slope is given by the conversion from θ_{in} to θ_{out}, and $|S_{21}|$ relates to the leakage factor. Furthermore, Fig. 4.8b shows that the majority of the unit cells present losses below 10% in simulation, very similar to the predicted ones, which is a satisfactory result.

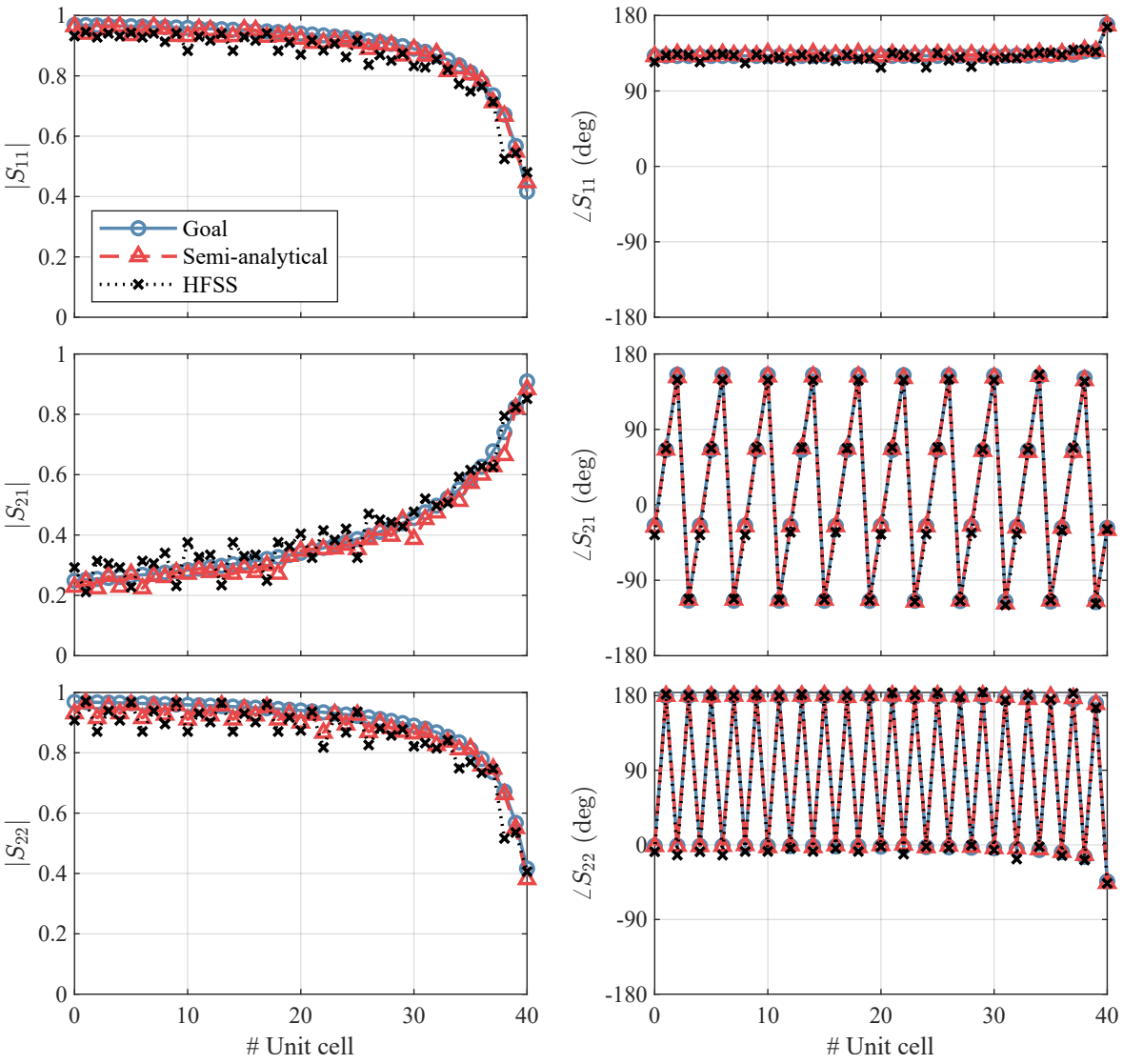

(a)

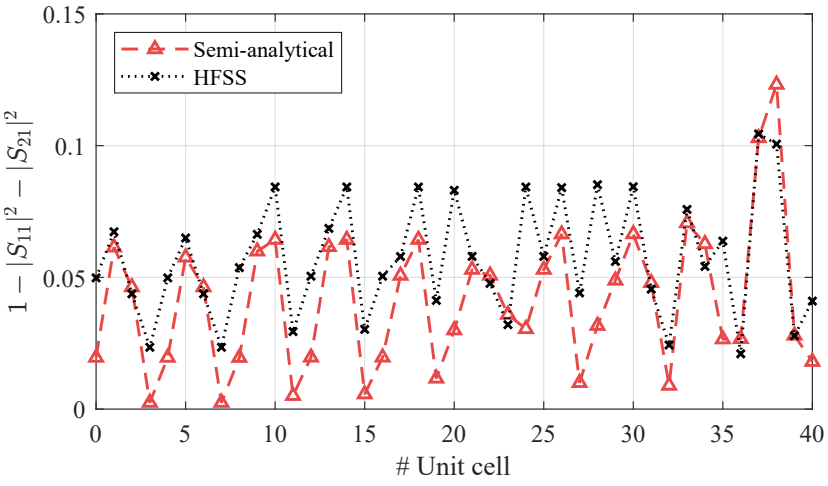

(b)

Figure 4.8: Unit-cell (a) generalized S-parameters and (b) associated losses for Design 2 with Uniform window aperture distribution.

4.6 Simulation Results

In order to carry out the full-wave simulation of the designs in Ansys HFSS, PEC sheets are placed on planes $x = \pm\lambda_0/12$ to emulate the x-axis infinite periodicity needed for the desired TE mode. This allows for the use of only one row of meta-atoms along the antenna length. In addition, a current line source in the x-axis is used as excitation instead of a waveport, as the excited field profile of the latter would not match that inside the waveguide. These simulations are computationally intensive, converging in around 7 hours on average and using up to 100 GB of RAM in a 24 logic cores computer running a 2020th 4 GHz AMD processor. Therefore, ideal simulations are previously carried out as an intermediate step, using ideal unit cells like the one shown in Fig. 2.9a. These can be simulated using ideal, analytical impedance boundary conditions available in HFSS, which allows reaching a good convergence in under 30 minutes using a maximum of 20 GB of RAM.

For brevity, only one aperture distribution case of each of the three designs is shown in Fig. 4.9, where a comparison of the electric field magnitude along the yz plane between the theoretical derivation [based on (4.1)–(4.2) and the radiated field calculations explained in Subsection 2.2.3] and the realistic simulation results (using the unit cells from Sections 4.4 and 4.5) is displayed. A very good agreement can be observed for the three shown cases. As designed, each case presents a different output angle while all having a similar input angle. It can also be noted how the field profile inside the waveguide is slightly cut before it reaches a null at $z = 0$ (as would happen in a PEC guide) and, yet, the BHMS guarantees its propagation.

The top (Figs. 4.9a, 4.9b) and bottom (Figs. 4.9e, 4.9f) displayed cases, respectively Design 1 and Design 3, both present a uniform aperture, employing (4.18). This is clearly visible as the power radiated along the metasurface remains relatively constant, even though the power inside the waveguide clearly decays. Unlike a constant-α case, this allows taking advantage of all the antenna extent while radiating the majority of the available power before it reaches the end, thus achieving both high aperture and radiation efficiencies. The middle displayed design (Figs. 4.9c, 4.9d) is the Hamming aperture case of Design 2, which employs (4.19). In this case, the field is mainly radiated at the middle of the BHMS, which offers lower secondary lobes at the expense of a lower aperture efficiency. The interaction of the field with the metasurfaces in the realistic simulations can be appreciated at $z \approx 0$ in the figures on the right.

As the radiation characteristics have been designed for a 2-D configuration, the 2-D

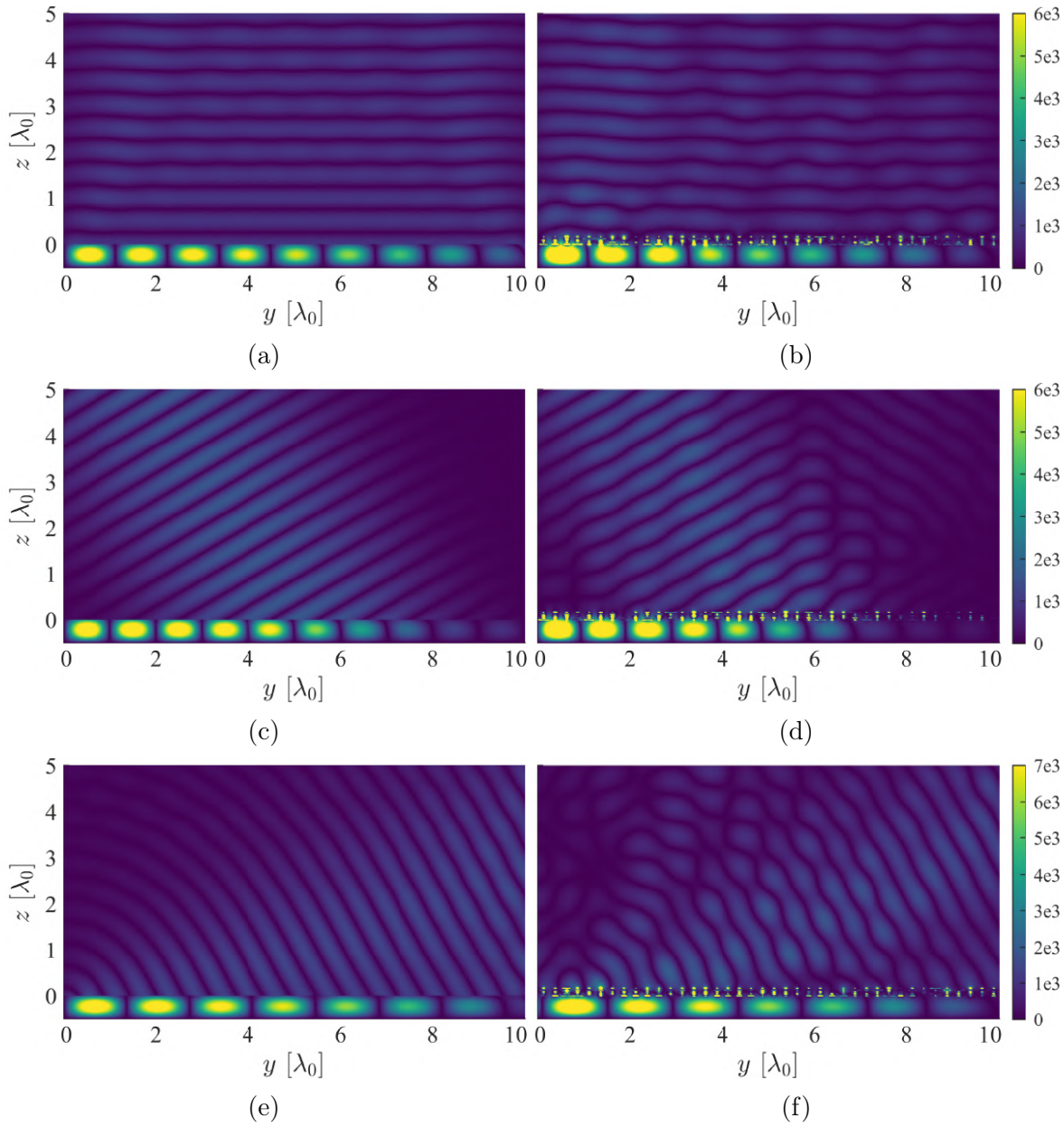

Figure 4.9: Field distributions $|\Re\{E_x(y,z)\}|$ (V/m) of (a,c,e) theoretical predictions and (b,d,f) realistic electromagnetic simulations, for (a)–(b) Design 1 and (e)–(f) Design 3 with Uniform apertures, and (c)–(d) Design 2 with Hamming aperture.

directivity is calculated as [6]

$$D_{\text{2D}} = \frac{2\pi\, U(\theta, \phi = \pi/2)}{\int_0^{\pi} U(\theta, \phi = \pi/2)\, d\theta}\,, \tag{4.20}$$

where $U(\theta, \phi)$ is the radiation intensity. Hence, the associated 2-D directivity diagrams are shown in Fig. 4.10, where a very good agreement between theory and simulations can be observed. Theoretical far-field components are calculated using radiation in-

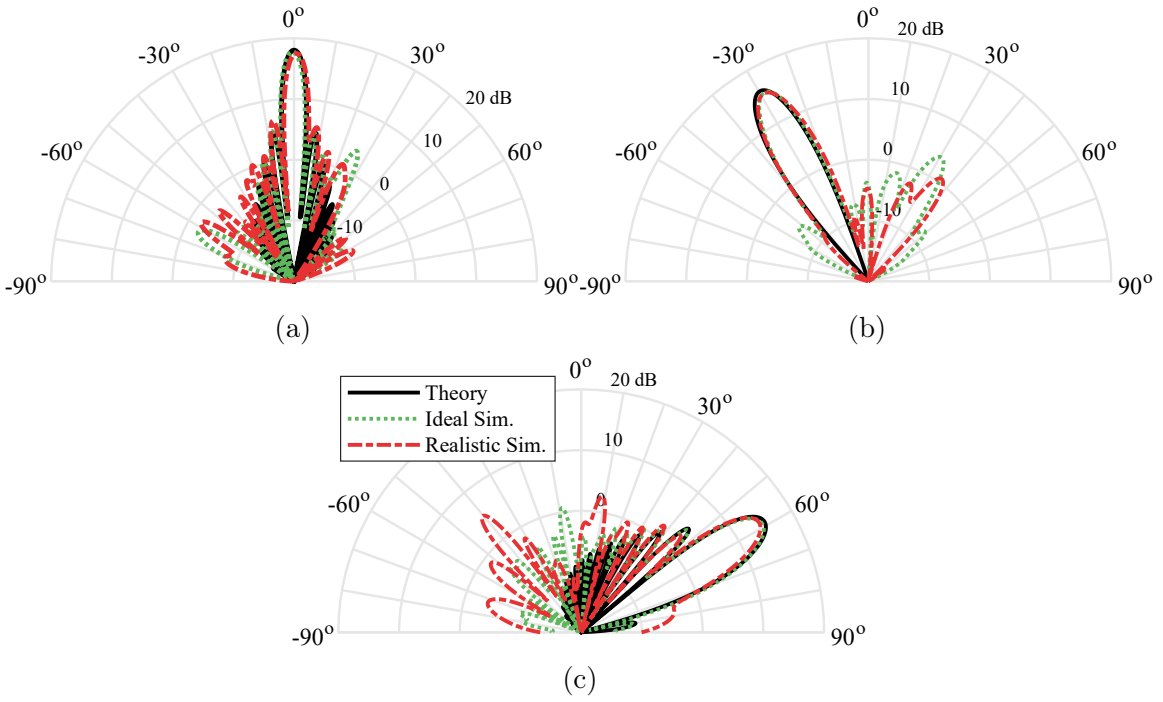

Figure 4.10: 2-D directivity radiation patterns in the yz plane from theoretical derivation and electromagnetic simulations: (a) Design 1 with Uniform aperture, (b) Design 2 with Hamming aperture, and (c) Design 3 with Uniform aperture.

tegrals from the fields at the metasurface aperture, as described in Subsection 2.2.3. It can be noted that some undesired secondary lobes appear, although some of them are already present in the ideal simulations. Thus, they may be caused by the very high values chosen for the radiation efficiency, which could take the SVAA approach beyond its strict validity, thus exciting spurious spatial modes. Regardless, the three shown cases present very high radiation efficiencies and, still, the used methodology holds. The step from the ideal reactance metasurfaces to the realistic ones does not considerably degrade the radiation characteristics, as can be noted from the figures of merit in Table 4.2, in which D_0 refers to the maximum 2-D directivity level, and the aperture efficiency is $\eta_{\text{ap}} = D_0\lambda_0/(2\pi L)$. A high similarity between theory and simulations can be noticed for all the designs. This demonstrates the potential of the synthesis methodology, taking into account that no full-wave optimization of the unit cells nor the complete BHMS has been carried out.

4.7 Experimental Validation

To verify the presented concept in practice, three BHMS prototypes have been fabricated, corresponding to Design 2 with the three different aperture distributions.

Table 4.2: Figures of merit of the presented designs.

			θ_{out} (°)	D_0 (dBi)	η_{ap} (%)	η_{rad} (%)	SLL (dB)
Design 1	**Constant**	Theory	0	15.9	61.4	99.8	-
		Ideal Sim.	0.1	15.4	55.5	99.6	-19.6
		Real. Sim.	0.4	14.8	48.5	99.9	-25.4
	Uniform	Theory	0	18.1	100	99	-13.4
		Ideal Sim.	-0.4	17.8	94.8	97.7	-12.8
		Real. Sim.	0.6	17.5	89.4	99.9	-10.9
	Hamming	Theory	0	16.6	73.5	97	-43.6
		Ideal Sim.	-1.2	16.4	69.4	96.2	-13.5
		Real. Sim.	-0.1	16.0	63.1	99.2	-14.6
Design 2	**Constant**	Theory	-30	16.4	70.2	97.7	-
		Ideal Sim.	-29.8	16.9	77.7	93.0	-18.8
		Real. Sim.	-27.4	16.0	62.7	99.1	-11.9
	Uniform	Theory	-30	17.4	88.2	97	-12.6
		Ideal Sim.	-30	17.2	83.7	87.5	-13.2
		Real. Sim.	-28.7	17.2	83.0	99.2	-11.7
	Hamming	Theory	-29.5	16.0	63.8	99	-41.4
		Ideal Sim.	-28.8	15.5	56.2	95.8	-11.8
		Real. Sim.	-29.1	15.4	54.7	99.9	-14.7
Design 3	**Uniform**	Theory	59	15.3	53.3	99	-10.7
		Ideal Sim.	59.1	14.8	47.7	99.7	-10.5
		Real. Sim.	58.3	14.4	43.9	99.9	-9.3
	Hamming	Theory	58	14.0	40.2	99	-37.8
		Ideal Sim.	58.7	13.5	36.0	97.7	-11.2
		Real. Sim.	57	13.0	31.4	99.9	-10.0

4.7.1 Manufacturing and Feeding Considerations

Pasternack PE44343 SMA connectors are used to feed these antennas. The connector is inserted at the beginning of the waveguide through a lateral wall with the pin exposed in the x direction to excite the TE mode of interest. In order to avoid any disturbances that the coupling from the feeding-probe coaxial mode to the waveguide mode may cause in the BHMS performance, non-radiating sections are added to both ends of the fabricated metasurfaces. These sections have a length of $\lambda_0/2$ (2 unit cells long) and ensure that the guided mode presents the profile that the radiating BHMS section expects, thus guaranteeing good matching between sections.

The unit cells of these edge sections must be non-radiating. Consequently, they are grounded at the top, making their implementation much simpler, as only the S_{11} parameter must be synthesized. By using the formulas from Section 4.3 with the parameters corresponding to Design 2 in Table 4.1 while imposing $\alpha = 0$, then a required $S_{11} = e^{j125.3^\circ}$ is obtained. The unit-cell geometry considered here only presents the copper dogbone of the bottom layer (see Fig. 4.2), and the remaining layers are totally metalized. The value of W_5 is swept in an HFSS parametric simulation of the complete described configuration, obtaining the synthesizable S_{11} values. Fig. 4.11 shows the obtained results, along with a representation of the non-radiating unit cell, in which only layers 5 and 4 are shown, as the latter one being a copper plane makes the rest of the layers electromagnetically negligible. Hence, in this case, $W_5 = 0.87\,\text{mm}$ achieves the reflection coefficient which is maximum in magnitude and closest in phase to the required one.

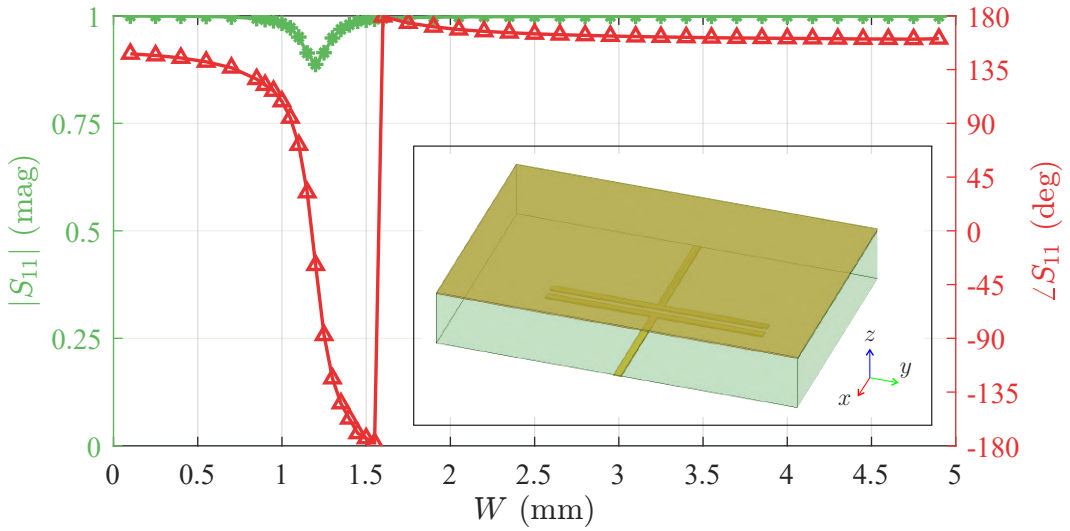

Figure 4.11: Simulated reflection coefficient with respect to the single-geometry capacitor width of the non-radiating unit cell, represented in the inset.

The exact location where the connector is inserted to achieve a good matching is obtained by a parametric analysis in HFSS. It is carried out using ideal impedance boundary conditions to speed up the process, and the chosen location is then verified in a realistic simulation. Thus, the coaxial probe is inserted at $\Delta y = 4\,\text{mm}$ from the start of the waveguide, $\Delta z = 5.6\,\text{mm}$ from the bottom (where the field profile has its maximum), and the exposed pin penetrates $\Delta x = 2.33\,\text{mm}$ into the guide. This point provides consistent matching across designs, enabling a single manufactured waveguide for all measurements. A second, mirrored connector at the waveguide end, terminated with a matched load, ensures the dissipation of the remaining power and avoids unwanted reflections. In fact, this complete feeding configuration is simulated to obtain the η_{rad} values from Table 4.2. For the realistic simulations, load termination

and ohmic losses are accounted for by this efficiency, consequently higher values are expected. As seen, the theoretical and simulation values are in good agreement, with very high values in general, guaranteeing almost no power is dissipated at the load.

The metasurfaces, manufactured by Printech Circuit Laboratories Ltd, comprised three meta-atom rows along the x-axis to physically enforce the desired periodicity to an extent, mitigating manufacturing tolerances. The tripled waveguide width than initially simulated requires the coaxial probe depth to be readjusted. A new $\Delta x = 3.5\,\text{mm}$ is obtained from parametric simulation with ideal impedance boundary conditions, as realistic simulations with the three-rows BHMSs were computationally prohibitive.

The waveguide itself was manufactured in two longitudinal aluminum pieces at the University of Málaga. Both pieces were CNC-machined and then assembled together using metallic screws, as shown in Fig. 4.12. The waveguide walls extend 2 mm above the BHMS top height in order to ensure that the conductor condition at both of its sides is sufficiently satisfied. Due to fabrication errors, the coaxial connectors holes were located at a displaced $\Delta y = 4.42\,\text{mm}$ which, although not optimal, should provide an acceptable matching. Each fabricated metasurface is mounted into the waveguide and measured in the same anechoic chamber as in Subsection 3.6.2. A matched load is connected to the end port, and radiation is measured in the yz plane.

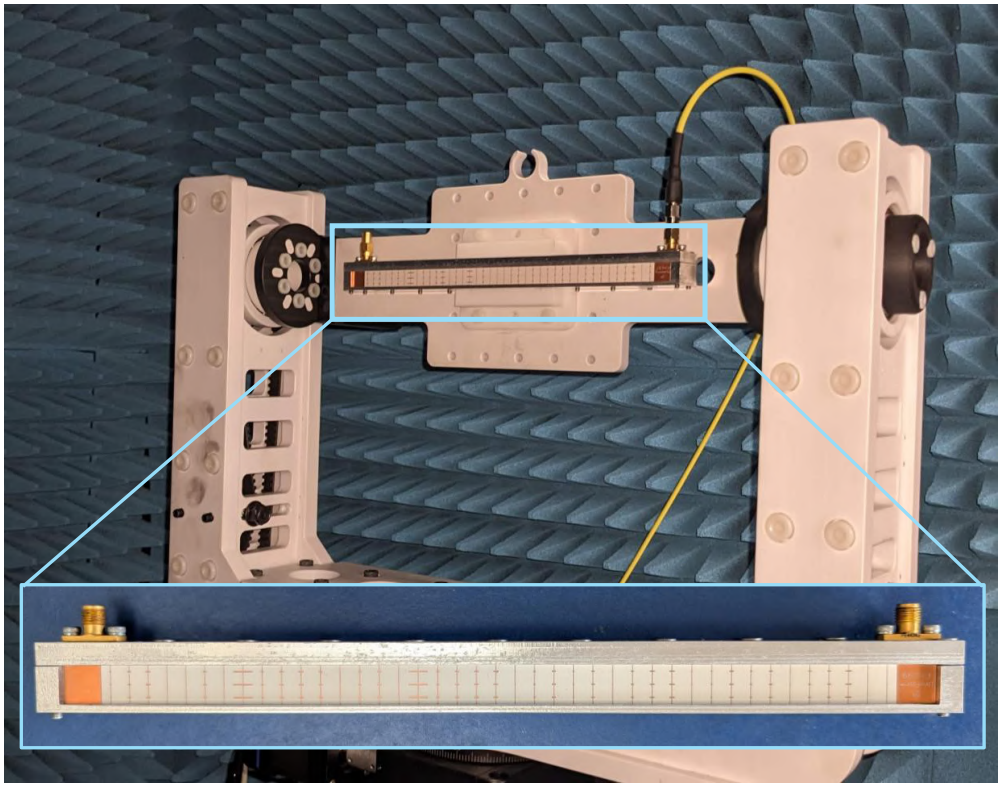

Figure 4.12: LWA prototype with one of the BHMS, mounted on the positioner inside the anechoic chamber, along with a top view inset.

4.7.2 Measured Results

An overview of the measurements results in comparison with those from realistic simulations is shown in Fig. 4.13, where the maximum 2-D directivity and the main pointing angle as functions of frequency are shown for the three aperture distribution cases. The bottom graph only shows the pointing angle for the bands of interest, in order to avoid representing noisy values when the directivity is not high enough (and secondary lobes start becoming the main one).

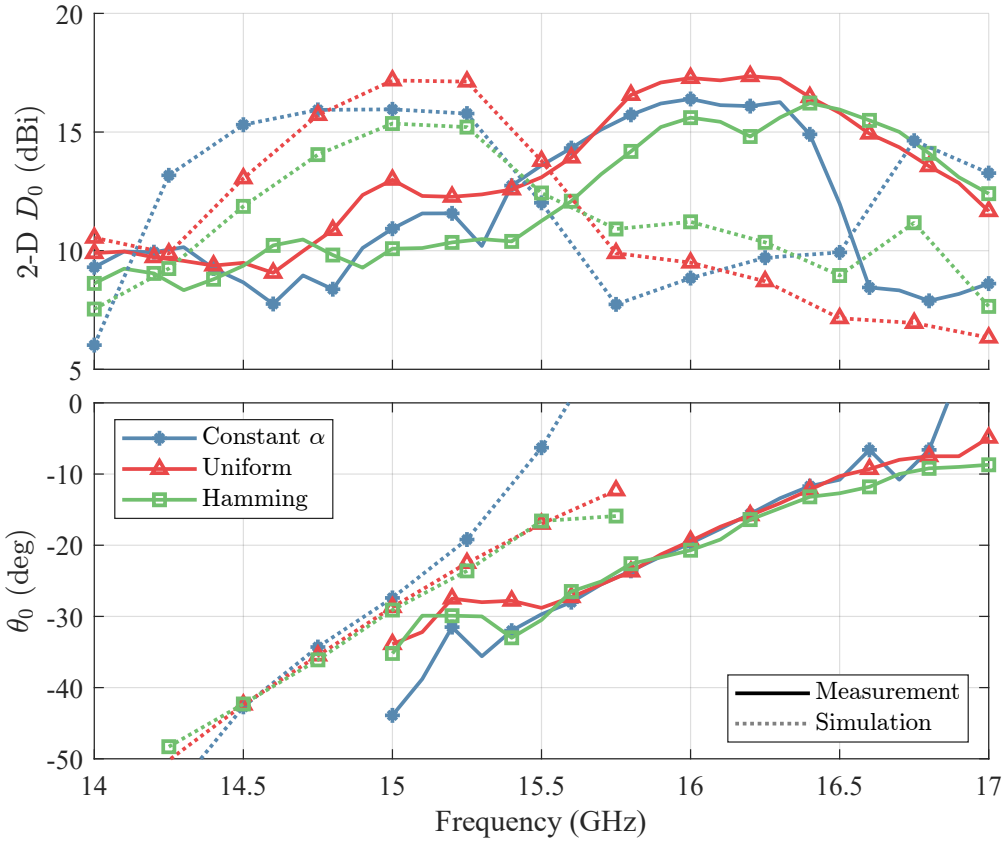

Figure 4.13: Measured and simulated maximum 2-D directivity (top) and corresponding pointing angle (bottom) for the three aperture cases of Design 2.

First, it is noticed that the maximum measured directivity occurs around 16 GHz for all cases, whereas it was expected at the design frequency of 15 GHz, as in simulations. Therefore, the expected behavior has undergone a systematic frequency shift. Nonetheless, the measured radiation characteristics remain very close to those from simulation. The maximum 2-D directivity levels reach their expected values, and their frequency behaviors are very similar to the simulated ones, being almost flat in the corresponding band of interest. In that band, where the BHMS characteristics can be assumed to remain similar, the main change is produced in the pointing angle due to the expected frequency scanning. Furthermore, because of this, the measured pointing

angle at the shifted frequency is displaced to around $-20°$, as seen in the bottom plot of Fig. 4.13.

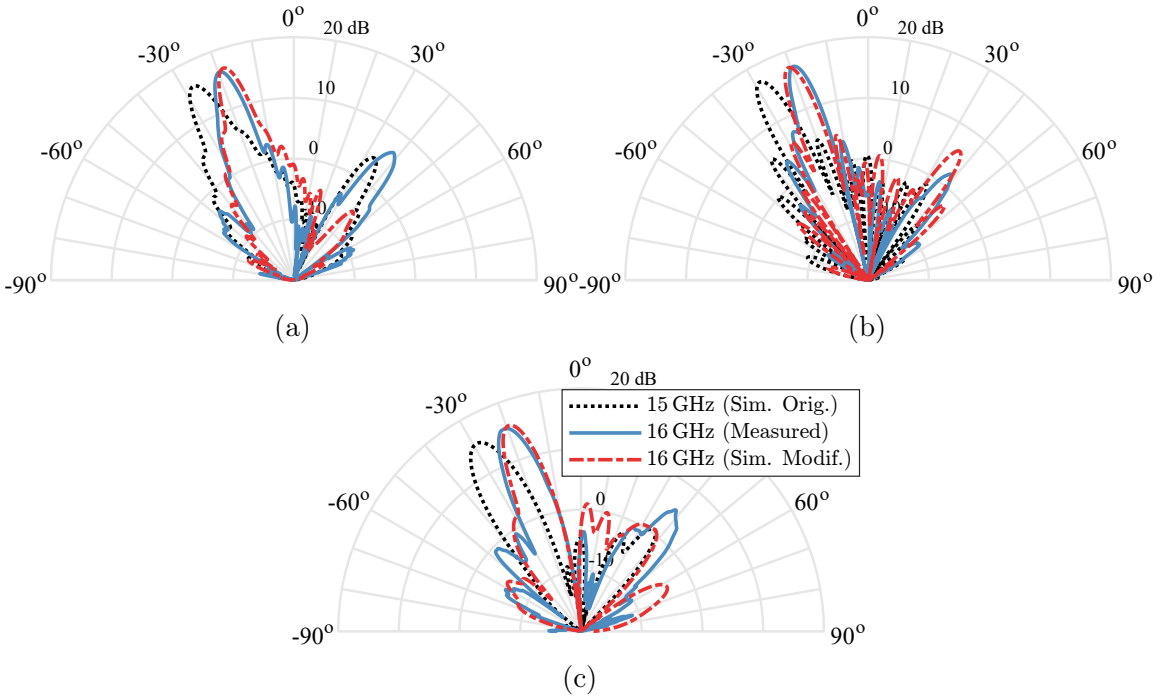

Figure 4.14: Measured and simulated 2-D directivity patterns at their peak performance frequency for the (a) constant α, (b) Uniform and (c) Hamming aperture distribution cases of Design 2, in addition to the simulated patterns assuming a 14% permittivity deviation.

Fig. 4.14 shows a comparison with the simulated directivity patterns at their corresponding peak performance frequency for the three aperture cases. As can be noted, although shifted in frequency, and consequently in angle too, the measured patterns highly resemble those from simulation. Greater sidelobes are noticed with respect to simulations, which is attributed to the slight behavior degradation expected from the undesired frequency shift. The Hamming aperture case is very sensitive to deviations from the theoretical expectations, as high sidelobe levels (SLLs) defeat its purpose; even so, the experimental result is within simulation expectations, as the SLL around the main lobe is lower than -15 dB, and the forward spurious lobe was expected. Therefore, omitting the frequency shift, simulations and measurements are in close agreement.

4.7.3 Investigation on Observed Deviations

The observed frequency shift is a systematic error, as the 1 GHz upshift is observed for every measured design. Therefore, an investigation on the potential causes was carried

out, for which multiple tests were performed. This process was extensive and thorough, so only a summary of the investigation tests and results is provided here:

- **Copper trace dimensions:** Microscopic inspection showed that the fabricated copper strips had length and width-related dimensional errors below 10 µm, with random (non-systematic) variations. Simulations with slightly narrower traces confirmed negligible impact on performance.
- **Layer misalignment:** Although slight misalignments between the layers were detected (especially in the bottom layer), reverse mounting experiments and detailed inspection showed that these did not cause the frequency upshift. Simulations with observed misalignments also confirmed minimal influence.
- **Non-radiating metasurface test:** In the same fabrication batch, a completely non-radiating metasurface was also manufactured for testing purposes, composed only of unit cells like the one shown in Fig. 4.11. Even using single-layer unit cells and with the radiation problem decoupled, this metasurface exhibited a similar frequency shift when compared to simulations, confirming that inter-layer misalignment was not responsible for the observed discrepancy.
- **Substrate and Bondply thickness deviations:** Manufacturer-provided data and visual inspection revealed that Bondply layers were thinner than nominal, leading to an overall thinner substrate stack, and potentially leading to voids between the Bondply and copper traces. Simulations showed that thinner substrates cause an upshift in frequency, consistent with measurements.
- **Waveguide and metasurface width:** The waveguide and metasurface widths were checked and matched closely to nominal values. Simulations showed that small width mismatches could affect performance, but experimental sealing of gaps with copper tape did not improve agreement with simulations, indicating correct physical assembly.
- **Vertical placement of the metasurface:** Tests involving slight height variations showed expected angular deviations but did not explain the measured frequency shift. The non-radiating metasurface was also used to confirm correct vertical alignment within the waveguide.
- **Connector effects:** The influence of coaxial connectors was considered negligible, as they only impact impedance matching and not the radiation characteristics, which do not depend on the non-radiating sections.
- **Substrate permittivity deviation:** Simulations assuming a lower effective permittivity, distributed between the RO3003 and 2929 Bondply layers, provided

the best match to experimental results. A downward deviation of around 14% ($\varepsilon_r = 2.6$ for RO3003 and $\varepsilon_{r,bp} = 2.5$ for 2929 Bondply) reproduced the measured behaviors accurately.

Thus, after this qualitative sensitivity study, it is found that the permittivity deviation is the only reasonable source of error that could gracefully shift the frequency behavior without totally degrading the radiation characteristics. Although the 14% shift is considerably large, it can be treated as a macroscopic averaged error that may arise from a combination of factors summarized above, such as minor fabrication tolerances (e.g., reduced thickness, potential air voids, layer misalignments) and other added factors that are difficult to estimate directly (e.g., copper roughness [83], material anisotropy).

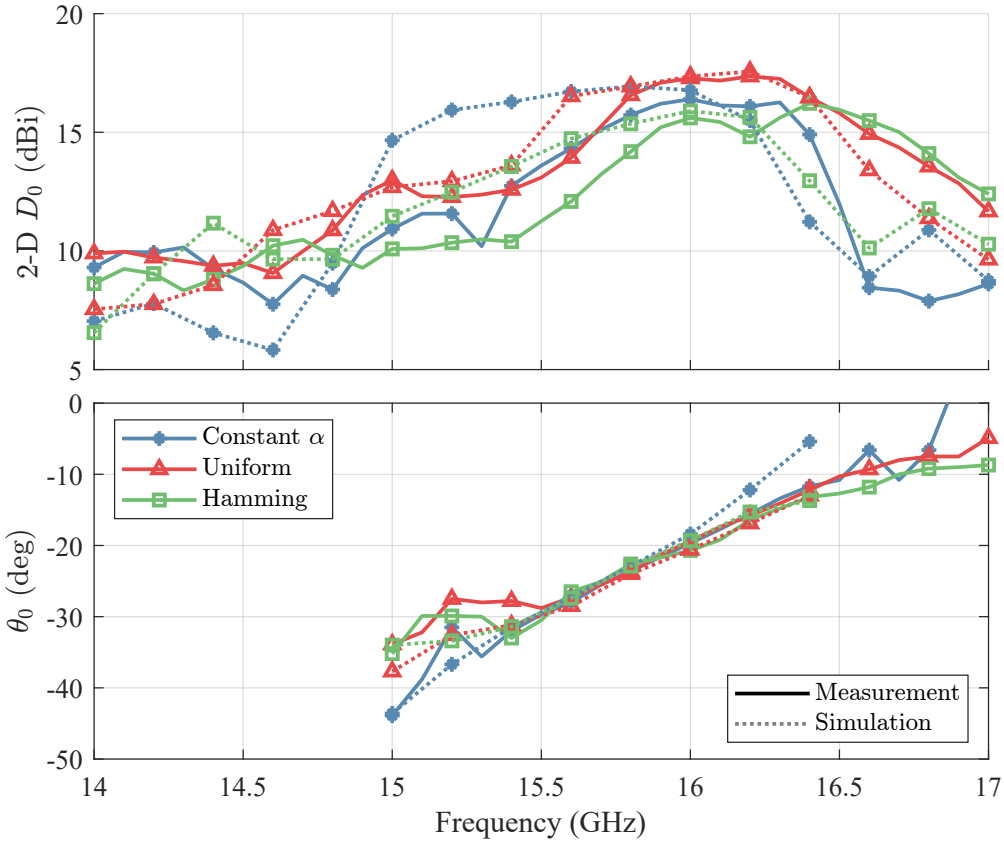

Figure 4.15: Simulated maximum 2-D directivity (top) and corresponding pointing angle (bottom) for the three aperture cases of Design 2, assuming a 14% permittivity deviation. Measurements included again for better comparison.

This permittivity deviation would make the unit cells electrically shorter, thus increasing the frequency for which they present the expected electrical length and, consequently, a behavior similar to the nominally designed. This behavior is in close correspondence to the one found in measurements and also in simulations where this permittivity deviation is considered, whose results are also plotted in Fig. 4.14 for

comparison. The simulated patterns that take into account this error are remarkably similar to those from the experiments, both in shape and in the peak performance frequency and pointing angle. The slight discrepancies in pointing angle can be attributed to measurement misalignments. Furthermore, Fig. 4.15 presents the radiation characteristics with respect to frequency for these modified simulations (again, the pointing angle is only displayed for sufficiently differentiated main beams). Compared to the measured behaviors, the resemblance is clear for the three designs, as summarized in Table 4.3, where $\Delta\theta_{3\text{dB}}$ is the half-power beam-width and HPBW is the half-power bandwidth. Finally, a highly similar frequency scanning performance is observed, thus validating the hypothesis. Nevertheless, based on what has been observed, it would be advisable for next batches to also manufacture some electromagnetic device that explicitly helps to extract the effective permittivity of the substrate stack, for example a ring resonator.

Table 4.3: Figures of merit of the measured prototypes and corresponding modified simulations for Design 2.

		θ_{out} (°)	D_0 (dBi)	$\Delta\theta_{3\text{dB}}$ (°)	SLL (dB)	HPBW (GHz)
Constant	Measured	-19.7	16.4	5.9	-13.6	0.99
	Mod. Sim.	-18.4	16.8	5.9	-14.7	1.31
Uniform	Measured	-19.4	17.3	5.4	-10	1.05
	Mod. Sim.	-20.6	17.4	5.2	-11.4	1.07
Hamming	Measured	-20.7	15.6	7.7	-16.3	1.2
	Mod. Sim.	-19.3	15.9	7.2	-14.9	1.14

In any case, the relation between the directivity levels of the different aperture cases highly relates to that expected from theory and simulation. This demonstrates that the desired aperture distributions have been achieved and that the operating principle of these aperiodic BHMSs works as expected, demonstrating the concept. In addition, frequency scanning is achieved for frequencies around the peak performance one, as shown in Fig. 4.16 for the uniform aperture case. The metasurface is able to reasonably maintain the main beam shape and directivity level in this band. Note that this occurs even when the suppression of spurious spatial modes is not guaranteed (and higher sidelobes are observed, in consequence) for frequencies different from that the pure transformation is designed for.

The reflection coefficient of these measured prototypes is shown in Fig. 4.17. The matching at the design frequency of 15 GHz is acceptable, although not great, due to the discussed metasurface fabrication tolerances and the aforementioned deviation in

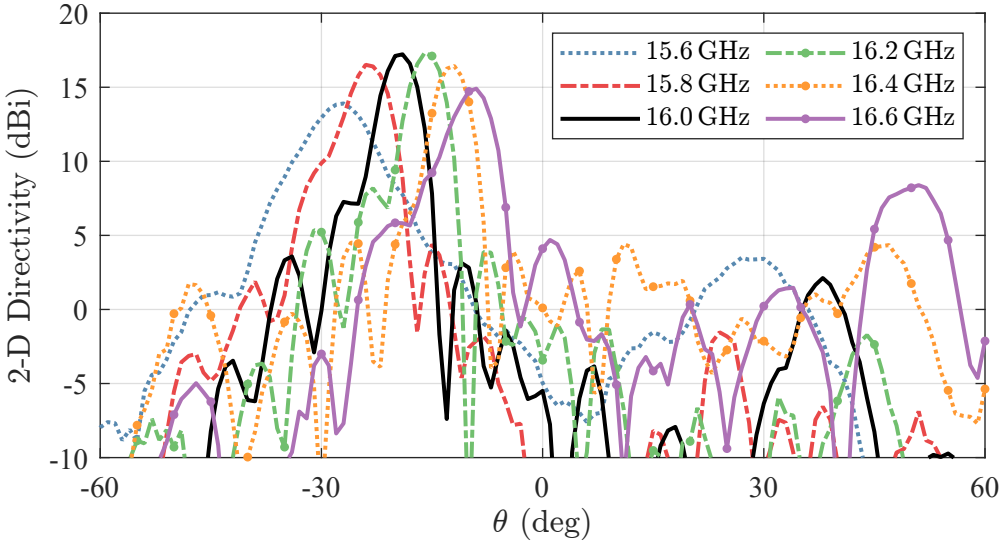

Figure 4.16: Measured 2-D directivity at different frequencies for the Uniform aperture distribution case of Design 2.

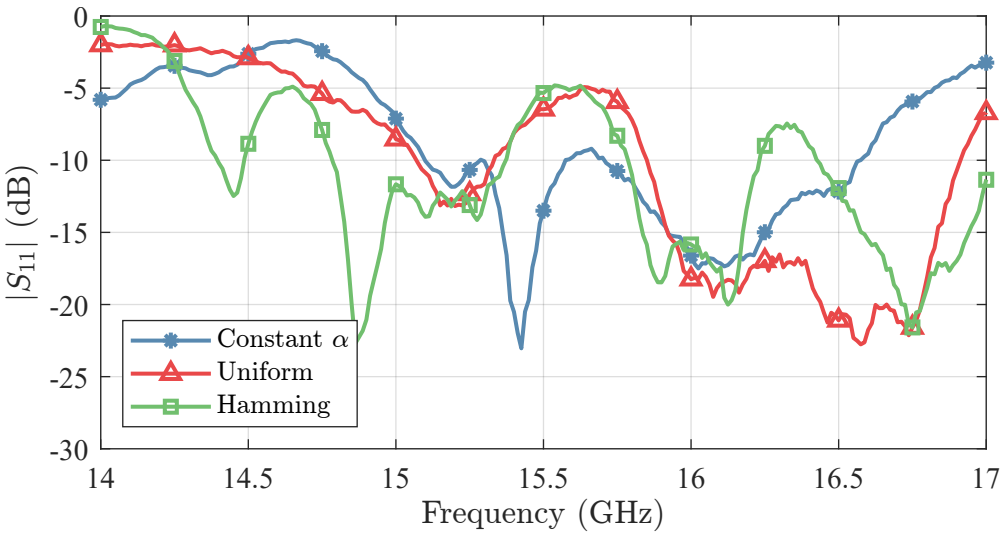

Figure 4.17: Measured reflection coefficient for every aperture case of Design 2.

the designed connector location. However, the matching around the shifted frequency of 16 GHz is very good for all cases. This is reasonable as the BHMS works as designed in this band, forcing a single TE mode inside the waveguide to propagate without major reflections, guaranteeing a maximum accepted power. The good matching level is achieved even with the encountered fabrication tolerances, showcasing the resilience of the designs.

4.8 Conclusions

A methodology for the design of LWAs with aperture control using bianisotropic Huygens' metasurfaces has been presented. A rigorous theoretical analysis has been followed, and the inclusion of a non-constant leakage factor along the antenna has been made possible through a slowly varying amplitude approximation approach. This comprises another degree of freedom, in addition to the independent control of the pointing angle or the waveguide height, among others, making the proposed antennas very versatile. The variable leakage factor makes the metasurface physically non-periodic. Therefore, its appropriate radiation can not be simply attributed to an excitation of a given spatial Floquet mode, but to the successful boundary condition implemented by the BHMS.

Several designs with different pointing angles and aperture field distributions have been presented to verify the theoretical derivation. Ideal simulations with impedance conditions have been used to test the used approach, which holds even for very high radiation efficiencies. Then, the microscopic design for the realistic implementation of the unit cells has been assessed. A novel field-based semi-analytical synthesis algorithm that takes into account the inter-layer coupling has been used. The remarkable similarity between the algorithm-obtained and simulated S-parameters for the synthesized geometries has allowed the avoidance of time-consuming full-wave optimization. Realistic simulations of the complete antennas have been carried out, obtaining a very good agreement with the theoretical predictions, and clearly showing how the field power profile along the antenna aperture behaves as desired.

Finally, several prototypes have been manufactured and measured. A frequency shift with respect to simulations has been observed, attributed to fabrication-related issues. Even so, the desired radiation characteristics are achieved, and the predicted relation between different aperture cases is well appreciated, demonstrating the successful control of the variable leakage factor. In addition, good matching is obtained, and the antennas are able to perform frequency scanning in the band around where peak performance is observed. The successful experimental validation of the presented methodology represents a step forward in the efficient design of metasurface-based leaky-wave antennas. By overcoming previous fundamental limitations through a rigorous theoretical formulation, radiation patterns can be engineered, making these antennas more versatile for their use in modern wireless systems.

Chapter 5

Extending FPCA Capabilities Using 2-D BHMSs

The FPCAs studied in Chapter 3 allow the design of pencil beam patterns, but they are limited to broadside radiation (or conical beams for frequencies higher than the design one). On the other hand, the BHMS-based LWAs in Chapter 4 enable increased control of the radiated beam characteristics, such as the output angle. However, that control is constrained to a single plane only, as the LWA configuration is one-dimensional. Hence, the logical next step is to combine both ideas in order to achieve a kind of FPCA based on BHMSs that should allow enhanced control over the pencil beam by enabling, at least, the selection of the output angle, similarly to other 2-D LWA works in the literature [5, 84].

Technically, FPCAs are so named because they exploit a sort of cavity resonance, given by the splitting condition (2.4), to achieve broadside radiation. In the present study, however, the beam-shaping function will be performed by the BHMS, which carries out the required field transformation without necessarily requiring the splitting condition fulfillment. Therefore, the concept presented in this chapter does not strictly constitute a FPCA in general; instead, it is more appropriately described as a two-dimensional BHMS-based LWA.

However, as explored in Chapter 4, the design of BHMSs requires knowing the electromagnetic field expressions at both of its sides. This implies formulating the electromagnetic problem much more rigorously than in Chapter 3 for a 2-D PPW configuration. Furthermore, with respect to the LWA scenario in Chapter 4, the introduction of an additional geometrical dimension poses a challenge in multiple aspects, such as the available guided modes and how they interact (and with which polarization) with the metasurface.

This chapter aims to explore this 2-D PPW-based LWA configuration to allow steerable pencil-beam radiation patterns through a comprehensive field stipulation and BHMS design. For this purpose, the chapter is structured as follows: The field stipulation is carried out in Section 5.1, where the made assumptions are highlighted. Then, Section 5.2 presents the design methodology, while the BHMS unit-cell ideal implementation is described in Section 5.3. Three different design examples are showcased in Section 5.4, where theoretical predictions and simulation results are compared. Finally, Section 5.5 presents some conclusions and considerations for future work.

5.1 Field Stipulation

The structure under consideration, following the aforementioned description, is depicted in Fig. 5.1. As shown, the BHMS should allow an arbitrary radiation direction $\{\phi_{\text{out}}, \theta_{\text{out}}\}$ while guaranteeing the propagation of the guided field between it and the PEC plane, located at a distance d. Furthermore, similarly to Chapter 3, the waveguide will be center-fed. This fact, added to the three-dimensionality of the structure, does not allow assuming any geometric invariance, as done in Chapter 4 to simplify the analysis. Hence, the stipulation of the fields below and above the BHMS requires a more elaborate assessment.

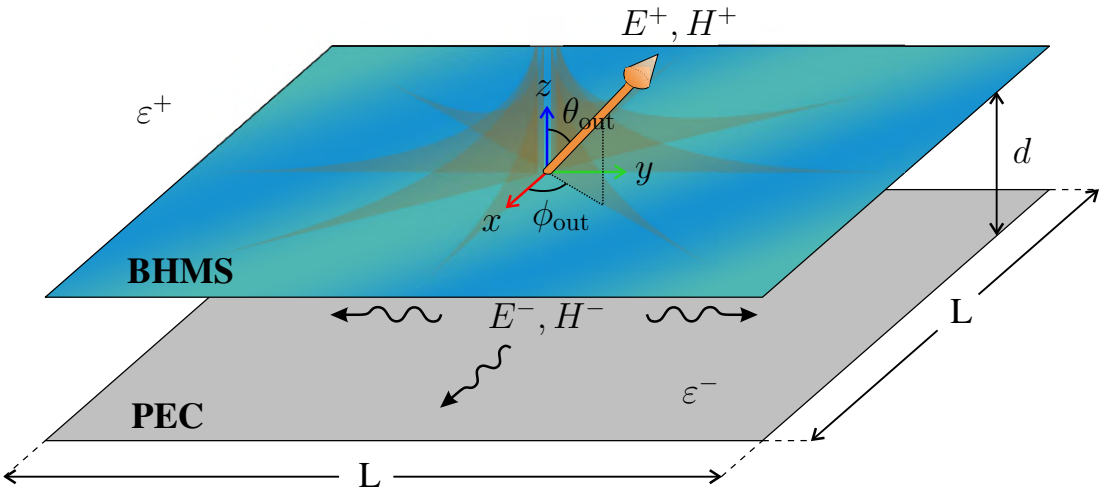

Figure 5.1: Diagram of the 2-D BHMS-based LWA configuration radiating towards an arbitrary direction.

5.1.1 Guided Field

Electromagnetic scenarios with boundary conditions coinciding with canonical coordinate surfaces are usually simpler to analyze in those coordinate systems. Thus, the electromagnetic analysis of a structure like the 2-D PPW in Fig. 5.1 is more sensibly

carried out by solving Maxwell's equations in cylindrical coordinates, as the field propagates radially. By assuming separation of variables, the solutions for the Helmholtz equation adopt elementary wave functions presenting harmonic equations for the azimuth angle ϕ and height z, and Bessel equations for the radial distance ρ. Particularizing for center-excited parallel-plate radial waveguides, the possible wave functions present the following general expression [69]:

$$\psi = h(k_z^- z)g(n\phi)H_n^{(2)}(k_\rho^- \rho) \tag{5.1}$$

where h and g are harmonic functions, and $H_n^{(2)}$ is the nth-order Hankel function of the second kind, which accounts for the outwards radial propagation considered here. The radial and transverse wavenumbers are k_ρ^- and k_z^-, respectively, while the azimuthal behavior is given by the order $n \in \mathbb{N}$ of the Hankel function. This set of solutions implies that the wavenumbers are constant and are related by

$$k_\rho^{-2} + k_z^{-2} = k^{-2} \tag{5.2}$$

with $k^- = 2\pi/\lambda$ related to the media below the metasurface. Consequently, and considering the increased complexity compared to the 1-D case, the leakage factor is assumed to be constant in this study.

For the case of the desired structure, in which a PEC ground plane is located at $z = -d$, and an arbitrary boundary condition at $z = 0$, the TM^z and TE^z wave functions are given, respectively, by

$$\psi_n^{\mathrm{TM}} = \cos(k_z^-(z+d)) \begin{Bmatrix} \cos(n\phi) \\ \sin(n\phi) \end{Bmatrix} H_n^{(2)}(k_\rho^- \rho)\,, \tag{5.3a}$$

$$\psi_n^{\mathrm{TE}} = \sin(k_z^-(z+d)) \begin{Bmatrix} \cos(n\phi) \\ \sin(n\phi) \end{Bmatrix} H_n^{(2)}(k_\rho^- \rho)\,. \tag{5.3b}$$

Note that, if the boundary condition at $z = 0$ is also a PEC, then $k_z^- = m\pi/d$ with $m \in \mathbb{N}$ (giving a second subscript to $\psi_{mn}^{\mathrm{TM/TE}}$), which would be identical for both mode configurations. This way, the set of modes supported by an ideal closed PPW can be calculated. It can be seen, for example, that for $m = n = 0$, the wave function of the fundamental TEM^ρ mode is obtained. However, given an arbitrary boundary condition, TE^z and TM^z wavenumbers for the same mode order will generally be different from each other. This will be the case for the BHMS, which will, in fact, guarantee the proper field propagation.

A choice on the desired guided modes must now be made. The TM_{00}^z (TEM^ρ)

mode of an ideal, closed PPW would not be suitable in this case as it offers no electric components tangential to the metasurface, as depicted in Fig. 5.2a. This would conflict with the BHMS design methodology and the ability to characterize its unit cells through plane-wave incidence as detailed in Subsection 2.2.1. Hence, the following simplest modes are the TM^z_{10} and TE^z_{10}, which do offer tangential components and are radially symmetric, as shown in Figs. 5.2b and 5.2c, respectively. The latter characteristic, though advantageous for design simplicity, hinders the ability to radiate at broadside [11]. Hence, the metasurface would need to present microscopic field polarization rotation capabilities (requiring chirality as in [85]) or macroscopic phase shifting (consequently obtaining circular polarization as in [86]).

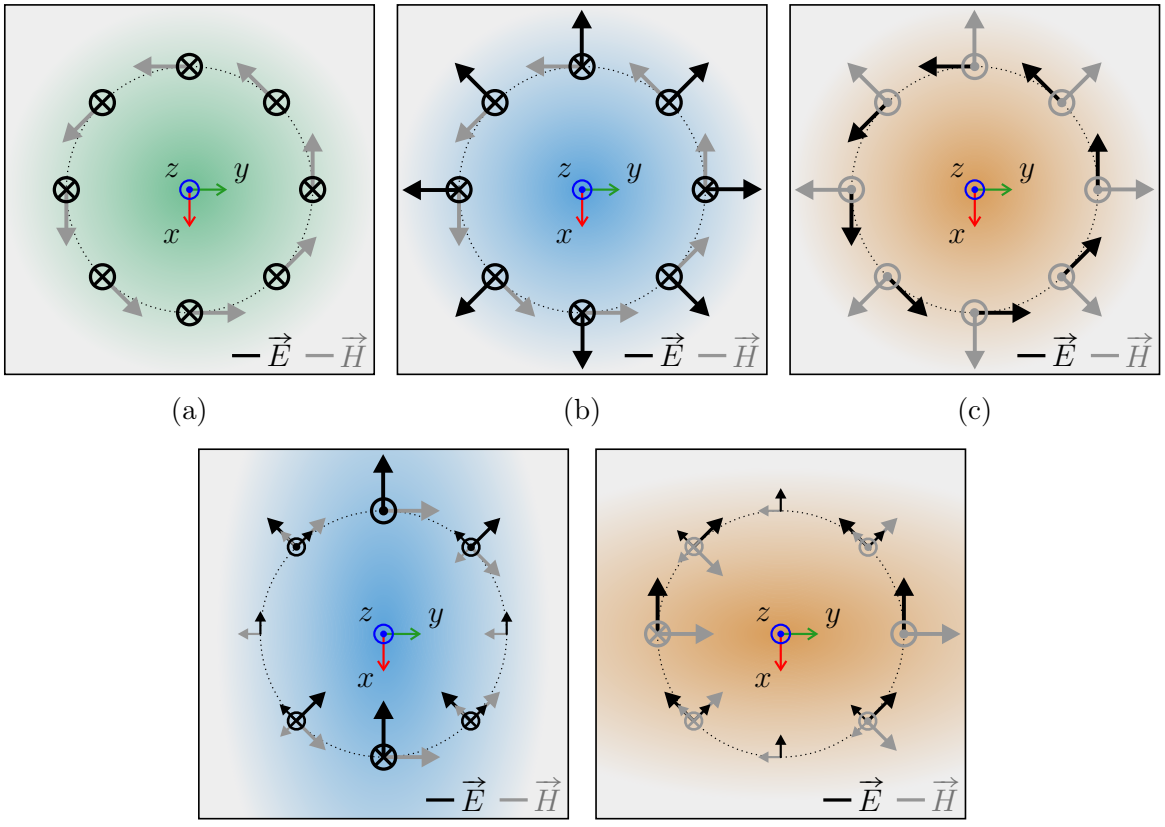

Figure 5.2: Top view diagrams of the cylindrical-system field components for several azimuthal directions: (a) TEM^ρ, (b) TM^z_{10}, (c) TE^z_{10}, (d) TM^z_{11}, and (e) TE^z_{11}.

In an attempt to avoid the challenges posed by the aforementioned modes, and also to leverage the insight gained from FPCAs in Chapter 3, their same modal characteristics are selected for the current configuration. This way, as will be shown, the electric field tangential components will be mainly contained in a single cartesian direction, offering radiation with practically linear polarization and avoiding destructive interference in any direction by default. In this case, a pair of TE^z/TM^z modes exist,

each one being predominant in a different orthogonal direction [37]. This phenomena is rigorously accounted for by choosing $n = 1$ and a different azimuthal harmonic function for each mode configuration in (5.3). Hence, selecting $\cos\phi$ in (5.3a), the TM^z_{11} mode would present the behavior depicted in Fig. 5.2d. Analogously, choosing $\sin\phi$ in (5.3b) results in a TE^z_{11} mode with the field behavior diagrammatically shown in Fig. 5.2e. This way, the electromagnetic configuration of a FPCA can be described as the coherent sum of both mode fields. Mathematically, these modes are given by the following magnetic $\vec{A}$ and electric $\vec{F}$ vector potentials

$$\vec{A} = \hat{z}\, C^{\mathrm{TM}} \psi_1^{\mathrm{TM}} = \hat{z}\, C^{\mathrm{TM}} \cos\left(k_z^{\mathrm{TM}}(z+d)\right) \cos\phi\, H_1^{(2)}\left(k_\rho^{\mathrm{TM}}\rho\right) , \tag{5.4a}$$

$$\vec{F} = \hat{z}\, C^{\mathrm{TE}}\, \psi_1^{\mathrm{TE}} = \hat{z}\, C^{\mathrm{TE}}\, \sin\left(k_z^{\mathrm{TE}}(z+d)\right) \sin\phi\, H_1^{(2)}\left(k_\rho^{\mathrm{TE}}\rho\right) , \tag{5.4b}$$

where C^{TM} and C^{TE} are the complex amplitudes of each vector. Note that, in general, each mode will offer a different wavenumber, indicated with the corresponding superscript. Moreover, they are assumed constant in the present analysis:

$$k_z^{\mathrm{TM}} = \beta_z^{\mathrm{TM}} - j\alpha_z^{\mathrm{TM}}; \qquad k_\rho^{\mathrm{TM}} = \beta_\rho^{\mathrm{TM}} - j\alpha_\rho^{\mathrm{TM}}, \tag{5.5a}$$

$$k_z^{\mathrm{TE}} = \beta_z^{\mathrm{TE}} - j\alpha_z^{\mathrm{TE}}; \qquad k_\rho^{\mathrm{TE}} = \beta_\rho^{\mathrm{TE}} - j\alpha_\rho^{\mathrm{TE}}. \tag{5.5b}$$

From these vector potentials, all the electromagnetic field components can be derived [87]. In particular, the TM^z_{11} would present

$$E_\rho^- = j\, C^{\mathrm{TM}} \frac{k_\rho^{\mathrm{TM}}}{\mu^- Y^{\mathrm{TM}}} \sin\left(k_z^{\mathrm{TM}}(z+d)\right) \cos\phi \left[H_0^{(2)}\left(k_\rho^{\mathrm{TM}}\rho\right) - \frac{H_1^{(2)}\left(k_\rho^{\mathrm{TM}}\rho\right)}{k_\rho^{\mathrm{TM}}\rho}\right] , \tag{5.6a}$$

$$E_\phi^- = -j\, C^{\mathrm{TM}} \frac{k_\rho^{\mathrm{TM}}}{\mu^- Y^{\mathrm{TM}}} \sin\left(k_z^{\mathrm{TM}}(z+d)\right) \sin\phi\, \frac{H_1^{(2)}\left(k_\rho^{\mathrm{TM}}\rho\right)}{k_\rho^{\mathrm{TM}}\rho} , \tag{5.6b}$$

$$E_z^- = -j\, C^{\mathrm{TM}} \frac{(k_\rho^{\mathrm{TM}})^2}{\mu^- Y^{\mathrm{TM}} k_z^{\mathrm{TM}}} \cos\left(k_z^{\mathrm{TM}}(z+d)\right) \cos\phi\, H_1^{(2)}\left(k_\rho^{\mathrm{TM}}\rho\right) , \tag{5.6c}$$

$$H_\rho^- = -C^{\mathrm{TM}} \frac{k_\rho^{\mathrm{TM}}}{\mu^-} \cos\left(k_z^{\mathrm{TM}}(z+d)\right) \sin\phi\, \frac{H_1^{(2)}\left(k_\rho^{\mathrm{TM}}\rho\right)}{k_\rho^{\mathrm{TM}}\rho} , \tag{5.6d}$$

$$H_\phi^- = -C^{\mathrm{TM}} \frac{k_\rho^{\mathrm{TM}}}{\mu^-} \cos\left(k_z^{\mathrm{TM}}(z+d)\right) \cos\phi \left[H_0^{(2)}\left(k_\rho^{\mathrm{TM}}\rho\right) - \frac{H_1^{(2)}\left(k_\rho^{\mathrm{TM}}\rho\right)}{k_\rho^{\mathrm{TM}}\rho}\right] , \tag{5.6e}$$

$$H_z^- = 0 , \tag{5.6f}$$

with

$$Y^{\mathrm{TM}} = \frac{\omega\varepsilon^-}{k_z^{\mathrm{TM}}} = \frac{k^-}{\eta^- k_z^{\mathrm{TM}}} , \tag{5.7}$$

while the TE^z_{11} would present

$$E^-_\rho = -C^{\mathrm{TE}} \frac{k^{\mathrm{TE}}_\rho}{\varepsilon^-} \sin\left(k^{\mathrm{TE}}_z (z+d)\right) \cos\phi \, \frac{H^{(2)}_1\left(k^{\mathrm{TE}}_\rho \rho\right)}{k^{\mathrm{TE}}_\rho \rho}\,, \tag{5.8a}$$

$$E^-_\phi = C^{\mathrm{TE}} \frac{k^{\mathrm{TE}}_\rho}{\varepsilon^-} \sin\left(k^{\mathrm{TE}}_z (z+d)\right) \sin\phi \left[H^{(2)}_0\left(k^{\mathrm{TE}}_\rho \rho\right) - \frac{H^{(2)}_1\left(k^{\mathrm{TE}}_\rho \rho\right)}{k^{\mathrm{TE}}_\rho \rho}\right], \tag{5.8b}$$

$$E^-_z = 0\,, \tag{5.8c}$$

$$H^-_\rho = -j\, C^{\mathrm{TE}} \frac{k^{\mathrm{TE}}_\rho Y^{\mathrm{TE}}}{\varepsilon^-} \cos\left(k^{\mathrm{TE}}_z (z+d)\right) \sin\phi \left[H^{(2)}_0\left(k^{\mathrm{TE}}_\rho \rho\right) - \frac{H^{(2)}_1\left(k^{\mathrm{TE}}_\rho \rho\right)}{k^{\mathrm{TE}}_\rho \rho}\right], \tag{5.8d}$$

$$H^-_\phi = -j\, C^{\mathrm{TE}} \frac{k^{\mathrm{TE}}_\rho Y^{\mathrm{TE}}}{\varepsilon^-} \cos\left(k^{\mathrm{TE}}_z (z+d)\right) \cos\phi \, \frac{H^{(2)}_1\left(k^{\mathrm{TE}}_\rho \rho\right)}{k^{\mathrm{TE}}_\rho \rho}\,, \tag{5.8e}$$

$$H^-_z = -j\, C^{\mathrm{TE}} \frac{(k^{\mathrm{TE}}_\rho)^2 Y^{\mathrm{TE}}}{\varepsilon^- k^{\mathrm{TE}}_z} \sin\left(k^{\mathrm{TE}}_z (z+d)\right) \sin\phi \, H^{(2)}_1\left(k^{\mathrm{TE}}_\rho \rho\right)\,, \tag{5.8f}$$

with

$$Y^{\mathrm{TE}} = \frac{k^{\mathrm{TE}}_z}{\omega \mu^-} = \frac{k^{\mathrm{TE}}_z}{\eta^- k^-}\,. \tag{5.9}$$

Improved physical intuition into these expressions arises from the large-argument approximation of Hankel functions:

$$H^{(2)}_v(x) \xrightarrow{x\to\infty} \sqrt{\frac{2j}{\pi x}}\, j^v e^{-jx}\,. \tag{5.10}$$

Accordingly, in the principal orthogonal directions, the TM^z_{11} mode exhibits field components attenuating as follows: at $\phi = 0°$ ($\hat\rho = \hat x$, $\hat\theta = \hat y$), $\{E^-_\rho, E^-_z, H^-_\phi\}$ decay as $e^{-\alpha^{\mathrm{TM}}\rho}\rho^{-1/2}$, whereas at $\phi = 90°$ ($\hat\rho = \hat y$, $\hat\theta = -\hat x$) only $\{E^-_\phi, H^-_\rho\}$ are present, decaying as $e^{-\alpha^{\mathrm{TM}}\rho}\rho^{-3/2}$, as depicted in Fig. 5.2d. Analogously, the TE^z_{11} mode exhibits $\{E^-_\rho, H^-_\phi\}$ at $\phi = 0°$ decaying as $e^{-\alpha^{\mathrm{TE}}\rho}\rho^{-3/2}$, while the predominant components $\{E^-_\phi, H^-_\rho, H^-_z\}$ are found at $\phi = 90°$ with a decay proportional to $e^{-\alpha^{\mathrm{TE}}\rho}\rho^{-1/2}$, as seen in Fig. 5.2d. Hence, each mode is predominant in a different orthogonal direction, as qualitatively represented in Fig. 5.3, in which they present the usual components related to the given mode nature, as expected from Chapter 3.

According to [37], and similarly to what was explained in Section 3.4, these two modes can be excited by a x-directed horizontal electric dipole (HED), or a y-directed horizontal magnetic dipole (HMD), inside the PPW, respectively giving rise to a TM^x or TE^y mode assuming a classic, closed waveguide. As explored in Chapter 3, this type of sources offer another advantage, as they are incompatible with the always-propagative, undesired TEM^ρ mode. The described modal behavior can be derived from the previous expressions as follows: If a HED source at the radial origin is chosen,

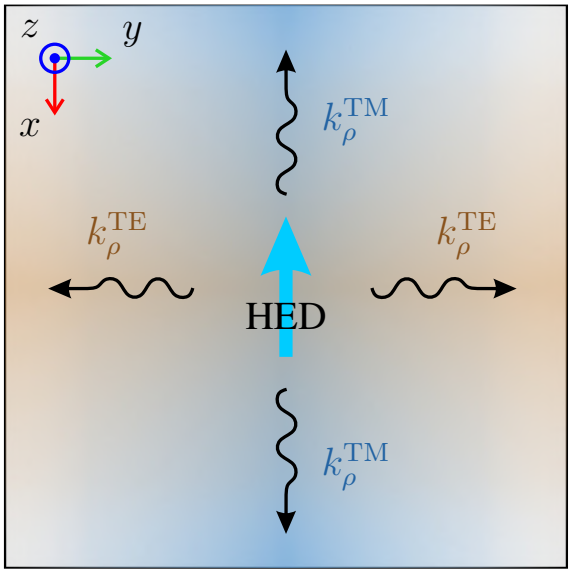

Figure 5.3: Dominant mode propagation directions inside a PPW center-fed by a HED.

then it generates a magnetic field around it, which will excite the magnetic components of both modes. Hence, assuming the magnetic field components of both modes will be equal in magnitude and phase at that point, the required relation between both modes' complex amplitudes is

$$\left.\frac{C^{\mathrm{TE}}}{C^{\mathrm{TM}}}\right|_{\mathrm{HED}} = -j\,Y^{\mathrm{TM}}\frac{k_\rho^{\mathrm{TM}}\cos\left(k_z^{\mathrm{TM}}(z+d)\right)}{k_\rho^{\mathrm{TE}}\cos\left(k_z^{\mathrm{TE}}(z+d)\right)} \xrightarrow{k_\rho^{\mathrm{TM}}=k_\rho^{\mathrm{TE}}=k_\rho^-} -j\,Y^{\mathrm{TM}}\,. \tag{5.11}$$

As noted, the relation is simplified when both modes' wavenumbers are equal, which occurs for ideal PPWs. In that case, by assuming $k_z^{\mathrm{TM}} = k_z^{\mathrm{TE}} = k_z^-$ (and, consequently, $k_\rho^{\mathrm{TM}} = k_\rho^{\mathrm{TE}} = k_\rho^-$), taking $C^{\mathrm{TM}} = -\mu/k_\rho^-$ for normalization purposes in (5.6), and using relation (5.11) in (5.8), the sum of both fields corresponds to the aforementioned TM^x mode, whose cartesian field components are given by

$$E_x^- = -j\sin(k_z^-(z+d))\left[\left(\frac{\sin^2\phi}{Y^{\mathrm{TE}}}+\frac{\cos^2\phi}{Y^{\mathrm{TM}}}\right)H_0^{(2)}(k_\rho^-\rho) + \left(\frac{1}{Y^{\mathrm{TE}}}-\frac{1}{Y^{\mathrm{TM}}}\right)\cos(2\phi)\frac{H_1^{(2)}(k_\rho^-\rho)}{k_\rho^-\rho}\right], \tag{5.12a}$$

$$E_y^- = j\,\eta^-\sin\left(k_z^-(z+d)\right)\sin(2\phi)\frac{k_\rho^{-2}}{k\,k_z^-}\left[\frac{H_0^{(2)}(k_\rho^-\rho)}{2}-\frac{H_1^{(2)}(k_\rho^-\rho)}{k_\rho^-\rho}\right], \tag{5.12b}$$

$$E_z^- = j\,\frac{k_\rho^-}{Y^{\mathrm{TM}}k_z^-}\cos\left(k_z^-(z+d)\right)\cos\phi\,H_1^{(2)}\left(k_\rho^-\rho\right), \tag{5.12c}$$

$$H_x^- = 0\,, \tag{5.12d}$$

$$H_y^- = \cos(k_z^-(z+d))\, H_0^{(2)}\left(k_\rho^- \rho\right) , \tag{5.12e}$$

$$H_z^- = \frac{k_\rho^-}{k_z^-} \sin\left(k_z^-(z+d)\right) \sin\phi\, H_1^{(2)}\left(k_\rho^- \rho\right) , \tag{5.12f}$$

and shown in an example ideal waveguide for several azimuthal planes in Fig. 5.4.

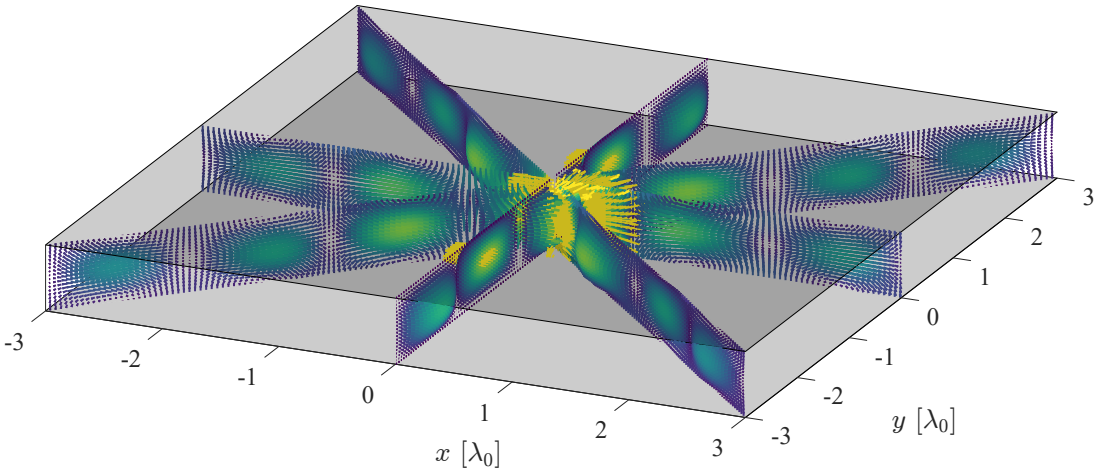

Figure 5.4: TM^x mode $\vec{E}$ field in an ideal, center-excited PPW with $d = 0.55\lambda_0$.

Furthermore, when $k_z^- \to k^-$, as happens in FPCAs, the resulting TM^x mode converges to a quasi-TEM one, with $Y^{\mathrm{TE}} \simeq Y^{\mathrm{TM}} \simeq 1/\eta^-$ and $k_\rho^- \to 0$. Thus, E_z^- and H_z^- will tend to zero, and the following electric field components can be simplified as

$$E_x^- \approx -j\,\eta^- \sin(k_z^-(z+d)) \left[H_0^{(2)}(k_\rho^- \rho) + \frac{k_\rho^-}{k^- k_z^-} \frac{H_1^{(2)}(k_\rho^- \rho)}{\rho} \cos(2\phi) \right] , \tag{5.13a}$$

$$E_y^- \approx -j\,\eta^- \sin\left(k_z^-(z+d)\right) \sin(2\phi) \frac{k_\rho^-}{k^- k_z^-} \frac{H_1^{(2)}(k_\rho^- \rho)}{\rho} . \tag{5.13b}$$

In the proximity of $\rho = 0$, these expressions cannot be further simplified. However, for $\rho \gg k_\rho^-$, the factor multiplying the first order Hankel functions would tend to zero, and the previous field component expressions would tend to

$$E_x^- \to -j\,\eta^- \sin(k_z^-(z+d)) H_0^{(2)}(k_\rho^- \rho) , \tag{5.14a}$$

$$E_y^- \to 0 , \tag{5.14b}$$

evidencing the quasi-TEM nature of the assumptions made in (5.13), as only E_x^- and H_y^- are relevant components. A completely analogous process can be carried out if a HMD source is selected, by taking $C^{\mathrm{TE}}/C^{\mathrm{TM}} = -j\,Y^{\mathrm{TE}}$ and $C^{TE} = j\varepsilon/k_\rho^-$. This way, the same quasi-TEM mode is obtained, but with (5.14a)–(5.14b) being the exact electric components, and (5.12d)–(5.12e) the approximate magnetic ones.

The previous mode analysis with assumptions helps understanding the field be-

havior in a FPCA from a rigorous approach. However, for the general BHMS-based configuration under study, the previous assumptions must not necessarily be true. Nevertheless, some insights remain useful to design the BHMS. In particular, it has been found that the main tangential field components are E_x^- and H_y^- given that the radial wavenumber is not considerably large. This fact will be leveraged in the stipulation of the radiated field, while the general TM_1^z (5.6) and TE_1^z (5.8) mode expressions will be used for the guided field, assuming a HED source excites it.

Finally, an expression for the power density $P_z^- = (1/2)\Re\{E_\rho^- H_\phi^{-*} - E_\phi^- H_\rho^{-*}\}$ flowing through the BHMS is not straightforward due to the Hankel functions. Hence, the local power conservation condition will be forced numerically by imposing the same power profile P_z^- across the metasurface aperture to the field above it.

5.1.2 Radiated Field

A plane wave traveling towards an arbitrary direction $\{\phi_{\text{out}}, \theta_{\text{out}}\}$, as shown in Fig. 5.1, is stipulated above the BHMS. The electric field tangential to it is stipulated as

$$E_x^+ = |E_{\text{out}}|\, e^{-jk_x^+ x} e^{-jk_y^+ y} e^{-jk_z^+ z} e^{j\xi}\,, \tag{5.15a}$$

$$E_y^+ = 0\,, \tag{5.15b}$$

where ξ is an additional degree of freedom. The wavenumbers are related to the beam direction and to each other as

$$k_x^+ = k^+ \sin\theta_{\text{out}} \cos\phi_{\text{out}}\,, \tag{5.16a}$$

$$k_y^+ = k^+ \sin\theta_{\text{out}} \sin\phi_{\text{out}}\,, \tag{5.16b}$$

$$k_z^+ = k^+ \cos\theta_{\text{out}}\,, \tag{5.16c}$$

$$k^{+2} = k_x^{+2} + k_y^{+2} + k_z^{+2}\,. \tag{5.16d}$$

This electric field stipulation is chosen because, as previously discussed, the main electric component below the metasurface is the x-directed one. Hence, E_y^- can be reasonably neglected, thus avoiding any need for chiral capabilities. This way, moreover, the radiated field will be linearly polarized in the x direction.

In order to obtain the tangential magnetic field components, E_z^+ must also be obtained first. As, for a plane wave, both the electric and magnetic field vectors must be perpendicular to the propagation direction, i.e.

$$\vec{E}^+ \cdot \vec{k}^+ = E_x^+ k_x^+ + E_y^+ k_y^+ + E_z^+ k_z^+ = 0\,, \tag{5.17}$$

then, by using (5.15), the electric field z component is

$$E_z^+ = -\frac{k_x^+}{k_z^+} E_x^+ = -\frac{k_x^+}{k_z^+} |E_{\text{out}}|\, e^{-jk_x^+ x} e^{-jk_y^+ y} e^{-jk_z^+ z} e^{j\xi}\,, \tag{5.18}$$

and the magnetic field components can then be obtained as

$$H_x^+ = \frac{j}{k^+\eta^+}\left(\frac{\partial E_z^+}{\partial y} - \frac{\partial E_y^+}{\partial z}\right) = -\frac{k_x^+ k_y^+}{k^+\eta^+ k_z^+} E_x^+\,, \tag{5.19a}$$

$$H_y^+ = \frac{j}{k^+\eta^+}\left(\frac{\partial E_x^+}{\partial z} - \frac{\partial E_z^+}{\partial x}\right) = \frac{1}{k^+\eta^+}\left(k_z^+ + \frac{k_x^{+2}}{k_z^+}\right) E_x^+\,, \tag{5.19b}$$

$$H_z^+ = \frac{j}{k^+\eta^+}\left(\frac{\partial E_y^+}{\partial x} - \frac{\partial E_x^+}{\partial y}\right) = -\frac{k_y^+}{k^+\eta^+} E_x^+\,. \tag{5.19c}$$

The average power density flowing through the metasurface is

$$\begin{aligned} P_z^+ &= \frac{1}{2}\Re\left[E_x^+ H_y^{+*}\right]\Big|_{z=0} = \frac{1}{2}\Re\left[\frac{|E_{\text{out}}|^2}{k^+\eta^+}\left(k_z^+ + \frac{k_x^{+2}}{k_z^+}\right)^* e^{-2\alpha_x x} e^{-2\alpha_y y}\right] \\ &= \frac{1}{2}\frac{|E_{\text{out}}|^2}{k^+\eta^+}\left(\beta_z^+ + \frac{\left(\beta_x^{+2} - \alpha_x^{+2}\right)\beta_z^+ + 2\beta_x^+\alpha_x^+\alpha_z^+}{\beta_z^{+2} + \alpha_z^{+2}}\right) e^{-2\alpha_x x} e^{-2\alpha_y y}\,. \end{aligned} \tag{5.20}$$

The value of $|E_{\text{out}}|$ must be chosen to satisfy the local power conservation condition (2.31). However, the stipulated field expressions on both sides of the BHMS do not present similar analytic formulas, exhibiting Hankel or complex exponential functions, respectively for each. Therefore, it is not straightforward to relate the attenuation factors in both regions analytically, as done in Section 4.1 for 1-D LWAs. Consequently, for simplicity, the attenuation factors in region 2 $\{\alpha_x^+, \alpha_y^+, \alpha_z^+\}$ are assumed to be zero (hence the stipulated radiated fields are only valid at the aperture), and all the spatial power variation is assumed by $|E_{\text{out}}|$, which, rearranging (5.20), is given by

$$|E_{\text{out}}| = \sqrt{\frac{2k^+\eta^+ P_z^+}{\beta_z^+ + \dfrac{\beta_x^{+2}}{\beta_z^+}}} = \sqrt{\frac{2k^+\eta^+ P_z^-}{\beta_z^+ + \dfrac{\beta_x^{+2}}{\beta_z^+}}}\,. \tag{5.21}$$

5.2 Design Methodology

Once the fields are stipulated, the design methodology is similar to the one presented in Section 4.3, but with additional considerations due to the two-dimensional aperture. The selection of the radiated field wavenumbers is straightforward from the desired beam direction $\{\phi_{\text{out}}, \theta_{\text{out}}\}$ through (5.16). However, the guided mode wavenumbers

requires a more careful assessment. For a desired angle of incidence θ_{in} inside the waveguide, it cannot be directly related to both modes (TM_{11}^z and TE_{11}^z) wavenumbers through (2.1), as their different nature impedes their characteristics to be identical, in general, for an arbitrary boundary condition. The reason for this is that each mode will individually satisfy the transverse resonance condition with a slightly different wavenumber, depending on the leaky surface characteristics and the waveguide height.

In order to guarantee that both mode wavenumbers are physically consistent and their sum always offer $P_z^- \geq 0$, the TRM is used (see Subsection 2.1.2) with the corresponding equivalent transverse TL characteristic admittance for each mode. The BHMS input admittance Y_L required in (2.19) is assumed the same for both modes, and a way to retrieve its value is depicted in the diagram of Fig. 5.5 and described as follows: For a given frequency, waveguide height d and initial radial wavenumber k_ρ^- with the desired attenuation factor α_ρ^- and phase constant

$$\beta_\rho^- \simeq k^- \sin\theta_{\text{in}} \tag{5.22}$$

[from which k_z^- is retrieved through (5.2)], the TRM is first solved for Y_L assuming a TEM mode ($k_z^- = k^-$). Once the Y_L value is obtained, the TRM can be separately solved for k_z^{TM} and k_z^{TE}, which will both deviate from the initial k_z^-, more as the BHMS boundary condition is less similar to a PEC. In this sense, note that, although the waveguide height is a degree of freedom, the guided field wavenumbers are dependent on it. Hence, in order to obtain an aperture power profile that is sufficiently radially symmetric, then $d \to \pi/\beta_z^-$, which will also offer field expressions more similar to (5.12), thus guaranteeing E_x^- and H_y^- are the dominant tangential components given that θ_{in} is not considerably large.

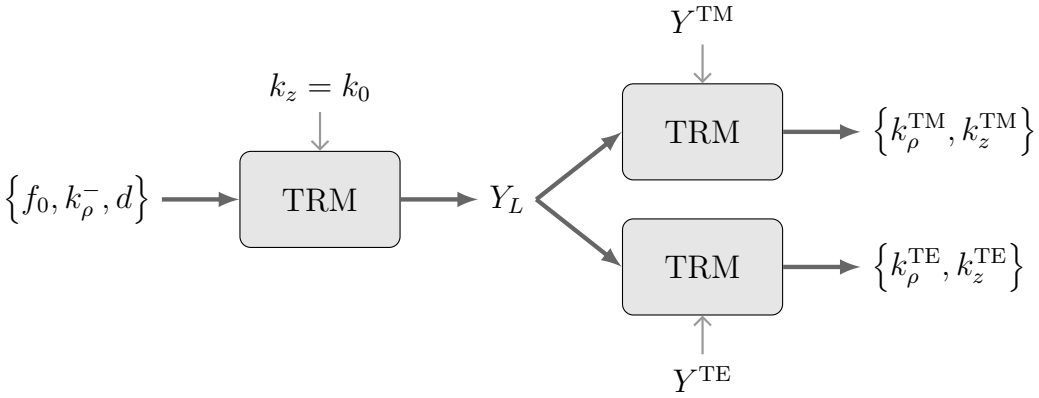

Figure 5.5: Diagram of TM_{11}^z and TE_{11}^z mode wavenumber calculation.

The previous considerations are relevant as the BHMS parameters acquisition is carried out assuming that the E_y and H_x components are not relevant, thus enabling

the use of the simplified equations in (2.32). This is advantageous for reduced design complexity, which would also facilitate the potential future addition of reconfiguration capabilities. The microscopic design is hence performed as done in Section 4.3: the BHMS boundary condition is discretized along the x and y coordinates. For simplicity, the sampling rate will be equal for both directions, and chosen $\Delta_x = \Delta_y = \lambda_0/5$, resulting in the sub-wavelength meta-atoms size. The square shape of the meta-atoms is the reason the antenna is chosen squared, with a total side length L in both directions. As previously mentioned, the tangential field components $[E_x^-, H_y^-, E_x^+, H_y^+]$ evaluated at $z \to \pm 0$, given by numerically adding expressions (5.6) and (5.8), are used in (2.32) to obtain the local $\{Z_{\text{se}}^{xx}, Y_{\text{sm}}^{yy}, K_{\text{em}}^{xx}\}$ values. These are transformed to the 2×2 $[\mathbf{Z}]$ matrices characterizing each meta-atom through (2.34), and then converted to S-parameters through (2.22).

5.3 Ideal Implementation

The meta-atoms can be ideally implemented with unit cells consisting of three cascaded reactance sheets, as depicted in Fig. 2.9. In this case, as the guided wave propagates radially, two orthogonal polarizations should in general be considered at each unit-cell port to correctly account for the complete electromagnetic interaction. However, as it has been assumed that only $\{E_x, H_y\}$ are relevant, only a single field polarization needs to be accounted for, facilitating the unit-cell design. In other words, the unit cells do not require to implement cross-polarization capabilities, which translates into the BHMS being non-chiral, as it was desired.

Although a realistic BHMS design needs physically-realizable unit cells, the aim of this study is to verify the macroscopic design functionality, as experimental verification of this type of metasurfaces was already offered in Chapter 4. Hence, ideal unit cells will be used, for which equations in (2.35) are employed to calculate their three reactance values. The chosen unit-cell substrate characteristics for the following design examples are a thickness $t = 50.8\,\mu\text{m}\,(2\,\text{mils})$ and relative permittivity $\varepsilon_{r,\text{sub}} = 3$. The equivalent TL phase constant is

$$\beta_{\text{sub}} = \frac{2\pi}{\lambda_0}\sqrt{\varepsilon_{r,\text{sub}}}\cos\theta_{\text{sub}} \tag{5.23}$$

with the $\cos\theta_{\text{sub}}$ term accounting for the oblique incidence propagation, whereas θ_{sub} is the incidence angle inside the substrate, which is obtained from Snell's law as

$$\theta_{\text{sub}} = \arcsin\left(\sqrt{\frac{\varepsilon^-}{\varepsilon_{r,\text{sub}}}}\sin\theta_{\text{in}}\right). \tag{5.24}$$

As each mode exhibits a different equivalent TL characteristic impedance,

$$Z_{\text{sub}}^{\text{TM}} = \frac{\eta_0 \cos\theta_{\text{sub}}}{\sqrt{\varepsilon_{r,\text{sub}}}}\,, \tag{5.25a}$$

$$Z_{\text{sub}}^{\text{TE}} = \frac{\eta_0}{\sqrt{\varepsilon_{r,\text{sub}}}\cos\theta_{\text{sub}}}\,, \tag{5.25b}$$

the unit-cell characteristics cannot be optimized for both modes at the same time. Hence, an intermediate $Z_{\text{sub}} = \eta_0/\sqrt{\varepsilon_{r,\text{sub}}}$ will be used without taking into account the $\cos\theta_{\text{sub}}$ factor. Consequently, it is convenient that θ_{sub} takes considerably low values.

5.4 Design Examples and Simulations

In this section, several designs are carried out in order to verify the theoretical derivation and test some of the capabilities of the studied antenna configuration. The operating frequency is chosen to be $f_0 = 14\,\text{GHz}$ and $\varepsilon^- = \varepsilon^+ = \varepsilon_0$ is assumed. In addition to the numerical results, simulated ones will also be presented, for which HFSS is employed, using analytical impedance boundary conditions for the idealized unit-cell reactances implementation, and an infinitesimal HED at the middle of the cavity. Consequently, for the moment, no numerical results related to the impedance matching of these designs can be presented as the used ideal HED does not provide that information. In that sense, although the achievable bandwidth will mainly depend on the BHMS frequency behavior, a study on this aspect shall be performed once the realistic unit cells and feeder have been implemented in future work.

Note that, as these antennas are two-dimensional, their size grows quadratically with the side length L, hence becoming electrically large very quickly. This poses a challenge to the used general-purpose simulator, exhibiting difficulties to achieve convergence, thus potentially impacting result accuracy. Therefore, the values of L will be chosen significantly small. In this sense, if the fields at the edges of the laterally-open PPW were not sufficiently attenuated, their refraction would compromise the analytical field stipulation. Hence, the α_ρ^- value must be chosen to offer a high radiation efficiency.

5.4.1 Classical FPCA Test Case

As a first design attempt, one of the simplest cases would be to design a classical FPCA, i.e. to obtain broadside radiation by satisfying the splitting condition (2.4). Therefore, the boundary condition implemented by the BHMS should be considerably homogeneous. Moreover, it enables the direct comparison with the homogeneous FPCA design from Section 3.5.2, from which the required design characteristics are taken, and

summarized in Table 5.1.

Table 5.1: LWA design parameters for the classical FPCA case design.

θ_{in}	$\alpha_\rho\,[k_0]$	θ_{out}	ϕ_{out}	ξ	$d\,[\lambda_0]$	$L\,[\lambda_0]$
7.64°	0.133	0°	0°	0°	0.486	3.5

After applying the process described in Fig. 5.5, the obtained mode-specific characteristics are $\beta_\rho^{\text{TM}} = 0.134k_0$, $\alpha_\rho^{\text{TM}} = 0.136k_0$ and $\beta_\rho^{\text{TE}} = 0.132k_0$, $\alpha_\rho^{\text{TE}} = 0.130k_0$, which are considerably similar, as expected. For these characteristics, the computed radiation efficiency is $\eta_{\text{rad}} \approx 98\%$. It is calculated by first defining two PPW-centered, vertically-matched rectangular regions with respective sides $\lambda_0/40$ and L, and then taking the ratio of the numerically integrated outward power through their surfaces, using the analytical field expressions from Subsection 5.1.1.

The surface parameters $\{Z_{\text{se}}^{xx}, Y_{\text{sm}}^{yy}, K_{\text{em}}^{xx}\}$ achieved from the BHMS design methodology, explained in Section 5.2, are considerably radially symmetric, as seen in Fig. 5.6. Moreover, their values do not exhibit a significant change across the aperture, consistent with the splitting condition ensuring broadside radiation for a homogeneous leaky surface. The mentioned spatial properties are better appreciated by transforming these parameters to their microwave network equivalents. Note that, in the following figures, for visualization purposes, the parameter values are truncated to the colorbar limits.

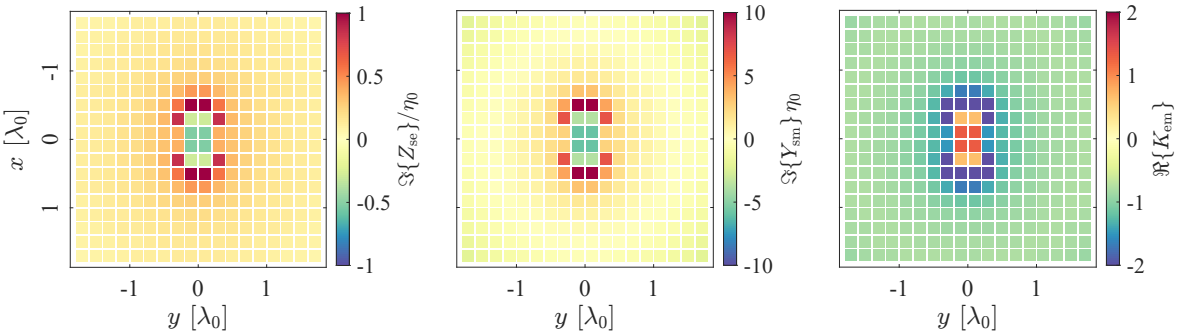

Figure 5.6: Computed normalized BHMS parameters, namely (a) Z_{se}^{xx}, (b) Y_{sm}^{yy} and (c) K_{em}^{xx}, for the classical FPCA case design.

The local η_0-referenced S-parameters, shown in Fig. 5.7, offer a better understanding of the unit-cells physical behavior. In particular, the $\angle S_{11}$ values are practically the same for all the unit cells, as noted in Fig. 5.7a, analogously to the case of 1-D BHMS-based LWAs. This behavior is reasonable as a stable surface impedance, or reflection phase shift, is required for the guided modes to properly propagate. Moreover, the resulting $\angle S_{11} = 170°$ is necessarily consistent with the specified value for

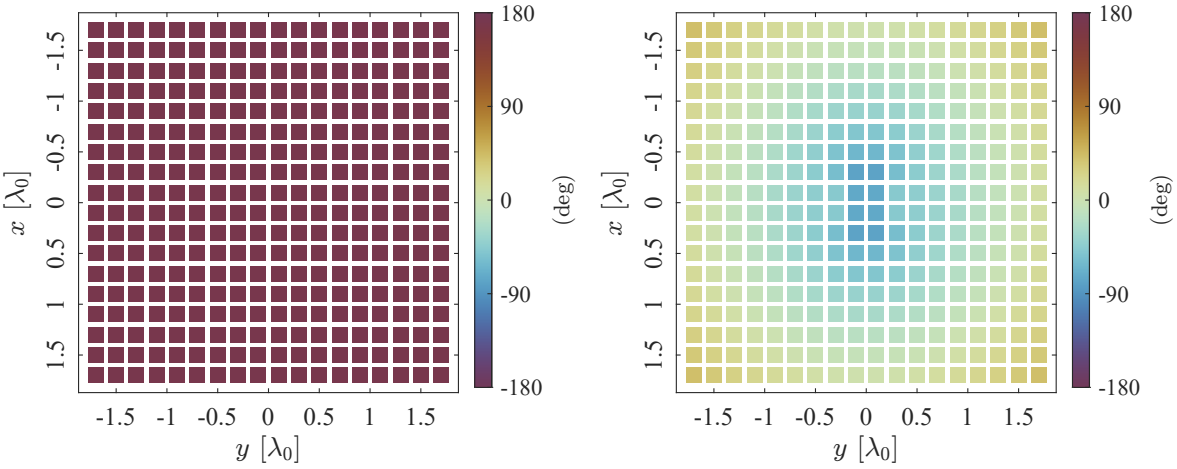

Figure 5.7: Computed η_0-referenced local S-parameters (a) reflection and (b) transmission phase, for the classical FPCA case design.

the FPCA designs in Chapter 3. Similarly, a $|S_{11}| \simeq 0.9$ value is obtained for all unit cells, which is the same as stipulated in Subsection 3.5.2, supporting the validity of the result. In addition, Fig. 5.7b shows the $\angle S_{21}$ values range from $-70°$ at the center unit cells to 40° at the diagonal corners. This moderate variation compensates for the small phase shift produced by the low β_ρ^-, ensuring the phase of the field above the BHMS is constant across the whole aperture.

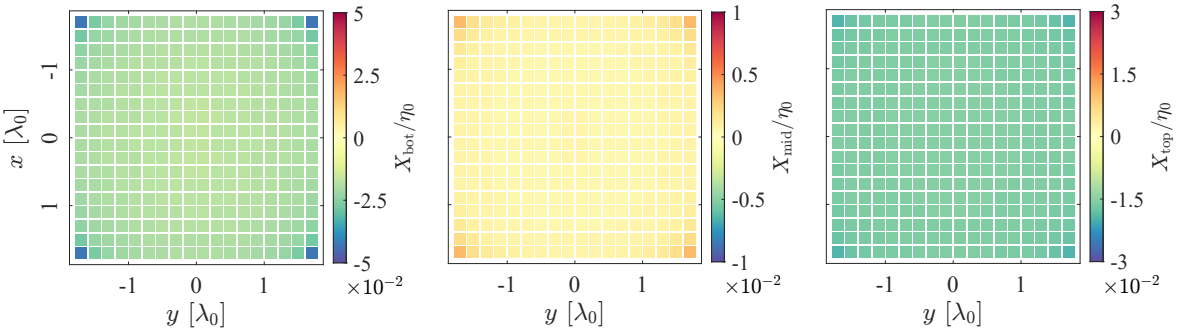

Figure 5.8: Idealized unit-cell normalized reactance values (a) X_{bot}, (b) X_{mid} and (c) X_{top} for the classical FPCA case design.

The minor variations in the BHMS characteristics are more evident in Fig. 5.8, where the implemented unit-cell three reactance values are shown, following the process in Section 5.3. As noted, the metasurface is almost homogeneous, as the reference FPCA design, and the slight variations account for transmission phase corrections that are not straightforward to implement in classical FPCA designs.

The LWA with the achieved BHMS is simulated in HFSS, leaving the waveguide

edges open. The idealized unit cells are implemented with isotropic impedance sheet conditions due to the assumption that the field is mainly contained in one cartesian direction, as previously discussed. On the other hand, the theoretical radiated fields are computed from the upper-region tangential aperture field components in Subsection 5.1.2 across the BHMS aperture, using the procedure described in Subsection 2.2.3. The accuracy of the solution depends on the aperture field discretization resolution which, for all designs, is chosen $\delta x = \delta y = \lambda_0/30$. This way, the total electric field magnitude is represented in Fig. 5.9, comparing theory and simulations.

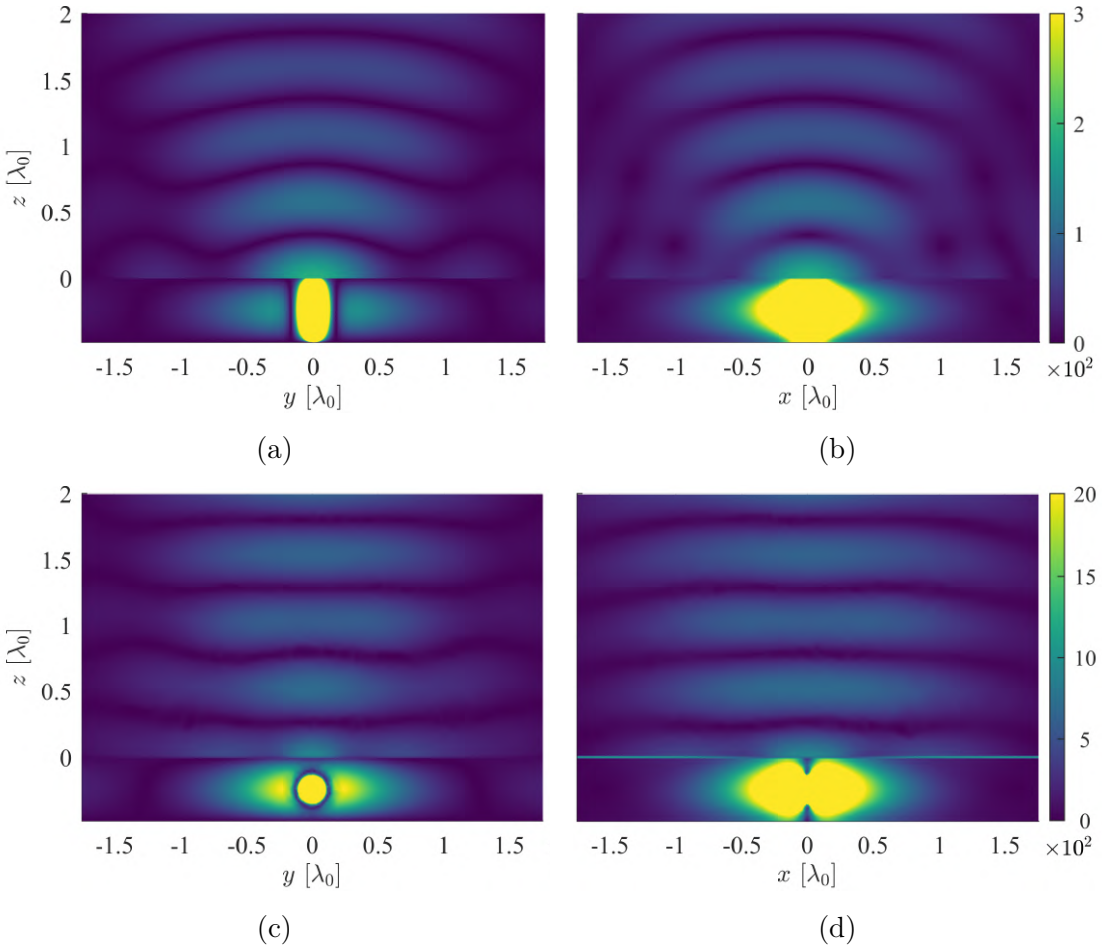

Figure 5.9: Field distributions $|\Re\{\vec{E}(x,y,z)\}|$ (V/m) cuts in the (a,c) YZ and (b,d) XZ planes from (a)–(b) theoretical predictions and (c)–(d) idealized simulations for the classical FPCA design.

The wavefront propagates toward the broadside direction on both shown planes, as stipulated, which translates into broadside radiation patterns. This is shown in the associate directivity 3-D patterns of Fig. 5.10, which are a cartesian projection of the positive spatial semi-sphere. In addition, the guided field exhibits an intensity peak at the center, where it is generated. Although, in theory, the power density would approach infinity, in simulation it becomes clear that at that point the field generated

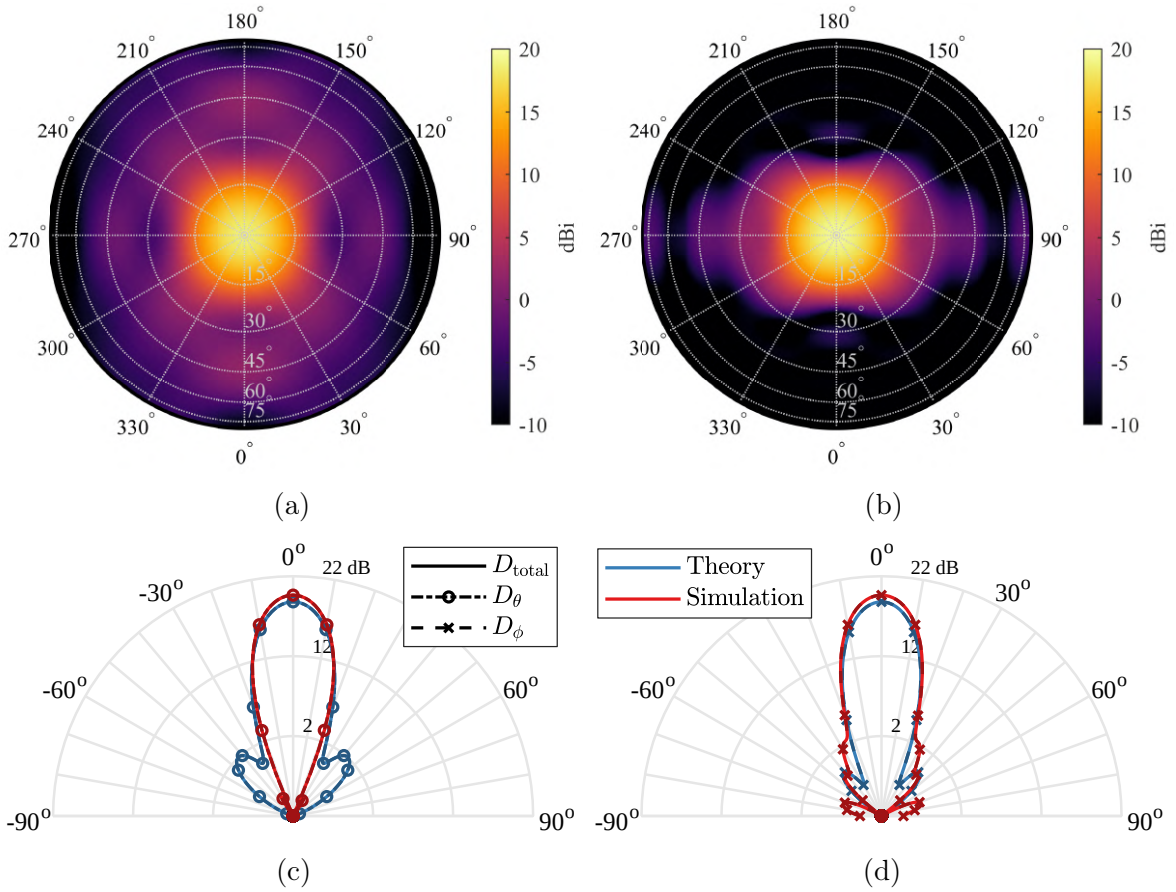

Figure 5.10: 3-D directivity patterns from (a) theoretical predictions and (b) idealized simulations, and their (c) $\phi = 0°$ and (d) $\phi = 90°$ cuts, for the classical FPCA design.

by the HED excitation is coupling to the PPW-supported modes, making the field profiles near the center to differ from theory to simulation.

Interestingly, it can also be observed that the radiated wavefronts in theory are more curved than in simulation, which translates into slightly higher simulated directivity and lower SLL especially in the $\phi = 0°$ plane, as seen in the comparison from Fig. 5.10c. This discrepancy may be caused by a set of non-idealities from the simulation environment and theoretical derivation assumptions. For example, the contribution of the fields refracted at the waveguide edges is not accounted for in the theoretical derivation, nor the effects of the potential evanescent modes excited by the HED source. In addition, the BHMS design-related assumptions made to simplify the design process may contribute to the observed discrepancies. It must also be mentioned that, in general, the electromagnetic simulator had difficulties reaching proper convergence, which is another potential source of disparity. Nonetheless, certain discrepancies persist across all cases and will be examined in more detail at a later stage.

Regardless, even considering all the potential error sources, the desired broadside

beam is achieved, also showing highly linear polarization. The obtained simulation results are consistent with the theoretical predictions, as detailed in the figures of merit of Table 5.2, where D_0 is the maximum directivity, and θ_0 and ϕ_0 are the radiation angles at which it is found. Comparing these to the ideal simulation results from the homogeneous FPCA (Design 2) in Table 3.1, it is found that the transmission phase correction offered by the BHMS leads to a noteworthy increase in the directivity level, representing a 50% greater η_{ap}.

Table 5.2: Achieved far-field figures of merit for the first design.

	D_0	θ_0	ϕ_0	η_{ap}
Theory	18.8 dBi	0°	0°	49.2%
Simulation	19.6 dBi	0°	0°	59.6%

5.4.2 Broadside Compensation Case

After confirming that the BHMS operates as intended in the baseline FPCA example, now less conventional characteristics will be demanded to exploit the potential of the BHMS wavefront transformation capabilities. In this sense, it was already seen in Chapter 3 that FPCAs face fundamental limitations related to the maximum achievable directivity (see Section 3.4). These are related to the splitting condition fulfillment forcing the guided modes to approach cut-off. Fortunately, the studied 2-D BHMS-based LWA configuration is, in principle, able to offer an arbitrary radiation angle without relying on the guided mode wavenumbers. Hence, the current design example represents the logical step to overcome the FPCA limitation, by specifying a broadside radiated beam while enforcing a guided phase constant far from cut-off. The design characteristics are summarized in Table 5.3.

Table 5.3: LWA design parameters for the second design.

θ_{in}	$\alpha_\rho\,[k_0]$	θ_{out}	ϕ_{out}	ξ	$d\,[\lambda_0]$	$L\,[\lambda_0]$
25°	0.133	0°	0°	0°	0.552	6

Note that, from (5.22), the chosen θ_{in} corresponds to a $\beta_\rho^- = 0.423k_0$, so the splitting condition (2.4) is clearly not satisfied. The waveguide height is chosen for a guided field profile similar to that from an ideal PPW. In this case, the computed mode properties are $\beta_\rho^{\text{TM}} = 0.415k_0$, $\alpha_\rho^{\text{TM}} = 0.145k_0$ and $\beta_\rho^{\text{TE}} = 0.428k_0$, $\alpha_\rho^{\text{TE}} = 0.121k_0$. Furthermore, the antenna size is bigger in this example to ensure a considerable field phase shift is produced across the aperture, thereby properly testing the BHMS, which will need to

compensate for it. As the previous leakage factor is used with a larger antenna size, the computed radiation efficiency for this design is a higher $\eta_{\text{rad}} = 99.7\%$, which will necessarily lead to a lower aperture efficiency.

The required BHMS surface parameters (not shown for brevity) now offer greater variation across the antenna than in the previous example, and the corresponding local S-parameters are represented in Fig. 5.11. The reflection phase remains constant with $\angle S_{11} = -175.3°$ across the aperture to guarantee the guided modes propagate properly, whereas the reflection magnitude presents a constant $|S_{11}| = 0.65$. The transmission phase, on the other hand, presents an almost radially-symmetric phase shift. This is the case due to the broadside beam requirement, as the periodicity of the BHMS-implemented transmission phase shift will generally be different along every radial direction. In this case, the metasurface is periodic along the x axis (dominant TM^z_{10} mode) with a period $2.42\lambda_0$, whereas a similar $2.32\lambda_0$ periodicity is found along the y axis (dominant TE^z_{10} mode), both correctly predicted by the Floquet's theorem expression (4.16) when using the corresponding dominant-mode radial phase constant.

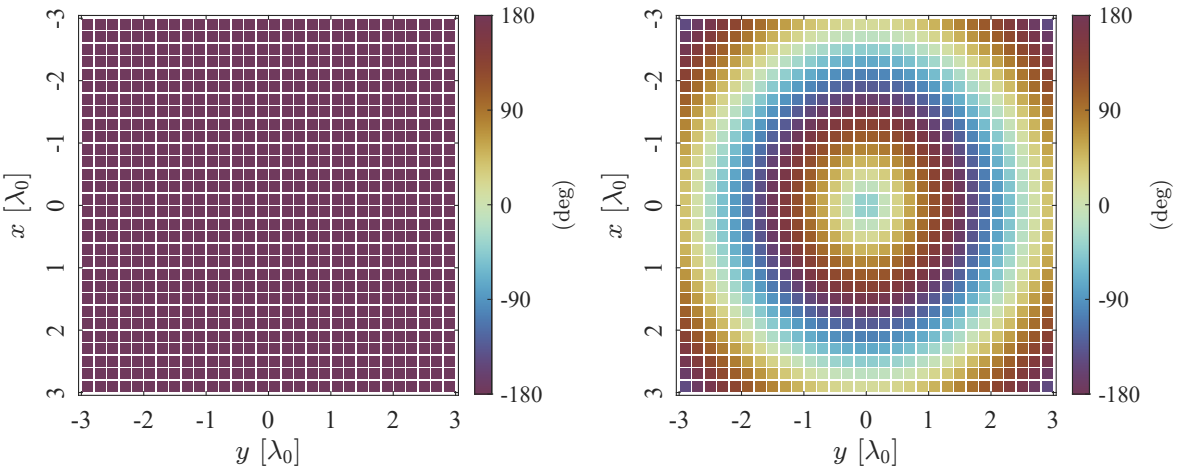

Figure 5.11: Computed η_0-referenced local S-parameters (a) reflection and (b) transmission phase, for the second design.

The unit-cell S-parameters are implemented with the idealized reactance sheets, whose values are shown in Fig. 5.12. It is clearly seen that they also adopt an almost radially-symmetric behavior, as expected. This way, the complete antenna is simulated in the same way as in the first design example, and the resulting guided and radiated fields are compared to the theoretical ones in Fig. 5.13 along the two main orthogonal planes. From the theoretical fields in Figs. 5.13a and 5.13b it is observed that, although the radiated field is very similar to the first design example, the guided modes below the BHMS plane are clearly experiencing a considerable phase shift, as several local maxima along the propagation direction are observed. The same behavior is found

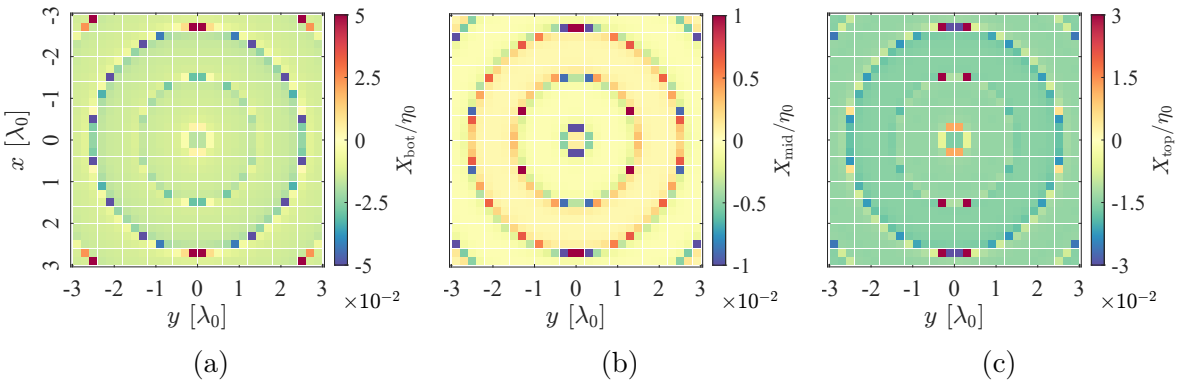

Figure 5.12: Idealized unit-cell normalized reactance values (a) X_{bot}, (b) X_{mid} and (c) X_{top} for the second design.

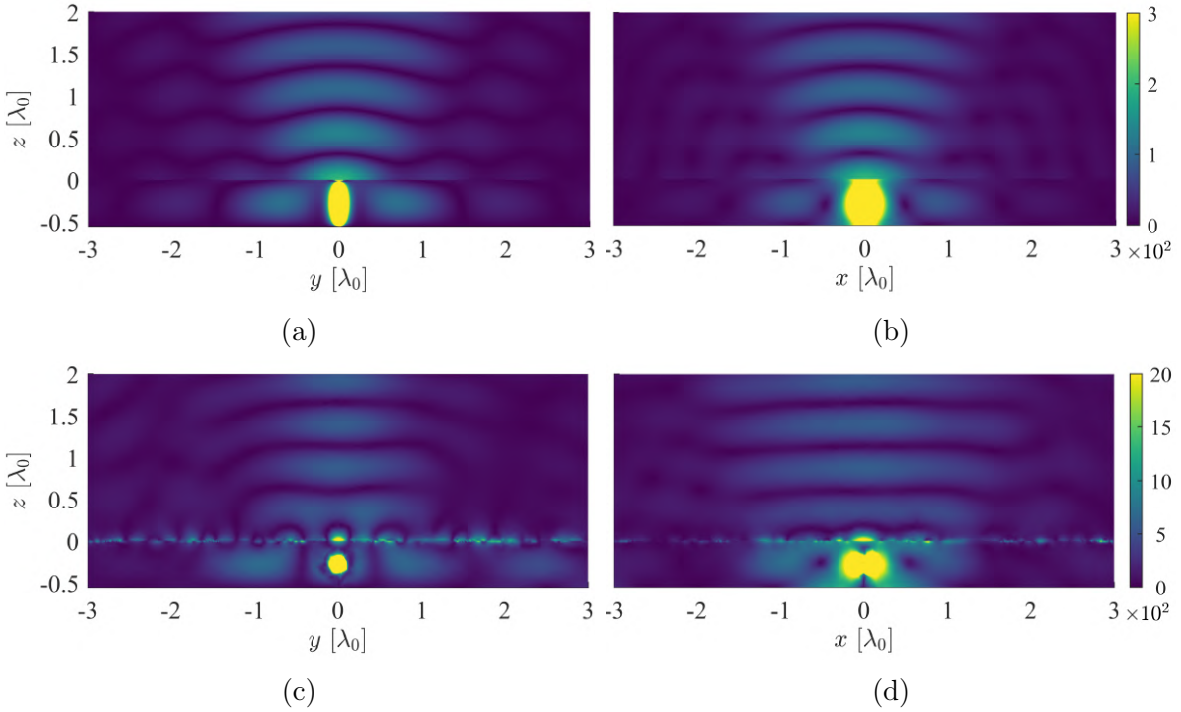

Figure 5.13: Field distributions $|\Re\{\vec{E}(x,y,z)\}|$ (V/m) cuts in the (a,c) YZ and (b,d) XZ planes from (a)–(b) theoretical predictions and (c)–(d) idealized simulations for the second design.

from simulations in Figs 5.13c and 5.13d, where the field interaction with the BHMS can be noticed along the $z = 0$ plane. Similarly to the first example, at the center of the cavity, the field is slightly different compared to theory due to the coupling from the source. Nevertheless, the guided field propagates with the expected characteristics, whereas the transmitted wave is directed towards broadside as intended.

The corresponding directivity patterns are depicted in Fig. 5.14. It can be observed how the beam is directed towards the normal direction, both in theory and simulations.

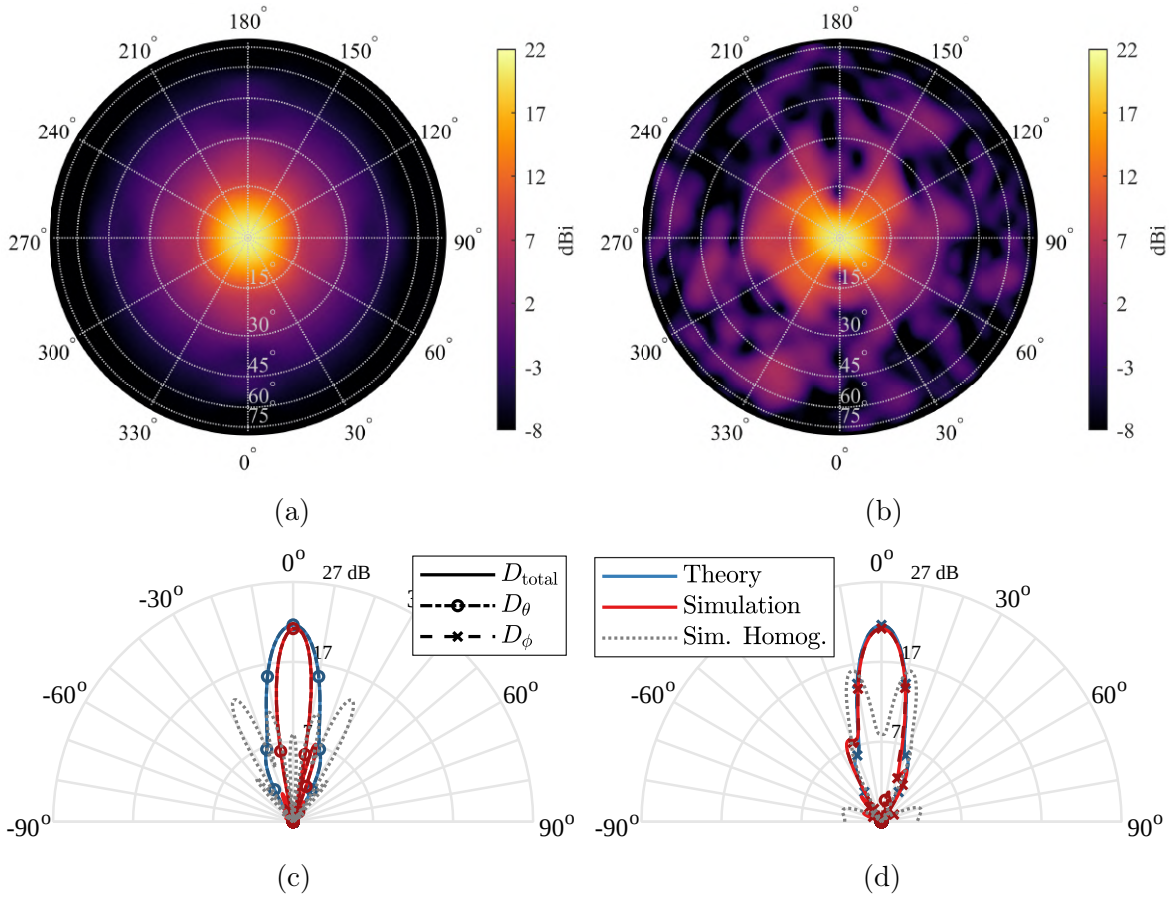

Figure 5.14: 3-D directivity patterns from (a) theoretical predictions and (b) idealized simulations, along with their (c) $\phi = 0°$ and (d) $\phi = 90°$ cuts, for the second design. A simulated homogeneous BHMS case is also represented for comparison.

Although the theoretical diagram in Fig. 5.14a is more ideal, the simulated results in Fig. 5.14b achieve a directivity level that is practically the same, as detailed in Table 5.4, considering the expected numerical and convergence-related errors.

Table 5.4: Achieved far-field figures of merit for the second design.

	D_0	θ_0	ϕ_0	η_{ap}
Theory	21.5 dBi	0°	0°	31.4%
Simulation	21.2 dBi	1°	25°	29.2%

Note that the simulated diagram presents more sidelobes across the 3-D plane but, as can be especially observed in Fig. 5.14c, the beam is narrower than expected along the $\phi = 0°$ plane, consequently slightly increasing the directivity level. This effect is similar to the one encountered in the first example: the field behavior partially differs from the expected along the direction where the TM^z_{10} mode is dominant. Nevertheless, the BHMS is successfully compensating the guided field phase shift, preventing

the radiated beam from splitting into a conical pattern. This latter scenario is also simulated with a metasurface for which all the unit cells are identical and equal to one of the original-BHMS corner unit cells, and the directivity pattern is also depicted in Figs. 5.14c and 5.14d for reference. As a side note related to those polar plots (applying also to the equivalent plots for the other designs), their grid maximum limit is chosen as the rounded maximum achievable directivity for the physical aperture size projected onto the desired beam direction, thus giving a sense of how efficiently the aperture is illuminated.

This example hence confirms the capability of the BHMS to overcome the limitations of FPCAs regarding the required mode characteristics for broadside radiation. This way, the presented design should facilitate the real feeding of the waveguide, as the modes are no longer near the cut-off condition. Furthermore, it enables achieving higher directivity levels for greater antenna sizes and lower leakage factor values.

5.4.3 Tilted Beam Case

As a last design example to showcase the presented configuration capabilities, the radiated beam is desired to be tilted in some off-broadside direction. The antenna parameters are specified in Table 5.5.

Table 5.5: LWA design parameters for the third design.

θ_{in}	$\alpha_\rho\,[k_0]$	θ_{out}	ϕ_{out}	ξ	$d\,[\lambda_0]$	$L\,[\lambda_0]$
7.64°	0.133	33°	70°	0°	0.486	6

The antenna size is maintained from the previous example, but the θ_{in} reverts to that of the first design, as lower β_ρ^- values tend to offer better results in simulation. The computed mode properties are $\beta_\rho^{\text{TM}} = 0.134k_0$, $\alpha_\rho^{\text{TM}} = 0.136k_0$ and $\beta_\rho^{\text{TE}} = 0.132k_0$, $\alpha_\rho^{\text{TE}} = 0.130k_0$, necessarily the same as in the design of Subsection 5.4.1, as the waveguide height is also the same. In this case, similarly to the design in Subsection 5.4.2, the computed radiation efficiency is $\eta_{\text{rad}} = 99.75\%$.

In the same fashion as the previous examples, the required local S-parameters, calculated from the metasurface ones, are represented in Fig. 5.15. As expected, the reflection angle $\angle S_{11} = 170°$ is practically the same for all unit cells, although presenting a slight ripple due to the mismatch of the chosen η_0 as S-parameter reference impedance and the actual wave impedance on both sides of the BHMS. This ripple is also noticed in the reflection magnitude, whose average is $|S_{11}| = 0.9$. The transmission phase is not radially symmetric in this case, as the radiated beam is tilted, so the BHMS needs to compensate the guided field phase shift in different ways for

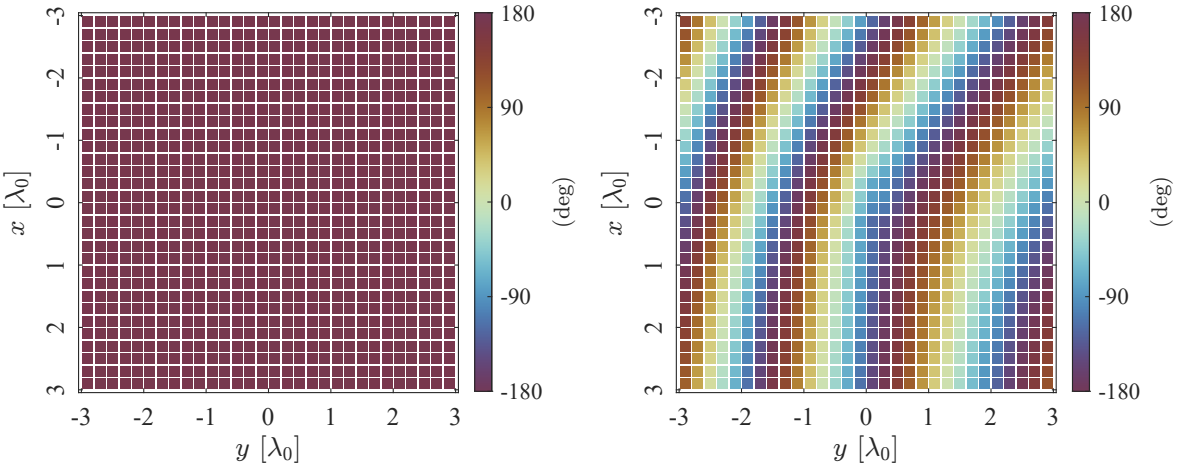

Figure 5.15: Computed η_0-referenced local S-parameters (a) reflection and (b) transmission phase, for the third design.

each radial direction. The transmission phase periodicity will be larger in directions along which the guided and radiated fields present similar phase progressions, and vice versa. The ideal three-stack reactance sheet values adopt the same spatial behavior, as depicted in Fig. 5.16.

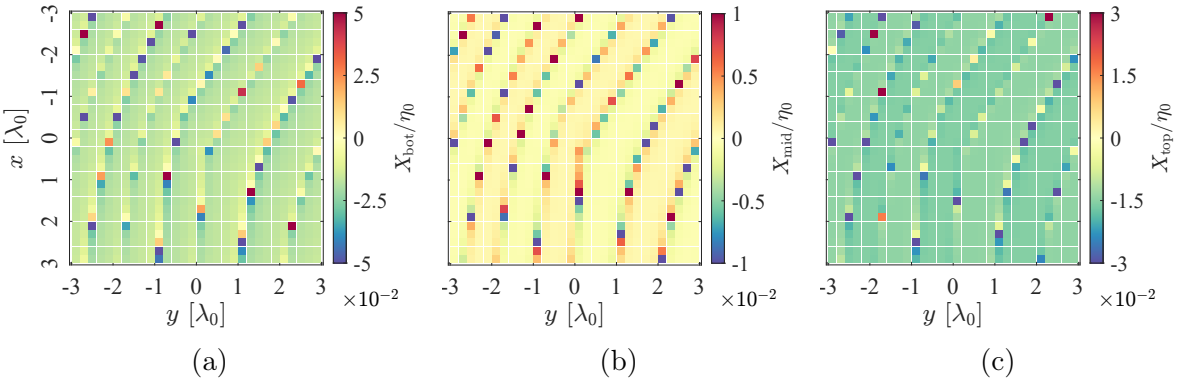

Figure 5.16: Idealized unit-cell normalized reactance values (a) X_{bot}, (b) X_{mid} and (c) X_{top} for the third design.

This last antenna design is simulated in the same way as the previous ones, and Fig. 5.17 shows the resulting electric field in the main orthogonal planes along with the theoretical predictions. Considering the non-idealities, the degree of agreement between theory and simulations is highly satisfactory. The simulated radiated wavefronts travel towards the predicted directions, and the radial power decay behaves as expected. It must be mentioned that not every combination of design parameters offered results with the same degree of agreement as the shown here. In particular, higher values of θ_{in}, as previously mentioned, tend to produce more degraded results in simulation. This may be attributed, in part, to the decreasing validity of the assumption that practically

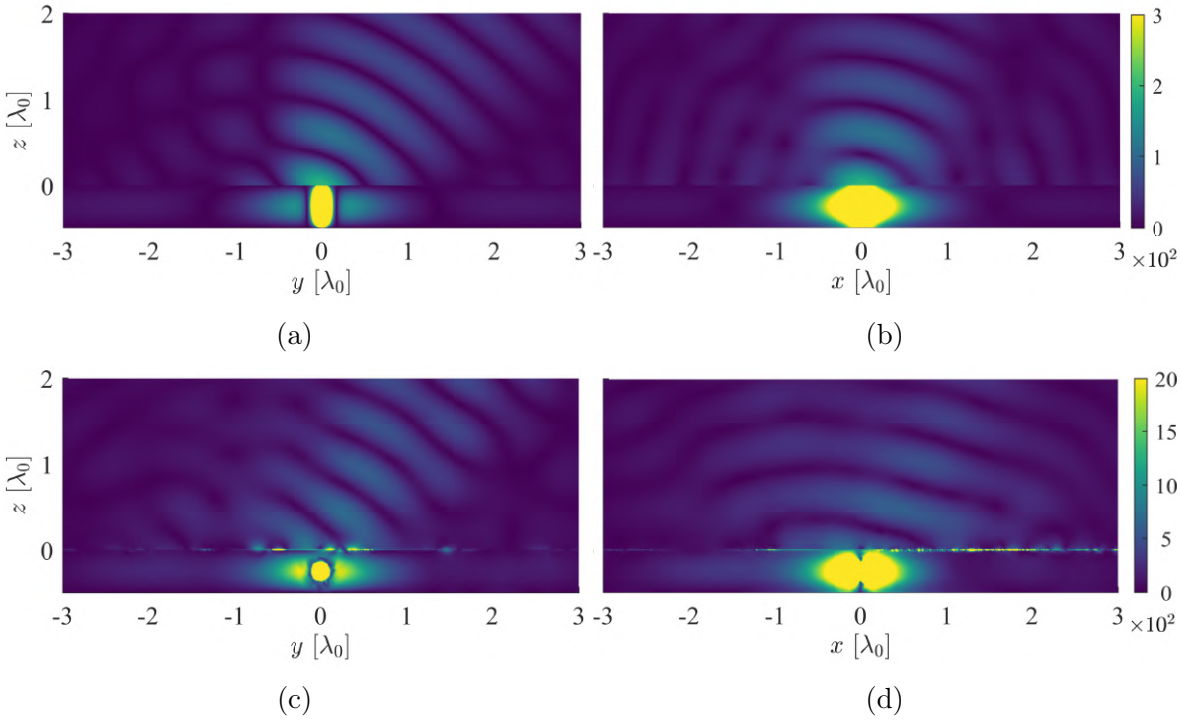

Figure 5.17: Field distributions $|\Re\{\vec{E}(x,y,z)\}|$ (V/m) cuts in the (a,c) YZ and (b,d) XZ planes from (a)–(b) theoretical predictions and (c)–(d) idealized simulations for the tilted beam design.

only E_x and H_y components are present, as well as to the increasing mismatch between substrate impedance Z_{sub} used in the ideal unit-cell implementation in Section 5.3 and the actual mode-specific equivalent TL characteristic impedances given in (5.25).

Finally, the associated far-field patterns in Fig. 5.18 show a strong correlation between theory and simulations. Again, results from the latter are not as ideal, but they are considerably similar to the expected around the main beam direction. This is also observed in the main $\phi = 70°$ cut comparison from Fig. 5.18c, where the theoretical and simulated total directivity diagrams practically overlap around the main beam. The field is also highly linearly polarized, although a slight difference is obtained in the direction it is contained. This is very minor, but the $\hat{\phi}$ direction not coinciding with the $\hat{y}$ one in this diagonal plane exaggerates its apparent significance. Regardless, the beam direction and directivity levels are highly similar to the theoretically-obtained one, as is summarized in Table 5.6, confirming the successful results.

Table 5.6: Achieved far-field figures of merit for the third design.

	D_0	θ_0	ϕ_0	η_{ap}
Theory	20.1 dBi	32°	70°	22.5%
Simulation	20.0 dBi	32°	70°	22.1%

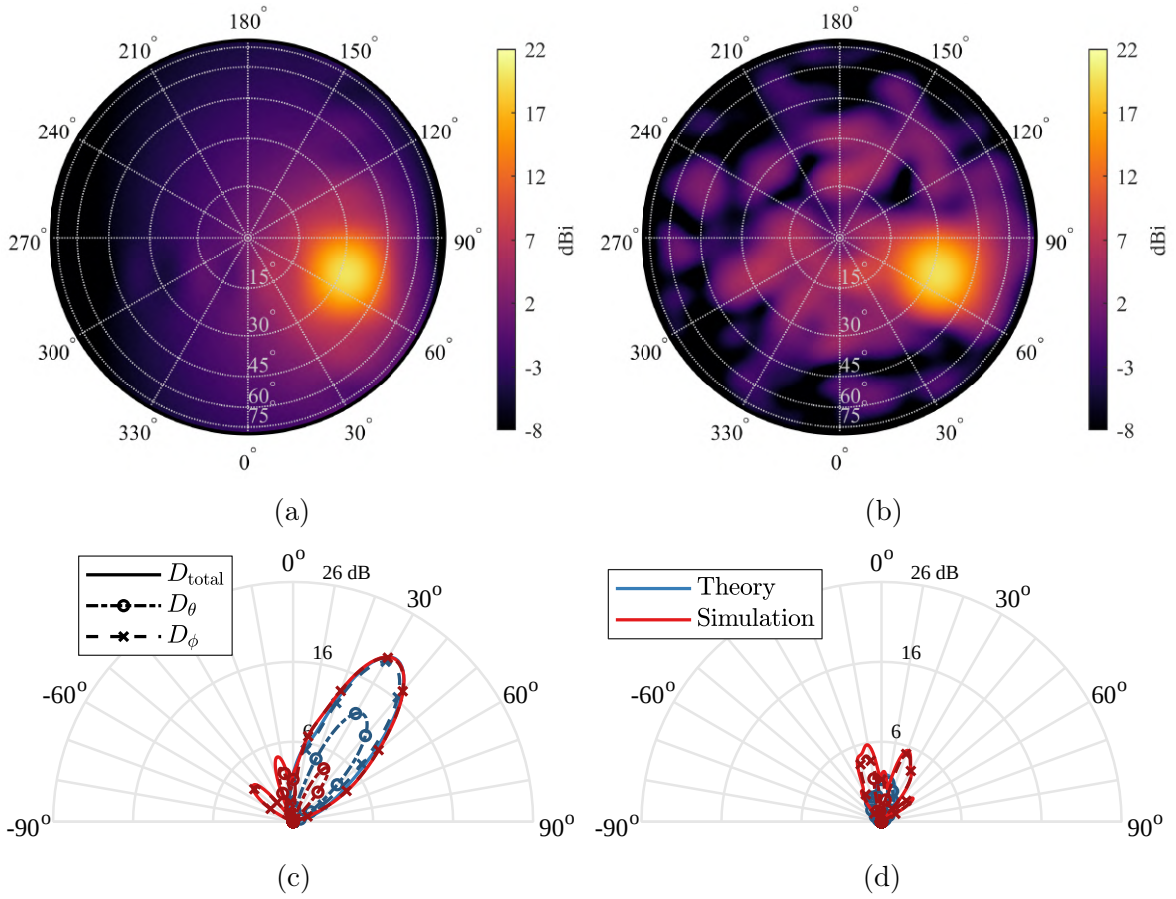

Figure 5.18: 3-D directivity patterns from (a) theoretical predictions and (b) idealized simulations, along with their main (c) $\phi = 70°$ and (d) $\phi = 160°$ orthogonal cuts, for the tilted beam design.

This design example showcases the successful capabilities of the designed BHMS to tilt the beam in the presented 2-D LWA configuration. However, considering also the previous design examples, directions close to $\phi = 90°$ (dominant TE mode) are always more similar to theory than directions close to $\phi = 0°$ (dominant TM mode). In the latter ones, more radiation nulls can be appreciated in all designs, resulting in less sidelobes or narrower beamwidths in the broadside designs. This effect leads to increasingly degraded main-beam characteristics when ϕ_{out} values closer to the x axis are desired. One of the possible reasons for this persistent discrepancy is that the assumed existing mode configuration may not be entirely accurate (in terms of their excited amplitude and phase), and the used source might be enabling the partial excitation of other modes preferentially along the x axis. This could be the case for the other propagative TM_{00}^{z} (TEM^{ρ}) mode which could be getting undesirably excited, degrading the expected results. However, properly accounting for these would require a mode expansion sum of the fields generated by the source, which would increase the formulation complexity. In the presented work, an approach based on reasonable assumptions

has been followed to reduce the complexity of the problem, enabling a simplified and completely analytical formulation. Consequently, a considerably straightforward design methodology has been achieved, which produces satisfactory results for a wide variety of cases, as shown in this section.

5.5 Conclusions and Considerations

In this chapter, a rigorous, systematic approach for designing versatile 2-D PPW-based LWAs has been presented. The comprehensive methodology enables the selection of several antenna parameters, with some restrictions related to the assumptions made to simplify the BHMS design. The concept has been verified in simulation with idealized meta-atoms. Physical unit cells may be implemented with simple square-symmetric, non-polarization-rotating geometries, thanks to the reduced BHMS complexity due to the single direction field components accounted for.

Regarding the simulation discrepancies, aside from the potential improvements (with the corresponding complexity increase) to the theoretical analysis, simulator related issues cannot be ignored. HFSS, as a general-purpose electromagnetic simulator, faces challenges with electrically large structures composed of numerous electrically small elements. This not only prevents from even attempting to simulate electrically large versions of the presented antenna configuration, but also the presented examples showed notable limitations regarding convergence and simulation time, even using the analytical impedance boundary conditions. Hence, the use of other simulation tools—or even some specialized method-of-moments approach as in [88]—more optimized for this type of structures may prove greatly beneficial in the verification of these designs.

As seen in the showcased designs, the obtained aperture efficiencies are considerably low, due to the inherent radial decay and the high α_ρ^-. However, this guarantees highly attenuated refracted fields at the cavity edges, preventing the generation of relevant standing wave patterns (which, for the chosen squared aperture, would not even present cylindrical symmetry) and the consequent invalidation of the stipulate guided field expressions. Nevertheless, similarly to the works from Chapters 3 and 4, aperture efficiency can be improved by modulating the leakage factor along the aperture. This would require integrating the argument of the Hankel functions in Subsection 5.1.1, which moreover would affect differently to each mode, thus increasing the complexity of the analysis and design processes. In the presented work, it has been preferred to keep the constant leakage factor strategy for design simplicity. However, a variable leakage factor is expected to be introduced in future work, as it is necessary to design more interesting radiation patterns and improve the antenna efficiency.

Chapter 6

Towards Reconfigurability: Characterizing Liquid Crystals

The previous chapters have shown the potential of metasurface-based antennas in achieving a wide range of radiation characteristics. In that sense, modern wireless communication systems increasingly require reconfiguration capabilities. The studied antennas could also provide this feature, as long as a mechanism able to modify one or several physical characteristics on demand is introduced. Traditionally, fixed-frequency beam steering has been achieved either mechanically, which results in bulky structures, or by implementing phased arrays, which lead to complex and expensive feeding networks. An alternative technology to reconfigurable components such as varactors or micromechanical actuators is nematic liquid crystals (LCs) [89]. These tunable materials are potential candidates for reconfigurable antennas [90], especially at high frequencies for which mechanical actuators and integrated devices suffer high transmission losses. Additionally, tunable materials have the main advantage of reconfiguring the whole structure at once for modern directive planar antennas, such as reflectarrays [91, 92], leaky-wave [93], or metasurface-based antennas [74, 94], in which particular interest resides here. In any case, the first step in introducing these reconfigurability mechanisms is their proper characterization.

In their nematic phase, LCs are anisotropic materials with tunable electric permittivity through a biasing voltage [95]. Although LCs for optical applications have been studied extensively, their use is not so extended at microwave frequencies. The broadband characterization of its effective dielectric constant is crucial to enable the design of reconfigurable antennas using this technology. In general, dielectric and transmission line characterization methods have been divided into two groups: resonant and broadband. Methods based on the former type have been used with multilayer struc-

tures based on microstrip [96], substrate-integrated transmission lines [97] or planar patch resonators [98] among others, but they are inherently narrowband. Broadband characterization methods have been proposed in works such as [99], which needs thru and line standards and thus requires fabricating and measuring additional structures.

There has also been research on the characterization of LCs in the time domain for many years [100, 101]. Time-gating techniques have been traditionally used to avoid undesired effects, such as noise or reflections. In devices whose different section responses are not physically separable, the undesired section contributions can still be mostly removed in the time domain (e.g., [102]), enabling dielectric materials characterization [103]. This chapter proposes a time-gating technique to characterize the relative permittivity of LCs inside microstrip lines fabricated using additive manufacturing. The chosen structure offers low manufacturing complexity, while enabling the use of very low LC volume. This approach allows the fabrication and measurement of a single prototype while enabling broadband characterization. As main advantage, it does not require any in-fixture calibration of the analyzer [104, 105] or the use of more than one transmission line needed by differential length characterization techniques [106, 107], which considerably facilitates its application due to the difficulty of manufacturing this type of structure.

The chapter is based on one of the author's works [J4] and organized as follows. Section 6.1 describes the proposed structure, its stack-up and the manufactured prototype. Section 6.2 illustrates the proposed method based on time-gating to extract the dielectric permittivity of the LC. Section 6.3 shows the validation through simulation and experimental results. Finally, conclusions are drawn in Section 6.4.

6.1 Structure Description

The proposed microstrip transmission line stack-up is shown in Fig. 6.1a. As seen, it consists of four layers. The first one from the bottom is made of copper and plays the role of ground plane. The second layer is a thin polyimide (kapton) sheet to ensure the correct LC molecules orientation at rest [89]. The third one is the pool where the LC is contained, whereas the pool edges are made of high-impact polystyrene (HIPS) using additive manufacturing. Fig. 6.1b shows a top view of the structure described. In the top layer is a strip milled from a 350 µm-thick copper sheet and an overlay of HIPS with a groove in which the strip fits and stays correctly suspended above the LC pool. In this layer, two perforations allow the LC pool to be filled using a syringe. All junctions between layers are performed using screws located outside the pool and non-conductive epoxy to prevent fluid leakages. Fig. 6.1 details the structure's main dimensions, which

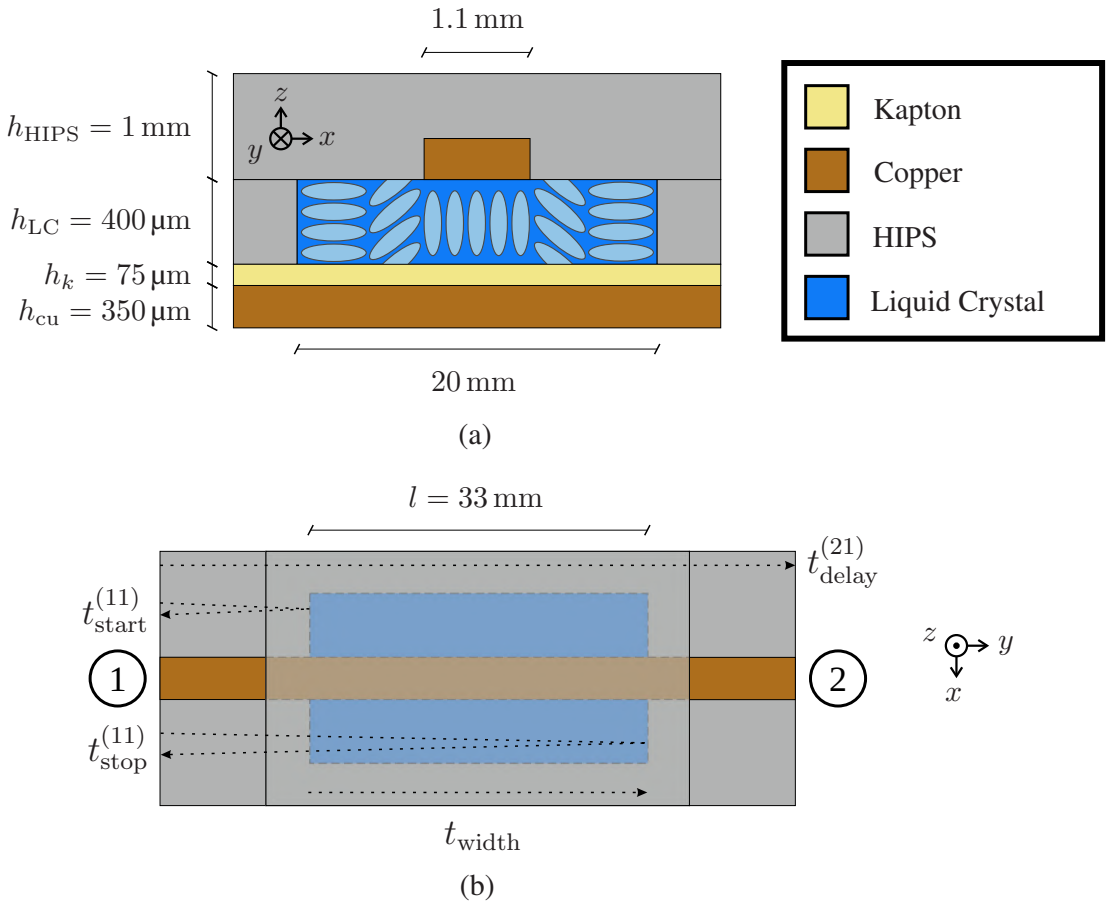

Figure 6.1: Not-to-scale diagram of (a) the stack up with the LC molecules polarized and (b) top view of the proposed covered microstrip line.

is 60 mm long in total. Note that the pool length is chosen to ensure a sufficient effect over the complete electromagnetic response of the structure. Moreover, the pool width is chosen to guarantee that the microstrip mode is practically not affected by the HIPS lateral borders.

Regarding HIPS, it was proposed for microwave applications and characterized in [108]. It is a material for fused filament fabrication with excellent electromagnetic properties due to its low loss tangent and relative permittivity, close to 2.45. Additionally, HIPS is durable and possesses good impact resistance together with the fact that remains stable when exposed to moisture. For the proposed experiment, it was printed out using the Ultimaker 3 printer, setting the infill to 100%. The extrusion and bed temperatures were established to 240 °C and 90 °C, respectively, and the layer height was set to 60 µm. The HIPS layers (including structural support), along with the rest of them used in the structure, are shown side by side in Fig. 6.2a, and the assembled and sealed prototype in Fig. 6.2b.

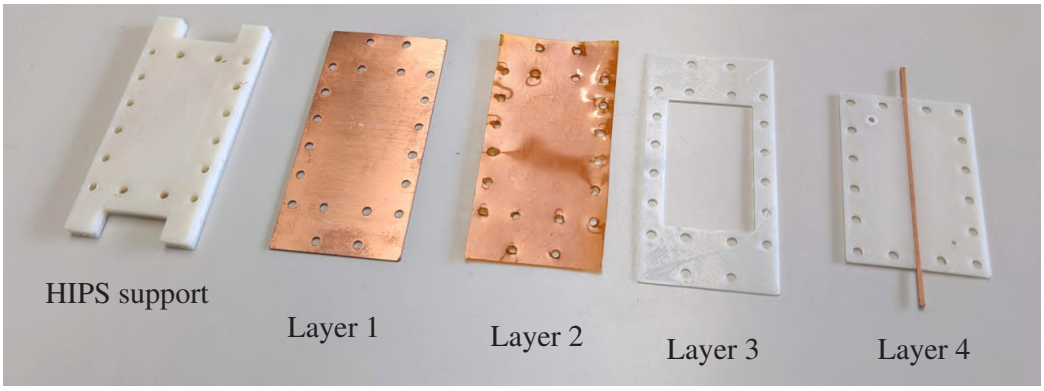

(a)

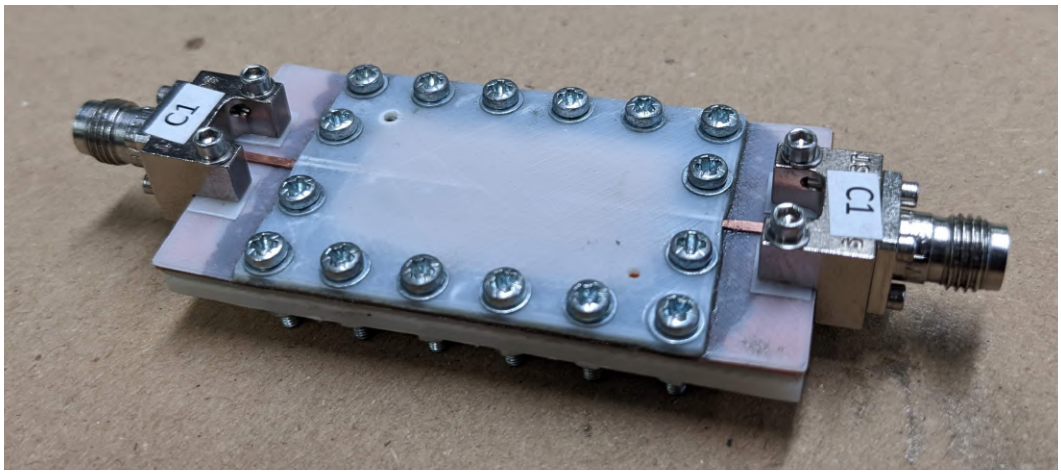

(b)

Figure 6.2: Fabricated prototype (a) as a side-by-side view of its layers and (b) fully assembled and sealed.

6.2 Characterization Method

6.2.1 Time-Gating

The time domain processing from frequency domain measurements is used to remove the undesired contribution from the sections of the transitions between the ports and the pool (see Fig. 6.1b), thus moving the reference planes to the pool outer interfaces. Firstly, the measured S-parameters are re-sampled to present 2^n frequency points evenly spaced along the whole bandwidth, starting from DC. As the original measurements from a vector network analyzer will probably not include DC, a sensible assumption is to consider it a short circuit. Thus, an Inverse Fast Fourier Transform (IFFT) is adequately applied to every S-parameter to obtain their time domain responses. These are the convolution of the impulse responses with a sinc function due to the measured frequency response truncating the actual band-unlimited one.

Another type of window (Hamming, Blackman, etc.) can be applied before the IFFT to reduce the impulse response widening and thus improve its visualization. Furthermore, applying frequency-domain zero-padding in the IFFT is recommended to increase time resolution. Then, if the zero-padding order n_z represents the factor by which the number of frequency points is increased, the achieved time resolution will be $dt = 1/(2n_z f_{max})$, with f_{max} being the maximum measured frequency.

The time interval, in reflection, related to the LC section (when does it start, $t^{(11)}_{\text{start}}$, and end, $t^{(11)}_{\text{stop}}$) can be derived from previous knowledge of the structure dimensions and the widened impulse response of the S_{11}. This time response will be composed of several widened deltas, among which the $t^{(11)}_{\text{start}}$ timestamp will correspond with the peak of one of the most relevant ones, and for which a fine time resolution is needed for its proper identification. Additionally, as the structure shown in Fig. 6.1b is symmetric and its delay $t^{(21)}_{\text{delay}}$ can be obtained as the main peak timestamp in the S_{21} time response, $t^{(11)}_{\text{stop}}$ directly arises from $t^{(11)}_{\text{start}}$, once derived, as follows:

$$t^{(11)}_{\text{stop}} = 2t^{(21)}_{\text{delay}} - t^{(11)}_{\text{start}}\,. \tag{6.1}$$

The time-gate width can then be calculated as

$$t_{\text{width}} = \left(t^{(11)}_{\text{stop}} - t^{(11)}_{\text{start}}\right)/2\,, \tag{6.2}$$

which is divided by two to account for the round-trips in the reflection signals, as shown in Fig. 6.1b.

This way, the time-gating timestamps for the rest of the S-parameters can be geometrically derived from the port 1 timestamps. Transmission parameters time-responses will consist of a main pulse (whose peak's timestamp determines the signal delay between both ports) followed by the contributions of several internal reflections. Using the t_{width} value also for these parameters, the time-gating timestamps for the transmission from port 1 to port 2, for example, would be

$$t^{(21)}_{\text{start}} = t^{(21)}_{\text{delay}} - t_{\text{width}}/2\,, \tag{6.3a}$$
$$t^{(21)}_{\text{stop}} = t^{(21)}_{\text{delay}} + t_{\text{width}}/2\,, \tag{6.3b}$$

thus applying the time-gate around the main pulse arrival. For reflection parameters, the corresponding timestamps can be geometrically derived from Fig. 6.1b provided that the time delay between port 1 and the port of interest is already known. For

example, port 2 reflection timestamps would be calculated as follows:

$$t_{\text{start}}^{(22)} = 2t_{\text{delay}}^{(21)} - t_{\text{stop}}^{(11)}\,, \tag{6.4a}$$
$$t_{\text{stop}}^{(22)} = 2t_{\text{delay}}^{(21)} - t_{\text{start}}^{(11)}\,. \tag{6.4b}$$

Following the approach from [109], a high-order Butterworth filter window is used as the time gate to prevent amplitude distortion within the interval of interest (from t_{start} to t_{stop}) while significantly attenuating the rest of the response without introducing abrupt changes. The corresponding time window is multiplied by each impulse response, and the result is shifted towards the time origin to remove the undesired sections' contribution to the equivalent transmission line length. The time shift will depend on the specific parameter

$$t_{\text{shift}}^{(ii)} = t_{\text{start}}^{(ii)}\,, \tag{6.5a}$$
$$t_{\text{shift}}^{(ji)} = t_{\text{delay}}^{(ji)} - t_{\text{width}}\,. \tag{6.5b}$$

Finally, the impulse responses are transformed back to the frequency domain by applying a Fast Fourier Transform (FFT), reverting zero-padding and dividing by the used frequency window to remove the amplitude distortion, if needed. Thus, an approximation of the LC section's S-parameters is obtained.

6.2.2 Permittivity Extraction

Considering that the processed S-parameters have a good impedance matching and represent a transmission line, then its effective permittivity can be estimated from the transmission parameter

$$S_{21} = e^{-jkl} = e^{-\alpha l}e^{-j\beta l} = e^{-j\frac{2\pi f}{c}\sqrt{\varepsilon_{\text{eff}}}l}\,, \tag{6.6}$$

where l is the pool length (Fig. 6.1b). To extract ε_{eff} from the complex exponential without facing problems related to the phase wrapping and phase reference, its value is reconstructed from both the magnitude and the unwrapped phase of S_{21} as follows

$$\sqrt{\varepsilon_{\text{eff}}} = \sqrt{\varepsilon' - j\varepsilon''} = x + jy\,, \tag{6.7a}$$
$$|S_{21}| = |e^{-\alpha l}| \;\Rightarrow\; y = \frac{c}{2\pi f l}\log|S_{21}|\,, \tag{6.7b}$$
$$\angle S_{21} = -\beta l \;\Rightarrow\; x + f\frac{\partial x}{\partial f} = -\frac{c}{2\pi l}\frac{\partial \text{unwrap}(\angle S_{21})}{\partial f}\,, \tag{6.7c}$$
$$\varepsilon_{\text{eff}} = (x^2 - y^2) + j(2xy)\,. \tag{6.7d}$$

The first-order differential equation from (6.7c) can be numerically solved (using, for instance, the function `ode45` in MATLAB ®). Thus, by inserting (6.7b) and (6.7c) into (6.7d), the LC-section effective relative permittivity is calculated. For this process, it is assumed that there is a linear S_{21} phase variation with frequency, which is the natural behavior in a transmission line.

However, this work aims to characterize the liquid crystal's nominal permittivity ε_r, not the whole stack of different materials. Hence, a multilayered microstrip model is considered. First, the HIPS overlay used to seal the LC container is taken into account using the model from [110], which, although not frequency-dependent, allows the direct calculation of the microstrip substrate permittivity ε'_r from ε_{eff}. In addition, the substrate comprises both LC and kapton. The latter is well known and used in microwave applications, having a relative permittivity $\varepsilon_{r_k} = 3.5$. The equivalent single-layer permittivity of these materials can be obtained using [111]

$$\varepsilon'_r = \frac{\varepsilon_{r_k}\varepsilon_r\,(h_k + h_{\text{LC}})}{\varepsilon_{r_k} h_{\text{LC}} + \varepsilon_r h_k}\,. \tag{6.8}$$

This model can be used considering the liquid crystal as a lossy dielectric since it only considers the electromagnetic properties of the material (ε_r, $\tan\delta$) and not its mechanical characteristics, which also change with the bias voltage. Knowing the layers heights (see Fig. 6.1a), the LC permittivity ε_r can be retrieved from the previously calculated substrate permittivity ε'_r through (6.8).

On the other hand, determining the loss tangent requires reliable information solely about the transmission magnitude of the pool section. Applying the time gate in the middle of an already brief time response induces distortion in the reflection response and results in the main transmission response peak being a composite of inseparable contributions from the entire prototype. Consequently, when time-gating the transmission response around the main peak, only the contribution of secondary internal reflections occurring outside the time gate will be eliminated (thus conveniently smoothing the transmission parameter). However, the magnitude of the gated peak remains identical to that of the original ungated response. Therefore, deriving a loss tangent from this parameter lacks physical validity, as it would encompass losses from undesired sections outside the pool, thereby distorting the actual pool-section losses.

6.3 Validation

In this section, both preliminary simulation tests and experiments using a manufactured prototype will be carried out using the GT7-29001 LC from Merck, which offers the

electromagnetic and mechanical characteristics summarized in Table 6.1 according to available datasheet, where $\Delta\varepsilon$ is the low-frequency dielectric anisotropy, K_{11} and K_{33} are elastic constants, γ is the rotational viscosity, and V_{th} is the threshold voltage.

Table 6.1: GT7-29001 LC characteristics at 19 GHz

$\varepsilon_{r_\perp}$	$\tan\delta_\perp$	$\varepsilon_{r_\parallel}$	$\tan\delta_\parallel$	$\Delta\varepsilon$	K_{11}	K_{33}	γ	V_{th}
2.46	0.0116	3.53	0.0064	22	14.3 pN	18.7 pN	316 mPa s	0.85 V

6.3.1 Simulation Test

The structure is first simulated in ANSYS HFSS, as shown in Fig. 6.3, to verify the proper signal processing operation with ideal and controlled data. Three cases are simulated: the pool filled with LC in ON and OFF states, and air-filled used as reference.

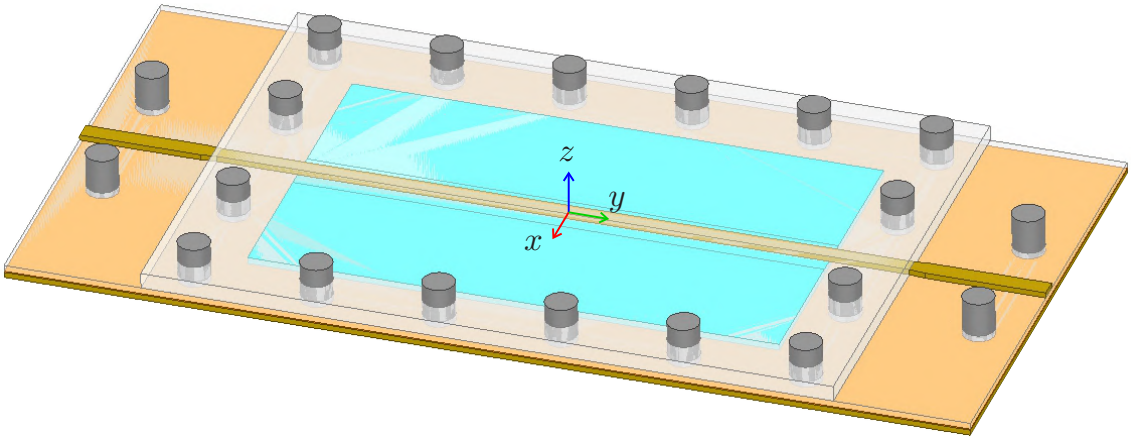

Figure 6.3: Proposed LC-filled microstrip transmission line prototype in HFSS.

The whole pool, entirely filled with LC, is assumed to offer the permittivity $\varepsilon_{r_\perp}$ in the electric field main direction for the OFF state. In the ON state, however, the LC will not be homogeneously polarized for two main reasons. First, under electric field biasing, the LC molecules orient differently along the LC layer height, with a behavior modeled by the differential equations governing the nematic liquid crystals physics [112, 113]. This effect translates into an average LC molecules tilt angle θ_m, with respect to the OFF state, lower than 90°. Then, the LC permittivity tensor can be calculated in the chosen coordinates system and biasing field direction as

$$\overline{\overline{\varepsilon_r}} = \begin{pmatrix} \varepsilon_\perp + \Delta\varepsilon_r \cos^2\theta_m & 0 & \Delta\varepsilon_r \cos\theta_m \sin\theta_m \\ 0 & \varepsilon_\perp & 0 \\ \Delta\varepsilon_r \cos\theta_m \sin\theta_m & 0 & \varepsilon_\perp + \Delta\varepsilon_r \sin^2\theta_m \end{pmatrix}, \tag{6.9}$$

where $\Delta\varepsilon_r = \varepsilon_{r_\parallel} - \varepsilon_{r_\perp}$. Nevertheless, θ_m can be calculated following the approach in [90, Section II]: by solving an integral equation, the LC molecules orientation along the layer thickness can be obtained, which is represented in Fig. 6.4 for two different biasing voltages, $20\,\mathrm{V_{pp}}$ and $100\,\mathrm{V_{pp}}$, anticipating those used in experiments. Then, θ_m is the average of those functions, which results in approximately 82° and 88° for each biasing case, respectively. Thus, it can be concluded that for sufficiently high biasing voltages, $\theta_m \approx 90°$, allowing this effect to be neglected in simulations.

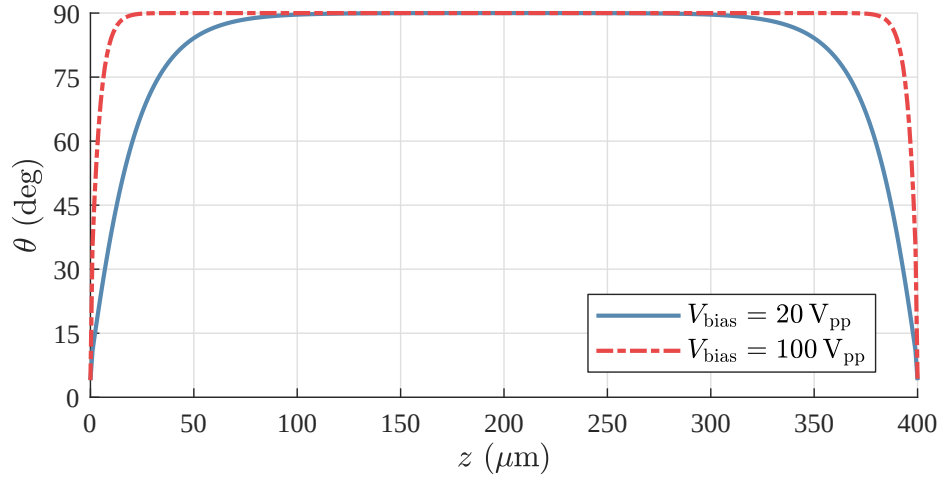

Figure 6.4: LC molecules orientation along the layer thickness for two biasing voltages.

The second cause for inhomogeneity comes from the bias voltage being applied to the microstrip itself, thus only fully polarizing the LC immediately below it and partially polarizing the LC beyond the microstrip width. Hence, as the microstrip width is not much greater than the pool height, the fringing fields' contribution to the effective permittivity should be considered [91]. Thus, the ON state is simulated by stratifying the pool media, where the LC below the line presents a permittivity tensor given by (6.9) with $\theta_m = 90°$, the LC alongside the microstrip (with a width equal to the microstrip width on each side) has $\theta_m = 45°$ and the rest is assumed not polarized at all, just as schematically shown in Fig. 6.1a. From simulations and bibliography, this scenario was chosen as a good estimation.

The S-parameters obtained from the simulations for the LC-filled pool cases are presented in Fig. 6.5 with dotted lines, where a good matching and a linear transmission phase variation are appreciated, as expected. These are transformed to the time domain after applying a Hamming window to improve visualization, and the resulting S_{11} and S_{21} time responses are represented in Fig. 6.6 with dotted lines. The first reflection peak, where the three responses begin to differ, indicates the timestamp when the pool section starts $t_{\mathrm{start}}^{(11)} = 133\,\mathrm{ps}$ (represented with a black dashed vertical line). The structure delay for each case is obtained as the timestamp of the main transmis-

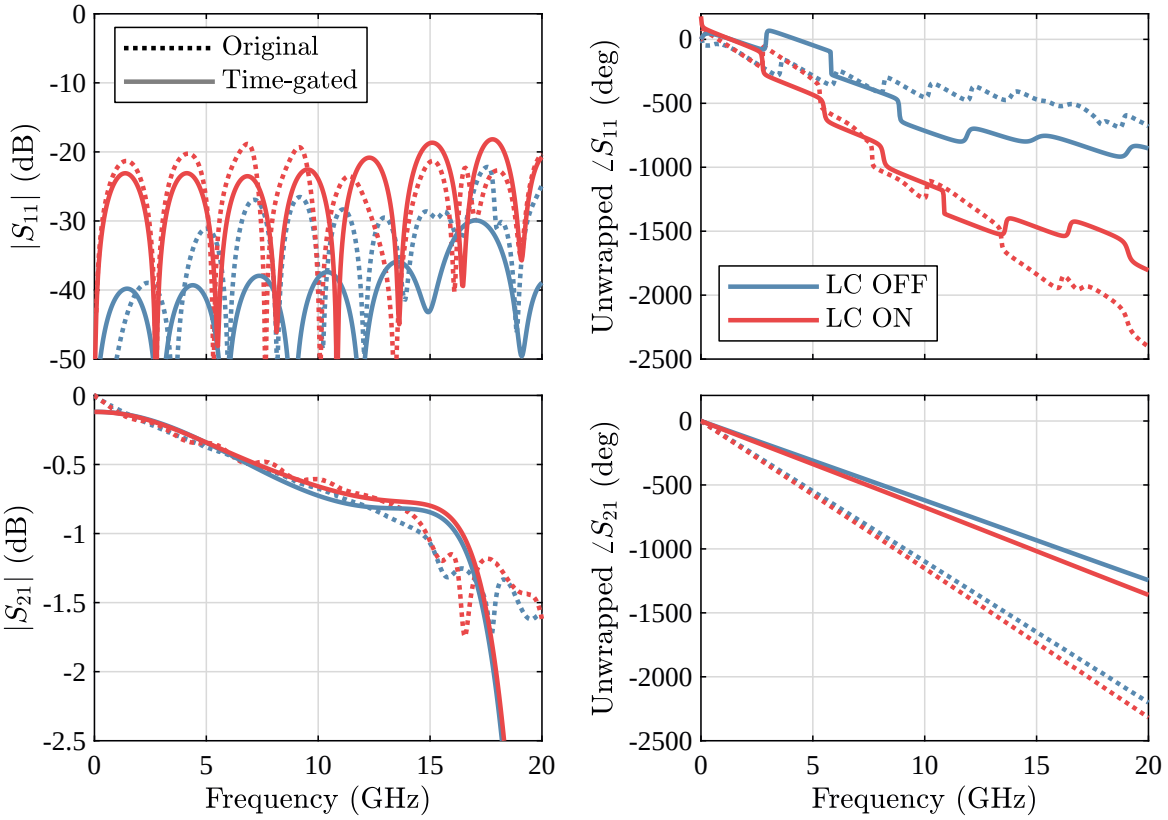

Figure 6.5: Original and time-gated simulated S-parameters for the ON and OFF LC states.

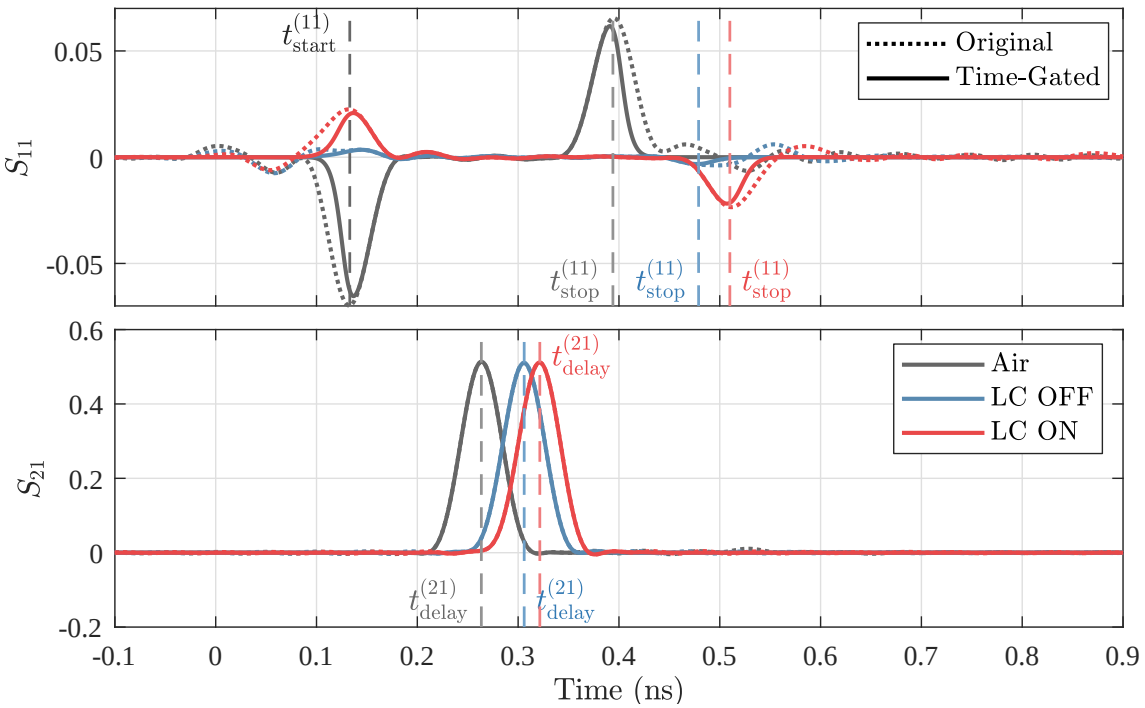

Figure 6.6: Widened impulse responses of the simulated S_{11} (up) and S_{21} (down) before and after the time-gating, and with their timestamps.

sion peak. Then, as explained in Subsection 6.2.1, due to the structural symmetry, the timestamps when the pool ends $t_{\text{stop}}^{(11)}$ are automatically obtained for each case (represented with vertical dashed lines colored as their corresponding response), coinciding with the reflection peaks at the exit of the pool section, which is electrically longer as the filling substrate permittivity increases.

Note that the 20 GHz simulated bandwidth would give a time resolution of $dt = 25$ ps, too coarse for the proper determination of the time-gating timestamps in such a small device. Consequently, an IFFT zero-padding order of $n_z = 50$ was used, thus giving a smaller step $dt = 0.5$ ps. From tests with the studied configuration, steps of dt in the $t_{\text{start}}^{(11)}$ value produce variations less than ± 0.02 in the obtained pool-section ε_{eff}.

The time responses are time-gated using the obtained timestamps, resulting in the solid lines in Fig. 6.6. $t_{\text{start}}^{(11)}$ becomes the new time origin for the reflection response, the transmission one is shifted following (6.5), and the responses are transformed back to the frequency domain, resulting in the time-gated S-parameters represented in Fig. 6.5 with solid lines, from which the processing described in Subsection 6.2.2 is carried out. The obtained permittivities are shown in Fig. 6.7, from the complete DUT to the extracted pool-media ones. In addition, the effective permittivity of the pool section alone has also been simulated, and it is in excellent agreement with the one obtained from the time-gated parameters, thus validating the time-gating approach.

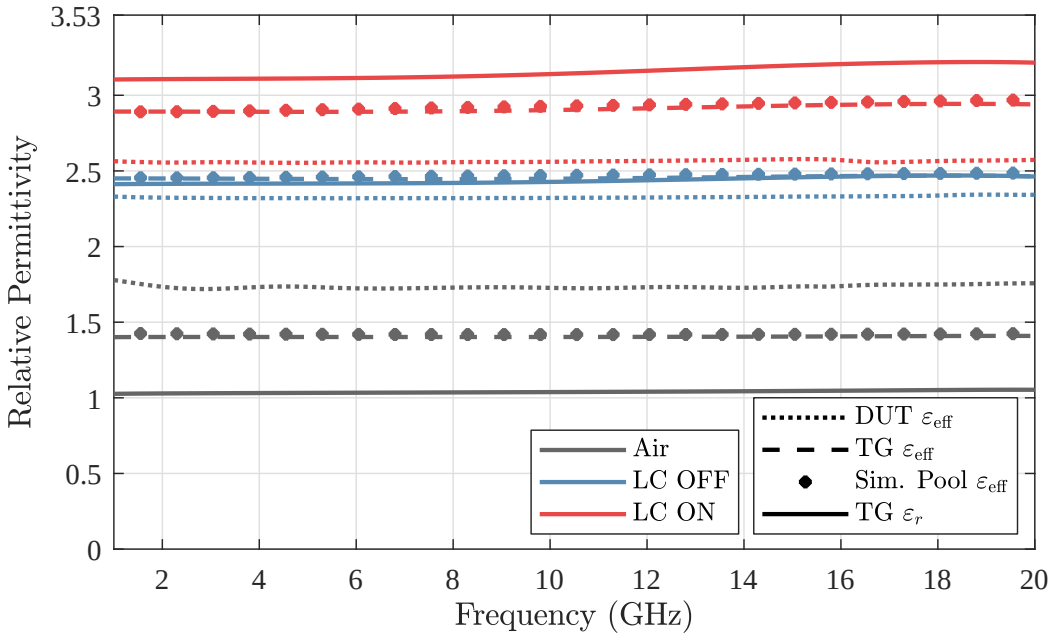

Figure 6.7: Relative permittivities obtained from the processed simulations for different pool substrate scenarios.

The reference air-filled case gives a ε_r close to 1, thus confirming the proper selection of the time-gating timestamps. It can be noted that the OFF-state LC ε_r is practically

equal to $\varepsilon_{r_\perp}$, while for the ON state, the LC permittivity that the microstrip "perceives" is lower than $\varepsilon_{r_\parallel}$ (which is the plot ordinate higher limit) due to the LC anisotropy and the stratified media configuration, which prevents the full polarization of the whole LC filling the pool. These results will serve as a reference for the real experiments.

The choice of the particular frequency window applied before the IFFT must take into account that, although higher time-domain sidelobe suppression may facilitate the main widened deltas recognition, they also significantly suppress higher frequencies, which degrades the permittivity extraction accuracy in that range. This effect is shown in Fig. 6.8 for different applied frequency windows, from where it is clear that the majority of the bandwidth remains unaffected. After correct timestamp determination, the frequency window offering less distortion in the band edge should be used. Moreover, the time window itself mainly distorts the lowest frequencies, so the results are always shown from 1 GHz onward, except in Fig. 6.8 for illustrating the explained artifacts. This should not be an issue for reconfigurable devices designed for microwave frequencies.

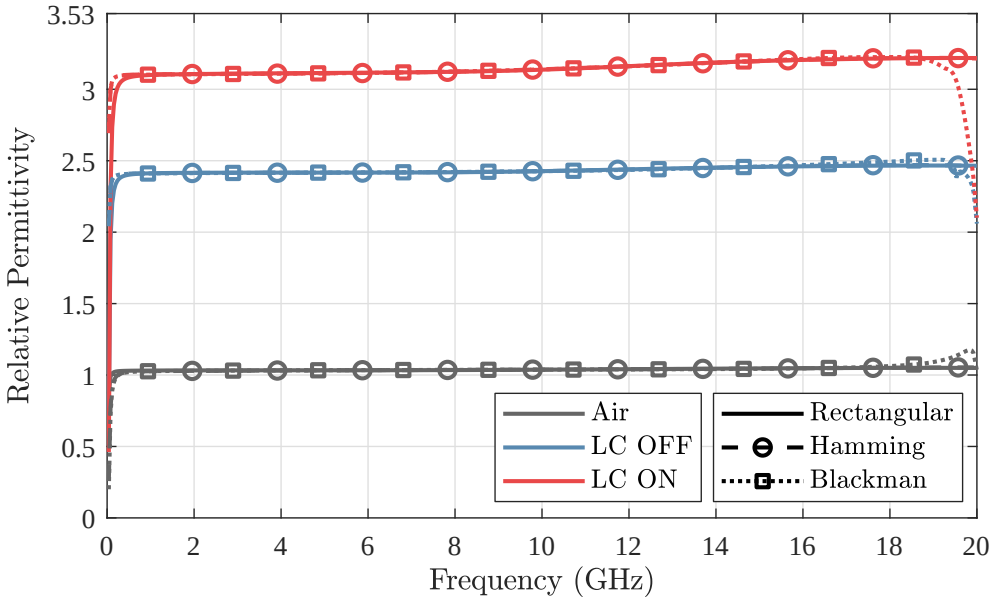

Figure 6.8: Comparison of simulation extracted ε_r for different applied frequency windows.

6.3.2 Experimental Results

The fabricated prototype is shown in Fig. 6.2b. Southwest 2.4 mm end launch connectors are used, whose contribution will also be removed through time-gating. Port 1 of the prototype is connected to a bias T, where the 1 kHz sinusoidal bias signal is input, and port 2 is connected to a DC block. The measurements are carried out with a

Keysight PNA-X N5247A network analyzer configured with a frequency sweep of 6401 points from 10 MHz to 20 GHz. The bandwidth of the intermediate frequency (IF) bandpass filter is set at 10 kHz, whereas the port power is −5 dBm.

As in Subsection 6.3.1, the S-parameters are measured for the same three pool-media cases (air, LC OFF, and LC ON). In addition, for the LC ON state, two biasing voltages are tested, 20 V_{pp} and 100 V_{pp}, and the measurements are presented in Fig. 6.9 as dotted lines, which are saved upon stabilization of the S_{21} phase. Worse matching and greater losses concerning simulations are appreciated, which can be attributed to manufacturing imperfections, the applied epoxy, and the connectors. The time responses obtained from applying the same processing as in the previous section are shown in Fig. 6.10. In this case, it may not be so evident which $t_{start}^{(11)}$ value should be selected, as the responses are expectably not as clean as in simulations. Thus, the air-filled pool case is advantageous to undergo a final calibration, ensuring its extracted relative permittivity is consistently close to 1 along the bandwidth. This is achieved by choosing $t_{start}^{(11)} = 235$ ps, higher than in simulations due to the connectors contribution.

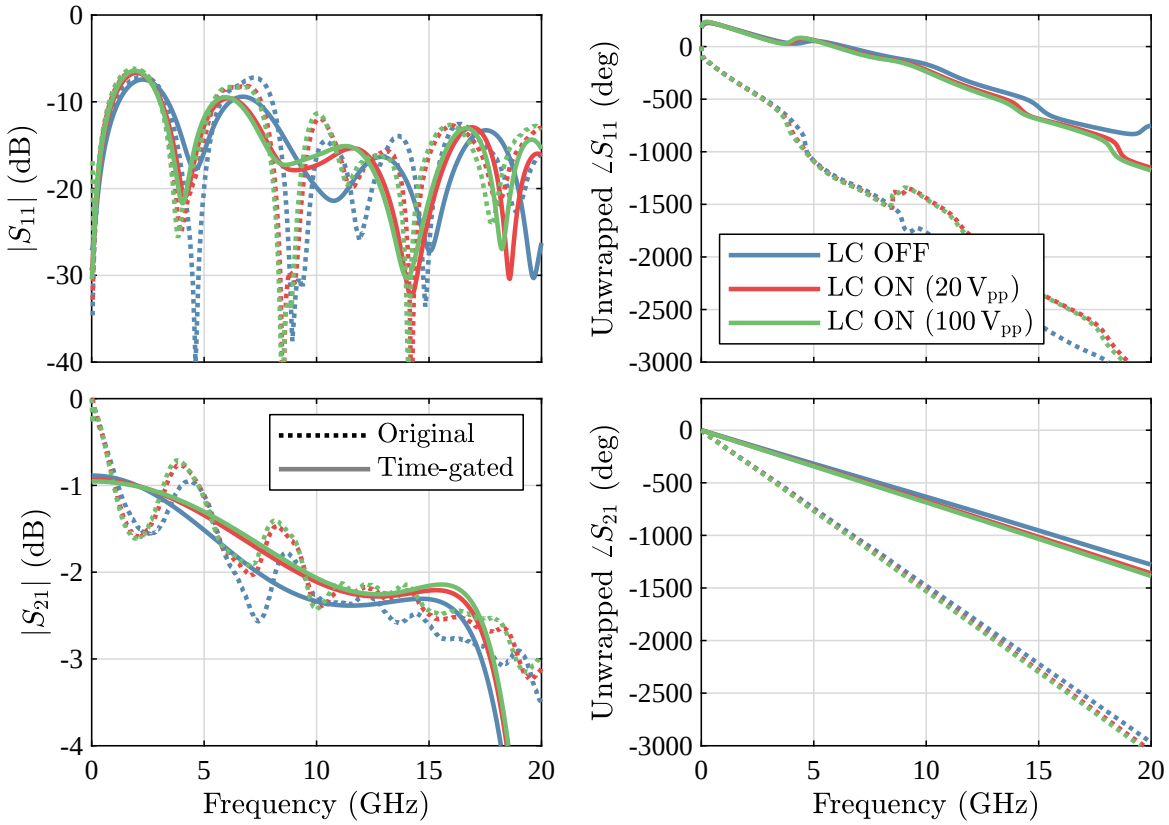

Figure 6.9: Original and time-gated measured S-parameters for the ON and OFF LC states.

The time-gated S-parameters are shown as solid lines in Fig. 6.9. Note that although a quantitative assessment of the LC $\tan\delta$ can not be carried out, the material

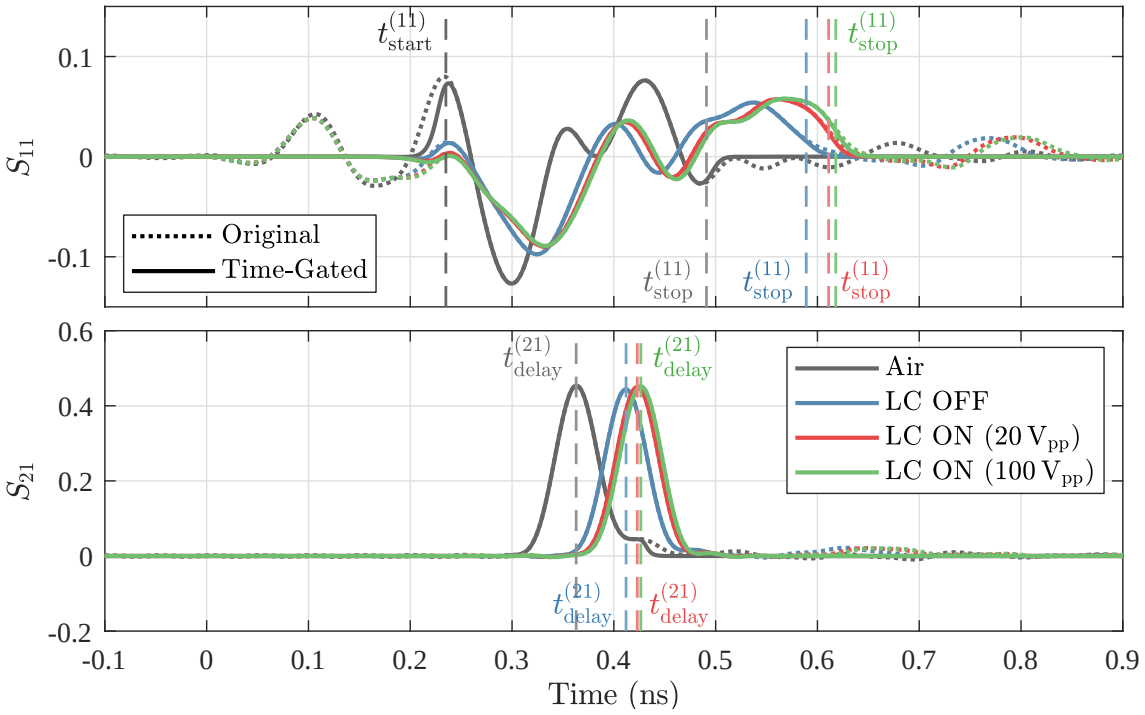

Figure 6.10: Widened impulse responses of the measured S_{11} (up) and S_{21} (down) before and after the time-gating, and with their timestamps.

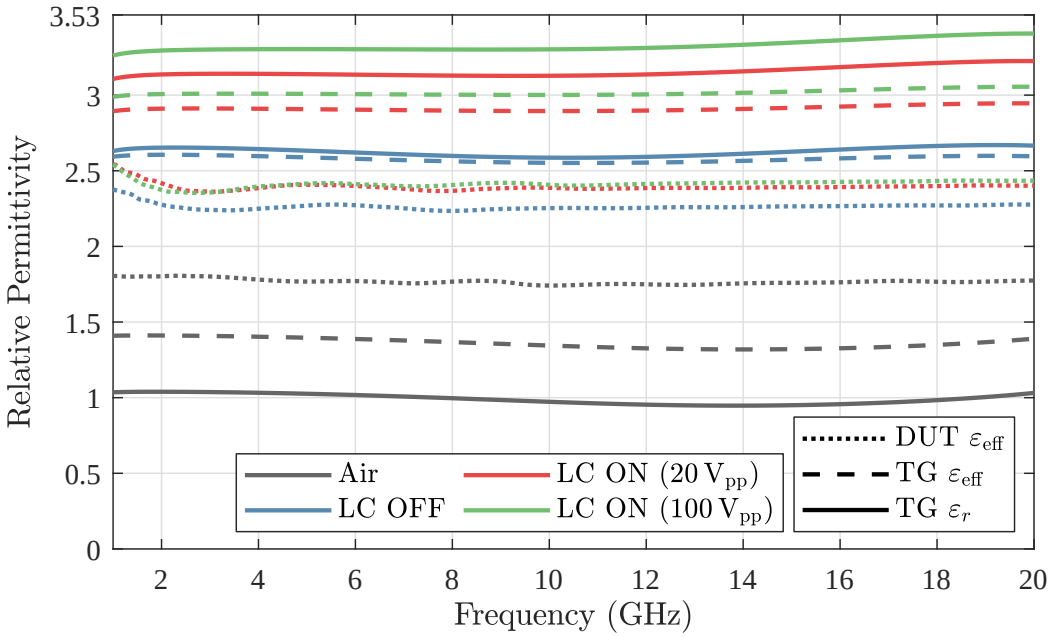

Figure 6.11: Effective and relative permittivities obtained from the original and time-gated measurements for different pool substrate scenarios.

is qualitatively behaving as expected, offering lower losses as it is increasingly polarized. Fig. 6.11 present the permittivity values extracted from these parameters. It is observed how the time-gating, and then the multilayered model, effectively transform the permittivity values from those of the whole structure to the pool media ones. The results, although not as ideal, are considerably similar to those from simulations in Fig. 6.7. The fact that the OFF state presents a $\varepsilon_{r_\parallel} > \varepsilon_{r_{\text{OFF}}} > \varepsilon_{r_\perp}$ is mainly due to the high pool thickness, which prevents the rubbed kapton layer from correctly orienting the LC molecules that are far from it, thus realizing an intermediate permittivity given by a $\theta_m > 0°$. For the ON state, the higher values obtained for the $100\,\text{V}_{\text{pp}}$ bias signal indicate that the $20\,\text{V}_{\text{pp}}$ bias was insufficient to polarize the LC fully. Furthermore, the achieved permittivity value is very similar to the simulation one (taking into account fabrication tolerances) and, hence, less than $\varepsilon_{r_\parallel}$, due to the inhomogeneous LC polarization by the narrow microstrip. In any case, these results show the achievable ε_r values for this physical configuration.

The results could be different if another type of geometry (for example, other transmission lines, substrate height, or microstrip width) were used, a problem arising from the anisotropic physical properties of the LCs. However, the aim of this work has been focused on extracting the achievable permittivities for any specific structure considered as a transmission line, which can significantly facilitate the work of researchers to know the effective range of variation of the relative permittivity of LCs when designing reconfigurable devices. For instance, if a leaky-wave antenna based on a periodically-loaded microstrip line is built, this experiment is of direct utility to have a model for the LC permittivity and be able to design the reconfigurability range of its beam directions.

Finally, Fig. 6.12 shows the LC permittivity's time evolution for both polarization voltages, obtained with a PNA-X script that periodically saves measurements while the LC is being polarized. A higher bias voltage achieves not only a greater permittivity but also a faster polarization response (10%–90% response time of 68 sec for $20\,\text{V}_{\text{pp}}$ and less than 3 sec for $100\,\text{V}_{\text{pp}}$), as is the expected behavior for the characteristics of this GT7-29001 LC (see Table 6.1). The return to the OFF state has a similar evolution in both cases, with a response time around 350 sec. These values are in close agreement with the theoretical expressions from [89].

6.4 Conclusions

In this chapter, an efficient method for characterizing the dielectric permittivity of nematic liquid crystals in broadband has been presented, contributing to the advancement of reconfigurable devices for microwave and millimeter-wave applications. The

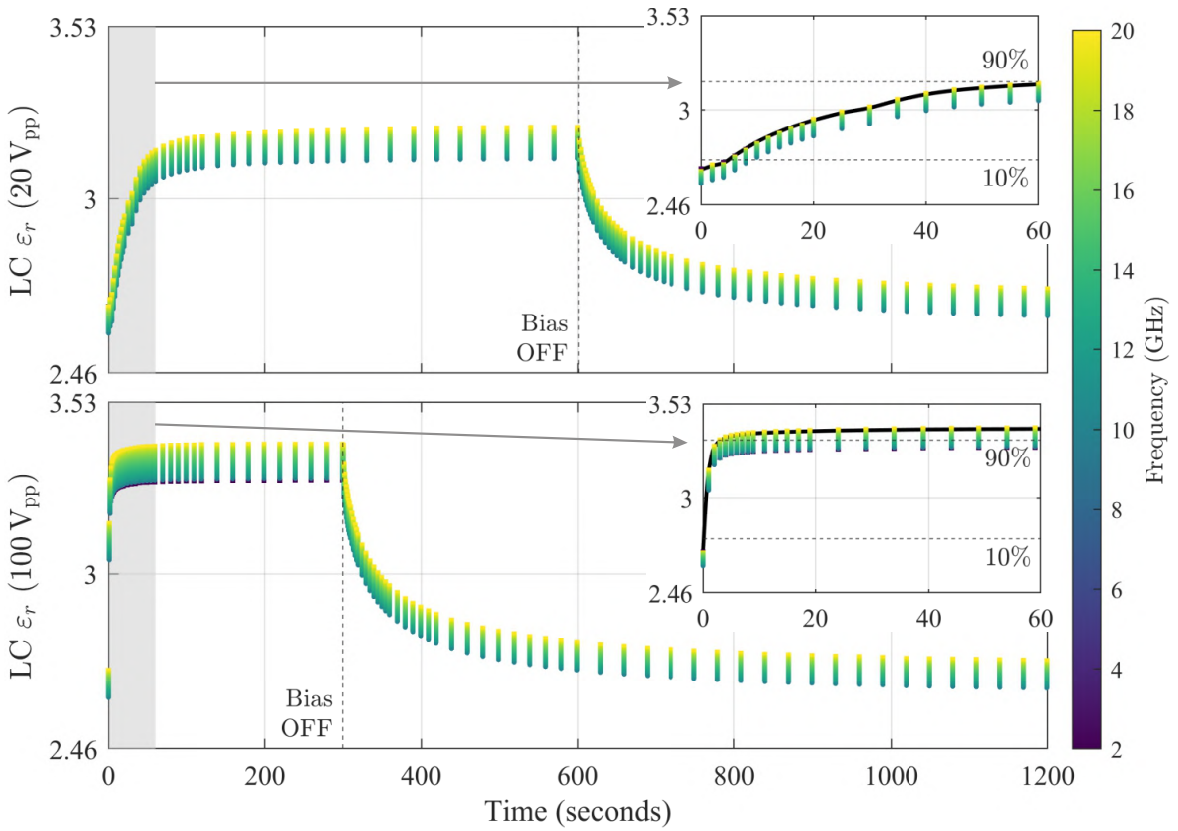

Figure 6.12: Temporal change in the calculated permittivity of the LC from OFF to ON states and vice-versa for 20 V_{pp} (top) and 100 V_{pp} (bottom) bias voltages.

approach uses additive manufacturing technology to fabricate a microstrip line that accommodates liquid crystals, making it easy to polarize and achieve a dynamic modulation of its permittivity. Using additive manufacturing and eliminating the need for in-fixture calibration, such as through-reflect-line (TRL), in favor of time-gating offer a practical and effective approach for efficiently characterizing LC-based reconfigurable devices. The validity of this method has been assessed through a comprehensive evaluation involving a combination of simulations and experimental measurements. The results are reliable, demonstrating the accuracy of the proposed technique, which is more straightforward than others found in the state of the art.

Chapter 7

Conclusions and Outlook

This final chapter summarizes the research work developed in this thesis and highlights the main contributions. Lastly, it points out different perspectives of future work to carry on from this research.

7.1 Summary and Conclusions

Several metasurface-based leaky-wave antennas have been comprehensibly studied in this Ph.D. thesis. They are supported by PPW configurations and offer aperture field distribution control to different extents. Depending on the particular configuration, their radiating properties can be conveniently selected in terms of main radiation direction, directivity level and radiation pattern shape, while potentially improving the aperture efficiency and bandwidth, and allowing multiple design degrees of freedom.

Starting with FPCAs, they offer a simplified analysis with straightforward design expressions. The combination of the approximate ray-optics approach with classical leaky-wave theory has enabled the engineering of the PRS frequency response. Hence, although only broadside (or conical) radiation can be achieved with this methodology, it succeeds in improving both aperture efficiency and bandwidth, respectively through spatial modulation and a positive-slope phase technique for the PRS reflection producing a local non-Foster behavior. Additionally, excitation limitations and considerations have been addressed, showing the increasing matching difficulty as directivity increases for this type of antennas. Moreover, as the spatial modulation allows the control of the aperture field distribution, the radiation pattern can be shaped for different desired characteristics. This has been verified through the fabrication of three distinct prototypes, whose measurements show strong agreement with simulations, confirming the desired properties and achieving directivity-bandwidth products higher than those

achievable from homogeneous designs.

Subsequently, a step forward in complexity has been taken by introducing bianisotropic Huygens' metasurfaces in the LWA design. By using a BHMS as the top plate of a 1-D leaky PPW configuration, increased design flexibility is achieved. In particular, the arbitrary wavefront transformations offered by these metasurfaces, for which a rigorous field analysis is required, enables the independent selection of several radiation characteristics. In this sense, complete aperture field distribution control has been achieved by rigorously addressing the wave equation when the wavenumbers are variable, and employing a slowly varying amplitude approximation to enable a simplified design methodology where the phase constant and a modulated leakage factor can be independently chosen. As the BHMS is not physically periodic when the leakage factor is modulated, an efficient unit-cell synthesis procedure is necessary to avoid computationally-intensive parametric simulations. Hence, a semi-analytical algorithm has been used to obtain the unit-cell dimensions without further full-wave optimization. Several designs have been carried out to verify the concept and the configuration capabilities, showing strong agreement with the theoretical predictions. Furthermore, different metasurface prototypes have been fabricated, which can be mounted in the same manufactured coaxial-fed rectangular waveguide, equivalent to the theoretical x-invariant PPW configuration. Measurements in an anechoic chamber have confirmed the expected behaviors, although with a frequency shift that can be attributed to several manufacturing tolerances.

In connection to the previous field analysis, insight has also been gained on the limitations of the general leakage factor formula for modulated 1-D LWAs. In particular, as the usual separation relation cannot be rigorously used when the guided mode wavenumbers are varied along the antenna, the considerations that must be made for the well-known leakage factor formula to hold have been derived for the studied scenario. In addition, and in connection with the metasurface microscopic design, the high complexity in the use of five-layer unit cells led to a specific study on the capabilities of much simpler two-layer unit cells for implementing the required BHMSs. Though simplified and idealized, the transmission line model revealed that it is theoretically possible to use these simple unit-cell configurations to design 1-D BHMS-based LWAs with some limitations in the achievable leakage factor and without relying on near-field coupling as an additional degree of freedom. However, careful attention must taken with the losses of the unit-cell layers, as they rapidly shrink the available solution space.

The insights from both previous works have led to the combination of ideas in a 2-D BHMS-based LWA. The resulting structure is similar to the studied FPCAs, but the PRS is replaced by a more versatile BHMS. Although both are metasurfaces in essence, they differ in their underlying design methodologies, thus the latter can be

seen as an evolution of the former. This way, the previously studied 1-D BHMS-based LWA configuration is extended for an additional dimension, increasing the complexity of the analysis, which has led to an extensive study on the modal properties of the radial PPW guided fields. By rigorously stipulating the same guided modes that exist in a FPCA, deeper insight has been gained about their modal behavior. But, more importantly, the obtained field is practically contained in the same direction across the aperture, which enables linearly-polarized pencil beams toward arbitrary directions. This concept also requires proper control over the aperture field magnitude and phase, though conveniently cross-polarization requirements for the unit cells have been avoided by making some reasonable assumptions in the theoretical derivation. Thus, a design methodology has been achieved that is straightforward, comprehensive and does not rely on numerical optimization. Some designs have been carried out with idealized unit cells, showcasing different radiation capabilities. Good agreement between theory and simulation has been found, which demonstrates the potential of the presented concept.

The previous antenna configurations offer a flexible selection of the design characteristics. Furthermore, they allow for the use of the same manufactured PPW platform to obtain different radiation properties by simply changing the metasurface. However, if dynamic reconfiguration is desired with the same metasurface, it becomes clear the need for some reconfigurability mechanism. It is in this context that, as a final work in this thesis, LCs have been experimentally characterized in a common microwave device configuration. For that purpose, the LC has been used as substrate of an additive-manufactured microstrip, which is, in turn, responsible for its biasing. A time-gating approach has been used to treat the measurement results, which has proven to be an effective approach, avoiding the need for more than one prototype and for any in-fixture calibration. The experimental results agree with simulations, and they allow to effectively know the practical permittivity ranges in real microwave devices, which will serve as an useful guide for designing reconfigurable antennas in the future.

7.2 Original Contributions

While the bandwidth enhancement technique in FPCAs and the spatial modulation in general LWAs are well-established within the antenna research community, the systematic integration of both approaches had not been sufficiently addressed in the existing literature. Here lies the first main contribution: a methodology combining both ray-optics and leaky-wave theory to significantly improve the directivity-bandwidth product of these antennas (or, alternatively, to shape their radiation patterns), while requiring only a single, both-side-etched laminate PRS. Furthermore, the in-depth investigation of the proper excitation of the cavity modes is also relevant, regarding the

fundamental limitations related to the maximum achievable directivity and impedance matching capability.

Another major contribution is the successful verification of the full aperture field control in the presented 1-D BHMS-based LWAs, overcoming limitations in [6]. The theoretical advancements introduced here have enabled the inclusion of a variable leakage factor while preserving the rigorous analytical framework. This eliminates the need for any optimization during both the design and simulation phases, in contrast to other approaches reported in the literature. As a result, the work in this thesis has enabled radiation pattern shaping capabilities for this antenna configuration. The rigorous field analysis has also shed more light into the limitations of the leakage factor formula that is commonly used in tapered LWA designs.

In addition, the application of the semi-analytical unit-cell synthesis algorithm to the realization of BHMSs for LWAs is also noteworthy, as this method had previously only been employed in open-space, incident plane-wave scenarios. The successful performance of these unit cells has facilitated the efficient implementation of the designed BHMSs, a task that would have been significantly more challenging without the use of accurate, near-field-aware circuit models. In contrast, the study on two-layer unit-cells to facilitate the implementation has helped understanding the possibilities of this limited meta-atom configuration to realized BHMS-based LWAs.

Another significant contribution of this thesis is the development of 2-D BHMS-based LWAs within a PPW platform, which had not been found before in the literature. It is noteworthy that this configuration allows for linearly-polarized beam steering in a complete half-space with a single metasurface not requiring chiral properties. Furthermore, the analysis is also completely analytical, without relying on numerical optimization for the field stipulation, in contrast to other reported methodologies. The versatile selection of several design parameters as degrees of freedom that offers the presented methodology, moreover, allows some of the aforementioned FPCA limitations to be overcome. As the BHMS is now responsible for implementing the desired field transformation without being limited by the guided modes behavior, it notably eliminates the need for satisfying the splitting condition and avoids operation near cut-off, thus representing another clear advantage over conventional FPCA configurations.

Finally, the proposed LC characterization technique, while sufficiently accurate, has proven to be more straightforward than others found in the literature, particularly in technical environments lacking specialized equipment for characterizing liquid materials. In contrast to most existing methods, it is also particularly relevant that the time-gating approach adopted here requires only a single prototype, thereby reducing potential repeatability issues associated with additive manufacturing.

7.3 Future Work

The following ideas outline several potential directions for extending the research presented in this dissertation:

- **Refine 2-D LWA field stipulation**

  As discussed in Chapter 5, the beam tilting capabilities of the 2-D BHMS-based LWAs exhibited performance degradation when the desired azimuthal direction was close to $\phi = 0°$. Although this may be caused by the theoretical assumptions, these discrepancies call for a more detailed investigation to identify their underlying cause. As an initial step in this analysis, the actual guided modes excited by the used source should be numerically determined through a proper mode expansion of the source-generated fields. This analysis may lead to a refinement of the field stipulation, potentially addressing the observed performance issues.

- **Allow for variable leakage factors in 2-D BHMS-based LWAs**

  While the 1-D BHMS-based LWA configuration now allows for the variation of the leakage factor, the field stipulation in the 2-D configuration has, thus far, been restricted to constant α values. A logical progression of this work would involve extending the theoretical framework to accommodate spatially varying leakage factors across the aperture. As with conventional FPCAs, this would enable radiation pattern shaping and improve both aperture and illumination efficiencies.

- **Try alternative radially-symmetric field stipulation**

  The previous idea may be challenged by the co-existence of two guided modes, each exhibiting slightly different characteristics and, consequently, distinct leakage behaviors. To simplify the engineering of the dispersion properties, an alternative and potentially advantageous strategy would be to employ a different field stipulation in the 2-D LWA, based on a single radially-symmetric mode. This, however, would require accounting for electromagnetic field components in both orthogonal directions tangential to the BHMS, potentially requiring polarization conversion capabilities. Investigating the trade-offs associated with this possible field stipulation and identifying the achievable radiation characteristics would be a valuable direction for future work.

- **Improve simulation efficiency for 2-D metasurfaces**

  Electromagnetic simulation of metasurfaces presents significant challenges related to computational time, memory consumption, and convergence reliability. These issues were not critical in the case of 1-D LWAs, due to their limited thickness

and reduced simulation domain, which allowed accurate results to be obtained in HFSS within a few hours even with realistic unit cells. However, the quadratic increase in computational domain size for 2-D metasurfaces—presenting a large number of subwavelength elements—entails a substantial burden on general-purpose solvers, often hindering convergence. Hence, an immediate next step involves exploring strategies to make simulations more efficient, including the use of alternative simulators, either commercial tools or custom in-house implementation tailored to the specific characteristics of these structures.

- **Implementation of LC-based reconfigurability in LWAs**

  The desired dynamic beam steering capabilities requires the incorporation of some reconfiguration mechanism. Taking advantage of the characterized LC materials, it would be interesting to include them into the studied LWA configurations. As introducing LC inside the metasurfaces would be very challenging, a sensible approach would be partially filling the PPW with the liquid. This approach is already being preliminarily studied in the research group, and further investigation is required to integrate these materials effectively without significantly impacting losses or fabrication complexity.

- **Incorporation of reconfigurable mechanisms in unit-cell design**

  Another approach to enabling reconfiguration in the studied antennas is to integrate tuning mechanisms directly into the unit-cell design, as proposed in various works in the literature. The studied two-layer unit-cell configuration offers a clear advantage in this context, as it supports reduced implementation complexity. Minimizing the number of tunable elements per unit cell would also be essential to simplify control and fabrication. The choice of tuning components, such as varactors, must be made carefully to ensure minimal losses in order not to severely constrain the achievable local S parameters, as has already been observed theoretically.

- **Use of multimodal techniques for modeling of arbitrary unit cells**

  Regarding the previous point, circuit models that accurately account for near-field coupling effects—as the one used in Chapter 4, but generalized to arbitrary geometries—may aid in the synthesis process. For this purpose, multimodal techniques such as [114] could be employed.

Appendix A

On the General 1-D LWA Leakage Factor Formula

To the authors' knowledge, R. Honey was the first to present in [14] the closed expression (2.8) to calculate the required leakage factor that a 1-D LWA must present to synthesize a given aperture field distribution $A(y)$, repeated below for convenience:

$$\alpha_y(y) = \frac{1}{2} \frac{|A(y)|^2}{\frac{1}{\eta_{\text{rad}}} \int_0^L |A(\tau)|^2 \, d\tau - \int_0^y |A(\tau)|^2 \, d\tau} \,. \tag{A.1}$$

This expression is still widely used nowadays in the design of LWAs, due to its simplicity and usefulness. It is obtained from a qualitative understanding of how the power varies along the guiding structure, as described in Subsection 2.1.1. Particularly, (A.1) assumes that the variation in power only depends on the function $\alpha_y(y)$, as described by (2.7). However, when the rectangular waveguide was rigorously analyzed in Chapter 4, a general expression for the power density flowing through the leaky surface (4.4a) was obtained (repeated here for convenience):

$$P_z(y) = -\frac{|E_{\text{in}}|^2}{k\eta} \big(\beta_z(y) \sinh(2\alpha_z(y)d) - \alpha_z(y) \sin(2\beta_z(y)d)\big) \, e^{-2\int_0^y \alpha_y(\tau)\, d\tau} \,. \tag{A.2}$$

This power density is proportional to the aperture power distribution $|A(y)|^2$. However, it can be noted that it does not depend only on the leakage factor $\alpha_y(y)$, but also on the transverse dispersion characteristics. Hence, it seems to be an inconsistency with how the leakage factor is usually obtained in (A.1).

Qualitatively, the rightmost exponential term in (A.2) represents the remaining available power inside the waveguide at each point, which unavoidably decays along

the propagation direction. On the other hand, the terms related to $\beta_z(y)$ and $\alpha_z(y)$ can be interpreted as how much of the remaining power the mode allows to leak at each position along the antenna length just below the leaky surface. Actually, this term is related to the fact that the proportionality factor relating $P_z(y)$ and $|A(y)|^2$ is not constant when the wavenumbers are variable, as the guided field impedance changes along the leaky surface plane. Hence, the actual electromagnetic modes carrying the power seem to be relevant in the leakage calculation, and thus (A.1) is necessarily an approximation that does not take into account how the transverse power profile changes as α_y is varied, as briefly commented in Section 4.3. In fact, in [7], it is only advised not to choose a very high η_{rad} to avoid obtaining very large values of α_y.

Nevertheless, in Section 4.3 the expression (A.1) was used anyway. Therefore, this Appendix explores why this expression worked in that case, and under which circumstances does it hold in the studied scenario, i.e. a leaky rectangular waveguide with a single propagating TE mode. It can be noted that this scenario is sufficiently general, and not specific for metasurface-based applications, as it only assumes that the electric field must vanish at $z = -d$. In fact, the considered guided field expressions (4.1) can be particularized for $d = \pi/\beta_z$ with the wavenumbers constant, obtaining the TE_{10} mode of a classical waveguide.

A.1 From the Rigorous to the Approximate Formula

In Section 4.2, the well-known dispersion relation

$$k_0^2 \approx k_y^2(y) + k_z^2(y) \tag{A.3}$$

was found to only strictly hold when the wavenumbers are constant, and that it is a good approximation in a scenario where β_y is constant and α_y varies slowly. Although there exist tapered LWA designs in which β_y is varied along the aperture (see, e.g. [115]), the previous assumptions are usually valid for most LWA design cases, where the leakage factor also typically tends to be small. Thus, hereinafter, β_y is assumed constant in the following analysis.

By employing the wavenumbers definition (4.3a) in the dispersion relation (A.3), and equaling the imaginary parts, the following relation can be obtained:

$$\beta_z(y)\,\alpha_z(y) = -\beta_y\,\alpha_y(y)\,. \tag{A.4}$$

Expression (A.2) can be expanded, by employing (A.4), as

$$P_z(y) = \frac{|E_{\text{in}}|^2}{k\eta}\left[\frac{\beta_y\alpha_y(y)}{\alpha_z(y)}\sinh(2\alpha_z(y)d) - \frac{\beta_y\alpha_y(y)}{\beta_z(y)}\sin(2\beta_z(y)d)\right] e^{-2\int_0^y \alpha_y(\tau)\,d\tau}\,. \quad \text{(A.5)}$$

Then, if it is assumed that $|2\alpha_z(y)d| \ll 1$ and that the transverse field profile suffers almost no change ($\beta_z(y) \approx \beta_z(0)$), the power density expression (A.5) can be approximated as

$$P_z(y) \approx \frac{|E_{\text{in}}|^2}{k\eta}\beta_y\left[2d - \frac{\sin(2\beta_z(0)d)}{\beta_z(0)}\right]\alpha_y(y)\, e^{-2\int_0^y \alpha_y(\tau)\,d\tau}\,. \quad \text{(A.6)}$$

This way, (A.6) only varies due to $\alpha_y(y)$, with the rest of the values constant, and it can be simplified even more if a TE_{10}-like mode is considered[1]. In order to obtain the time-averaged power density inside the waveguide at each longitudinal point, $P(y)$, conservation of energy is applied. This approach is chosen as it is simpler than calculating the integral along the waveguide height of the power density flowing in the y-direction as $-(1/2)\,\text{Re}\{E_x H_z^*\}$. It is straightforward to notice that the decrease of the power propagating inside the waveguide is due to the power density leaking outside, being the same concept represented in Fig. 2.3. According to the Poynting theorem, this idea mathematically translates into

$$-\frac{\partial P(y)}{\partial y} = P_z(y)\,. \quad \text{(A.8)}$$

Then, substituting (A.6) into (A.8) and integrating along y:

$$P(y) \approx P(0)\, e^{-2\int_0^y \alpha_y(\tau)\,d\tau}\,, \quad \text{(A.9)}$$

with

$$P(0) = \frac{|E_{\text{in}}|^2}{k\eta}\beta_y\left[d - \frac{\sin(2\beta_z(0)d)}{2\beta_z(0)}\right]. \quad \text{(A.10)}$$

Finally, from (A.8) and (A.9), the common differential equation is obtained

$$-\frac{\partial P(y)}{\partial y} \approx 2\alpha_y(y)P(y)\,, \quad \text{(A.11)}$$

identical to (2.6), from which the widely-used leakage factor formula (A.1) can be

[1] In this case, then $\beta_z \approx \pi/d$ and expression (A.6) can be simplified to

$$P_z(y) \approx 2\frac{|E_{\text{in}}|^2}{k\eta}d\beta_y\alpha_y(y)\, e^{-2\int_0^y \alpha_y(\tau)\,d\tau}\,. \quad \text{(A.7)}$$

deduced as explained in Subsection 2.1.1. However, the rigorous approach used to arrive to this expression now allows knowing the necessary approximations for it to work properly, at least in the considered scenario.

A.1.1 Radiation Efficiency Considerations

As explained, the approximation (A.1) relies on the power density expression from (A.9), from which the radiation efficiency (assuming a lossless scenario) can be calculated as usual:

$$\eta_{\text{rad}} = 1 - \frac{P(L)}{P(0)} \approx 1 - e^{-2\int_0^L \alpha_y(\tau)\,d\tau}\,. \tag{A.12}$$

However, this result is necessarily also an approximation that neglects the actual mode-dependent behavior of the leaky power density (A.2) when the leakage factor is modulated. In order to take it into account, equation (A.8) is integrated over the antenna length as

$$\int_0^L P_z(\tau)\,d\tau = P(0) - P(L)\,, \tag{A.13}$$

from which, rearranging, the following expression is obtained

$$\eta_{\text{rad}} = 1 - \frac{P(L)}{P(0)} = \frac{1}{P(0)}\int_0^L P_z(\tau)\,d\tau\,, \tag{A.14}$$

allowing the exact calculation of the radiation efficiency from the effectively leaked power density (A.2). The input power $P(0)$ can be computed from (A.10), or more rigorously as

$$\begin{aligned} P(0) &= \int_{-d}^{0} -\frac{1}{2}\,\text{Re}\{E_x H_z^*\}\big|_{y=0}\,dz \\ &= \frac{|E_{\text{in}}|^2}{k\eta}\beta_y(0)\left[\frac{\sinh(2\alpha_z(0)d)}{2\alpha_z(0)} - \frac{\sin(2\beta_z(0)d)}{2\beta_z(0)}\right]. \end{aligned} \tag{A.15}$$

It can be observed that (A.15) is equivalent to (A.10) when the assumptions from Section A.1 are applied. Lastly, it must be noted that using the rigorous power density function (A.2) in (A.14) under the dispersion relation (A.3) is strictly an approximation when the wavenumbers are variable, and it may lead to physical inconsistencies if its underlying assumptions are not met.

A.2 Approximations Implications

It can be numerically verified that the most limiting approximation made to reach (A.1) is assuming that

$$|2\alpha_z(y)d| \ll 1\,. \tag{A.16}$$

In order to relate this condition to the value of the leakage factor α_y, it is convenient to rearrange the dispersion relation (A.3), with the help of the wavenumbers definition (4.3a), as

$$k_z(y) = \sqrt{(k_0^2 - \beta_y^2 + \alpha_y^2(y)) + j(2\beta_y\alpha_y(y))}\,. \tag{A.17}$$

Also, the principal value of the square root of a complex value is given by

$$\sqrt{a+jb} = \sqrt{\frac{\sqrt{a^2+b^2}+a}{2}} + j\,\mathrm{sgn}(b)\sqrt{\frac{\sqrt{a^2+b^2}-a}{2}}\,, \tag{A.18}$$

where

$$\mathrm{sgn}(b) = \begin{cases} -1 & \text{if } b < 0 \\ +1 & \text{if } b \geq 0\,. \end{cases} \tag{A.19}$$

By comparing expressions (4.3a), (A.17) and (A.18), -$\alpha_z(y)$ can be expressed as the right imaginary term in (A.18) with

$$a = k_0^2 - \beta_y^2 + \alpha_y^2(y)\,, \tag{A.20a}$$

$$b = 2\beta_y\alpha_y(y)\,, \tag{A.20b}$$

where $\mathrm{sgn}(b) = 1$ as β_y and $\alpha_y(y)$ are always positive numbers, thus resulting in

$$\alpha_z(y) = -\sqrt{\frac{1}{2}\left[\sqrt{\left(k_0^2 - \beta_y^2 + \alpha_y^2(y)\right)^2 + \left(2\beta_y\alpha_y(y)\right)^2} - \left(k_0^2 - \beta_y^2 + \alpha_y^2(y)\right)\right]}\,. \tag{A.21}$$

Finally, by inserting (A.21) into inequality (A.16) and rearranging:

$$\alpha_y \ll \sqrt{\frac{k_0^2 - \beta_y^2 + 1/(2d)^2}{4d^2\beta_y^2 - 1}}\,. \tag{A.22}$$

Moreover, relating the phase constant to the angle of incidence θ_{in} inside the waveguide as in (4.15), the values of condition (A.22) can be represented with respect to the waveguide height d for different values of θ_{in}, as shown in Fig. A.1. As a note, when

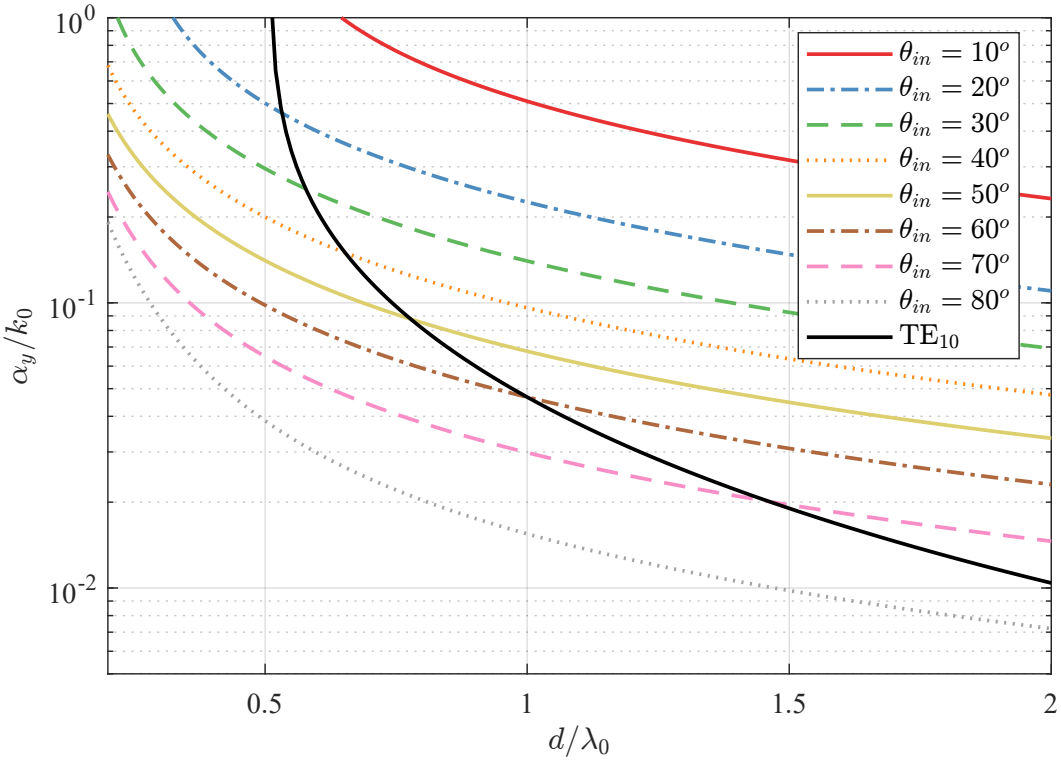

Figure A.1: Maximum leakage factor values, normalized to k_0, from inequality (A.22), for different values of θ_{in} and the particular case for a TE_{10}-like field profile.

$d/\lambda_0 \gg 1/(4\pi)$, as is usually the case, and using (4.15), inequality (A.22) tends to

$$\alpha_y \ll \frac{1}{2d\tan\theta_{\mathrm{in}}}\,, \tag{A.23}$$

which offers greater mathematical and physical intuition. In principle, as seen in Chapter 4, a metasurface could allow any given θ_{in} to be supported inside the waveguide. Thus, it is interesting to note that as the value of θ_{in} increases, the values of α_y that can invalidate (A.1) become lower. Qualitatively, as θ_{in} increases, k_z will be smaller, and it will be more strongly affected by a change in α_y, which will produce a non-negligible change in the vertical field profile, as derived from the field expression (4.1). Higher values of d amplify this effect, as seen in the graph.

In addition, a black line in Fig. A.1 shows the condition for the particular case in which the field profile resembles a TE_{10} mode, for which θ_{in} and d are related as

$$\theta_{\mathbf{in}}^{\mathrm{TE}_{10}} \approx \sin^{-1}\sqrt{1-\left(\frac{\pi}{k_0 d}\right)^2}\,. \tag{A.24}$$

Taking into account that single-mode regime is commonly desired in classical waveguides, then the region of interest is $0.5 < d/k_0 < 1$. There, the most restrictive α_y

value is found in the upper limit, being close to $0.05k_0$, which is already a considerably high leakage factor value. This insight allows for a better understanding of why (A.1) holds for classical LWA designs.

A.3 Design Examples

First of all, it is worth exploring the specific design cases presented in Section 4.5 for the 1-D BHMS-based LWAs. From Table 4.1 it is seen that the designs presented θ_{in} values ranging from 21.5° to 30°, and $d = 0.5\lambda_0$ was chosen for all of them. Moreover, for the different leakage factor functions used and shown in Fig. 4.6, it is noted that only the Uniform window cases reached values of $\alpha_y > 0.1k_0$, and even those aperture cases were below the $0.2k_0$ threshold for almost the entire length of the antenna. Hence, for the chosen antenna parameters, it is clear from Fig. A.1 that those designs presented leakage factors considerably below the threshold given by (A.22). Thus, the functions obtained from the approximate leakage factor expression (A.1) could be confidently trusted. This way, not only simulations from Section 4.6 verified that the designs worked as expected, but now the underlying reason is better understood theoretically.

In any case, it is interesting to examine designs which clearly fail to comply with the threshold condition given by (A.22). Hence, two analytical examples are shown to illustrate how limit cases can challenge the validity of the approximate leakage factor formula (A.1). The chosen radiation angle is $\theta_{\text{out}} = 0°$, the length of the antennas $L = 10\lambda_0$, and $|E_{\text{in}}| = 1$ is assumed. The radiation patterns are numerically computed using the procedure explained in Subsection 2.2.3, by imposing the tangential fields just above the leaky surface to follow the calculated power density $P_z(y)$.

A.3.1 Classical Waveguide with TE_{10}-like Mode

Consider the common study case in which the leaky surface only introduces a small perturbation in the guided mode of a classical closed waveguide. Then, the values of d and θ_{in} are related through expression (A.24). By choosing $d = \lambda_0$ to work at the limit of the single-mode regime, then $\theta_{\text{in}} = 60°$ is obtained. The transformation from this incidence angle to the desired broadside radiation angle could be achieved by means of some periodic modulation of the leaky surface, as seen in Section 2.1. The goal is to obtain, with a very high $\eta_{\text{rad}} = 0.99$, an uniform aperture field distribution $|A(y)| = b$, with b constant, as it is a commonly desired aperture for offering maximum directivity. These design parameters are used in (A.1), obtaining the leakage factor shown in Fig. A.2a with a blue solid line, which increases to compensate for the exponential power decay inside the waveguide, as expected. Inserting this function into the approximate

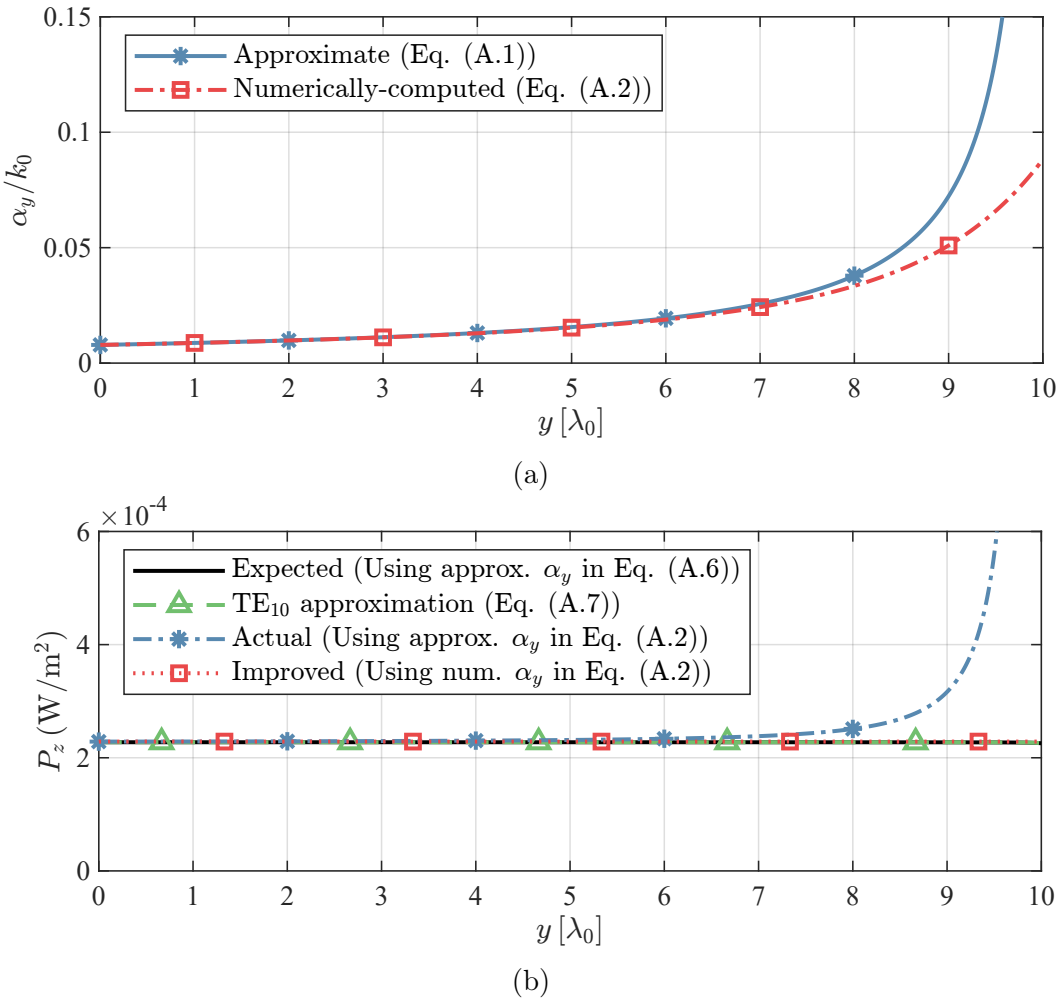

Figure A.2: Comparison of (a) the leakage factor functions and (b) associated aperture power profiles between using the approximate and the mode-aware approaches, for a desired uniform distribution with $\eta_{\mathrm{rad}} = 0.99$, $d = \lambda_0$ and TE_{10}-like field profile.

aperture power density formula (A.6), the expected uniform aperture is obtained, as shown with a black solid line in Fig. A.2b. In addition, as discussed in the previous section, (A.7) would also be a valid approximation (green dashed line) due to the TE_{10}-like mode profile.

However, when the mode-aware aperture power density expression (A.2) is evaluated with the approximate leakage factor, it is seen that the actual aperture distribution (blue dash-dotted line in Fig. A.2b) diverges from the desired one as the value of α_y increases. As known from Fig. A.1, when the value of $0.05k_0$ is surpassed for this case, the divergence is more acute, with the actual P_z being around 140 times the expected from the approximation at the end.

By numerically solving (A.2) for the expected aperture power profile, then the more accurate leakage factor function can be obtained (red dash-dotted line in Fig. A.2a),

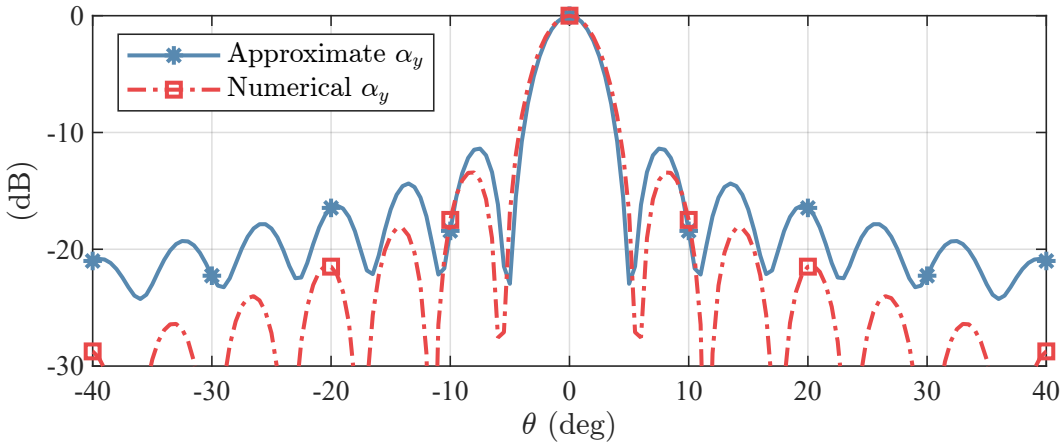

Figure A.3: Radiation patterns comparison for the TE_{10}-like field profile case.

correctly synthesizing the desired distribution (red dotted line in Fig. A.2b), which obtains the nominal η_{rad} when inserted in (A.14). Although the approximate and numerically-computed $\alpha_y(y)$ notably diverge only near the antenna end, this provokes a noticeable discrepancy between their achieved radiation patterns, shown in Fig. A.3. The side-lobes from the approximate α_y are higher, with a difference of 2 dB in the SLL with respect to the desired radiation pattern, correctly obtained from the accurate α_y. Even so, the 2-D directivity level [D_{2D}, calculated as (4.20)] would not be significantly affected, as summarized in Table A.1. Since this example represents a worst-case scenario, the results confirm that the approximation (A.1) remains sufficiently accurate for classical rectangular waveguide designs.

Table A.1: Radiation figures comparison for the different designs.

	Design Fig. A.3		**Design Fig. A.5**	
Used $\alpha_y(y)$	Approx.	Num.	Approx.	Num.
D_{2D} [dBi]	17.7	18.1	16.1	16.6
SLL [dBi]	-13.4	-11.4	-37	-43

A.3.2 Metasurface-Based Case

Now, a metasurface is considered that allows an arbitrary θ_{in} to be chosen. For illustrative purposes, an extremely high $\theta_{\text{in}} = 80°$ is selected, along with $d = 0.8\lambda_0$. In this case, the transverse field profile inside the waveguide would appear truncated at its maximum by the metasurface. Although highly uncommon in classical waveguides, this scenario is theoretically possible when employing the metasurfaces seen in Chapter 4, so it is worth exploring.

If an uniform aperture is desired as in the previous example, then an even higher

approximation error is computed, with a 3.8 dB deterioration in the SLL, and almost 1 dB in the directivity level, compared to the numerical $\alpha_y(y)$ case. However, in order to illustrate an aperture distribution with different characteristics, a Hamming window with $\eta_{\text{rad}} = 0.92$ is selected instead, given by (4.19).

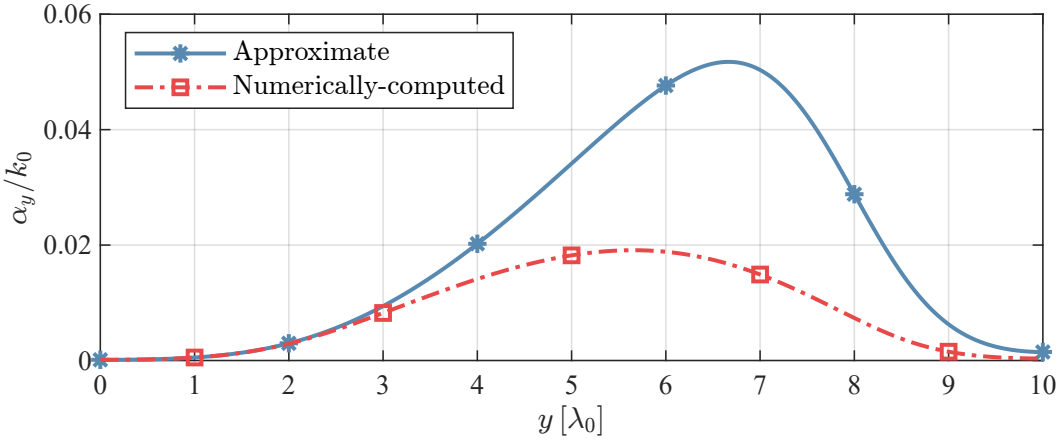

(a)

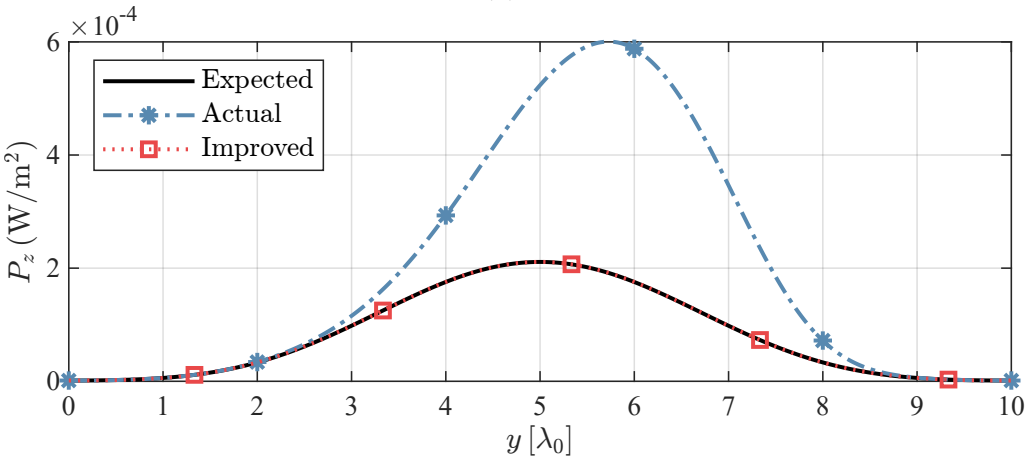

(b)

Figure A.4: Comparison of (a) the leakage factor functions and (b) associated aperture power profiles between using the approximate and the mode-aware approaches, for a desired Hamming window distribution with $\eta_{\text{rad}} = 0.92$, $\theta_{\text{in}} = 80°$ and $d = 0.8\lambda_0$.

In this case, it is known from Fig. A.1 that the approximation requires $\alpha_y \ll 0.02k_0$ to be accurate. This is not satisfied along a considerable portion of the aperture by the approximate leakage factor (solid blue line in Fig. A.4a) calculated from (A.1), consequently causing the observed divergence between the expected and the actual power profiles in Fig. A.4b. By numerically extracting the $\alpha_y(y)$ function from (A.2), a significant deviation from the approximate one is observed. The needed maximum leakage factor value is lower, making it less rapidly varying, which will also better satisfy the dispersion relation assumptions, improving its expected accuracy. Their corresponding radiation patterns are shown in Fig. A.5, where it is shown that the approximate

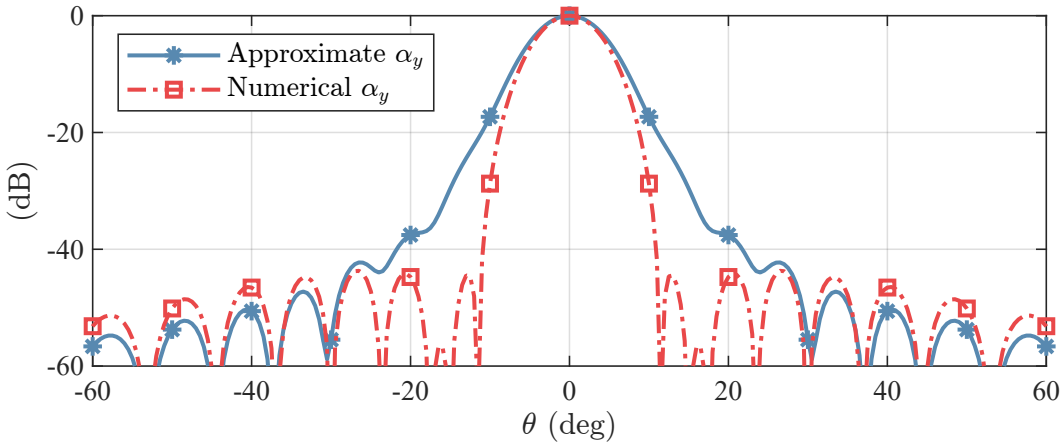

Figure A.5: Radiation patterns comparison for the metasurface case.

$\alpha_y(y)$ struggles to synthesize the expected SLL from the theoretical radiation pattern, obtained through the more accurate solution. A widening of the main beam is also observed, translating into a 0.5 dB deterioration in the directivity level (as shown in Table A.1). Hence, although the impact on radiation characteristics depends on the design's sensitivity to aperture power profile deviations, this case shows that under unusual conditions, the standard α approximation could lead to non-negligible errors.

A.4 Conclusions

The guided field stipulation from Chapter 4, based on a rectangular waveguide supporting an arbitrary leaky boundary condition, has been leveraged to thoroughly assess the validity of the general leakage factor formula (A.1) for modulated LWAs. This way, the conditions for it to hold have been quantified based on its maximum required values and other design parameters.

Approximate formulas are often used without a proper understanding of their limitations. Revisiting them helps clarify their range of validity and the conditions under which they hold. The studied analytical examples show that, if the explored limitations are ignored, the resulting aperture field distribution can differ from the desired one, potentially degrading the radiation characteristics. While such discrepancies become noticeable only under circumstances that may be unusual, the rise of metasurfaces with advanced field transformation capabilities calls for a more careful assessment of these approximations. Moreover, considering the negligible increase in computational complexity introduced by the more rigorous analysis, its adoption may prove valuable in emerging scenarios where accuracy might be critical. Finally, although the analysis is specific to this leaky-wave structure, the methodology and insights may inform how to address these limitations in other configurations, motivating further research.

Appendix B

Study on Two-Layer BHMS Unit Cells for 1-D LWAs

The multilayer unit cells implemented in Chapter 4 for the 1-D BHMS-based LWAs present five copper layers. As discussed in Section 4.4, this choice responded to the need for a sufficiently complete local S-parameters solution space, required for implementing any arbitrary aperture field distribution. Although this approach resulted satisfactory, the synthesis and fabrication challenges associated with such a unit-cell configuration were evident. Not only their synthesis had to rely on a complex near-field-aware methodology, but also their fabrication proved to be difficult in terms of proper layer alignment, trace dimensions precision and proper middle-layer geometries verification. It should be noted that these problems have already arisen in a passive scenario where the unit-cells behavior are fixed for each design.

In this sense, if reconfiguration capabilities are desired, unit cells presenting so many layers would be even more challenging to design and fabricate. Hence, it is interesting to explore simpler unit-cell configurations that could ease the addition of reconfiguration mechanisms afterwards. As taking advantage of well-established PCB fabrication methods remains to be a sensible approach, the simpler multilayer configuration would result from using only two layers. In principle, by allowing both layers to be different from each other, the unit cells would present an asymmetric scattering behavior, which is a requirement for BHMSs. The physical implementation of both layers would then be carried out with some copper geometries, as shown in Section 4.4. However, the interest of this study is to analytically understand the capabilities and limitations of using such a simple unit-cell configuration, and explore its viability in the BHMS-based LWAs, which require a wide transmission phase range with an almost constant reflection coefficient phase.

B.1 Ideal Circuit Model Analysis

A straightforward, though limited, method for analyzing the unit cell involves employing a simple TL circuit model, as explained in Subsection 2.2.2, conducted in Section 3.2 and briefly revisited in Section 4.4. This circuit model accounts only for the fundamental propagating mode and, therefore, cannot capture near-field coupling effects, which arise from the excitation of higher-order modes dependent on the specific copper geometries. Nevertheless, as inter-layer coupling implies an additional degree of freedom in designing the scattering behavior, this simple circuit model approach represents a worst case scenario regarding the achievable parameters for a two-layer configuration. This way, it can be determined whether a two-layer unit cell can provide a sufficiently rich solution space for BHMSs without relying on near-field interactions. On that basis, the actual scattering parameters from the physically-realistic geometries can be later extracted from parametric simulations, as the simple configuration makes that computationally-intensive process more practical.

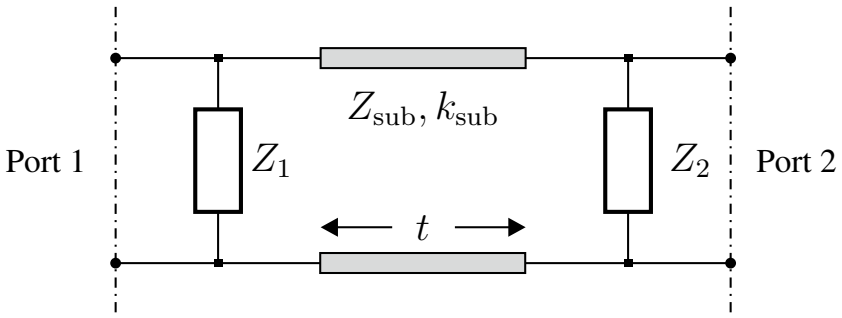

Figure B.1: TL circuit model of periodic 2-layer unit cell.

In the same fashion as in Fig. 2.9, the unit-cell layers (assumed very thin) are modeled as shunt impedances, as depicted in Fig. B.1. The transmission line models the substrate between both layers with thickness t, assumed non-magnetic and with a given dielectric constant $\varepsilon_{\text{sub}} = \varepsilon_0\varepsilon_r(1 - j\tan\delta)$. Thus, the TL parameters, namely its propagation constant and characteristic impedance, are respectively calculated as

$$\gamma_{\text{sub}} = jk_{\text{sub}} = j\frac{\omega}{v_p}\cos\theta_r = j2\pi f\sqrt{\mu_0\varepsilon_{\text{sub}}}\cos\theta_r\,, \tag{B.1a}$$

$$Z_{\text{sub}} = \sqrt{\frac{\mu_0}{\varepsilon_{\text{sub}}}}\cos\theta_r\,, \tag{B.1b}$$

where θ_r accounts for the oblique incidence of the TE wave, related to θ_{in} (4.15) through Snell's law, assuming the unit cell is surrounded by air:

$$\theta_r = \arcsin\left(\frac{\sin\theta_{\text{in}}}{\sqrt{\varepsilon_r}}\right)\,. \tag{B.2}$$

By analyzing the circuit, its Z-matrix elements are obtained as

$$Z_{11} = \frac{\cosh(\gamma_{\text{sub}}t) + Y_2 Z_{\text{sub}} \sinh(\gamma_{\text{sub}}t)}{\Delta Z}\,, \tag{B.3a}$$

$$Z_{12} = Z_{21} = \frac{1}{\Delta Z}\,, \tag{B.3b}$$

$$Z_{22} = \frac{\cosh(\gamma_{\text{sub}}t) + Y_1 Z_{\text{sub}} \sinh(\gamma_{\text{sub}}t)}{\Delta Z}\,, \tag{B.3c}$$

with

$$\Delta Z = (Y_1 + Y_2)\cosh(\gamma_{\text{sub}}t) + \left(\frac{1}{Z_{\text{sub}}} + Z_{\text{sub}} Y_1 Y_2\right)\sinh(\gamma_{\text{sub}}t) \tag{B.4}$$

and $Y_1 = 1/Z_1$, $Y_2 = 1/Z_2$ being the layers' admittance form. Rearranging expressions (B.3a)–(B.3c), the values of the layers' impedances can be expressed as functions of the Z parameters as

$$Z_1 = \frac{Z_{12} Z_{\text{sub}} \sinh(\gamma_{\text{sub}}t)}{Z_{22} - Z_{12}\cosh(\gamma_{\text{sub}}t)}\,, \tag{B.5a}$$

$$Z_2 = \frac{Z_{12} Z_{\text{sub}} \sinh(\gamma_{\text{sub}}t)}{Z_{11} - Z_{12}\cosh(\gamma_{\text{sub}}t)}\,. \tag{B.5b}$$

On the other hand, as the 2×2 S-matrices needed to synthesize passive BHMSs are lossless and reciprocal, then their coefficients can be expressed in terms of the three relevant degrees of freedom, i.e. one magnitude $\Gamma \in [0, 1]$ and two phases, as

$$S_{11} = \Gamma e^{j\varphi_r}\,, \tag{B.6a}$$

$$S_{12} = S_{21} = \sqrt{1-\Gamma^2}\, e^{j\varphi_t}\,, \tag{B.6b}$$

$$S_{22} = -\Gamma e^{j(2\varphi_t - \varphi_r)}\,. \tag{B.6c}$$

This way, employing the inverse transformation to (2.21) to convert from S to Z parameters with the same reference impedance Z_0 for both ports, the Z parameters can be expressed in general as

$$Z_{11} = Z_0 \frac{\cos\varphi_t + \Gamma\cos(\varphi_t - \varphi_r)}{\Delta S}\,, \tag{B.7a}$$

$$Z_{12} = Z_{21} = Z_0 \frac{\sqrt{1-\Gamma^2}}{\Delta S}\,, \tag{B.7b}$$

$$Z_{22} = Z_0 \frac{\cos\varphi_t - \Gamma\cos(\varphi_t - \varphi_r)}{\Delta S}\,, \tag{B.7c}$$

with

$$\Delta S = -j\left(\sin\varphi_t - \Gamma\sin(\varphi_t - \varphi_r)\right)\,. \tag{B.8}$$

Moreover, by using (B.7) in (B.5), the layers' impedance values can be retrieved from the scattering degrees of freedom as

$$Z_1 = j\frac{Z_{\text{sub}}\sin(k_{\text{sub}}t)\sqrt{1-\Gamma^2}}{\cos\varphi_t - \Gamma\cos(\varphi_t-\varphi_r) - \sqrt{1-\Gamma^2}\cos(k_{\text{sub}}t)}\,, \tag{B.9a}$$

$$Z_2 = j\frac{Z_{\text{sub}}\sin(k_{\text{sub}}t)\sqrt{1-\Gamma^2}}{\cos\varphi_t + \Gamma\cos(\varphi_t-\varphi_r) - \sqrt{1-\Gamma^2}\cos(k_{\text{sub}}t)}\,. \tag{B.9b}$$

Note that, in this case, necessarily $\varepsilon_{\text{sub}} \in \mathbb{R}$ in (B.1) as (B.6) assumes the network is lossless. Hence, $k_{\text{sub}} \in \mathbb{R}$, clearly revealing that Z_1 and Z_2 will be purely imaginary.

As the TL characteristics are fixed by the chosen substrate, only two degrees of freedom exist in this configuration, one for each impedance layer. Hence, not any arbitrary S-parameters combination in (B.6) will be possible, as the reflection and transmission coefficients of this circuit model are coupled. In this sense, by analyzing the circuit model in Fig. B.1 to directly retrieve its S-parameters, the relation between the reflection and transmission coefficients is calculated, obtaining

$$S_{21} = \frac{1-S_{11}}{\Delta Z(Z_0+Z_{22})}\,, \tag{B.10}$$

which can be expanded by using (B.3c) and (B.4). Doing so, inserting (B.9) in the expanded expression, and rearranging, the following expression is obtained:

$$\frac{\sin^2\varphi_t - \Gamma^2\sin^2(\varphi_t-\varphi_r)}{Z_{\text{sub}}\sin(k_{\text{sub}}t)\sqrt{1-\Gamma^2}} = -\frac{\sin\varphi_t - \Gamma\sin(\varphi_t-\varphi_r)}{Z_0}\,. \tag{B.11}$$

Expression (B.11) will help searching the complete solution space of achievable scattering coefficients (in the absence of losses), by fixing the TL parameters and two from $\{\Gamma, \varphi_r, \varphi_t\}$, and numerically solving for the third, unfixed one.

B.2 Achievable Solution Space Investigation

In order to explore the solution space of achievable scattering parameters, the TL characteristics must be previously defined. Therefore, this study has been carried out assuming a substrate with $\varepsilon_r = 3$ and $t = 0.762\,\text{mm}\,(30\,\text{mil})$ is used at a frequency $f = 15\,\text{GHz}$, similar to what was performed in Chapter 4. The substrate is firstly assumed lossless, obtaining an ideal case. In addition, the incidence angle is selected to be $\theta_{\text{in}} = 30°$, in accordance to Design 2 in Table 4.1. Nevertheless, the general findings of the solution space do considerably hold for different design characteristics.

As only two degrees of freedom exist in this configuration, it is still practical to

numerically explore the solution space by sweeping Z_1 and Z_2 over a wide range of purely imaginary values, and computing the S-parameters through (B.3) and (2.22) with reference impedance $Z_0 = \eta_0$. Then, by exploring the range $Z_{1,2} \in j[-10^4, 10^4]$, the achievable scattering parameters are obtained and represented in Fig. B.2. Firstly, it is observed that, as expected, not every scattering parameter combination can be achieved, neither in phase nor in magnitude. However, as noted in Section 4.5, for any given BHMS-based LWA design, two main requirements for the scattering parameters need to be fulfilled: (i) a practically constant reflection coefficient phase, and (ii) a complete transmission coefficient phase range to synthesize the given θ_{in} to θ_{out} conversion (see Fig. 4.8a).

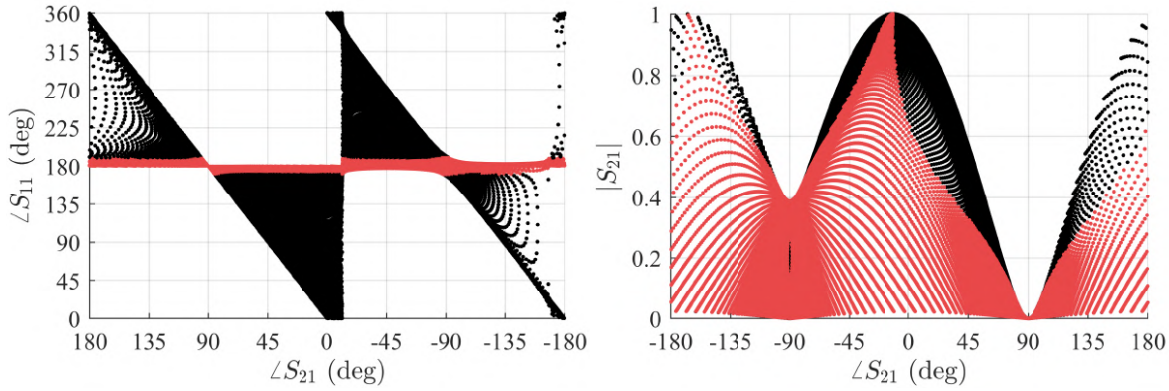

(a) (b)

Figure B.2: Achievable S-parameters for the studied two-layer unit-cell circuit model by sweeping $Z_{1,2} \in j[-10^4, 10^4]$. The transmission phase is plotted versus (a) the reflection phase and (b) the transmission magnitude. Red colored solutions present $\angle S_{11} \in [170°, 190°]$.

From Fig. B.2a it is clear that not every potential $\angle S_{21}$ value can be achieved for a single $\angle S_{11}$ value, not even for exactly 180°, as it may seem in the figure. However, it can be observed that specifically for $\angle S_{11} = 180°$, there exist solutions in its close proximity covering the complete range of transmission phases. This is convenient for two reasons: the guided mode should allow a small variation around a given reflection phase value and still propagate adequately, and 180° is precisely the reflection phase value needed for the guided mode to resemble a TE_{10} configuration, which usually facilitates the LWA implementation. Hence, by allowing, for example, a variation of $\angle S_{11} = 180° \pm 10°$, the complete set of transmission phases is achieved, as depicted with red dots in Fig. B.2a. For this subset of solutions, the achievable transmission magnitudes are also represented with red dots in Fig. B.2b. It shows that, although not all magnitudes are achievable (the worst case occurs around $\angle S_{21} = 90°$), and consequently not any leakage factor value will be possible, the offered combinations should enable some LWA designs.

A more convenient way to explore the solution space is by numerically solving the non-linear expression (B.11). This way, not only it ensures the complete solution space can be discovered without relying on specific, preselected Z_1 and Z_2 ranges, but it also allows obtaining the layers' impedances for desired scattering coefficients. Hence, (B.11) can be solved for an equispaced set of scattering coefficients to build a LUT that will ease the unit-cell synthesis afterwards. For example, by specifying $|S_{21}| \in \{0.01, 0.02, \ldots, 1\}$ and $\angle S_{21} \in \{-180°, -179°, \ldots, 180°\}$, and constraining the solution to satisfy $\angle S_{11} \in [170°, 190°]$, the available solution space is shown in Fig. B.3 as two colormaps representing the layer reactance values that synthesize the scattering parameters. Note that the colorbar only covers a limited range of values (in which most of the solution space reactances reside) for improved visualization.

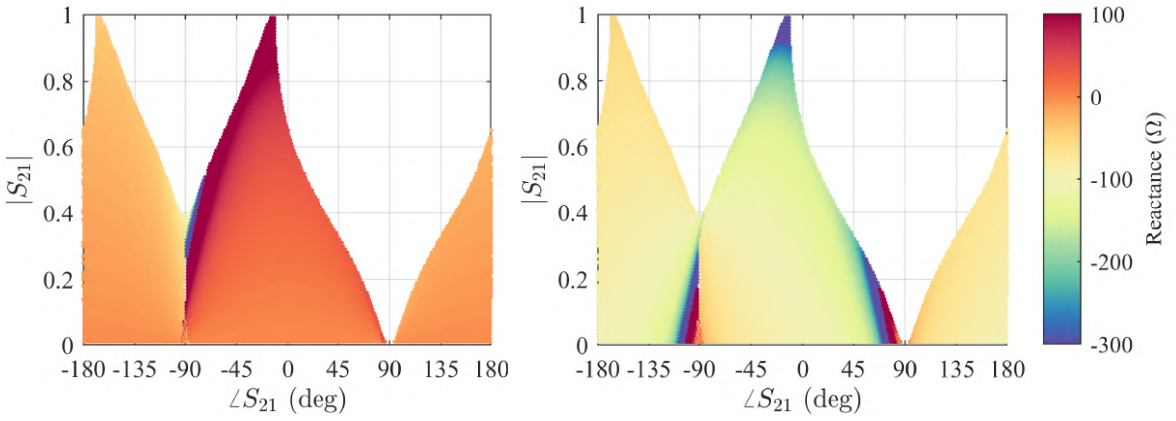

Figure B.3: Colormap of the (a) $X_1 = \Im[Z_1]$ and (b) $X_2 = \Im[Z_2]$ values that synthesize the achievable S-parameters for the studied two-layer unit-cell circuit model, constrained to $\angle S_{11} \in [170°, 190°]$.

Firstly, it can be noticed that, effectively, practically the entire solution space had been explored in Fig. B.2 with the selected reactances range and, hence, there exist no values of Z_1 and Z_2 able to achieve the scattering parameters located in the uncolored regions of Fig. B.3 for the chosen circuit model and parameters. Secondly, it is apparent that the majority of achievable scattering parameters are synthesized through a narrow set of reactances, with X_1 close to $0\,\Omega$ and X_2 in the proximity of $-100\,\Omega$. This can be better observed in Fig. B.4, where the layer reactance values are plotted as functions of the transmission phase, for all the available transmission magnitudes (and the reflection phase constraints). From these curves, it becomes clear that, although achieving any scattering combination in the solution space from Fig. B.3 is theoretically possible, it will heavily rely on the ability of the layer geometries to provide a very sensitive control of their reactance values around the aforementioned central values.

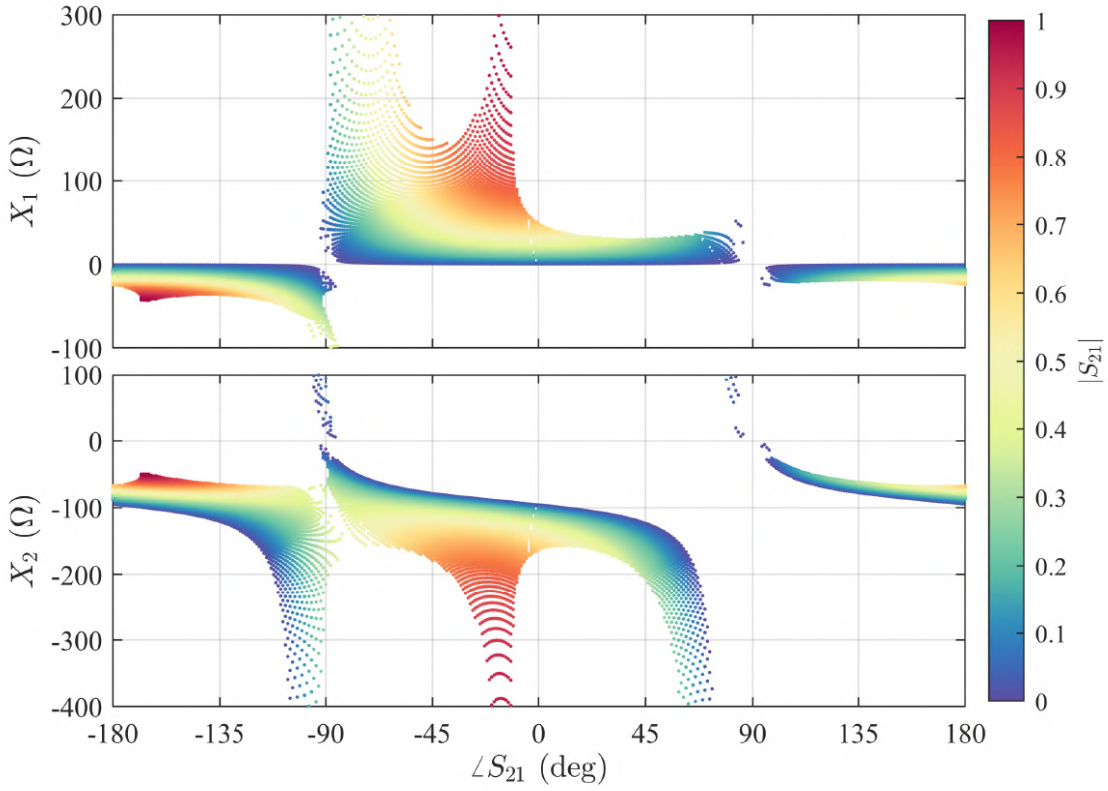

Figure B.4: Required reactance values for (a) Z_1 and (b) Z_2 layer impedances with respect to the desired unit-cell transmission magnitude and phase, constrained to $\angle S_{11} \in [170°, 190°]$.

B.3 Effect of Losses

In real implementations, the layers' impedances will also present a resistive part. Even though it will usually be considerably small, it can get considerably large in comparison with the reactance when the latter presents a very small value, as happens with a substantial portion of the X_1 values in Fig. B.4. Although this study does not aim to design specific copper geometries, it is worth briefly examining how losses affect the solution space.

Introducing losses in the modeled layers implies that their impedances Z_1 and Z_2 are not purely imaginary anymore. Hence, (B.11) cannot be used to scan the solution space, as it relied on a lossless S-matrix (B.6). Nevertheless, the solution space can be obtained as carried out for Fig. B.2, by giving values to the layers' impedances and numerically obtaining the unit-cell S-parameters. This way, three different general cases are studied for a fixed resistance value that both layers may present: 1 Ω, 5 Ω and 20 Ω. Although in reality the resistance will change with the reactance, these cases will still provide some insight on how the solution space is reduced. The three cases are represented in Fig. B.5. As an additional note, although the substrate is

assumed lossless in these examples, the physical losses it would actually introduce can be considered implicitly accounted for through the layers' surface resistance, without any loss of generality in the overall analysis.

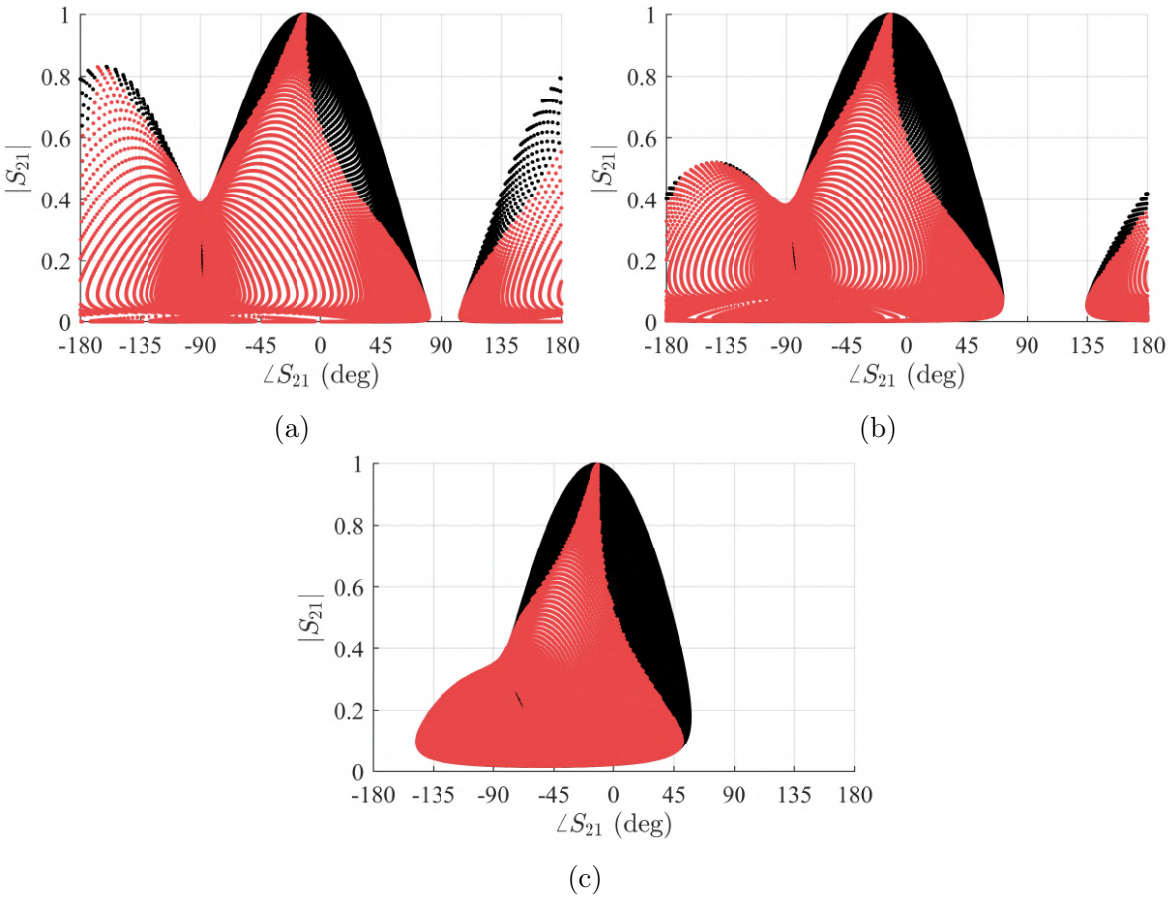

Figure B.5: Comparison of the achievable S-parameters when layer resistance of (a) $1\,\Omega$, (b) $5\,\Omega$ and (c) $20\,\Omega$ is considered. Red colored solutions present $\angle S_{11} \in [170°, 190°]$.

The solution space shrinks for greater resistance values, as can be expected. For small values of surface resistance, a wide range of transmission phase values is still achievable, as seen in Figs. B.5a–B.5b, albeit with even more limited magnitudes. Nonetheless, BHMS-based LWA designs should still be implementable, given that the required leakage factors present sufficiently low values. However, when the surface resistance of both layers considerably increases, as in Fig. B.5c, it is observed that practically half of the potentially required transmission phase values are unreachable. This occurs even if the constraint on the reflection phase were relaxed, as shown by the black dots representing the complete solution space without any constraints. Therefore, the layers' real copper geometries that implement the required impedances must be carefully designed to avoid significant losses. Otherwise, the realization of BHMS unit cells for this type of antennas would be severely hindered.

B.4 1-D BHMS-Based LWA Design

The preceding analysis is used to demonstrate the capabilities of two-layer unit cells in the design of the antennas shown in Chapter 4, as well as to highlight the benefits of prior knowledge of the available solution space.

A design is carried out to present the characteristics summarized in Table B.1. When reconfiguration capabilities are required, the unit-cell length Δy should be chosen as large as possible [116] to minimize the number of reconfigurable unit cells required in the design, while ensuring proper functionality and surface homogenization. However, here it is chosen smaller than in Section 4.5 both to avoid problems arising from a coarse discretization and to force some unit cells requiring transmission phase values difficult to achieve. The period p is chosen an integer number of times Δy to synthesize only the unit cells within a period, which results in the chosen output angle θ_{out}. The leakage factor α is constant and sufficiently low due to the considerations from the previous sections. Finally, the antenna length L is the same as in Chapter 4, and the waveguide height d is chosen for the guided mode to present a TE_{10}-like mode profile, relating to θ_{in} through (A.24), and ensuring a required $\angle S_{11} \approx 180°$.

Table B.1: LWA parameters for the two-layer unit-cells example design.

θ_{in}	θ_{out}	α	Δy	p	d	L
$30°$	$-20.93°$	$0.015k_0$	$\lambda_0/6$	$(7/6)\lambda_0$	$0.557\lambda_0$	$10\lambda_0$

The methodology presented in Section 4.3 is used to design the LWA. From the required S-parameters for each unit cell, their required reactances are obtained as follows. For each unit-cell parameters, the LUT generated in Section B.2 is used to search for a solution with the closest transmission phase and magnitude. If a combination exists within the achieved solutions from Fig. B.3, it is selected. If no solution exists for the required parameters, then the combination that minimizes Δ_{uc} is chosen, with the error calculated as

$$\Delta_{\text{uc}} = \left| |\hat{S}_{21}| - |S_{21}| \right| + \left| \frac{\angle \hat{S}_{21} - \angle S_{21}}{\pi} \right| , \tag{B.12}$$

where the hat symbol indicates the goal unit-cell parameters. This way, more weight is given to the phase error, which is more critical to correctly excite the desired radiating space harmonic only.

In addition, as a phase degree of freedom ξ exists in the radiated field expression (4.2), it is selected to avoid as much as possible requiring unit-cell parameters within the regions where no solutions exist in Fig. B.3. For that purpose, it is selected the ξ

value that minimizes the total achieved BHMS error Δ_{MS} as

$$\Delta_{\text{MS}} = \sum_{i=0}^{N-1} \left\{ \left| |\hat{S}_{21}| - |S_{21}| \right|^2 + \left| \frac{\angle \hat{S}_{21} - \angle S_{21}}{\pi} \right|^2 + \left| \frac{\angle \hat{S}_{11} - \angle S_{11}}{\pi} \right|^2 \right\}, \tag{B.13}$$

where i is the unit-cell index and $N = 7$ the total number of unit cells to synthesize. Note that the achieved unit-cell reflection phases are also accounted for to improve the BHMS behavior as much as possible. This way, $\xi = 70°$ is found to be the best option (basically ensures no unit cell requires $\angle S_{21} \approx 90°$), and the goal and achieved S-parameters and corresponding layer reactance values are presented in Fig. B.6.

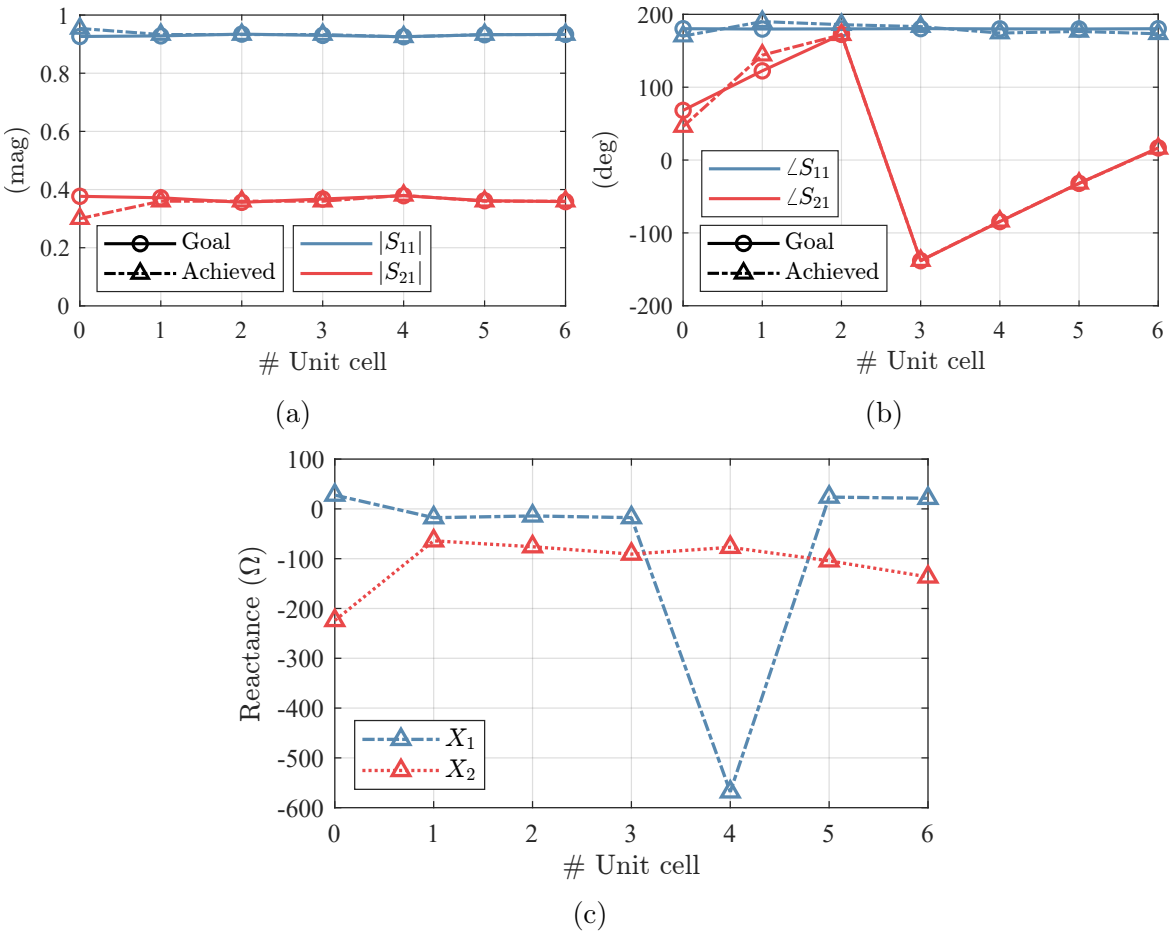

Figure B.6: Goal and achieved S-parameters in (a) magnitude and (b) phase, and (c) corresponding layer reactances for the example LWA design.

As seen, the achieved parameters for this design example highly approach the goal ones, being a very satisfactory result. In order to verify the design, it is simulated in HFSS with ideal impedance boundary conditions, as explained in Section 4.6. The structure is excited with waveports at the ends of the waveguide, as the TE_{10}-like guided field profile should guarantee a good energy coupling. The results are shown

in Fig. B.7. It is observed how the simulated field distribution highly resembles that from theory (whose radiated field is calculated as detailed in Subsection 2.2.3). The interaction between the guided and leaked fields is barely noticeable in Fig. B.7b as the two-layers-only BHMS is very thin.

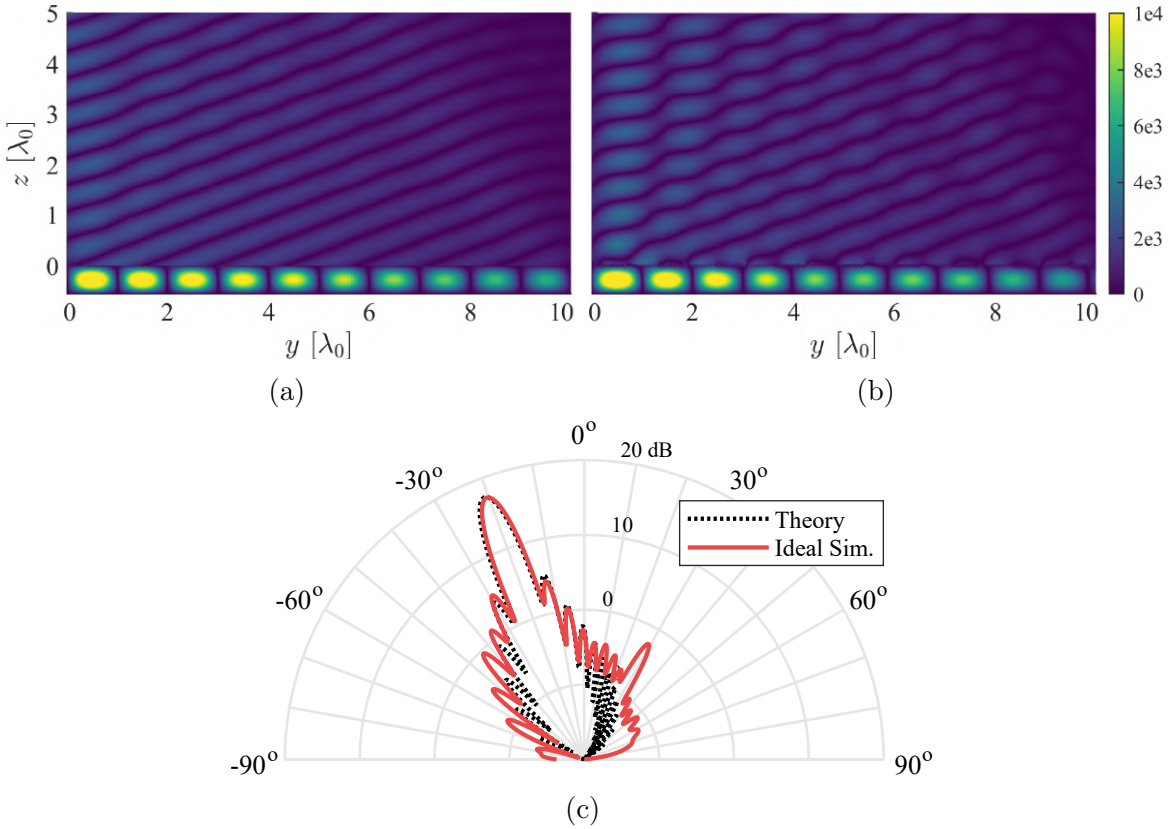

Figure B.7: Field distributions $|\mathrm{Re}(E_x(y,z))|$ (V/m) of (a) theoretical prediction and (b) ideal electromagnetic simulation, along with (c) their corresponding 2-D directivity patterns, for the example LWA design.

Fig. B.7c shows the good agreement in the expected 2-D directivity. It can be noticed that the spurious spatial harmonic corresponding to the guided mode wavenumber is not completely suppressed (very low secondary lobe at 30°), presumably due to the slight discrepancies between the goal and achieved unit-cell scattering parameters. Nevertheless, the BHMS is able to properly guide the field below it, and partially radiate it to the desired direction with almost identical characteristics to the prescribed ones. Therefore, the results are very satisfactory, and they serve as a preliminary example of the potential capabilities of two-layer unit cells to implement BHMS-based LWA designs intended for simplified fabrication and, potentially, reconfiguration purposes.

Appendix C

Publications Derived from this Thesis

Journals

[J1] P. Mateos-Ruiz, E. Abdo-Sánchez and C. Camacho-Peñalosa, "Revisiting the Conventional Formula for the Leakage Factor in Modulated Leaky-Wave Antennas from a Rigorous Perspective Based on Rectangular Waveguides," submitted for publication.

[J2] P. Mateos-Ruiz, E. Abdo-Sánchez and C. Camacho-Peñalosa, "Enhanced Bandwidth Fabry-Pérot Cavity Antenna Synthesis with Controlled Aperture Distribution and Practical Excitation," *IEEE Transactions on Antennas and Propagation*, vol. 73, no. 11, pp. 8412–8422, November 2025. DOI: 10.1109/TAP.2025.3591978.

[J3] P. Mateos-Ruiz, V. K. Killamsetty, A. Epstein and E. Abdo-Sánchez, "Arbitrary and Rigorous Aperture Illumination Synthesis in Huygens' Metasurface-Based Leaky-Wave Antennas," *IEEE Transactions on Antennas and Propagation*, vol. 73, no. 7, pp. 4208–4223, July 2025. DOI: 10.1109/TAP.2025.3550345.

[J4] P. Mateos-Ruiz, M. Pérez-Escribano, A. Hernández-Escobar, E. Abdo-Sánchez, E. Márquez-Segura, T. M. Martín-Guerrero and C. Camacho-Peñalosa, "Time-Domain Characterization of Nematic Liquid Crystals Using Additive Manufacturing Microstrip Lines," *IEEE Transactions on Instrumentation and Measurement*, vol. 73, pp. 1–8, 2024. DOI: 10.1109/TIM.2024.3413162.

Conferences

[C1] P. Mateos-Ruiz, E. Abdo-Sánchez, C. Camacho-Peñalosa and George V. Eleftheriades, "Overcoming Fabry-Pérot Cavity Antenna Limitations Using Two-Dimensional Huygens' Metasurfaces," submitted to the *20th European Conference on Antennas and Propagation (EuCAP)*, Dublin (Ireland), Apr. 2025.

[C2] P. Mateos-Ruiz and E. Abdo-Sánchez, "Teoría, Diseño y Verificación Experimental de Antenas Leaky-Wave Basadas en Metasuperficies con Síntesis de Iluminación," in *Proceedings of the XL Simposium Nacional de la Unión Científica de Radio (URSI 2025)*, Tarragona (Spain), Sep. 2025.

[C3] P. Mateos-Ruiz, E. Abdo-Sánchez and C. Camacho-Peñalosa, "A Hybrid Approach for Efficiently Illuminated Fabry-Pérot Cavity Antennas with Enhanced Bandwidth," in *Proceedings of the 19th European Conference on Antennas and Propagation (EuCAP)*, Stockholm (Sweden), Mar. 2025. DOI: 10.23919/EuCAP63536.2025.10999530.

[C4] P. Mateos-Ruiz, E. Abdo-Sánchez and C. Camacho-Peñalosa, "Antenas Fabry-Pérot con apertura uniforme y mejora del ancho de banda," in *Proceedings of the XXXIX Simposium Nacional de la Unión Científica de Radio (URSI 2024)*, Cuenca (Spain), Sep. 2024. Access: hdl.handle.net/10630/34660.

[C5] P. Mateos-Ruiz, E. Abdo-Sánchez and C. Camacho-Peñalosa, "Estudio del Desalineamiento entre Capas para Reducir el Acoplamiento en Metasuperficies," in *Proceedings of the XXXVIII Simposium Nacional de la Unión Científica de Radio (URSI 2023)*, Cáceres (Spain), Sep. 2023. Access: hdl.handle.net/10630/27584.

[C6] P. Mateos-Ruiz, V. K. Killamsetty, A. Epstein and E. Abdo-Sánchez, "Physical Implementation of Leaky-Wave Antenna with Engineered Aperture Distribution Based on Bianisotropic Huygens Metasurfaces," in *Proceedings of the 17th European Conference on Antennas and Propagation (EuCAP)*, Florence (Italy), Mar. 2023. DOI: 10.23919/EuCAP57121.2023.10133480.

[C7] P. Mateos-Ruiz, E. Abdo-Sánchez and C. Camacho-Peñalosa, "Aperture Illumination Control of Leaky-Wave Antennas Based on Bianisotropic Huygnes' Metasurfaces," in *Proceedings of the XXXVII Simposium Nacional de la Unión Científica de Radio (URSI 2022)*, Málaga (Spain), Sep. 2022. ***Received a *URSI Young Researchers Secondary Award***.

[C8] P. Mateos-Ruiz, E. Abdo-Sánchez and C. Camacho-Peñalosa, "Non-homogeneous Fabry-Pérot Antenna Design Process to Improve Aperture Efficiency," in *Proceedings of the 16th European Conference on Antennas and Propagation (EuCAP)*,

Madrid (Spain), Mar. 2022. DOI: 10.23919/EuCAP53622.2022.9769658.

[C9] P. Mateos-Ruiz, E. Abdo-Sánchez and C. Camacho-Peñalosa, "Non-homogeneous Fabry-Pérot Antenna Design at Ku-band," in *Proceedings of the XXXVI Simposium Nacional de la Unión Científica de Radio (URSI 2021)*, Remote format, Sep. 2021. Access: hdl.handle.net/10630/23612.

Apéndice D

Summary in Spanish

D.1 Introducción

D.1.1 Marco contextual

El mundo que nos rodea está experimentando una rápida transformación tecnológica. Mientras que hace solo unas décadas el acceso a la conectividad inalámbrica era limitado y a menudo restringido a bajas velocidades de datos, hoy en día es habitual que los usuarios en regiones desarrolladas puedan ver vídeos en alta resolución bajo demanda desde prácticamente cualquier lugar. Esta evolución ha sido impulsada por los avances en las tecnologías de comunicación inalámbrica, debidos a una mayor demanda de altas velocidades de descarga de datos, baja latencia y cobertura generalizada. Ahora, las aplicaciones emergentes, como los vehículos autónomos, las ciudades inteligentes, las constelaciones de satélites que proporcionan Internet y el Internet de las cosas (IoT), están empujando los límites de la infraestructura existente, lo que requiere no solo una comunicación más rápida, sino también más eficiente y compacta.

Uno de los componentes clave de estos sistemas de comunicación inalámbrica es la antena, que sirve de interfaz entre la energía electromagnética guiada y la radiada. Aun siendo solo una parte del conjunto, el diseño de la antena es crucial para transmitir y recibir correctamente ondas electromagnéticas con las características deseadas. Para satisfacer las exigencias de estos sistemas inalámbricos de última generación, las antenas no solo deben proporcionar una alta ganancia y radiación direccional, sino también ser de perfil bajo, altamente eficientes y capaces de controlar el haz de forma dinámica. Las soluciones tradicionales, como antenas reflectoras o *arrays* en fase, suelen conllevar estructuras voluminosas o redes de alimentación complejas, lo que limita su integración en plataformas compactas o dispositivos móviles.

Una solución alternativa y ampliamente estudiada desde el siglo pasado son las antenas de onda de fuga, o *leaky wave* (LWA) [1], que han suscitado un interés renovado en los últimos años debido a sus ventajosas características. Éstas son capaces de producir radiación direccional sirviéndose de una fuga de campo controlada desde una estructura de guiado, lo que ofrece una alimentación sencilla, una configuración generalmente pasiva y compatibilidad con tecnologías planares. Además, las capacidades inherentes de escaneo en frecuencia de las LWA aumentan su atractivo para aplicaciones prácticas que requieran control de la dirección del haz, como puedan ser las nuevas redes celulares. Sin embargo, las LWA convencionales suelen estar limitadas por una dependencia entre las propiedades modales de la estructura guiada y las características de radiación resultantes. Esta dependencia impone compromisos fundamentales entre el nivel de directividad, la capacidad de conformación del haz y el ancho de banda de operación, especialmente en configuraciones basadas en cavidades resonantes, como las antenas basadas en cavidades Fabry-Pérot (FPCA) [2].

En paralelo, el campo de las *metasuperficies* electromagnéticas ha ganado popularidad en la última década. Las metasuperficies, introducidas como análogas bidimensionales de los metamateriales [3], no se basan en materiales comunes, sino que están compuestas por pequeñas partículas, con tamaños muy inferiores a la longitud de onda, específicamente diseñadas para provocar interacciones electromagnéticas que no suelen existir de manera natural. De esta manera, estas superficies artificiales permiten un control sin precedentes sobre la amplitud, fase y polarización de los frentes de onda electromagnéticos. Como plataformas planares, generalmente pasivas y potencialmente de bajo coste, las metasuperficies ya han posibilitado numerosas aplicaciones, entre las que se incluyen lentes planas, convertidores de polarización, absorbentes y conformadores de haces holográficos, entre otras [4]. En particular, las metasurperficies de Huygens HMS destacan por su capacidad para implementar condiciones de contorno a voluntad, lo que permite transformaciones pasivas y sin pérdidas entre frentes de onda incidentes y transmitidos arbitrarios. Esta capacidad se deriva del control independiente de las respuestas eléctrica y magnética de los *meta-átomos* de las HMS, al tiempo que se garantiza la adaptación de impedancias en toda la interfaz.

La intersección entre la ingeniería de metasuperficies y las LWA abre nuevas posibilidades en el diseño de antenas. Dado que ambas tecnologías son planas, la radiación de ondas de fuga representa un mecanismo muy conveniente para diseñar antenas basadas en metasuperficies. De esta manera, el rendimiento de las LWA puede mejorarse, por ejemplo, independizando las características del campo guiado y el radiado, lo que permite un mejor control sobre la distribución de campo en la apertura, dirección de radiación, polarización y eficiencia, en general. Por lo tanto, se logra una mayor flexibilidad de diseño, lo que permite utilizar la misma estructura física para obtener

distintas características de radiación simplemente modificando los parámetros de la metasuperficie [5].

En este contexto, las LWA basadas en metasuperficies representan un área de investigación prometedora, generando un gran interés en la comunidad de electromagnetismo y antenas. La mejora de sus capacidades en términos de conformación pasiva del haz, ancho de banda y eficiencia de apertura es esencial para que esta tecnología madure completamente y se consolide como un componente robusto e integrado en los sistemas de comunicación de próxima generación e infraestructuras críticas. Desafíos clave, como el análisis y síntesis macroscópica de las metasuperficies, su integración en arquitecturas de antenas compactas, el diseño y modelado electromagnético de sus celdas unidad, la inclusión de mecanismos de reconfigurabilidad para el control dinámico del haz, y su fabricación práctica, siguen siendo objeto de una intensa investigación en curso, en cuyo marco se inscribe esta tesis.

D.1.2 Génesis

El desarrollo de esta tesis doctoral comenzó con un esfuerzo por profundizar en la comprensión de los mecanismos de radiación subyacentes de las FPCA. Aunque estas antenas son conocidas por su capacidad para generar haces directivos en dirección normal a la estructura, o *broadside*, presentan dos limitaciones fundamentales: un ancho de banda estrecho y una baja eficiencia de apertura. Estos problemas se deben principalmente al carácter resonante de la estructura y a la atenuación radial del campo cuando se alimenta desde el centro.

La mayoría de los trabajos previos se ha centrado en la mejora del ancho de banda, principalmente diseñando la respuesta en frecuencia de las celdas unidad periódicas que conforman la superficie a través de la que se radia el campo. Sin embargo, la eficiencia de apertura ha recibido una atención comparativamente menor. Además, son escasos los estudios que han abordado ambas limitaciones de forma conjunta y desde una perspectiva integral. Los primeros esfuerzos para cubrir esta carencia condujeron a la introducción de modulación espacial en la superficie radiante. Esta estrategia requirió el diseño de la respuesta en frecuencia de múltiples celdas unidad, lo que consecuentemente incentivó el desarrollo de modelos circuitales precisos que permitieran una síntesis analítica y eficiente de dichas celdas, sin depender exclusivamente de simulaciones electromagnéticas paramétricas computacionalmente demandantes. Estos avances se alinearon de forma orgánica con las metodologías de diseño empleadas en el campo de las metasuperficies, revelando así nuevas oportunidades de innovación.

Paralelamente, el grupo de investigación, apoyándose en su experiencia en líneas de

transmisión artificiales basadas en metamateriales así como en antenas de onda progresiva y arrays, estaba involucrado en un proyecto orientado a explorar tecnologías basadas en metasuperficies para el desarrollo de antenas con prestaciones mejoradas, dirigidas a los sistemas de comunicación emergentes. En ese contexto, se habían realizado trabajos previos sobre el uso de HMS aplicadas a LWA [6], en los que se lograba un control independiente de los campos guiado y radiado. Aunque el concepto presentaba una alta versatilidad para el diseño de antenas, el marco teórico desarrollado en dicho trabajo restringía el factor de fuga a un valor constante a lo largo de la estructura, lo que limitaba el control sobre la distribución de campo en la apertura y, por tanto, sobre el diseño del diagrama de radiación.

Otra línea de investigación complementaria se había centrado en el uso de cristales líquidos como materiales dieléctricos sintonizables para aplicaciones de alta frecuencia. Estos materiales ofrecen una alternativa pasiva y de bajas pérdidas frente a los varactores y actuadores mecánicos convencionales, y representan una vía potencial hacia la reconfiguración dinámica del haz. No obstante, antes de su integración en configuraciones de antena concretas, y debido a las dificultades asociadas a la manipulación de estos líquidos sin equipamiento especializado, se identificó la necesidad de desarrollar un método eficaz para la caracterización de sus propiedades electromagnéticas empleando equipamiento estándar de alta frecuencia.

En última instancia, la convergencia de estas líneas de investigación puso de manifiesto el potencial de las antenas basadas en metasuperficies. Esta tesis se apoya en dichos fundamentos para explorar y desarrollar configuraciones novedosas que ofrezcan características de radiación mejoradas y sienten las bases para futuros sistemas de antenas dinámicos y versátiles.

D.1.3 Objetivos

El interés principal de esta tesis doctoral es aprovechar la tecnología de LWA basadas en metasuperficies para obtener un rendimiento mejorado en radiación, especialmente en lo que respecta a conformación del haz, capacidad de orientación, eficiencia de apertura y ancho de banda. El objetivo general es desarrollar métodos integrales que permitan sintetizar la distribución del campo en la apertura, manteniendo al mismo tiempo una alta eficiencia general y aplicabilidad práctica.

Las configuraciones investigadas en esta tesis se basan en guías de placas paralelas (PPW) modificadas, como son las FPCA y las LWA en [6], donde la placa superior está diseñada para permitir una fuga de campo controlada. En tales diseños, las propiedades de radiación están vinculadas a la distribución de campo en la apertura de la antena,

lo que hace de su capacidad de síntesis una herramienta fundamental para mejorar las prestaciones de estas antenas.

Aunque las diversas contribuciones de esta tesis no son linealmente incrementales, están unificadas por el objetivo principal de avanzar en el diseño de antenas basadas en metasuperficies. Los objetivos específicos pueden describirse del siguiente modo:

- Desarrollar una metodología sistemática para mejorar las características de las FPCA, centrándose especialmente en su eficiencia de apertura inherentemente baja y evitando al mismo tiempo un deterioro significativo del ancho de banda. Esto incluye el diseño de la respuesta de frecuencia de las celdas unidad y la exploración de superficies parcialmente reflectoras moduladas espacialmente para permitir distribuciones de apertura más uniformes.

- Extender el enfoque de la LWA basada en HMS de [6] para permitir factores de fuga variables, permitiendo un control completo sobre la distribución de campo en la apertura. Esto requiere diseñar metasuperficies con todas sus celdas unidad generalmente distintas entre ellas, teniendo también en cuenta interacciones de acoplamiento mutuo dentro de ellas, lo que exige una investigación más profunda sobre el diseño eficiente de las celdas unidad.

- Diseñar, fabricar y medir prototipos de antenas para validar las predicciones teóricas en condiciones reales. Esto incluye garantizar una excitación eficiente y buena adaptación de impedancias, así como aprovechar las técnicas estándar de fabricación de placas de circuito impreso (PCB) para facilitar la implementación práctica de las metasuperficies.

- Combinar los conocimientos sobre FPCA y LWA basadas en HMS para diseñar antenas basadas en metasuperficies con apertura bidimensional capaces de ofrecer un control avanzado del haz. Esto potencialmente daría lugar a diseños de antenas eficientes, versátiles y reconfigurables capaces de escanear todo el semiespacio positivo.

D.1.4 Estructura de los contenidos

Esta subsección ofrece una breve explicación de los diferentes capítulos de esta tesis, destacando las principales contribuciones de cada uno de ellos.

El **Capítulo 2** proporciona los fundamentos teóricos relevantes, que sirven para introducir varios conceptos utilizados en el resto de la tesis. Se describen las principales características de las LWA, explicando sus mecanismos de radiación y las categorías en las que comúnmente se clasifican. Además, se explora cómo se comporta la dis-

tribución de potencia en la apertura tanto para estructuras unidimensionales como bidimensionales, y se explica el método de resonancia transversal, relevante para obtener las características de dispersión de los modos guiados. En este capítulo también se ofrece una introducción más teórica a las superficies periódicas, destacando su relevancia y practicidad, y centrándose específicamente en los principios fundamentales y derivaciones matemáticas propias de las HMS.

Las limitaciones de las FPCA se abordan en el **Capítulo 3**, donde estas antenas se estudian desde el modelo simplificado basado en rayos hasta una perspectiva más completa fundamentada en ondas de fuga. La combinación de ambos enfoques proporciona una comprensión más profunda de los mecanismos que controlan la resonancia responsable de la radiación broadside y el ancho de banda limitado, así como la tasa de decaimiento del campo en función del factor de fuga implementado. A partir de este análisis, se introduce un marco unificado para diseñar la superficie radiante que permite mejorar tanto la eficiencia de apertura como el ancho de banda, mediante una técnica de fase con pendiente positiva combinada con modulación espacial. Tras varias consideraciones prácticas sobre la alimentación, se fabrican tres prototipos con diferentes distribuciones de apertura para verificar el enfoque propuesto.

El **Capítulo 4** cambia el foco hacia LWA unidimensionales basadas en HMS en una configuración de placas paralelas. Una contribución clave de este trabajo es la superación de limitaciones anteriores en el factor de fuga constante mediante la introducción de una aproximación de amplitud lentamente variable, lo que permite cambiar la forma del diagrama de radiación. El espesor de la metasuperficie, mucho menor que la longitud de onda, conduce al uso de sustratos delgados para las celdas unidad. Por tanto, éstas se diseñan de manera eficiente con estructuras multicapa realistas, sintetizadas con un enfoque semianalítico capaz de tener en cuenta los efectos de acoplamiento mutuo entre capas. Se fabrican y miden varios prototipos, lo que valida la teoría y muestra la versatilidad de las LWA basadas en HMS para el control avanzado del haz.

Los conocimientos adquiridos en los capítulos anteriores se aplican en el **Capítulo 5** para proponer una novedosa configuración LWA bidimensional basada en HMS. Esta configuración busca combinar las capacidades de control angular y de conformación del haz que proporcionan las HMS con la apertura radiante 2-D de las FPCA. Se presenta una estipulación rigurosa del campo y una metodología de diseño, detallando ciertas aproximaciones adoptadas para reducir la complejidad del problema debida al aumento de la dimensionalidad. Se llevan a cabo distintos diseños para mostrar diversas prestaciones de esta configuración, que se verifican mediante simulaciones con celdas unidad ideales. Este capítulo sienta las bases para futuras implementaciones de antenas de apertura bidimensional, usando HMS y basadas en una configuración PPW, con capacidad de orientación del haz y mayor eficiencia.

El **Capítulo 6** aborda un reto complementario pero esencial para las futuras antenas reconfigurables: la caracterización práctica de cristales líquidos (LC), que pueden ser utilizados como dieléctricos sintonizables para radiofrecuencias. Se utilizan técnicas de fabricación aditiva para construir una estructura microstrip que puede rellenarse con LC, haciendo las veces de sustrato, y el cual se polariza mediante los dos conductores principales para modular su permitividad. Se emplea una técnica de enventanado temporal para extraer las propiedades dieléctricas sin necesidad de otras técnicas de calibración, y permitiendo la fabricación de un único prototipo. El método propuesto se valida tanto numérica como experimentalmente, mostrando resultados consistentes con las técnicas existentes y confirmando su potencial para la caracterización de LC eficiente y de bajo coste para aplicaciones de antenas reconfigurables.

Por último, el **Capítulo 7** resume los principales resultados y conclusiones de los capítulos anteriores, destacando sus contribuciones más relevantes. Además, se esbozan posibles direcciones futuras de investigación para continuar el trabajo de esta tesis.

En conjunto, estos capítulos representan una progresión coherente hacia configuraciones y metodologías de síntesis cada vez más complejas, al tiempo que abordan aspectos más prácticos, como su implementación y la caracterización de materiales. Cabe destacar que cada capítulo técnico proporciona el contexto necesario y una revisión específica de la bibliografía relevante para contextualizar el trabajo presentado.

Adicionalmente, se incluyen dos apéndices para profundizar en algunas cuestiones relacionadas con el Capítulo 4. En concreto, el **Apéndice A** hace uso de la derivación teórica rigurosa de las LWA 1-D basadas en HMS para revisar la conocida fórmula para calcular el factor de fuga en antenas moduladas espacialmente, justificando su validez y cuantificando sus limitaciones en el escenario estudiado. Por otro lado, el **Apéndice B** presenta un breve estudio sobre el uso de celdas unidad de dos capas para el diseño de las HMS empleadas. Aunque éstas son convenientes para simplificar la implementación, los grados de libertad disponibles se ven muy limitados, explorando así sus posibilidades. Finalmente, las publicaciones derivadas de esta tesis se enumeran en el **Apéndice C**.

D.2 Conclusiones y líneas futuras

En esta tesis doctoral se han estudiado en profundidad varias antenas de onda de fuga basadas en metasuperficies. Éstas usan configuraciones en guía de placas paraleles y ofrecen distintos grados de control sobre la distribución del campo en la apertura. Dependiendo de la configuración concreta, sus propiedades de radiación pueden seleccionarse convenientemente en términos de dirección principal de radiación, nivel de

directividad y forma del diagrama de radiación, al tiempo que permiten una mejora potencial de la eficiencia de apertura y del ancho de banda, así como múltiples grados de libertad en el diseño.

Comenzando por las antenas basadas en cavidades Fabry-Pérot, éstas ofrecen un análisis simplificado con expresiones de diseño sencillas. La combinación del enfoque aproximado de la óptica geométrica con la teoría clásica de ondas de fuga ha permitido diseñar la respuesta en frecuencia de la superficie parcialmente reflectora (PRS). Así, aunque esta metodología solo permite obtener radiación en broadside (o cónica), logra mejorar tanto la eficiencia de apertura como el ancho de banda, respectivamente mediante modulación espacial y una técnica de fase con pendiente positiva aplicada a la reflexión de la PRS, lo que genera un comportamiento local no Foster. Además, se han abordado las limitaciones y consideraciones relativas a la excitación, poniendo de manifiesto la creciente dificultad de adaptación a medida que aumenta la directividad en este tipo de antenas. Por otro lado, como la modulación espacial permite el control de la distribución de campo en la apertura, el diagrama de radiación puede moldearse para obtener diferentes características deseadas. Esto se ha verificado mediante la fabricación de tres prototipos distintos, cuyas medidas muestran un alto grado de concordancia con las simulaciones, confirmando las propiedades buscadas y alcanzando productos directividad-ancho de banda superiores a los que se pueden conseguir con diseños homogéneos.

Posteriormente, se ha dado un paso adelante en complejidad con la introducción de metasuperficies de Huygens bianisótropas en el diseño de antenas de onda de fuga. Al utilizar una BHMS como placa superior de una configuración PPW con propagación unidimensional que permite fugas de campo, se consigue una mayor flexibilidad en el diseño. En particular, las transformaciones arbitrarias del frente de onda que ofrecen estas metasuperficies, para las que se requiere un análisis de campo riguroso, posibilitan la selección independiente de diversas características de radiación. En este sentido, se ha logrado un control completo de la distribución de campo en la apertura mediante la resolución rigurosa de la ecuación de onda con números de onda variables, y la aplicación de una aproximación de amplitud lentamente variable que permite una metodología de diseño simplificada en la que se pueden elegir independientemente la constante de fase y un factor de fuga modulado. Dado que la BHMS deja de ser físicamente periódica cuando se modula el factor de fuga, es necesario un procedimiento eficiente de síntesis de celdas unidad para evitar simulaciones paramétricas intensivas. Para ello, se ha utilizado un algoritmo semianalítico que permite obtener las dimensiones de las celdas unidad sin necesidad de optimización electromagnética posterior. Se han llevado a cabo varios diseños para verificar el concepto y las capacidades de esta configuración, cuyas simlaciones muestran una gran concordancia con las predicciones

teóricas. Además, se han fabricado diferentes prototipos de estas metasuperficies, que pueden montarse sobre la misma guíaonda rectangular fabricada y alimentada por sonda coaxial, equivalente a la configuración teórica PPW invariante en x. Las medidas realizadas en cámara anecoica han confirmado los comportamientos esperados, aunque con un desplazamiento de frecuencia que puede atribuirse a diversas tolerancias de fabricación.

En relación con el previo análisis de campo, también se ha obtenido una mejor comprensión de las limitaciones de la fórmula general del factor de fuga en configuraciones LWA 1-D moduladas. En particular, dado que la relación de separación habitual no puede aplicarse rigurosamente cuando los números de onda del modo guiado varían a lo largo de la antena, se han derivado las consideraciones necesarias para que la fórmula clásica del factor de fuga sea válida en el escenario estudiado. Además, y en relación con el diseño microscópico de la metasuperficie, la elevada complejidad asociada al uso de celdas unidad de cinco capas motivó un estudio específico sobre las capacidades de celdas unidad mucho más simples, de tan solo dos capas, para implementar las BHMS requeridas. Aun tratándose de un modelo simplificado e idealizado, el modelo en línea de transmisión reveló que es teóricamente posible utilizar estas configuraciones de celdas unidad simples para diseñar LWA 1-D basadas en BHMS sin depender del acoplamiento entre capas como un grado de libertad adicional, si bien con ciertas limitaciones en el factor de fuga alcanzable. Sin embargo, se debe prestar especial atención a las pérdidas de las capas de las celdas unidad, ya que reducen rápidamente el espacio de soluciones disponible.

Las perspectivas de los dos trabajos anteriores han conducido a la combinación de ideas en una configuración LWA bidimensional basada en BHMS. La estructura resultante es similar a las FPCA estudiadas, pero con la PRS reemplazada por una BHMS más versátil. Aunque ambas son esencialmente metasuperficies, difieren en sus metodologías de diseño subyacentes, por lo que la segunda puede considerarse una evolución de la primera. De este modo, la configuración LWA 1-D basada en BHMS estudiada anteriormente se extiende a una dimensión adicional, lo que aumenta la complejidad del análisis y ha dado lugar a un estudio exhaustivo de las propiedades modales de los campos guiados en la PPW radial. Al estipular rigurosamente los mismos modos guiados que existen en una FPCA, se ha logrado una comprensión más profunda de su comportamiento modal. Pero, lo que es más importante, el campo obtenido está contenido prácticamente en la misma dirección cartesiana a lo largo de toda la apertura, lo que permite generar haces de tipo lápiz (*pencil beam*) linealmente polarizados en direcciones arbitrarias. Este concepto también requiere un control adecuado de la magnitud y fase del campo en la apertura aunque, convenientemente, se ha evitado que las celdas unidad deban presentar capacidades de conversión de polarización gra-

cias a algunas suposiciones razonables en la derivación teórica. Así, se ha desarrollado una metodología de diseño clara, completa y que no depende de procesos de optimización numérica. Se han llevado a cabo algunos diseños con celdas unidad ideales que muestran diferentes capacidades de radiación. Finalmente, se ha observado una buena concordancia entre la teoría y las simulaciones, lo que pone de manifiesto el potencial del concepto presentado.

Las configuraciones de antena presentadas ofrecen una selección flexible de las características de diseño. Además, permiten el uso de una misma plataforma de guiado ya fabricada para obtener diferentes propiedades de radiación simplemente cambiando la metasuperficie utilizada. No obstante, si se desea una reconfiguración dinámica sin cambiar la metasuperficie, se hace evidente la necesidad de incorporar algún mecanismo que aporte reconfigurabilidad. En este contexto, como trabajo final de esta tesis, se ha llevado a cabo una caracterización experimental de cristales líquidos en una configuración habitual de dispositivo de microondas. Para ello, se ha utilizado el LC como sustrato de una línea microstrip fabricada mediante fabricación aditiva, que a su vez se encarga de su polarización. Se ha utilizado una técnica de enventanado temporal para el tratamiento de las medidas, la cual ha demostrado ser eficaz, ya que evita la necesidad de fabricar más de un prototipo y de cualquier otra calibración externa. Los resultados experimentales concuerdan con las simulaciones y permiten conocer de forma efectiva los rangos prácticos de permitividad en dispositivos reales de microondas, lo que servirá como guía útil para el diseño de antenas reconfigurables en el futuro.

D.2.1 Contribuciones originales

Si bien las técnicas de mejora del ancho de banda en las FPCA y de modulación espacial en LWA son bien conocidas dentro de la comunidad de investigación en antenas, la integración sistemática de ambos enfoques no se había abordado suficientemente en la bibliografía existente. Aquí radica la primera contribución original: una metodología que combina la óptica geométrica con la teoría de ondas de fuga para mejorar significativamente el producto directividad-ancho de banda de estas antenas (o, alternativamente, para moldear sus diagramas de radiación), requiriendo únicamente una única PRS grabada por ambas caras. Además, el estudio en profundidad sobre la excitación adecuada de los modos de la cavidad resulta también relevante en lo que respecta a las limitaciones fundamentales asociadas a la directividad máxima alcanzable y la capacidad de adaptación de impedancia.

Otra contribución destacada es la verificación satisfactoria del control completo del campo en la apertura en las LWA 1-D basadas en BHMS presentadas, superando las limitaciones identificadas en [6]. Los avances teóricos introducidos han permitido la

inclusión de un factor de fuga variable, manteniendo al mismo tiempo marco analítico riguroso. Esto elimina la necesidad de procesos de optimización tanto en la fase de diseño y como en la de simulación, a diferencia de otros enfoques recogidos en la literatura. Como resultado, el trabajo de esta tesis ha habilitado capacidades de conformación del diagrama de radiación para esta configuración de antena. Asimismo, el riguroso análisis de campo también ha aportado una mejor comprensión de las limitaciones asociadas a la fórmula del factor de fuga comúnmente utilizada en diseños de LWA moduladas espacialmente.

Además, también cabe destacar la aplicación del algoritmo semianalítico de síntesis de celdas unidad a la realización de BHMS para las LWA, ya que este método solo se había empleado anteriormente en escenarios incidencia de onda plana en espacio libre. El buen rendimiento demostrado por estas celdas ha facilitado la implementación eficiente de las BHMS diseñadas, tarea que habría sido mucho más larga y tediosa sin el uso de modelos circuitales precisos en términos de interacciones de campo cercano. Por otro lado, el estudio sobre celdas unidad de dos capas orientado a facilitar la implementación ha ayudado a comprender las posibilidades de esta configuración limitada en grados de libertad para realizar LWA basadas en BHMS.

Otra contribución significativa de esta tesis es el desarrollo de LWA bidimensionales basadas en BHMS dentro de una plataforma PPW, configuración que no se había encontrado previamente en la literatura. Cabe destacar que esta configuración permite la orientación de haces linealmente polarizados en todo un semiespacio utilizando una única metasuperficie, y sin necesidad de propiedades quirales. Además, el análisis es también completamente analítico, sin depender de la optimización numérica para la estipulación del campo, a diferencia de otras metodologías reportadas. La metodología presentada ofrece una selección versátil de varios parámetros de diseño como grados de libertad, lo que además permite superar algunas de las limitaciones previamente mencionadas de las FPCA. Dado que la BHMS es ahora la encargada de implementar la transformación de campo deseada sin estar limitada por el comportamiento de los modos guiados, de manera relevante ésto elimina la necesidad de satisfacer la condición clásica de *splitting* de las LWA y evita la operación cerca del corte, lo cual representa otra ventaja clara frente a las configuraciones FPCA convencionales.

Por último, la técnica de caracterización de LC propuesta, además de suficientemente precisa, ha demostrado ser más sencilla que otras que disponibles en la literatura, especialmente en entornos técnicos que carecen de equipamiento especializado para caracterizar materiales líquidos. A diferencia de la mayoría de los métodos existentes, resulta especialmente relevante que el enfoque basado en enventanado temporal adoptado en este trabajo solo requiera un único prototipo, lo que contribuye a reducir posibles problemas de repetibilidad asociados a los procesos de fabricación aditiva.

D.2.2 Trabajo futuro

Las siguientes ideas esbozan varias direcciones posibles para ampliar la investigación presentada en esta tesis:

- **Refinar la estipulación del campo en las LWA 2-D**

  Tal y como expuso en el Capítulo 5, las capacidades de orientación del haz de las LWA bidimensionales basadas en BHMS mostraron una degradación de sus características cuando la dirección azimutal deseada se aproximaba a $\phi = 0°$. Aunque estas discrepancias pueden deberse a las suposiciones teóricas realizadas, los resultados obtenidos requieren una investigación más detallada que permita identificar su causa subyacente. Como primer paso en dicho análisis, deberían determinarse numéricamente los modos guiados realmente excitados por la fuente utilizada, mediante una expansión modal adecuada de los campos que ésta genera. Este estudio podría conducir a un refinamiento de los campos estipulados, lo que potencialmente permitiría abordar las deficiencias de rendimiento observados.

- **Permitir factores de fuga variables en las LWA 2-D basadas en BHMS**

  Si bien la configuración LWA 1-D basada en BHMS ahora permite la modulación del factor de fuga, la estipulación de campo en la configuración 2-D se ha restringido, hasta ahora, a valores constantes de α. Una progresión lógica de este trabajo implicaría ampliar el marco teórico para dar cabida a factores de fuga que varíen espacialmente a lo largo de la apertura. Al igual que con las FPCA convencionales, ello permitiría la conformación del diagrama de radiación, así como una mejora tanto de la eficiencia de apertura como de la de iluminación.

- **Probar estipulación alternativa de campo radialmente simétrico**

  La idea anteriormente planteada podría verse dificultada por la coexistencia de dos modos guiados, cada uno de los cuales con características ligeramente diferentes y, en consecuencia, comportamientos de fuga distintos. Para simplificar la ingeniería de las propiedades de dispersión, una estrategia alternativa y potencialmente ventajosa sería emplear una estipulación de campo diferente en la LWA 2-D, basada en un único modo radialmente simétrico. No obstante, esto requeriría tener en cuenta componentes de campo electromagnético en ambas direcciones ortogonales y tangenciales a la BHMS, lo que podría hacer más compleja la obtención de los parámetros de metasuperficie, así como requerir capacidades de conversión de polarización. Investigar las ventajas e inconvenientes asociados a esta posible estipulación de campo e identificar las características de radiación alcanzables supondría una dirección valiosa para futuros trabajos.

- **Mejorar la eficiencia de las simulaciones de metasuperficies 2-D**

  La simulación electromagnética de metasuperficies presenta desafíos significativos relacionados con el tiempo de cómputo, el consumo de memoria y la fiabilidad de la convergencia. Estos problemas no resultaban tan críticos en el caso de las LWA unidimensionales, debido a su reducido espesor y al tamaño limitado del dominio de simulación, lo que permitía obtener resultados precisos en HFSS en pocas horas, incluso con celdas unidad realistas. Sin embargo, el aumento cuadrático del tamaño del dominio computacional en metasuperficies bidimensionales, que además presentan multitud de elementos mucho menores a la longitud de onda, supone una carga considerable para los simuladores de propósito general, dificultando a menudo la obtención de una convergencia adecuada. Por lo tanto, un paso inmediato a considerar consiste en explorar estrategias para hacer las simulaciones más eficientes, incluyendo el uso de simuladores alternativos, ya sean herramientas comerciales o implementaciones personalizadas adaptadas a las particularidades de este tipo de estructuras.

- **Dotar a las LWA de reconfigurabilidad basada en LC**

  La implementación de capacidades de orientación dinámica del haz requiere la incorporación de algún mecanismo de reconfiguración. Aprovechando los materiales LC caracterizados, sería interesante incluirlos en las configuraciones LWA estudiadas. Dado que introducir LC dentro de las metasuperficies sería muy complicado, un enfoque más razonable sería rellenar parcialmente la guíaonda con el líquido. Este enfoque ya está siendo objeto de estudio preliminar en el grupo de investigación, si bien se requiere una investigación más profunda para integrar estos materiales de forma eficaz sin que ello implique un aumento significativo de las pérdidas o en la complejidad de fabricación.

- **Incorporar mecanismos de reconfiguración en las celdas unidad**

  Otra estrategia para habilitar la reconfiguración dinámica de las antenas estudiadas consiste en integrar mecanismos de sintonización directamente en el diseño de la celda unidad, tal y como se propone en diversos trabajos en la literatura. La configuración de celda unidad de dos capas estudiada en el Apéndice B ofrece una clara ventaja en este contexto, ya que permite reducir la complejidad de la implementación. Minimizar el número de elementos sintonizables por celda unidad también sería esencial para simplificar el control y la fabricación. La elección de los componentes de sintonización, como puedan ser los varactores, debe realizarse con especial cuidado para garantizar pérdidas mínimas, de modo que no limiten en exceso los parámetros S locales alcanzables, como ya se ha observado teóricamente.

- **Uso de técnicas multimodales para el modelado de celdas unidad arbitrarias**

  En relación con el punto anterior, también puede ayudar en el proceso de síntesis el uso de modelos circuitales que tengan en cuenta de manera precisa los efectos de acoplo de campo cercano, como el empleado en el Capítulo 4 pero generalizado a geometrías arbitrarias. Para ello, se podrían emplear técnicas multimodales como la detallada en [114].

Bibliography

[1] A. Hessel, "General characteristics of travelling-wave antennas," in *Antenna Theory*, R. Collin and F. Zucker, Eds. McGraw-Hill, 1969, no. part 2, ch. 19.

[2] P. Burghignoli, W. Fuscaldo, and A. Galli, "Fabry–Pérot cavity antennas: The leaky-wave perspective," *IEEE Antennas and Propagation Magazine*, vol. 63, no. 4, pp. 116–145, Aug. 2021.

[3] C. L. Holloway, E. F. Kuester, J. A. Gordon, J. O'Hara, J. Booth, and D. R. Smith, "An overview of the theory and applications of metasurfaces: The two-dimensional equivalents of metamaterials," *IEEE Antennas and Propagation Magazine*, vol. 54, no. 2, pp. 10–35, Apr. 2012.

[4] O. Quevedo-Teruel *et al.*, "Roadmap on metasurfaces," *Journal of Optics*, vol. 21, no. 7, p. 073002, Jul. 2019.

[5] M. Faenzi *et al.*, "Metasurface antennas: New models, applications and realizations," *Scientific Reports*, vol. 9, 12 2019.

[6] E. Abdo-Sánchez, M. Chen, A. Epstein, and G. V. Eleftheriades, "A leaky-wave antenna with controlled radiation using a bianisotropic Huygens' metasurface," *IEEE Transactions on Antennas and Propagation*, vol. 67, no. 1, pp. 108–120, 2019.

[7] A. A. Oliner, "Leaky-wave antennas," in *Antenna Engineering Handbook*, 3rd ed., R. C. Johnson, Ed. Georgia: McGraw-Hill, 1993, ch. 10.

[8] D. R. Jackson, C. Caloz, and T. Itoh, "Leaky-wave antennas," in *Proceedings of the IEEE*, vol. 100. Institute of Electrical and Electronics Engineers Inc., 2012, pp. 2194–2206.

[9] A. Galli, P. Baccarelli, and P. Burghignoli, "Leaky-wave antennas," in *Wiley Encyclopedia of Electrical and Electronics Engineering*. Hoboken, NJ, USA: John Wiley & Sons, Inc., May 2016, pp. 1–20.

[10] D. R. Jackson and A. A. Oliner, "Leaky-wave antennas," in *Modern Antenna Handbook*. John Wiley & Sons, Ltd, 2008, ch. 7, pp. 325–367.

[11] A. Ip and D. R. Jackson, "Radiation from cylindrical leaky waves," *IEEE Transactions on Antennas and Propagation*, vol. 38, no. 4, pp. 482–488, 1990.

[12] G. Lovat, P. Burghignoli, and D. Jackson, "Fundamental properties and optimization of broadside radiation from uniform leaky-wave antennas," *IEEE Transactions on Antennas and Propagation*, vol. 54, no. 5, pp. 1442–1452, May 2006.

[13] C. A. Balanis, *Antenna theory: analysis and design*, 3rd ed. Wiley-Interscience, 2005.

[14] R. Honey, "A flush-mounted leaky-wave antenna with predictable patterns," *IRE Transactions on Antennas and Propagation*, vol. 7, no. 4, pp. 320–329, 1959.

[15] M. Takahashi, J. I. Takada, M. Ando, and N. Goto, "A slot design for uniform aperture field distribution in single-layered radial line slot antennas," *IEEE Transactions on Antennas and Propagation*, vol. 39, no. 7, pp. 954–959, 1991.

[16] J. D. Joannopoulos, S. G. Johnson, J. N. Winn, and R. D. Meade, *Photonic crystals: molding the flow of light*, 2nd ed. Princeton Oxford: Princeton University Press, 2008.

[17] R. Marks and D. Williams, "A general waveguide circuit theory," *Journal of Research of the National Institute of Standards and Technology*, vol. 97, no. 5, p. 533, Sep. 1992.

[18] D. M. Pozar, *Microwave engineering*, 4th ed. Hoboken, NJ: Wiley, 2012.

[19] C. Huygens, *Traité de la Lumière*. Leiden, Netherlands: Pierre vander Aa, 1690.

[20] A. Ghaneizadeh and M. Joodaki, "Generalized sheet transition conditions (GSTCs) in electromagnetic metasurface modeling," *IEEE Access*, vol. 12, pp. 74 305–74 326, 2024.

[21] V. G. Ataloglou, M. Chen, M. Kim, and G. V. Eleftheriades, "Microwave Huygens' metasurfaces: Fundamentals and applications," *IEEE Journal of Microwaves*, vol. 1, no. 1, pp. 374–388, Jan. 2021.

[22] A. Epstein and G. V. Eleftheriades, "Passive lossless Huygens metasurfaces for conversion of arbitrary source field to directive radiation," *IEEE Transactions on Antennas and Propagation*, vol. 62, no. 11, pp. 5680–5695, Nov. 2014.

[23] ——, "Arbitrary power-conserving field transformations with passive lossless omega-type bianisotropic metasurfaces," *IEEE Transactions on Antennas and Propagation*, vol. 64, no. 9, pp. 3880–3895, Sep. 2016.

[24] M. Chen, "Design and applications of printed-circuit-board Huygens' metasurfaces," Ph.D. dissertation, University of Toronto, 2021. [Online]. Available: http://hdl.handle.net/1807/106482

[25] A. Epstein and G. V. Eleftheriades, "Huygens' metasurfaces via the equivalence

principle: design and applications," *J. Opt. Soc. Am. B*, vol. 33, no. 2, pp. A31–A50, Feb 2016.

[26] G. Trentini, "Partially reflecting sheet arrays," *IRE Transactions on Antennas and Propagation*, vol. 4, no. 4, pp. 666–671, Oct. 1956.

[27] Q. Wang, J. Qi, and A. Sihvola, "A triple-band uni-cavity Fabry–Pérot cavity antenna with hybrid excitation modes," *IEEE Transactions on Antennas and Propagation*, vol. 71, no. 6, pp. 4851–4861, 2023.

[28] R. De, M. P. Abegaonkar, and A. Basu, "A broadband circularly polarized Fabry Pérot antenna with spatially separated superstrate area excitation for CubeSat applications," *Scientific Reports*, vol. 13, p. 11224, 2023.

[29] W. Li *et al.*, "Polarization-reconfigurable circularly polarized planar antenna using switchable polarizer," *IEEE Transactions on Antennas and Propagation*, vol. 65, no. 9, pp. 4470–4477, 2017.

[30] Z. Liu, S. Liu, X. Zhao, X. Kong, Z. Huang, and B. Bian, "Wideband gain enhancement and RCS reduction of Fabry–Pérot antenna using hybrid reflection method," *IEEE Transactions on Antennas and Propagation*, vol. 68, no. 9, pp. 6497–6505, 2020.

[31] A. P. Feresidis and J. C. Vardaxoglou, "A broadband high-gain resonant cavity antenna with single feed," in *Proceedings of the First European Conference on Antennas and Propagation (EuCAP)*, Nice, France, Nov. 2006, pp. 1–5.

[32] N. Wang, Q. Liu, C. Wu, L. Talbi, Q. Zeng, and J. Xu, "Wideband Fabry-Pérot resonator antenna with two complementary FSS layers," *IEEE Transactions on Antennas and Propagation*, vol. 62, no. 5, pp. 2463–2471, May 2014.

[33] K. Konstantinidis, A. P. Feresidis, and P. S. Hall, "Multilayer partially reflective surfaces for broadband Fabry-Pérot cavity antennas," *IEEE Transactions on Antennas and Propagation*, vol. 62, no. 7, pp. 3474–3481, 2014.

[34] C. Mateo-Segura, A. P. Feresidis, and G. Goussetis, "Bandwidth enhancement of 2-D leaky-wave antennas with double-layer periodic surfaces," *IEEE Transactions on Antennas and Propagation*, vol. 62, no. 2, pp. 586–593, 2014.

[35] A. A. Baba, R. M. Hashmi, K. P. Esselle, and A. R. Weily, "Compact high-gain antenna with simple all-dielectric partially reflecting surface," *IEEE Transactions on Antennas and Propagation*, vol. 66, no. 8, pp. 4343–4348, 2018.

[36] M. Hussain, K.-G. Lee, and D. Kim, "Tapered high-gain Fabry–Pérot cavity antenna with high sidelobe suppression for 5G industry," *Scientific Reports*, vol. 13, no. 1, p. 15744, Sep. 2023.

[37] D. R. Jackson *et al.*, "The fundamental physics of directive beaming at microwave

and optical frequencies and the role of leaky waves," *Proceedings of the IEEE*, vol. 99, no. 10, pp. 1780–1805, Oct. 2011.

[38] A. T. Almutawa, A. Hosseini, D. R. Jackson, and F. Capolino, "Leaky-wave analysis of wideband planar Fabry–Pérot cavity antennas formed by a thick PRS," *IEEE Transactions on Antennas and Propagation*, vol. 67, no. 8, pp. 5163–5175, Aug. 2019.

[39] S. Sengupta, D. R. Jackson, A. T. Almutawa, H. Kazemi, F. Capolino, and S. A. Long, "Radiation properties of a 2-D periodic leaky-wave antenna," *IEEE Transactions on Antennas and Propagation*, vol. 67, no. 6, pp. 3560–3573, Jun. 2019.

[40] M. Garcia-Vigueras, P. DeLara-Guarch, J. L. Gomez-Tornero, R. Guzman-Quiros, and G. Goussetis, "Efficiently illuminated broadside-directed 1D and 2D tapered Fabry-Pérot leaky-wave antennas," in *Proceedings of the 6th European Conference on Antennas and Propagation (EuCAP)*, Prague, Czech Republic, Mar. 2012, pp. 247–251.

[41] Y. Ge, K. P. Esselle, and T. S. Bird, "The use of simple thin partially reflective surfaces with positive reflection phase gradients to design wideband, low-profile EBG resonator antennas," *IEEE Transactions on Antennas and Propagation*, vol. 60, no. 2, pp. 743–750, Feb. 2012.

[42] L. Zhou, X. Duan, Z. Luo, Y. Zhou, and X. Chen, "High directivity Fabry–Pérot antenna with a nonuniform partially reflective surface and a phase correcting structure," *IEEE Transactions on Antennas and Propagation*, vol. 68, no. 11, pp. 7601–7606, 2020.

[43] K. Konstantinidis, A. P. Feresidis, and P. S. Hall, "Dual-slot feeding technique for broadband Fabry–Pérot cavity antennas," *IET Microwaves, Antennas & Propagation*, vol. 9, no. 9, pp. 861–866, 2015.

[44] E. Negri, W. Fuscaldo, S. Tofani, P. Burghignoli, and A. Galli, "An efficient and accurate semi-analytical matching technique for waveguide-fed antennas," *Scientific Reports*, vol. 14, no. 1, p. 3892, Feb. 2024.

[45] R. M. Foster, "A reactance theorem," *Bell System Technical Journal*, vol. 3, no. 2, pp. 259–267, Apr. 1924.

[46] M. Poveda-Garcia and J. L. Gomez-Tornero, "Spectral analysis of broadband Fabry–Pérot antennas with multiple coupled cavities," *IEEE Transactions on Antennas and Propagation*, vol. 70, no. 1, pp. 167–179, Jan. 2022.

[47] J. L. Gomez-Tornero, D. Blanco, E. Rajo-Iglesias, and N. Llombart, "Holographic surface leaky-wave lenses with circularly-polarized focused near-fields - Part I:

Concept, design and analysis theory," *IEEE Transactions on Antennas and Propagation*, vol. 61, no. 7, pp. 3475–3485, 2013.

[48] A. Hosseini, F. De Flaviis, and F. Capolino, "Design formulas for planar Fabry–Pérot cavity antennas formed by thick partially reflective surfaces," *IEEE Transactions on Antennas and Propagation*, vol. 64, no. 12, pp. 5487–5491, Dec. 2016.

[49] Y.-F. Lu and Y.-C. Lin, "A hybrid approach for finite-size Fabry-Pérot antenna design with fast and accurate estimation on directivity and aperture efficiency," *IEEE Transactions on Antennas and Propagation*, vol. 61, no. 11, pp. 5395–5401, 2013.

[50] "Flat top weighted window," The MathWorks Inc., Natick, Massachusetts, United States, 2024. [Online]. Available: https://www.mathworks.com/help/signal/ref/flattopwin.html

[51] G. B. Wu, Q. L. Zhang, K. F. Chan, B. J. Chen, and C. H. Chan, "Amplitude-modulated leaky-wave antennas," *IEEE Transactions on Antennas and Propagation*, vol. 69, pp. 3664–3676, 7 2021.

[52] A. Araghi, M. Khalily, P. Xiao, and R. Tafazolli, "Holographic-based leaky-wave structures: Transformation of guided waves to leaky waves," *IEEE Microwave Magazine*, vol. 22, pp. 49–63, 6 2021.

[53] A. J. Martinez-Ros, J. L. Gomez-Tornero, and G. Goussetis, "Planar leaky-wave antenna with flexible control of the complex propagation constant," *IEEE Transactions on Antennas and Propagation*, vol. 60, no. 3, pp. 1625–1630, Mar. 2012.

[54] C. Pfeiffer and A. Grbic, "Planar lens antennas of subwavelength thickness: Collimating leaky-waves with metasurfaces," *IEEE Transactions on Antennas and Propagation*, vol. 63, no. 7, pp. 3248–3253, 2015.

[55] A. Epstein, J. P. S. Wong, and G. V. Eleftheriades, "Cavity-excited Huygens' metasurface antennas for near-unity aperture illumination efficiency from arbitrarily large apertures," *Nature Communications*, vol. 7, no. 1, p. 10360, Jan. 2016.

[56] M. Teniou, H. Roussel, N. Capet, G. P. Piau, and M. Casaletti, "Implementation of radiating aperture field distribution using tensorial metasurfaces," *IEEE Transactions on Antennas and Propagation*, vol. 65, pp. 5895–5907, 11 2017.

[57] G. Minatti, E. Martini, and S. Maci, "Efficiency of metasurface antennas," *IEEE Transactions on Antennas and Propagation*, vol. 65, pp. 1532–1541, 4 2017.

[58] V. G. Ataloglou and G. V. Eleftheriades, "Arbitrary wave transformations with Huygens' metasurfaces through surface-wave optimization," *IEEE Antennas and Wireless Propagation Letters*, vol. 20, no. 9, pp. 1750–1754, 2021.

[59] A. M. Patel and A. Grbic, "A printed leaky-wave antenna based on a sinusoidally-modulated reactance surface," *IEEE Transactions on Antennas and Propagation*, vol. 59, no. 6, pp. 2087–2096, 2011.

[60] B. B. Tierney and A. Grbic, "Controlling leaky waves with 1-D cascaded metasurfaces," *IEEE Transactions on Antennas and Propagation*, vol. 66, pp. 2143–2146, 4 2018.

[61] S. N. Tcvetkova, E. Martini, S. A. Tretyakov, and S. Maci, "Perfect conversion of a TM surface wave into a TM leaky wave by an isotropic periodic metasurface printed on a grounded dielectric slab," *IEEE Transactions on Antennas and Propagation*, vol. 68, pp. 6145–6153, 8 2020.

[62] C. Pfeiffer and A. Grbic, "Metamaterial Huygens' surfaces: Tailoring wave fronts with reflectionless sheets," *Phys. Rev. Lett.*, vol. 110, p. 197401, May 2013.

[63] F. Monticone, N. M. Estakhri, and A. Alù, "Full control of nanoscale optical transmission with a composite metascreen," *Phys. Rev. Lett.*, vol. 110, p. 203903, May 2013.

[64] M. Selvanayagam and G. V. Eleftheriades, "Discontinuous electromagnetic fields using orthogonal electric and magnetic currents for wavefront manipulation," *Opt. Express*, vol. 21, no. 12, pp. 14 409–14 429, Jun 2013.

[65] V. Popov *et al.*, "Omega-bianisotropic metasurface for converting a propagating wave into a surface wave," *Physical Review B*, vol. 100, p. 125103, 9 2019.

[66] P. Ang, G. Xu, and G. V. Eleftheriades, "Invisibility cloaking with passive and active Huygens's metasurfaces," *Applied Physics Letters*, vol. 118, p. 71903, 2 2021.

[67] A. Mehdipour, J. W. Wong, and G. V. Eleftheriades, "Beam-squinting reduction of leaky-wave antennas using Huygens metasurfaces," *IEEE Transactions on Antennas and Propagation*, vol. 63, pp. 978–992, 3 2015.

[68] H. Lee and D. H. Kwon, "Printed metasurface leaky wave antennas based on penetrable aperture field synthesis," *IEEE Transactions on Antennas and Propagation*, vol. 71, pp. 4724–4736, 6 2023.

[69] R. F. Harrington, *Time-harmonic electromagnetic fields*, ser. IEEE Press series on electromagnetic wave theory. New York: IEEE Press : Wiley-Interscience, 2001.

[70] C. Di Nallo, F. Frezza, A. Galli, and P. Lampariello, "Rigorous evaluation of ohmic-loss effects for accurate design of traveling-wave antennas," *Journal of Electromagnetic Waves and Applications*, vol. 12, no. 1, pp. 39–58, Jan. 1998.

[71] J. L. Gómez-Tornero, G. Goussetis, and A.Álvarez-Melcón, "Correction of dielec-

tric losses in practical leaky-wave antenna designs," *Journal of Electromagnetic Waves and Applications*, vol. 21, no. 8, pp. 1025–1036, Jan. 2007.

[72] W. Fuscaldo, "Rigorous evaluation of losses in uniform leaky-wave antennas," *IEEE Transactions on Antennas and Propagation*, vol. 68, no. 2, pp. 643–655, Feb. 2020.

[73] W. Fuscaldo, A. Galli, and D. R. Jackson, "Optimization of 1-D unidirectional leaky-wave antennas based on partially reflecting surfaces," *IEEE Transactions on Antennas and Propagation*, vol. 70, no. 9, pp. 7853–7868, Sep. 2022.

[74] E. Abdo-Sánchez, A. Epstein, and G. V. Eleftheriades, "Reconfigurability mechanisms with scanning rate control for omega-bianisotropic Huygens' metasurface leaky-wave antennas," *IEEE Access*, vol. 7, pp. 168 247–168 260, 2019.

[75] C. Pfeiffer and A. Grbic, "Bianisotropic metasurfaces for optimal polarization control: Analysis and synthesis," *Phys. Rev. Appl.*, vol. 2, p. 044011, Oct 2014.

[76] G. Xu, S. V. Hum, and G. V. Eleftheriades, "Augmented Huygens' metasurfaces employing baffles for precise control of wave transformations," *IEEE Transactions on Antennas and Propagation*, vol. 67, no. 11, pp. 6935–6946, 2019.

[77] *RO3000® Series Circuit Materials*, Rogers Corporation, 2024, rev. 1687 013024. [Online]. Available: https://rogerscorp.com/advanced-electronics-solutions/ro3000-series-laminates/ro3003-laminates

[78] *2929 Bondply Data Sheet*, Rogers Corporation, 2022, rev. 1584 072822. [Online]. Available: https://rogerscorp.com/advanced-electronics-solutions/2929-bondply

[79] S. Levy, Y. Kerzhner, and A. Epstein, "Rigorous analytical model for metasurface microscopic design with interlayer coupling," in *2019 IEEE International Symposium on Antennas and Propagation and USNC-URSI Radio Science Meeting*, 2019, pp. 195–196.

[80] O. Rabinovich and A. Epstein, "Arbitrary diffraction engineering with multilayered multielement metagratings," *IEEE Transactions on Antennas and Propagation*, vol. 68, no. 3, pp. 1553–1568, 2020.

[81] V. K. Killamsetty and A. Epstein, "Semianalyitcal synthesis scheme for multifunctional metasurfaces on demand," in *2021 Fifteenth International Congress on Artificial Materials for Novel Wave Phenomena (Metamaterials)*, 2021, pp. 123–125.

[82] S. Kuznetsov, M. Tumashov, V. K. Killamsetty, P. Lazorskiy, A. Epstein, and S. Glybovski, "Efficient anomalous refraction of THz beams with a multilayer metal–polymer Huygens' metasurface," *IEEE Transactions on Terahertz Science and Technology*, vol. 14, no. 1, pp. 109–121, 2024.

[83] J. Coonrod, "Understanding the variables of dielectric constant for PCB materials

used at microwave frequencies," in *2011 41st European Microwave Conference*, 2011, pp. 938–944.

[84] G. Minatti, F. Caminita, E. Martini, M. Sabbadini, and S. Maci, "Synthesis of modulated-metasurface antennas with amplitude, phase, and polarization control," *IEEE Transactions on Antennas and Propagation*, vol. 64, pp. 3907–3919, 9 2016.

[85] M. Kim and G. V. Eleftheriades, "Design and demonstration of impedance-matched dual-band chiral metasurfaces," *Scientific Reports*, vol. 8, no. 1, p. 3449, Feb. 2018.

[86] G. Minatti, F. Caminita, M. Casaletti, and S. Maci, "Spiral leaky-wave antennas based on modulated surface impedance," *IEEE Transactions on Antennas and Propagation*, vol. 59, no. 12, pp. 4436–4444, 2011.

[87] C. A. Balanis, *Advanced Engineering Electromagnetics*. Wiley, 1999.

[88] D. González-Ovejero and S. Maci, "Gaussian ring basis functions for the analysis of modulated metasurface antennas," *IEEE Transactions on Antennas and Propagation*, vol. 63, no. 9, pp. 3982–3993, 2015.

[89] D. C. Zografopoulos, A. Ferraro, and R. Beccherelli, "Liquid-crystal high-frequency microwave technology: Materials and characterization," *Advanced Materials Technologies*, vol. 4, no. 2, p. 1800447, 2019.

[90] A. Alex-Amor, Á. Palomares-Caballero, A. F. Palomares-Bautista, A. Tamayo-Domínguez, J. M. Fernández-González, and P. Padilla, "Generalized director approach for liquid-crystal-based reconfigurable RF devices," *IEEE Microwave and Wireless Components Letters*, vol. 29, no. 10, pp. 634–637, 2019.

[91] G. Perez-Palomino *et al.*, "Accurate and efficient modeling to calculate the voltage dependence of liquid crystal-based reflectarray cells," *IEEE Transactions on Antennas and Propagation*, vol. 62, no. 5, pp. 2659–2668, 2014.

[92] R. Guirado, P. De La Rosa, G. Perez-Palomino, M. Caño-García, E. Carrasco, and X. Quintana, "Characterization and application of dual-frequency liquid-crystal mixtures in mm-wave reflectarray cells to improve their temporal response," *IEEE Transactions on Antennas and Propagation*, vol. 71, no. 8, pp. 6535–6545, Aug. 2023.

[93] R. Tchema, N. C. Papanicolaou, and A. C. Polycarpou, "An investigation of the dynamic beam-steering capability of a liquid-crystal-enabled leaky-wave antenna designed for 5G applications," *Applied Physics Letters*, vol. 119, no. 3, p. 034104, 07 2021.

[94] T. Lira-Valdés, P. Mateos-Ruiz, and E. Abdo-Sánchez, "Liquid crystal reconfigurable leaky-wave antenna with Huygens' metasurface and gap waveguide," in

2025 19th European Conference on Antennas and Propagation (EuCAP), 2025, pp. 1–5.

[95] J. Parka, J. Krupka, R. Dąbrowski, and J. Wosik, "Measurements of anisotropic complex permittivity of liquid crystals at microwave frequencies," *Journal of the European Ceramic Society*, vol. 27, no. 8, pp. 2903–2905, 2007.

[96] H. Peng, Y. Zhang, S. Zhu, M. Temiz, and A. El-Makadema, "Determining dielectric properties of nematic liquid crystals at microwave frequencies using inverted microstrip lines," *Liquid Crystals*, vol. 49, pp. 2069–2081, 12 2022.

[97] V. Nova, C. Bachiller, B. Villacampa, R. Kronberger, and V. E. Boria, "Characterization of nematic liquid crystals at microwave frequencies," *Crystals*, vol. 10, no. 12, 2020.

[98] M. Yazdanpanahi, S. Bulja, D. Mirshekar-Syahkal, R. James, S. E. Day, and F. A. Fernandez, "Measurement of dielectric constants of nematic liquid crystals at mm-wave frequencies using patch resonator," *IEEE Transactions on Instrumentation and Measurement*, vol. 59, no. 12, pp. 3079–3085, 2010.

[99] P. Deo, D. Mirshekar-Syahkal, L. Seddon, S. E. Day, and F. A. Fernández, "Microstrip device for broadband (15–65 GHz) measurement of dielectric properties of nematic liquid crystals," *IEEE Transactions on Microwave Theory and Techniques*, vol. 63, no. 4, pp. 1388–1398, April 2015.

[100] M. El Kadiri, J. P. Parneix, and A. Chapoton, "General time domain analysis of T.D.S. data: Application to liquid crystals," *IEEE Transactions on Instrumentation and Measurement*, vol. IM-34, no. 1, pp. 70–74, 1985.

[101] K. Fidanboylu, S. Riad, and A. Elshabini-Riad, "An enhanced time-domain approach for dielectric characterization using stripline geometry," *IEEE Transactions on Instrumentation and Measurement*, vol. 41, no. 1, pp. 132–136, 1992.

[102] B. Archambeault, S. Connor, and J. Diepenbrock, "Time domain gating of frequency domain S-parameter data to remove connector end effects for PCB and cable applications," in *2006 IEEE International Symposium on Electromagnetic Compatibility, 2006. EMC 2006.*, vol. 1, 2006, pp. 199–202.

[103] A. M. H. Nasr, A. Y. Nashashibi, and K. Sarabandi, "Ultrawideband characterization of complex dielectric constant of planar materials for 5G applications," *IEEE Transactions on Instrumentation and Measurement*, vol. 70, no. 6009911, pp. 1–11, 2021.

[104] H.-J. Eul and B. Schiek, "A generalized theory and new calibration procedures for network analyzer self-calibration," *IEEE Transactions on Microwave Theory and Techniques*, vol. 39, no. 4, pp. 724–731, 1991.

[105] K. Silvonen, "Calibration of test fixtures using at least two standards (microwave

circuits)," *IEEE Transactions on Microwave Theory and Techniques*, vol. 39, no. 4, pp. 624–630, 1991.

[106] M. Pérez-Escribano and E. Márquez-Segura, "Random errors in broadband characterization of the propagation constant of transmission lines using multiple two-port measurements," *IEEE Access*, vol. 9, pp. 59 038–59 047, 2021.

[107] ——, "End-launcher repeatability in broadband methods for characterization of the propagation constant of transmission lines using two-port measurements," *IEEE Transactions on Instrumentation and Measurement*, vol. 71, pp. 1–4, 2022.

[108] ——, "Parameters characterization of dielectric materials samples in microwave and millimeter-wave bands," *IEEE Transactions on Microwave Theory and Techniques*, vol. 69, no. 3, pp. 1723–1732, 2021.

[109] Cadence ®, "TDR Gating Python Script - AWR Scripts," https://kb.awr.com/display/awrscripts/TDR+Gating+Python+Script, Last accessed on 2023-10-27.

[110] M. Couker and L. Kushner, "A microstrip phase-trim device using a dielectric overlay," *IEEE Transactions on Microwave Theory and Techniques*, vol. 42, pp. 2023–2026, 1994.

[111] A. Verma and G. Sadr, "Unified dispersion model for multilayer microstrip line," *IEEE Transactions on Microwave Theory and Techniques*, vol. 40, no. 7, pp. 1587–1591, 1992.

[112] D.-K. Yang and S.-T. Wu, *Fundamentals of liquid crystal devices*, ser. Wiley SID series in display technology. John Wiley & Sons, Ltd, 2006.

[113] R. Guirado, G. Perez-Palomino, M. Ferreras, E. Carrasco, and M. Cano-Garcia, "Dynamic modeling of liquid crystal-based metasurfaces and its application to reducing reconfigurability times," *IEEE Transactions on Antennas and Propagation*, vol. 70, pp. 11 847–11 857, 12 2022.

[114] F. Mesa, G. Valerio, R. Rodriguez-Berral, and O. Quevedo-Teruel, "Simulation-assisted efficient computation of the dispersion diagram of periodic structures: A comprehensive overview with applications to filters, leaky-wave antennas and metasurfaces," *IEEE Antennas and Propagation Magazine*, vol. 63, no. 5, pp. 33–45, Oct. 2021.

[115] P. Burghignoli, F. Frezza, A. Galli, and G. Schettini, "Synthesis of broad-beam patterns through leaky-wave antennas with rectilinear geometry," *IEEE Antennas and Wireless Propagation Letters*, vol. 2, pp. 136–139, 2003.

[116] C. Qi and A. M. H. Wong, "Discrete Huygens' metasurface: Realizing anomalous refraction and diffraction mode circulation with a robust, broadband and simple design," *IEEE Transactions on Antennas and Propagation*, vol. 70, no. 8, pp. 7300–7305, 2022.